

**Synthesis and evaluation of charge transport
property of ethynylene-bridged π -conjugated
system**

エチニレンで架橋された π 共役系化合物の合成と電
荷輸送特性評価に関する研究

A dissertation submitted
in partial fulfillment of the requirements for the degree of
Doctor of Philosophy in Engineering

Juanjuan Zhu

September 2021

Laboratory of Functional Organic Chemistry

Graduate School of Materials Science

Nara Institute of Science and Technology

Table of Contents

Chapter 1	1
General Introduction	
.....	1
1-1. Background on Organic field-effect transistors (OFETs)	2
1-2. Techniques for the fabrication of active layer in OFETs	5
1-2-1. Dip-coating technique	5
1-2-2. Drop-casting technique.....	6
1-3. Arylethylenes as molecular core for π-conjugated system	6
1-4. Aims and Outline	17
1-5. Reference	19
Chapter 2	24
Single Crystal Field-Effect Transistor of Tetrabenzoporphyrin with One-Dimensionally Extended Columnar Packing Motif Exhibiting Efficient Charge Transport Property	
.....	24
2-1. Introduction	25
2-2. Growth single crystals	29
2-3. X-ray single crystal structure	30
2-4. Out of plane XRD analysis	34
2-5. TEM and corresponding SAED patterns	37
2-6. Charge carrier mobility	39
2-7. Summary and outlook	44
2-8. Experimental Section	45
2-8-1. General: Materials and Methods	45
2-8-2. Morphology predictions	45
2-8-3. Fabrication and evaluation of the SC-OFFTs	46
2-9. Reference	47

Chapter 3. 52
Synthesis and Evaluation of Charge Transport Property of Ethynylene-bridged Anthracene Oligomers

..... **52**

3-1. Introduction 53

3-2. Molecular design and synthesis 57

3-3. Optical properties 59

3-4. Electrochemical properties 61

3-5. Thermal stability of anthracene-based oligomers 64

3-6. Solid state structure 65

3-7. Film Morphology of 2mer and 3mer 74

3-8. Molecular Orientation of anthracene-based oligomers 76

3-9. Charge-carrier mobilities 80

3-10. Summary and outlook 85

3-11. Experimental section 86

 3-11-1. General 86

 3-11-2. Synthetic procedures 87

3-12. Reference 99

3-13. Supporting information 103

 3-13-1. NMR spectrum 103

 3-13-2. MS spectrum 117

Chapter 4. 123
Conventional Reaction with Quinone and Lithiated Silylethynylene to Generate Long Ethynylene-bridged Oligomers in One-pot

..... **123**

4-1. Introduction 124

4-2. Synthesis of ethynylene-bridged pentacene dimer with TMSethynylene 126

4-3. Synthesis of ethynylene-bridged heptacene dimer 129

4-4. Oligomerization of ethynylene-bridged BCODquinone 140

4-5. Thermal conversion reaction of BCOD oligomers 144

4-7. Summary and outlook 149

4-8. Experimental section 150

 4-8-1. General: Materials and methods 150

4-8-2. Synthetic procedures.....	152
4-8-3. NMR spectrum.....	157
4-8-4. MS spectrum.....	174
4-9. Reference.....	183
Chapter 5.....	185
General Conclusion.....	185
List of Achievements.....	187
Acknowledgements.....	190

Abbreviations

1D: One-dimensional

2D: Two-dimensional

ADF: Amsterdam density functional

BP: Tetrabenzoporphyrin

BCOD: Bicyclo[2.2.2]octadiene

BGTC: Bottom-gate-top-contact

BFDH: Bravais–Friedel–Donnay–Harker

BHJ: Bulk heterojunction

CS₂: Carbon disulfide

CV: Cyclic voltammetry

CDPA: 12-cyclohexyldodecyl-phosphonic acid

CP: 1,4:8,11:15,18:22,25-tetraethano-29*H*,31*H*-tetrabenzo[*b,g,l,q*]porphyrin

Dip-TIPS: 6,6'-linked pentacene dimer

DPA: Di-anthrylene-ethynylene

DPV: Differential pulse voltammetry

DCM: Dichloromethane

HOMO: Highest occupied molecular orbital

H-Ant: 1,2-di(anthracen-9-yl)ethyne

HRMS: High resolution mass spectrum

LUMO: Lowest unoccupied molecular orbital

μ : Charge-carrier mobility

μ_h : Charge-carrier hole-mobility

m.p.: Melting point

MeOH: Methanol

MALDI-TOF-MS: Matrix-assisted laser desorption ionization–time of flight mass spectrometry

MOSFET: Metal-oxide-semiconductor field-effect transistor

***n*-BuLi:** *n*-butyllithium

NMR: Nuclear magnetic resonance

OFET: Organic field-effect transistor

OLED: Organic light emitting display

OSC: Organic semiconductor

OTS: Octadecyltrichlorosilane

POM: Polarized optical microscope

PCE: Power conversion efficiency

RT: Room temperature

SCFET: Single-crystal field-effect transistor

SAED: Selected area electron diffraction

SiO₂: Silicon oxide

SAM: Self-assembled monolayer

TIPS: Triisopropylsilyl

TMS: Trimethylsilyl

THF: Tetrahydrofuran

TEM: Transmission electron microscopy

TGA: Thermogravimetric analysis

TLC: Thin-layer chromatography

TBAF: Tetrabutylammonium fluoride

TIPS-PenD: 6,6'-linked (triisopropylsilylethynyl) ethynylene-bridged pentacene dimer

TIPS-Pen: 6,13-bis(triisopropylsilylethynyl)pentacene

TIPS-BP: 5,15-bis(triisopropylsilylethynyl) tetrabenzoporphyrin

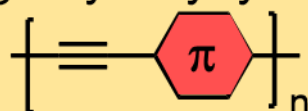
IR: Infrared spectroscopy

XRD: Out-of-plane X-ray diffraction

Chapter 1.

General Introduction

Oligoarylethynylenes



This dissertation focuses on the triple bond containing system, namely oligoarylethynylene. Tetrabenzoporphyrin and acenes were chosen as the π -conjugated core. In addition, the relationship between the packing structure, morphology and charge transport property were investigated in this dissertation.

Understanding the advantages of triple bond containing system is important for fine-tuning of molecular design. In this chapter, representative examples of ethynylene-bridged π -conjugated systems applied in the electronic devices were summarized to understand the excellent properties derived from ethynylene bridges.

1-1. Background on Organic field-effect transistors (OFETs)

Since 1960s, the first field-effect transistor with metal-oxide-semiconductor structure (MOSFET) was fabricated in Bell lab,¹ promoting the evolution of complementary circuits and microprocessors which has totally changed modern life. Currently, organic field-effect transistors (OFETs) have attracted much attention for the applications in flexible organic light emitting displays (OLEDs)² and bio sensor devices,³ owing to its merit in flexibility, light weight and low cost.⁴ For example, lightweight and flexible OFETs are expected to be used in applications that are difficult to realize with silicon-based semiconductors such as bendable electronic circuits and implantable biological sensors. Considering the spreading of internet of things and artificial intelligence, OFETs will definitely become more important than ever.

However, the performance, stability, reproducibility and reliability of organic semiconductors (OSCs) for OFETs are still lower than the silicon based inorganic field-effect transistors (FETs). The understanding of the relationships between working principle of OFETs and OSCs are important to overcome these problems.

Generally, bottom-gate-top-contact (BGTC) OFETs are preferred for quick screening of newly synthesized organic materials due to their ease of fabrication and processing.⁵ As shown in the Figure 1-1, a typical BGTC OFET consists of an active layer (organic

semiconductor film or single crystal), three electrodes (gate, source, and drain), and a gate dielectric (insulator).

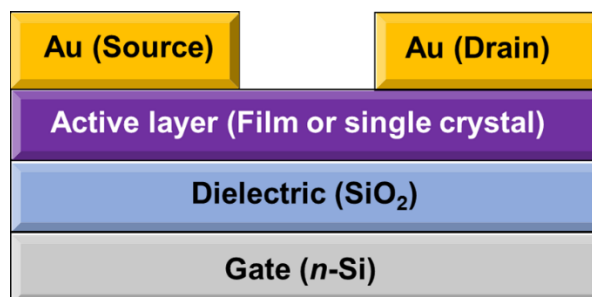


Figure 1-1. Schematic structure of BGTC OFET devices.

The highly doped silicon is chosen as both a substrate and a gate electrode. Silicon oxide (SiO₂) forms on the silicon surface by oxidation as the dielectric insulating layer. The organic semiconductors are directly deposited onto the dielectric layer. However, active hydroxyl groups (silanol) on the surface easily accumulate electrons on the interface.⁶ Thus, self-assembled monolayers (SAMs) such as organosilanes and phosphonic acids often are used for facilitating modified dielectric surface to improve the surface energy and roughness of dielectric layer.⁷⁻⁹

Figure 1-2 illustrates the working mechanism of p-type OFETs. During the device operation, when a negative voltage is applied on gate reaches to 0, holes cannot move due to the high resistance of organic semiconductors.¹⁰ When a voltage is increased, holes are

accumulated at the interface of the organic semiconductor and dielectric insulator. Thus, the source–drain current can be adjusted by the gate voltage.¹¹

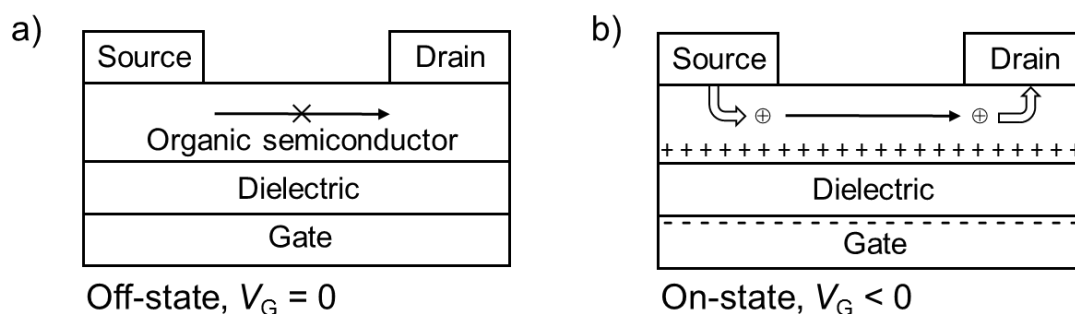


Figure 1-2. Working principle of p-type OFETs, a) off state, b) on-state.

Charge carrier mobility (μ) is directly proportional to channel current. Currently, the mobility greater than $1.0 \text{ cm}^2 \text{ V}^{-1} \text{ s}^{-1}$ is regarded as a high performance device because poly crystalline silicon (*c*-Si) based FETs show the similar mobilities.¹² π -Conjugated materials are well known as promising semiconductor materials, owing to the free movement of delocalized π -electrons in organic compounds. Therefore, chemical structure fine-tuning of π -conjugated materials together with their molecular arrangements is a critical approach to improve the charge-carrier mobility of OFETs.

1-2. Techniques for the fabrication of active layer in OFETs

1-2-1. Dip-coating technique

The solution processability of organic molecules and their compatibility with rapid and easily controllable deposition methods offer a simple route to realize low-cost flexible electronics.¹³ At present, the preparation of highly crystalline uniform organic semiconductor thin films exhibiting high field-effect mobility (exceeding $1.0 \text{ cm}^2 \text{ V}^{-1} \text{ s}^{-1}$) has been achieved by using spin-coating,^{14–16} drop-casting,^{17–19} and dip-coating^{20–22} methods. Recently, dip-coating method has attracted increasing interests because the drying speed during the dip-coating process can be quantitatively controlled by adjusting the substrate lifting rate to control the crystallinity of resulting organic thin film.²³

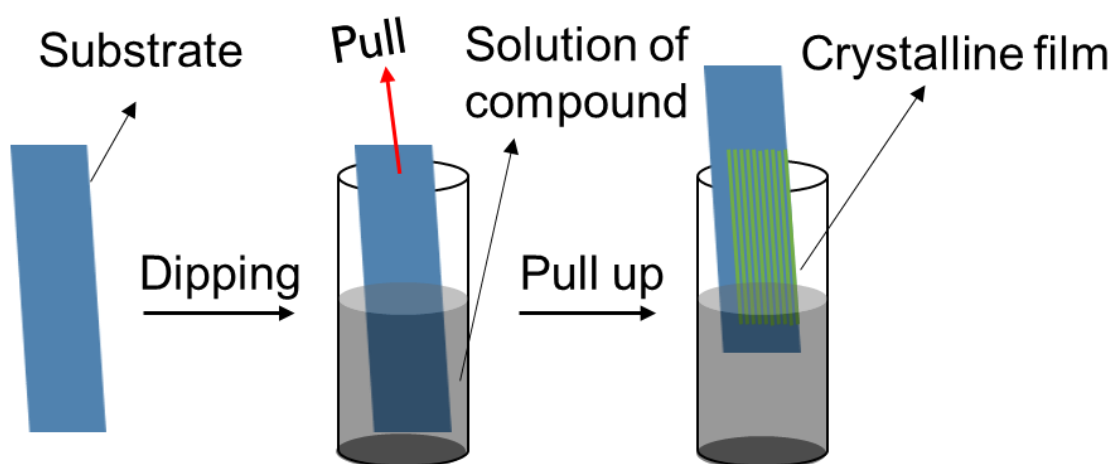


Figure 1-3 Organic thin film preparation by using “dip-coating” method.

1-2-2. Drop-casting technique

Slow evaporation of deposited solution on a substrate often gives crystals. By using this phenomenon, it is common to fabricate the BGTC OFET devices with prefabricated electrodes by drop-casting technique (Figure 1-4) due to its low-cost and easy processing.²⁴

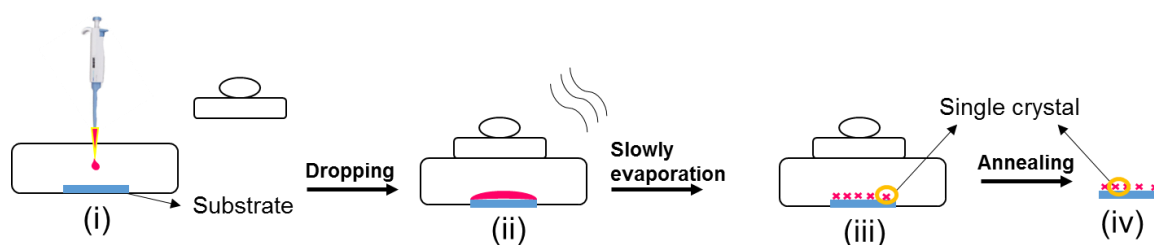


Figure 1-4 Growing single crystals by using “drop-casting” method.

1-3. Arylethylenes as molecular core for π -conjugated system

The advantage of OFETs is the possibility for fine-tuning of the property by chemical modification of organic semiconducting materials. The utilization of ethynylene units to create π -conjugated semiconductors (polymers and small molecules) have attracted much attentions because of the structural diversity. For example, conventional coupling reaction such as Sonogashira cross-coupling is often used for preparing ethynylene-bridged π -conjugated semiconductors. Taking advantage of the convenience of the reaction, optical and physical properties of ethynylene-bridged π -conjugated semiconductors are easily

tuned by coupling reaction with proper counterparts such as donor and acceptor moieties. In addition, ethynylene-bridged π -conjugated semiconductors could provide shape-persistent rod-like structures, controlling the length by changing the number of arylethynylene repeating units. At the same time, the ethynylene-bridge minimizes the steric repulsion between adjacent aromatic units, enhancing π -conjugation along the backbone. This effect ultimately has a positive impact on the charge carrier mobility. Here, representative prominent examples of triple-bond containing semiconductors and their performances in organic semiconductors were described.

OFETs were firstly fabricated with π -conjugated polymers.¹ However, due to strong intermolecular interactions, high-molecular-weight π -conjugated polymers are sometimes insoluble despite of long alkyl side chains. A recent attempt to enhance the solubility is to introduce arylene repeating units into the polymer. In the optimized molecular structure, a rod-shaped molecule is changed to a coil-shaped molecule with conformational freedom, breaking the rotation around the bond between phenylene units by introducing an ethynylene spacer unit. Meanwhile, introducing π -conjugated ethynylene spacer can improve the open circuit voltage, manipulating the HOMO energy level of the polymers. For instance, Cremer and coworkers synthesized a poly(ethynylene-bithienylene) (**PEBT**, Figure 1-5) and compared its photovoltaic

behavior with poly(3-hexylthiophene) (**P3HT**, Figure 1-5). This work indicated the positive influence of triple bond on the open circuit voltage, reaching an impressive enhancement of the open circuit voltage from 0.62 V to 1.03 V.²⁵

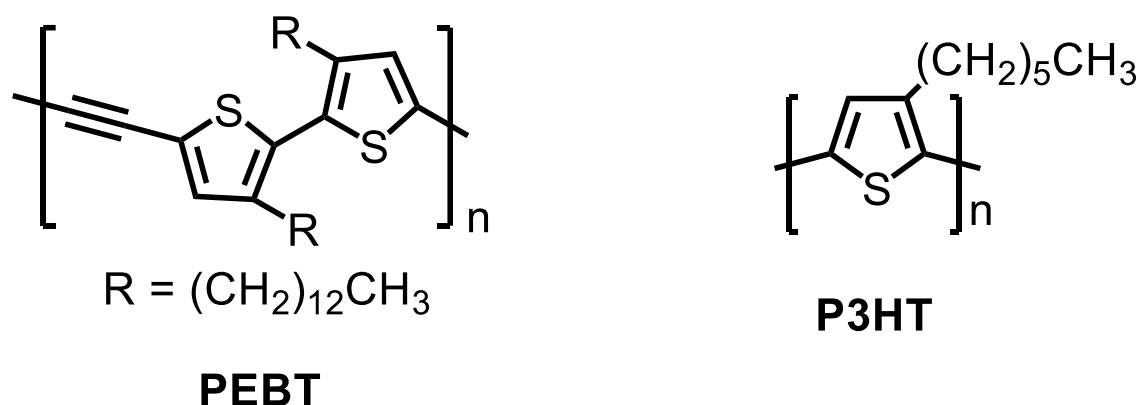


Figure 1-5. Chemical structure of **PEBT** and **P3HT** reported by Cremer and coworkers.

For small molecules, introduction of π -conjugated triple-bond-containing systems is also a promising strategy to form 2D π - π stacking packing motif by diminishing C-H $\cdots\pi$ interaction in acene core. For instance, Anthony and coworkers firstly reported the generation of 6,13-bis(triisopropylsilylethynyl)pentacene (**TIPS-Pen**, Figure 1-6).²⁶ Compared with pristine pentacene, the introduction of silylethynyl substituent at 6,13-positions of pentacene not only made the compound stable but also increased the degrees of π - π overlap and coupling, changing the packing motif from herringbone to 2D face-to-face π -stacking. In 2013, Bao and coworkers reported the maximum charge carrier

mobility of **TIPS-Pen** with thin film OFET benchmarked as high as $11 \text{ cm}^2 \text{ V}^{-1} \text{ s}^{-1}$. This result reveals that the introducing silylethynylene group is a promising strategy to tune the molecular arrangement in the solid state.²⁷

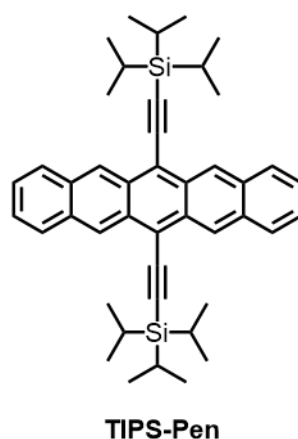


Figure 1-6. Chemical structure of **TIPS-Pen**.

In addition, Anthony and coworkers investigated a series of the pentacene derivatives with different silylethynylene groups to shed light on the relationship between functionalization, film formation, stability, and packing structure.²⁸ They confirmed that with a proper choice of the side chain, the modification could effectively disrupt the herringbone packing as seen in the case of pristine pentacene, providing the face-to-face arrangements, together with the improvement of the solubility in a variety of common organic solvents. For large π -conjugated systems such as porphyrin derivatives, this strategy also plays an important role in tuning the molecular arrangement. For example,

K. Takahashi and coworkers reported the synthesis of metal complexes of 5,15-bis(trimethylsilylethynyl)tetrabenzo-porphyrin (**TMS-H₂BP**) and 5,15-bis(triisopropylsilylethynyl)tetrabenzoporphyrin (**TIPS-H₂BP**), which have ethynylene unit in the system, and evaluated the charge transport property and applied them to bulk heterojunction (BHJ) solar cells.²⁹ The porphyrin derivatives showed the reasonable solubility and air stability. It was found that **TMS-H₂BP** and its metal complexes adopted flat molecular conformations and formed herringbone-type packing structures in the single crystal, while **TIPS-H₂BP** derivatives formed one-dimensional slipped-stack structures. These results also support that the silylethynylene moiety could affect the molecular arrangements and enhance the air stability and solubility at the same time.

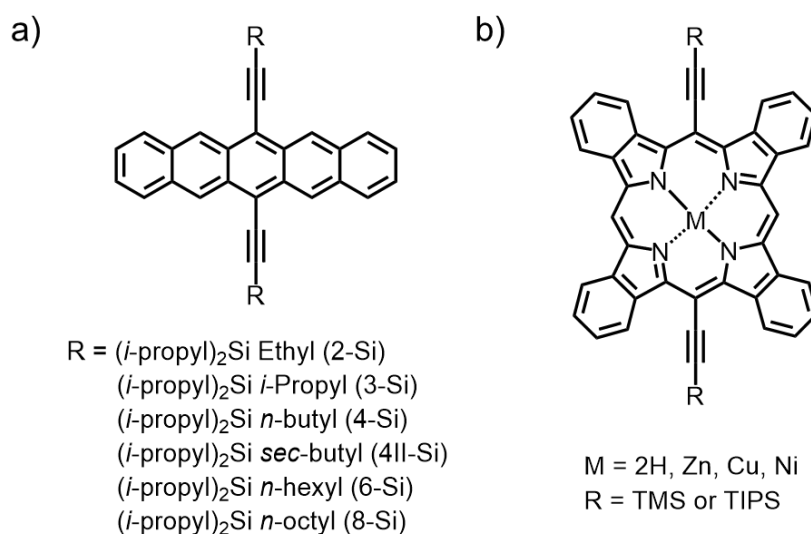


Figure 1-7. Chemical structure of silylethynylene substituted a) pentacene derivatives, and b) tetrabenzoporphyrin derivatives and its metal complexes.

H. Hayashi, and co-workers also reported a series of TIPSethynylene substituted anthracene derivatives with azaacene-containing iptycene units on both sides of anthracene to evaluate their performance of OLEDs. The π -expansion was realized by introducing different sized azaacenes to the iptycene wings by using a condensation reaction (Figure 1-8). Additionally, by introducing TIPSethynylene group, similar with the case of **TIPS-pen**, these large π -conjugated systems enabled to enhance the air stability and solubility in the common organic solvents. At the same time, the combination with iptycene and TIPS-ethynyl groups were expected to reduce aggregation in the solid state. The obtained electroluminescence with a luminance of over 920 cd m^{-2} by solution-processed OLEDs indicated that it is a promising strategy to design OLED materials by using iptycene and TIPSethynylene group.³⁰

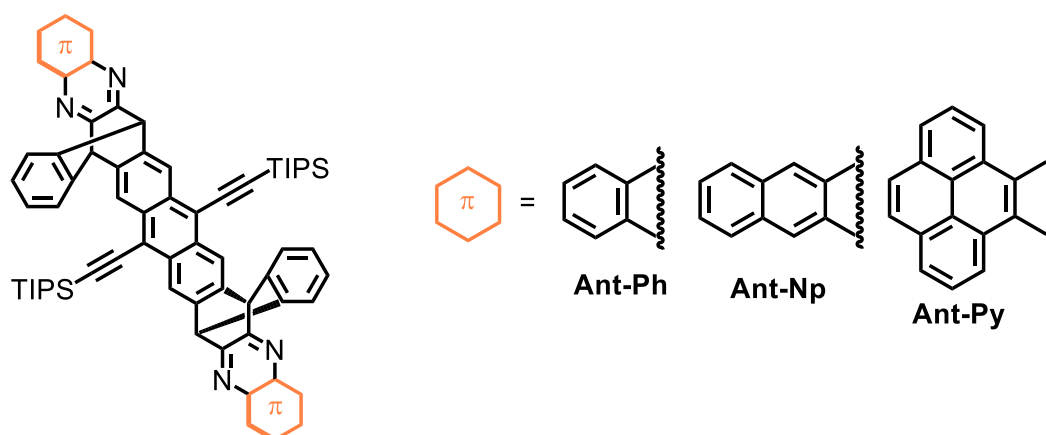


Figure 1-8. Chemical structure of TIPSethynylene substituted anthracene derivatives with azaacene-containing iptycene units.

The utilization of arylethynylenes is also a powerful tool to prepare a donor–acceptor system for the application in OPVs. For example, Peng group introduced ethynylene linkages to increase the planarity of polymers and porphyrin-based small molecules, improving the OPV performance.^{31, 32} Importantly, owing to the easiness of introducing of ethynylene group, the various electron withdrawing groups were investigated by conventional coupling reactions such as Sonogashira reaction. Among the porphyrin-based donor-acceptor systems, they reported a conjugated donor–acceptor porphyrin–5,15-bis(2,5-bis-(2-ethyl-hexyl)-3,6-di-thienyl-2-yl-2,5-dihydropyrrolo[3,4-c]pyrrole-1,4-dione-50-yl-ethynyl)-10,20-bis(4-octyloxy-phenyl)-porphyrin zinc (**DPPEZnP-O**, Figure 1-9) with excellent solubility in organic solvents such as chloroform and toluene exhibited a power conversion efficiency (PCE) of up to 7%, which was the highest value reported for solution-processed BHJ solar cells based on porphyrins.³³

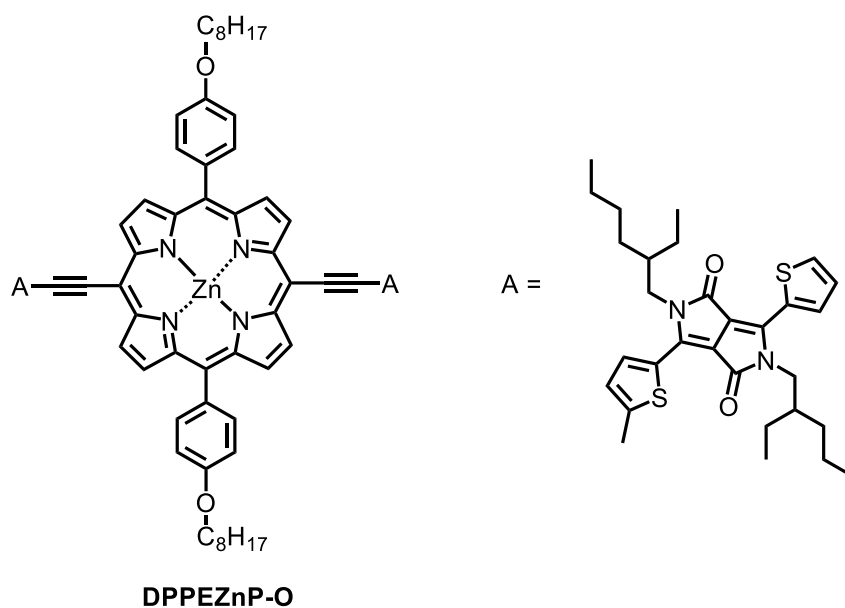


Figure 1-9. Chemical structure of **DPPEZnP-O**.

Along this line, K. Takahashi and coworkers also investigated the side chain engineering of porphyrin based OPV materials bridging. Taking advantage of the easy modification of ethynylene groups, a series of diketopyrrolopyrrole (DPP) with the different length of alkyl groups were successfully connected with benzoporphyrin through ethynylene units by using Sonogashira reaction.³⁴

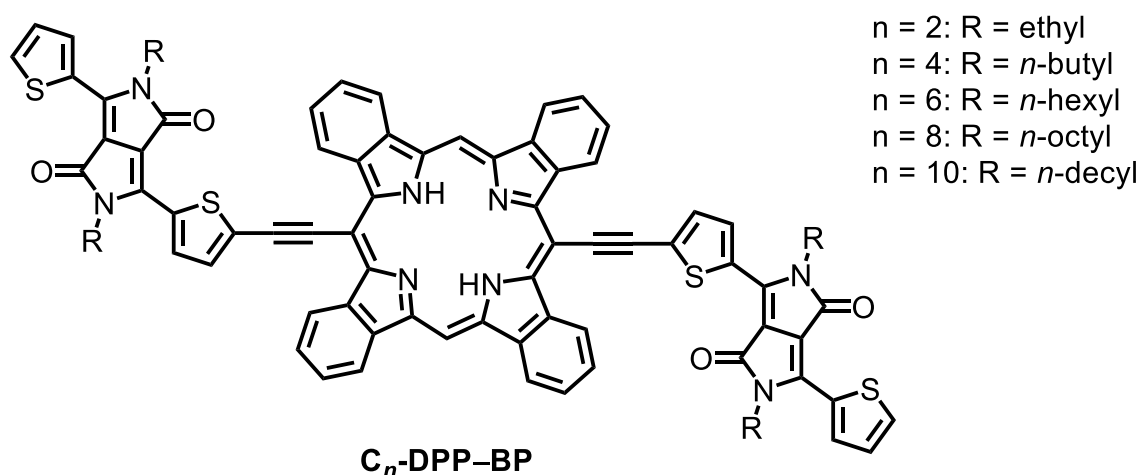


Figure 1-10. Chemical structure of *C_n-DPP-BP*.

Recently, Vaccaro group reported a family of anthracene-based arylethylenes for the application in OFETs and BHJ OPVs. For example, soluble π -extended arylethylenic optoelectronic materials **1a-d** (Figure 1-11) were designed with an anthracene core, linked to two ethynylene-phenylene units at both the 9- and 10-positions, functionalizing with electron-donating and electron-withdrawing groups. The molecules had a favorable push-pull effect stemming from donor/acceptor species connected with triple bond. Thus, the efficient intramolecular charge transfer might occur upon excitation, promoting the OPV performance.³⁵

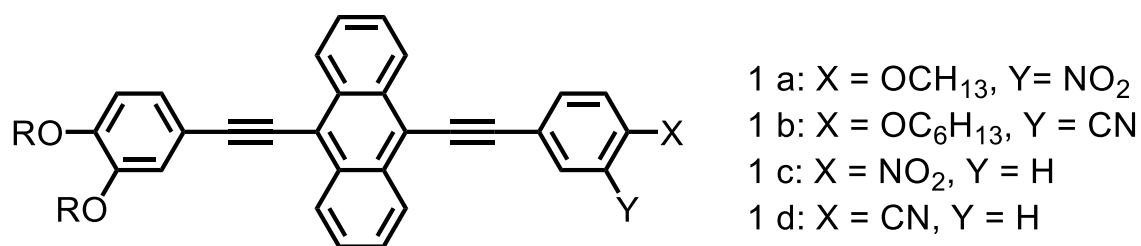


Figure 1-11. Chemical structure of anthracene derivatives reported by Vaccaro group.

Other attractive advantage of ethynylene group is to reduce the degree of rotational freedom compared with single or double bond, and this effect could increase the order of molecular packing. As shown in the figure 1-12, W. Hu and co-workers applied an 9,10-bis(phenylethynyl)anthracene (**BPEA**) in OFETs. The transistors based on nanorod-shaped (phase α , herringbone packing) and nanoribbon-shaped (phase β , face-to-face packing) single crystals showed the mobilities of $0.73 \text{ cm}^2 \text{ V}^{-1} \text{ s}^{-1}$ and $1 \times 10^{-2} \text{ cm}^2 \text{ V}^{-1} \text{ s}^{-1}$, respectively. In addition, both OFETs of crystals with the α and β phase exhibited photo response.³⁶ Subsequently, the introduction of triple-bond in thiophene systems was also investigated. For instance, in 2009, W. Hu and coworkers reported a series of ethynylene-bridged thiophene-phenylene derivatives (**2**, Figure 1-13). The introduction of the electron-withdrawing group into the molecular framework accounted for an enhanced electron affinity relative to the “single-bond-linked counterparts”, and consequently for a higher oxidation potential (i.e., improved oxidation stability) as well as a lower HOMO level (i.e., higher stability towards oxygen). Furthermore, single-

crystal analysis revealed that the introduction of ethynylene units efficiently eliminated the steric repulsion between adjacent aromatic rings that existed in single-bond-linked compounds.³⁷

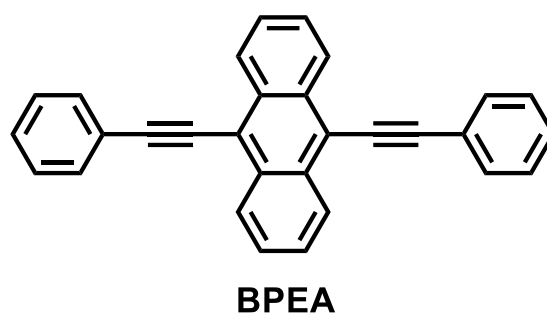


Figure 1-12. Chemical structure of **BPEA**.

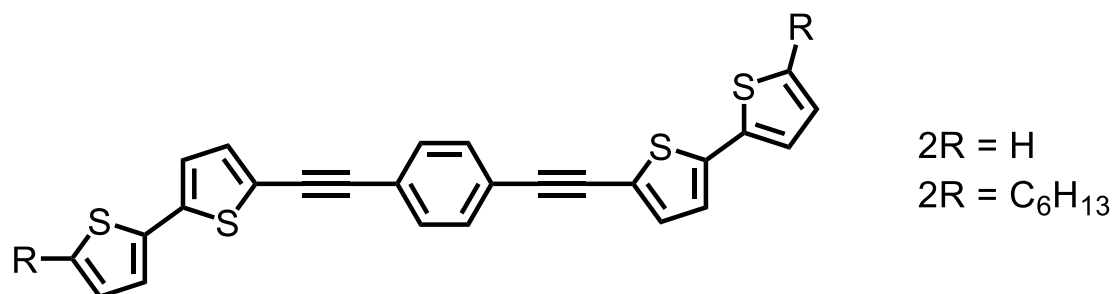


Figure 1-13. Chemical structure of thiophene-phenylene systems reported by Hu and co-workers.

As described above, the easy modification of molecular structure with π -conjugated triple bond-containing systems has attracted the intense interest for researchers. The controlling of the repeating unit of arylethynylene could efficiently tune the HOMO/LUMO energy gap.³⁸⁻⁴⁵ In addition, the introduction of arylethynylenes in the

system could be a good strategy to prepare suitable packing structures, improving the performance of OFET devices.⁴⁶⁻⁴⁸

1-4. Aims and Outline

As mentioned above, the advantage of using π -conjugated triple bond-containing systems is to provide an easy modification of molecular arrangements which is suitable for the application in p-type OFETs.

In this dissertation, the molecular backbones of oligoarylethylenes are consisted of the well-known p-type materials, tetrabenzoporphyrin (BP) and acene derivatives. In Chapter 1, the specific examples of ethynylene-bridged π -conjugated systems and how molecular structures affect the properties and device performance are described.

Chapter 2 focuses on **TIPS-BP** and its metal complexes with one-dimensionally extended columnar packing motif were prepared as micro/nanometre-sized crystals on a OTS modified substrate. By comparing molecular packing, charge carrier mobility, orientation of these three compounds, indicating the metalation effect in the charge transport property.

Chapter 3 describes the synthesis of ethynylene-bridged anthracene oligomers from monomer to tetramer. The molecular design of π -conjugated core was chosen as

anthracene units bridged with 9,10-substituted ethynylene to avoid steric hindrance between the adjacent anthracene units, conjugating anthracene units in a potentially planar or twisted structure. The characterization of ethynylene-bridged oligomers from monomer to tetramer revealed the oligomerization effect on the packing structure and charge transport property.

Related to the investigation of oligomerization of ethynylene-bridged anthracene oligomers, the synthesis of ethynylene-bridged π -extended acene oligomers was further studied in **Chapter 4**. A straightforward synthetic strategy towards a precursor of ethynylene-bridged heptacene dimer was successfully developed, skipping the conventional stepwise protection/deprotection approach. Additionally, it was found that the facile reaction with lithiated triisopropylsilylethynylene and quinone of pentacene precursor followed by the reductive aromatization afforded oligomers of ethynylene-bridged pentacene precursor. These discoveries provide a great clue to the effective synthetic approach of ethynylene-bridged π -conjugated systems.

Finally, **Chapter 5** describes the general conclusion of this dissertation and suggests future directions for the molecular design toward efficient organic semiconductors.

1-5. Reference

- (1) A. Tsumura, H. Koezuka and T. Ando, *Appl. Phys. Lett.*, **1986**, *49*, 1210–1212.
- (2) C. D. Müller, A. Falcou, N. Reckefuss, M. Rojahn, V. Wiederhirn, P. Rudati, H. Frohne, O. Nuyken, H. Becker, K. Meerholz, *Nature*, **2003**, *421*, 829–833.
- (3) L. Torsi, M. Magliulo, K. Manoli and G. Palazzo, *Chem. Soc. Rev.*, **2013**, *42*, 8612–8628.
- (4) C. Di, F. Zhang, D. Zhu, *Adv. Mater.* **2013**, *25*, 313–330.
- (5) *Chemical Solution Synthesis for Materials Design and Thin Film Device Applications* (Eds.: S. Das, S. Dhara), Elsevier, **2021**.
- (6) S. K. Parida, S. Dash, S. Patel, B.K. Mishra, *Advances in Colloid and Interface Science*, **2006**, *121*, 77–110.
- (7) J. Zaumseil and H. Sirringhaus, *Chem. Rev.*, **2007**, *107*, 1296–1323.
- (8) C.A. Di, Y. Liu, G. Yu, D. Zhu, *Acc. Chem. Res.*, **2009**, *42*, 1573–1583.
- (9) D. Liu, Z. He, Y. Su, Y. Diao, S. C. B. Mannsfeld, Z. Bao, J. Xu, Q. Miao, *Adv. Mater.*, **2014**, *26*, 7190–7196.
- (10) Y. Shen, A. R. Hosseini, M. H. Wong, G. G. Malliaras, *ChemPhysChem*, **2004**, *5*, 16–25.
- (11) *Semiconductor Device Fundamentals*, R. F. Pierret, Addison Wesley Longman,

- 1996, 525–732.
- (12) A. Y. Amin, A. Khassanov, K. Reuter, T. Meyer-Friedrichsen, M. Halik, *J. Am. Chem. Soc.* **2012**, *134*, 16548–16550.
- (13) Z. Lu, C. Wang, W. Deng, M. T. Achille, J. Jie, X. Zhang, *J. Mater. Chem. C*, **2020**, *8*, 9133–9146.
- (14) U. Bielecka, P. Lutsyk, K. Janus, J. Sworakowski, W. Bartkowiak, *Organic Electronics*, **2011**, *12*, 1769–1776.
- (15) J. Y. Na, B. Kang, D. H. Sin, K. Cho, Y. D. Park, *Sci Rep*, **2015**, *5*, 13288/1–14.
- (16) Q. Li, Z. F. Yao, Y. Lu, S. Zhang, Z. Ahmad, J. Wang, X. Gu, J. Pei, *Adv. Electron. Mater.* **2020**, *6*, 2000080/1–10.
- (17) M. Mas-Torrent, M. Durkut, P. Hadley, X. Ribas, C. Rovira, *J. Am. Chem. Soc.*, **2004**, *126*, 984–985.
- (18) M. Mas-Torrent, P. Hadley, S. T. Bromley, X. Ribas, J. Tarres, M. Mas, E. Molins, J. Veciana, C. Rovira, *J. Am. Chem. Soc.*, **2004**, *126*, 8546–8553.
- (19) H. Jiang, X. J. Yang, Z. D. Cui, Y. C. Liu, H. X. Li, W. P. Hu, Y. Q. Liu and D. B. Zhu, *Appl. Phys. Lett.*, **2007**, *91*, 123505/1–3.
- (20) *Physics and Applications of DIP Coating and Spin Coating*, L.E. Scriven, MRS Online Proceedings Library, **1988**, *121*, 717–729.

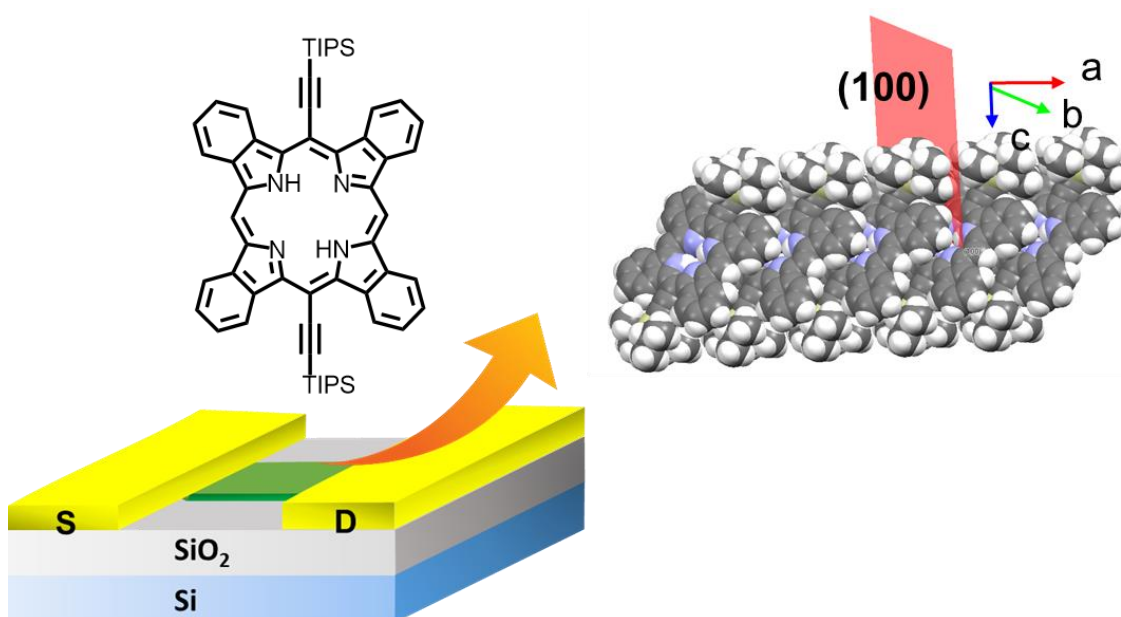
- (21) *Hydraulic Rubber Dam: An Effective Water Management Technology* (Eds.: S. Thomas, A. V. Rane, A. VK, K. Kanny, A. Dutta), William Andrew Publishing, **2019**.
- (22) H. N. Tsao, D. Cho, J. W. Andreasen, A. Rouhanipour, D. W. Breiby, W. Pisula, and K. Müllen, *Adv. Mater.* **2009**, *21*, 209–212.
- (23) J. Jang, S. Nam, K. Im, J. Hur, S. N. Cha, J. Kim, H. B. Son, H. Suh, M. A. Loth, J. E. Anthony, J. J. Park, C. E. Park, J. M. Kim, K. Kim, *Adv. Funct. Mater.* **2012**, *22*, 1005–1014.
- (24) A. L. Briseno, S. C. B. Mannsfeld, X. M. Lu, Y. J. Xiong, S. A. Jenekhe, Z. N. Bao, Y. N. Xia, *Nano Lett.*, **2007**, *7*, 668–675.
- (25) Q. Liu, J. Mao, Z. Liu, N. Zhang, Y. Wang, L. Yang, S. Yin, Y. Chen, *Nanotechnology*, **2008**, *19*, 115601/1–5.
- (26) J. E. Anthony, J. S. Brooks, D. L. Eaton, and S. R. Parkin, *J. Am. Chem. Soc.* **2001**, *123*, 9482–9483.
- (27) Y. Diao, B. C. Tee, G. Giri, J. Xu, D. H. Kim, H. A. Becerril, R. M. Stoltenberg, T. H. Lee, G. Xue, S. C. Mannsfeld, and Z. Bao, *Nat. Mater.* **2013**, *12*, 665–671.
- (28) J. Chen, S. Subramanian, S. R. Parkin, M. Siegler, K. Gallup, C. Haughn, D. C. Martin, J. E. Anthony, *J. Mater. Chem.* **2008**, *18*, 1961–1969.
- (29) K. Takahashi, N. Yamada, D. Kumagai, D. Kuzuhara, M. Suzuki, Y. Yamaguchi,

- N. Aratani, K. I. Nakayama, H. Yamada, *J. Porphyr. Phthalocyanines*, **2015**, *19*, 465–478.
- (30) H. Hayashi, Y. Kato, A. Matsumoto, S. Shikita, N. Aizawa, M. Suzuki, N. Aratani, T. Yasuda, H. Yamada, *Chem. Eur. J.* **2019**, *25*, 15565–15571.
- (31) H. Qin, L. Li, Y. Li, X. Peng, J. Peng, Y. Cao, N. Ismayil, W. Shi, *Eur. Polym. J.* **2012**, *48*, 2076–2084.
- (32) Y. Huang, L. Li, X. Peng, J. Peng, Y. Cao, *J. Mater. Chem.* **2012**, *22*, 21841–21844.
- (33) H. Qin, L. Li, F. Guo, S. Su, J. Peng, Y. Cao, X. Peng, *Energy Environ. Sci.* **2014**, *7*, 1397–1401.
- (34) K. Takahashi, D. Kumagai, N. Yamada, D. Kuzuhara, Y. Yamaguchi, N. Aratani, T. Koganezawa, S. Koshika, N. Yoshimoto, S. Masuo, M. Suzuki, K. I. Nakayama, H. Yamada, *J. Mater. Chem. A.* **2017**, *5*, 14003–14011.
- (35) E. Bartollini, M. Seri, S. Tortorella, A. Facchetti, T. J. Marks, A. Marrocchi, L. Vaccaro, *RSC Adv.* **2013**, *3*, 9288–9295.
- (36) C. Wang, Y. Liu, Z. Wei, H. Li, W. Xu, W. Hu, *Appl. Phys. Lett.* **2010**, *96*, 143302/1–3.
- (37) Q. Meng, J. Gao, R. Li, L. Jiang, C. Wang, H. Zhao, C. Liu, H. Li, W. Hu, *J.*

- Mater. Chem.* **2009**, *19*, 1477–1482.
- (38) C. Kästner, S. Rathgeber, D. A. M. Egbe, H. Hoppe, *J. Mater. Chem. A.* **2013**, *1*, 3961–3969.
- (39) C. Kästner, B. Muhsin, A. Wild, D. A. Egbe, S. Rathgeber, H. Hoppe, *J. Polym. Sci. Part B*, **2013**, *51*, 868–874.
- (40) S. Rochat, T. M. Swager, *ACS Appl. Mater. Interfaces*, **2013**, *5*, 4488–4502.
- (41) A. Marrocchi, I. Tomasi, L. Vaccaro, *Isr. J. Chem.*, **2012**, *52*, 41–52.
- (42) A. Operamolla, R. Ragni, O. H. Omar, G. Iacobellis, A. Cardone, F. Babudri, G. Farinola, *Curr. Org. Synth.*, **2012**, *9*, 764–778.
- (43) A. Operamolla, G. M. Farinola, *Eur. J. Org. Chem.*, **2011**, *3*, 423–450.
- (44) D. A. M. Egbe, B. Carbonnier, E. Birckner, U. W. Grummt, *Prog. Polym. Sci.*, **2009**, *34*, 1023–1067.
- (45) *Acetylene Chemistry: Chemistry, Biology, and Materials Science* (Eds.: F. Diederich, P. J. Stang, R. R. Tykwinski), Wiley-VCH, Weinheim, **2005**.
- (46) C. Li, Y. Li, *Macromol. Chem. Phys.*, **2008**, *209*, 1541–1552.
- (47) U. H. Bunz, *Chem. Rev.* **2000**, *100*, 1605–1644.
- (48) W. Zhang, S. Kraft, J. S. Moore, *J. Am. Chem. Soc.* **2004**, *126*, 329–335.

Chapter 2.

Single Crystal Field-Effect Transistor of Tetrabenzoporphyrin with One-Dimensionally Extended Columnar Packing Motif Exhibiting Efficient Charge Transport Property



$$\mu_{max, h} = 2.2 \text{ cm}^2 \text{ V}^{-1} \text{ s}^{-1}$$

In this chapter, the single-crystal organic field-effect transistors of 5,15-bis(triisopropylsilylethynyl) tetrabenzoporphyrin and its metal complexes were fabricated, and their intrinsic electronic properties were evaluated.

2-1. Introduction

The charge transport in organic semiconductors is achieved by the π orbital overlapping of the conjugated molecules along the direction of carrier flow. Therefore, organic semiconducting materials with a rigid and planar π -system have a great potential to provide the suitable packing to increase the π orbital overlapping.¹⁻⁴ In terms of the large and rigid π -system, tetrabenzoporphyrins (**BPs**) are promising candidates as efficient p-type semiconducting materials.^{5,6} However, at the same time, **BP** itself is hardly soluble in organic solvents, resulting in difficulty in the synthesis. The solubility is also an important factor not only for the solution-processable device fabrication but also for achieving the easy synthesis and purification. Although these factors, rigidity and solubility, are likely a trade-off relationship, several molecules perfectly satisfy these requirements. As mentioned in the first chapter, 6,13-bis(triisopropylsilylethynyl)pentacene (**TIPS-Pen**), which is a benchmark compound as an efficient organic semiconducting material, has proven to be quite successful, despite the fact that pentacene itself shows almost no solubility in any organic solvents.⁷ Taking advantage of the improved solubility by the introduction of TIPSethynyl groups, the solution sharing with a micropillar-patterned blade gave the hole mobility of up to $11 \text{ cm}^2 \text{ V}^{-1} \text{ s}^{-1}$,⁸ achieving clearly better hole mobility than pristine pentacene.

For **BPs** as well, recent synthetic efforts had solved the solubility problem by using “precursor method” (Figure 2-1), in which a soluble precursor compound, 1,4:8,11:15,18:22,25-tetraethano-29*H*,31*H*-tetrabenzo[*b,g,l,q*]porphyrin (**CP**), can be quantitatively converted to **BP** by a thermally induced retro-Diels-Alder reaction.^{6,9} The charge-carrier mobility of **BP** polycrystalline film obtained *via* precursor method was firstly evaluated by Aramaki, exhibiting the hole mobility of $0.017 \text{ cm}^2 \text{ V}^{-1} \text{ s}^{-1}$.¹⁰ The hole mobility was then slightly improved to $0.07 \text{ cm}^2 \text{ V}^{-1} \text{ s}^{-1}$, while the value was still low.¹¹

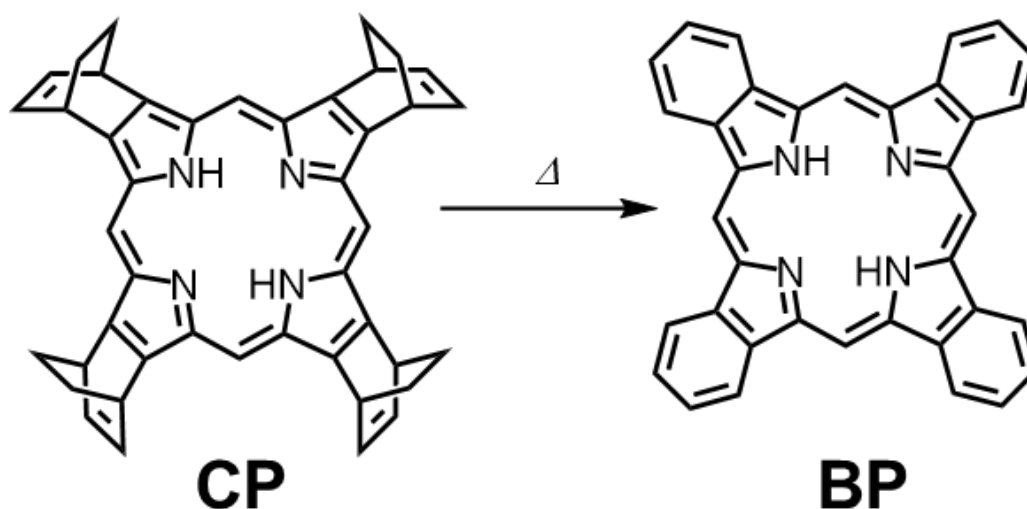


Figure 2-1. Thermal conversion of **CP** to **BP**.

Recently, the substituent effect was evaluated to obtain better charge transport property by controlling the packing orientation of **BP**. It was found that 5,15-bis(triisopropylsilylethynyl)-**BP** (**TIPS-H₂BP**) with reasonable solubility for solution-

processed organic thin film transistors formed two types of packing motifs: columnar motif by drop-casting motif and brickwork motif by dip-coating method.¹²

The drop-casting films with the columnar motif showed low hole mobility ($0.027 \text{ cm}^2 \text{ V}^{-1} \text{ s}^{-1}$), although such a columnar motif is also known to exhibit efficient charge transport property. On the other hand, the brickwork motif has two dimensionally extended π -stacking. The maximum hole mobility of dip-coating films reached $1.1 \text{ cm}^2 \text{ V}^{-1} \text{ s}^{-1}$, which was approximately 14 times higher than pristine free-base **BP** ($0.07 \text{ cm}^2 \text{ V}^{-1} \text{ s}^{-1}$). This disparity in charge transport property between drop-casting and dip-coating methods turned our attention to single-crystal field-effect transistors (SCFETs), which are able to unveil the intrinsic charge transport property of organic semiconducting materials due to ordered arrangement of molecules, free of grain boundaries and minimized defects. The obtained maximum hole mobility in the previous report implied that functionalized **BP** derivatives could be candidates for efficient charge transport materials. For further structural fine-tuning of **BP**, the potentials of **TIPS-H₂BP** towards efficient organic semiconducting material are necessary to be evaluated.

In this chapter, single crystals of **TIPS-H₂BP** and its metal complexes (Cu and Zn) were prepared on a substrate, and the molecular orientation in the single crystal was explored in detail. Then, the relationship between the molecular orientation and charge

transport property were investigated by preparing SCFETs. Here, zinc and copper metal complexes were chosen in this chapter. These metal complexes are widely used for porphyrin and phthalocyanines chemistry, because the introduction of metal often gives small change in the porphyrin structure (e.g. planarity). Thereby, the metal complexes sometimes exhibit the closer interplanar distance compared with free base porphyrins, resulting in the strong π - π stacking interactions between π -systems.¹³⁻¹⁶ Actually, high charge transport properties were reported by using zinc and copper metal complexes of porphyrin and phthalocyanine derivatives in previous reports.¹⁷⁻²⁰

The chemical structure of **TIPS-H₂BP**, **TIPS-ZnBP** and **TIPS-CuBP** employed in this chapter were described in the Figure 2-2.

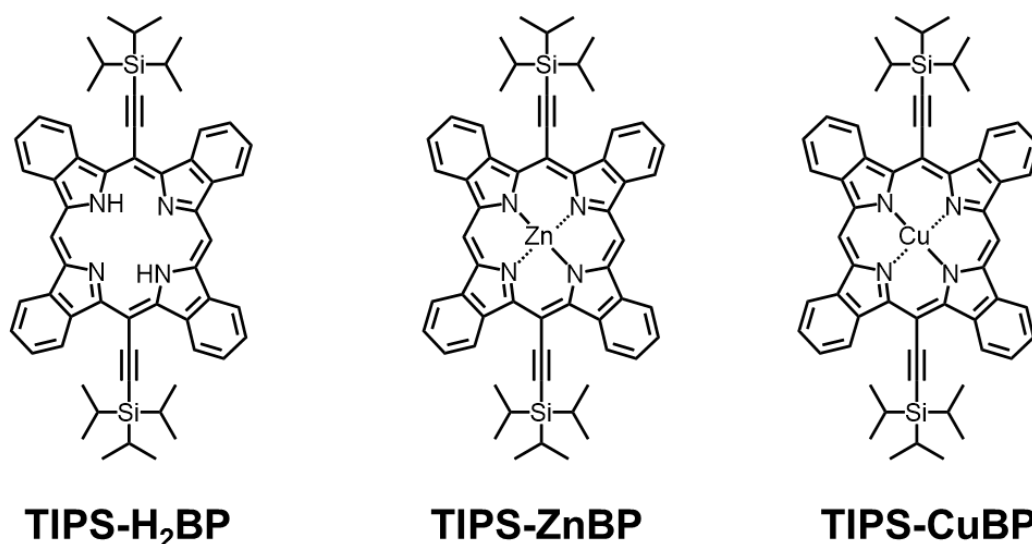


Figure 2-2. Chemical structures of **TIPS-H₂BP**, **TIPS-ZnBP** and **TIPS-CuBP**.

2-2. Growth single crystals

TIPS-H₂BP and the zinc(II) and copper(II) complexes (**TIPS-ZnBP** and **TIPS-CuBP**) were synthesized by following the previous reports.²¹ Then, their crystals were grown by drop-casting the toluene solution on octadecyltrichlorosilane (OTS) modified Si/SiO₂ surface. It was found that slow evaporation of the drop-casted toluene solution gave isolated and thin ribbon-shaped and/or wire-shaped single crystals on Si/SiO₂/OTS substrates (Figure 2-3).

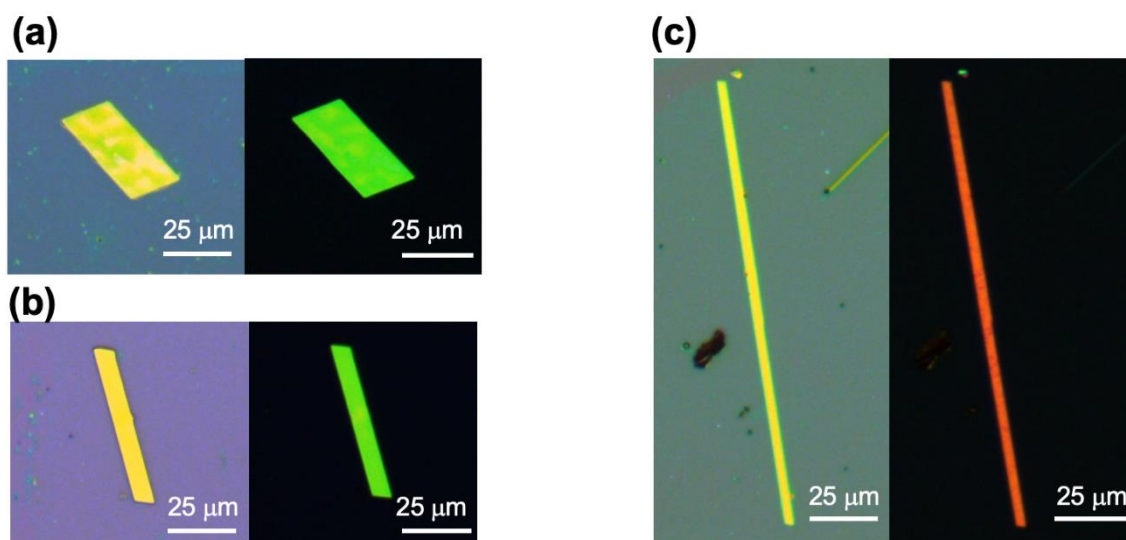


Figure 2-3. Typical POM images of ribbon-shaped single crystal of (a) **TIPS-H₂BP**, (b) **TIPS-ZnBP**, and (c) **TIPS-CuBP** on OTS modified Si/SiO₂ substrate. Concentrations for drop-casting of toluene solution: 1.0 mg/ml (**TIPS-H₂BP** and **TIPS-CuBP**), 0.5 mg/ml (**TIPS-ZnBP**).

Importantly, the changing of interfacial color in polarized optical microscope (POM) images supported that they were single crystals. Narrow ribbon-shaped crystals of **TIPS-**

H₂BP similar to the case of **TIPS-CuBP** were also observed. However, out-of-plane X-ray diffraction (XRD) and transmission electron microscopy (TEM) analyses indicated that the molecular orientation in these crystals were the same (*vide infra*). Indeed, the crystal was grown as the different shape probably because of the slightly different surface energy on a substrate.¹⁸ It was found that the order of ease of was as follows: **TIPS-H₂BP** > **TIPS-ZnBP** > **TIPS-CuBP**. Specifically, single crystals of **TIPS-CuBP** with suitable quality for SCFETs were hardly obtained on a Si/SiO₂/OTS substrate, often giving a fiber-like structure (Figure 2-4).

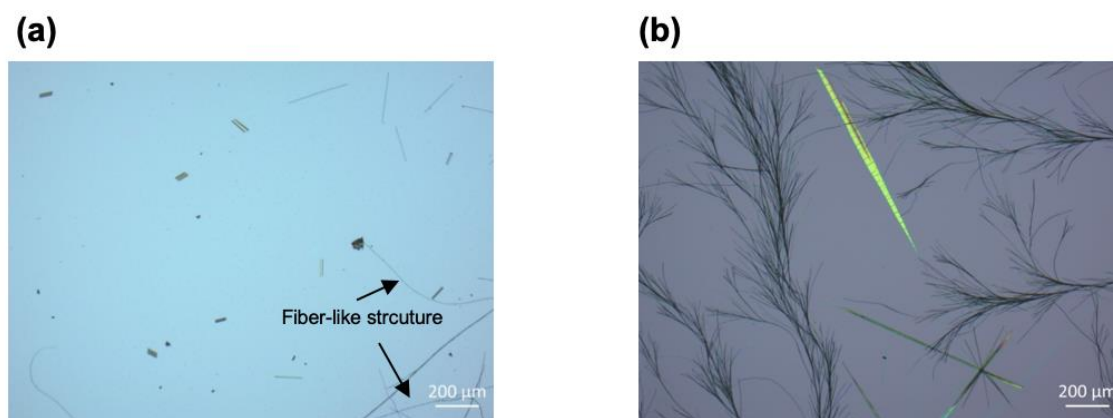


Figure 2-4. POM image of wire-shaped crystal and fiber-like structure of **TIPS-CuBP**. (b) Crystal formation of **TIPS-CuBP** on Si/SiO₂/OTS substrate with high humidity mainly gives fiber-like structure.

2-3. X-ray single crystal structure

Before examining the thin single crystal structure on a substrate, the bulk single crystal

structures for each **TIPS-BP** were analyzed in order to establish a referential basis for further discussion. Those single crystals were prepared from their respective toluene solutions, although the X-ray analysis had already been done for single crystals obtained from different solvent system in the previous report.^{11,12,21} In fact, solvents showed no effect on the packing structure. Briefly, a rigid and planar **TIPS-H₂BP** core (Figure 2-5) formed a one-dimensionally extended columnar π -stacking motif with the plane-to-plane distance of each **BP** of ca. 3.3 Å (Figure 2-6).²²

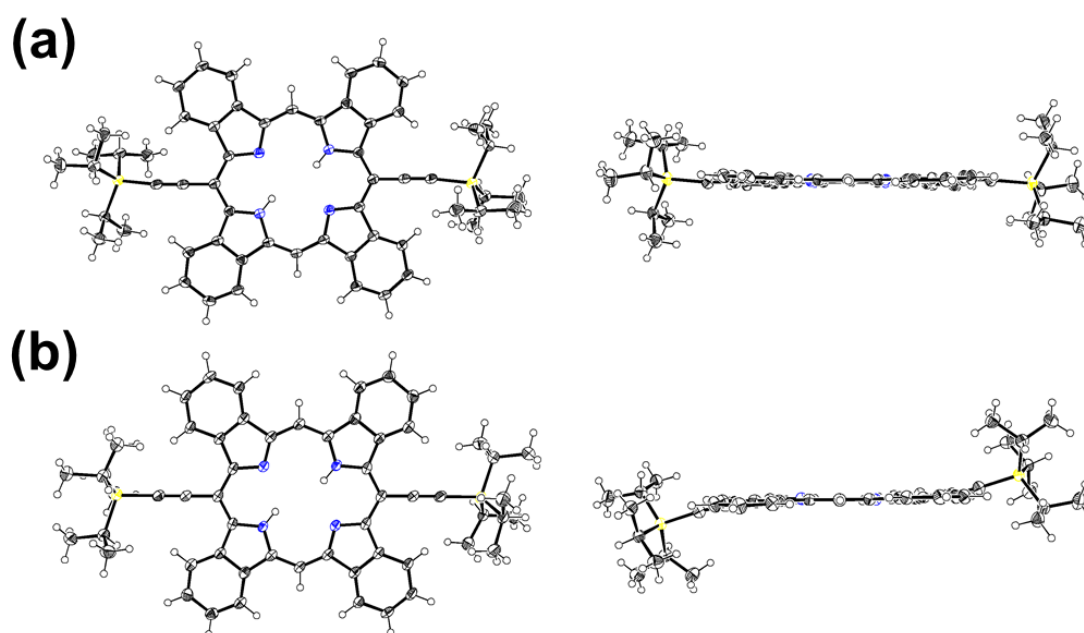


Figure 2-5. (a,b) Single crystal X-ray structure of **TIPS-H₂BP**. Thermal ellipsoids represent 50% probability.

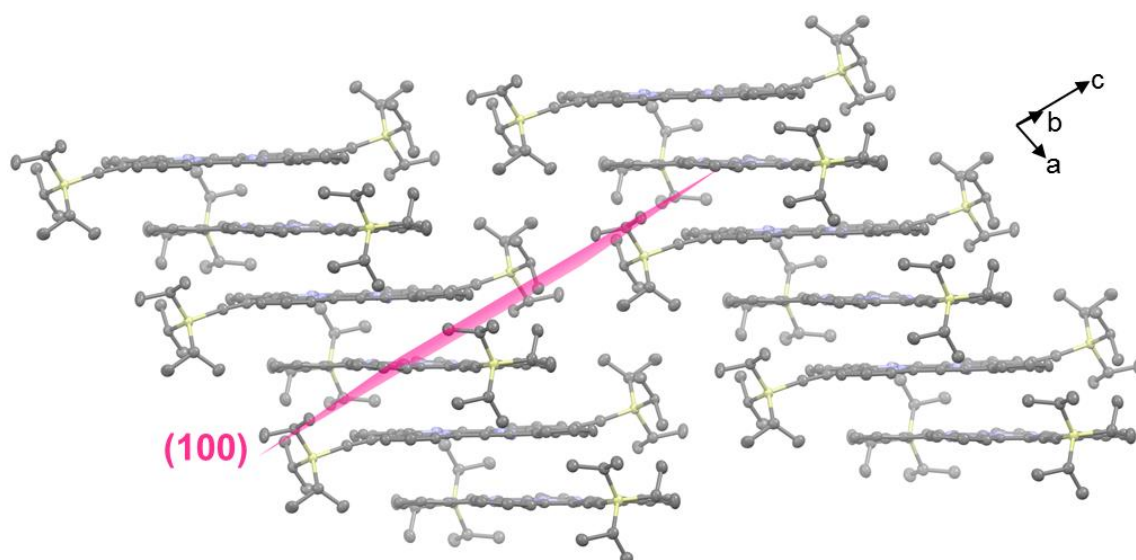


Figure 2-6. Packing structure of **TIPS-H₂BP** in the crystals obtained from toluene. Hydrogen atoms are omitted for clarity.

TIPS-H₂BP molecules stacked orthogonally in the packing, alternately possessing planar **TIPS-H₂BP** molecule (Figure 2-5a) and the one with two TIPSethynyl groups bend from the **BP** plane sigmoidally (Figure 2-5b). It is evident that the well-ordered alignment of **TIPS-H₂BP** facilitates the intermolecular charge transport in the column.

BP backbones of **TIPS-ZnBP**²³ (Figure 2-7a) and **TIPS-CuBP**²⁴ (Figure 2-7b) are similar to the one of **TIPS-H₂BP**. However, molecules in the single crystal form a triad-like structure where the molecules are stacked orthogonally.²⁵ In the triad-like structure, **TIPS-ZnBP** and **TIPS-CuBP** also have the plane-to-plane distance of ca. 3.3 Å, while the triad units are packed parallel to provide one-dimensional slip-stacked structures. In addition, planar **TIPS-ZnBP** or **TIPS-CuBP** molecule is sandwiched by the respective

metal complexes with sigmoidally bend TIPSethynyl groups in the triad-like structure.

As the result, a long-range molecular orientation is missing in the cases of **TIPS-ZnBP** and **TIPS-CuBP**, which is in contrast with that observed in **TIPS-H₂BP**.

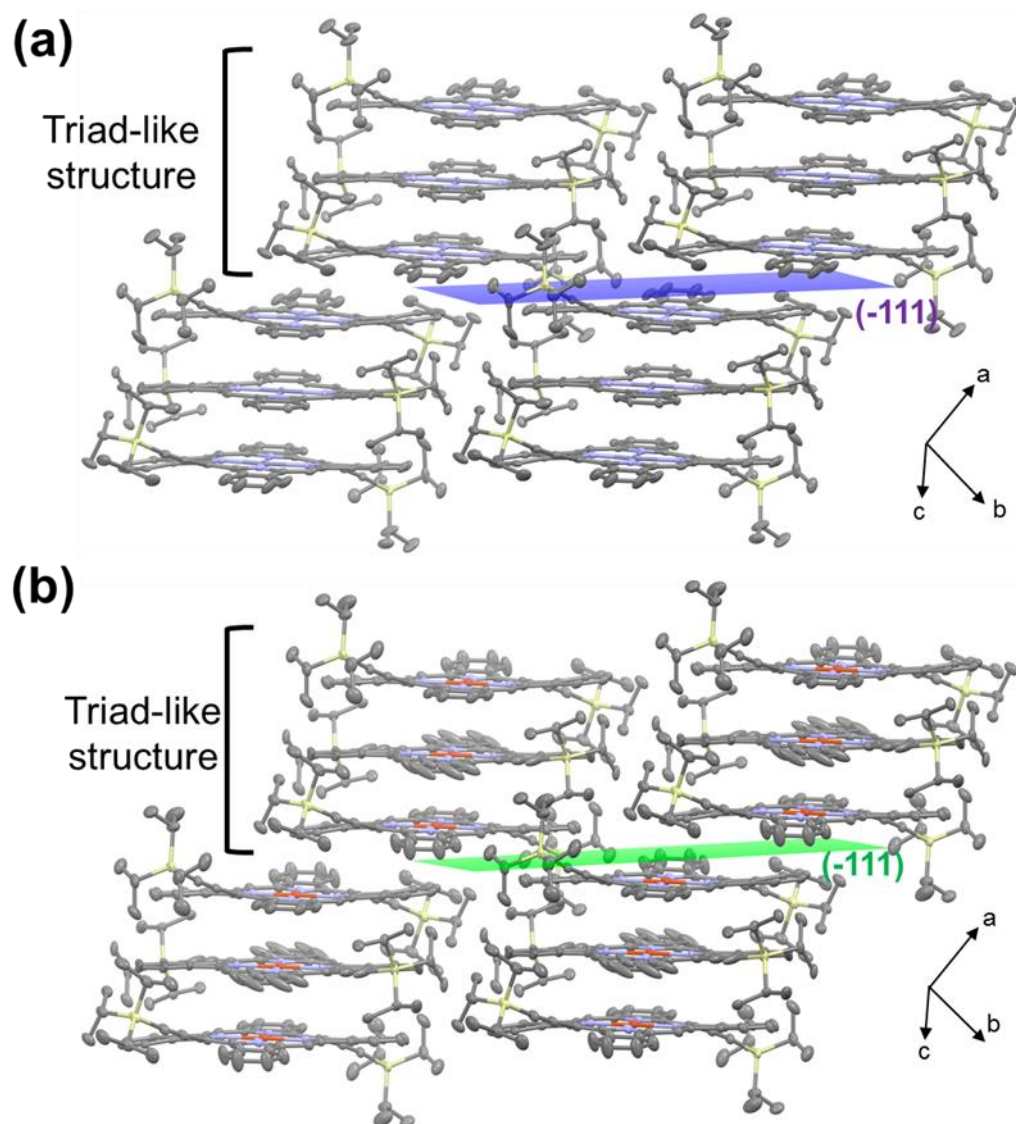


Figure 2-7. Packing structure of (a) **TIPS-ZnBP**, (b) **TIPS-CuBP** in the crystals obtained from toluene. Hydrogen atoms are omitted for clarity.

2-4. Out of plane XRD analysis

To shed light on the molecular orientation of single crystals on a substrate, out-of-plane XRD analysis was performed (Figure 2-8). In the case of **TIPS-H₂BP** (Figure 2-8a), the intense peaks at $2\theta = 5.16^\circ$ with a d -spacing of 17.1 Å together with peaks at $2\theta = 6.10^\circ$ (d -spacing = 14.5 Å) and at $2\theta = 6.23^\circ$ (d -spacing = 14.0 Å) were well-consistent with the simulated [001], [010], and [011] diffractions of one-dimensional columnar structure (Figure 2-8), respectively, according to the crystallographic data for the bulk crystal. In addition, these values match with the length of molecules (ca. 16 Å), implying the edge-on orientation of **TIPS-H₂BP** molecules on the substrate. These results support that the one-dimensional columnar packing in parallel to the substrate was grown through π - π stacking direction of **TIPS-H₂BP**. Note that a peak at 4.66° , which corresponds to [001] of the brickwork motif,⁶ was not observed, suggesting that one-dimensional columnar structure was selectively formed on a substrate from the toluene solution. Similarly, peaks at $2\theta = 5.02^\circ$ (d -spacing = 17.6 Å) and at $2\theta = 5.77^\circ$ (d -spacing = 15.3 Å) for **TIPS-ZnBP** are good agreement with the simulated [001] and [010] diffractions of **TIPS-ZnBP** columnar structure, respectively (Figure 2-8b). In the case of **TIPS-CuBP**, small peaks at $2\theta = 5.03^\circ$ (d -spacing = 17.6 Å) and at $2\theta = 5.82^\circ$ (d -spacing = 15.2 Å) which correspond to [001] and [010], respectively, could be observed (Figure 2-8c), while the

less amount of single-crystals on the substrate resulted in the overall weak peak intensity of XRD pattern. As described above, fiber-like structure also formed on a substrate together with ribbon-shaped crystals (Figure 2-4). Rigid π -systems sometimes form the crystalline nanofibers.^{25,26} Thus, these crystalline fibers account for the peaks at $2\theta = 4.87^\circ$ and $2\theta = 5.16^\circ$ which are not consistent with the simulated patterns of the one-dimensional columnar packing.

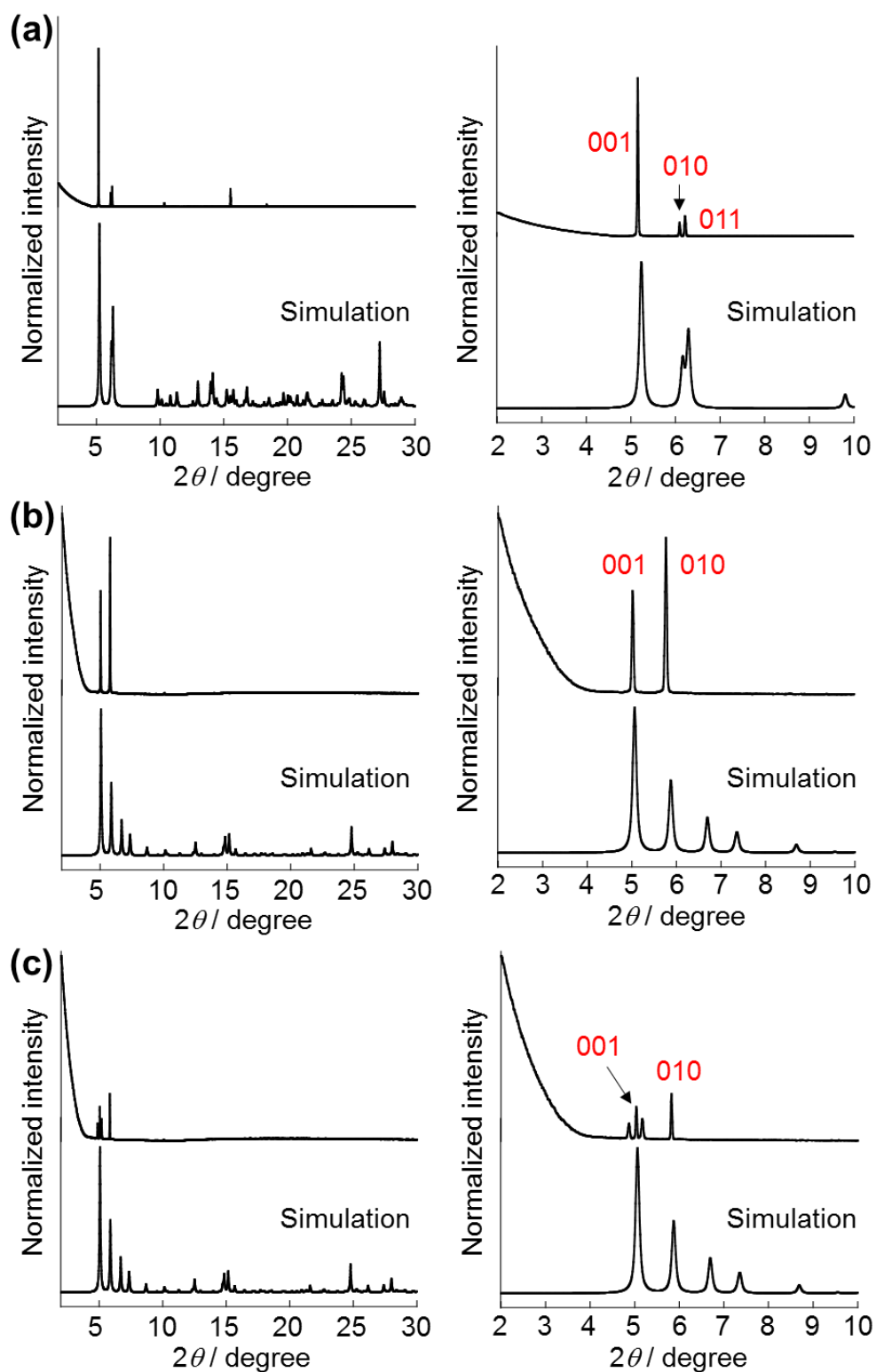


Figure 2-8. Experimental out-of-plane XRD and simulated powder XRD patterns of (a) TIPS-H₂BP, (b) TIPS-ZnBP, and (c) TIPS-CuBP. Intensified patterns from $2\theta = 2\text{--}10^\circ$ are also shown (right).

2-5. TEM and corresponding SAED patterns

In order to confirm the molecular arrangements in the ribbon-shaped crystals, TEM images and their corresponding selected area electron diffraction (SAED) patterns were collected from an individual ribbon-shaped crystal (Figure 2-9). The observed well-defined and bright diffraction spots demonstrate the single crystallinity. In addition, the SAED patterns could be indexed with its single crystal structure. As the results, it was found that the preferred crystal growth direction of **TIPS-H₂BP** (Figure 2-6), **TIPS-ZnBP** (Figure 2-7a), and **TIPS-CuBP** (Figure 2-7b) were [100], [-111], and [-111], respectively, which is in good agreement with the morphologies predicted through the Bravais–Friedel–Donnay–Harker (BFDH)^{27–29} method (Figure 2-10). Thus, SAED patterns and TEM analysis together with XRD measurement indicated that the growth direction of the ribbon-shaped crystals on the substrate was guided by π – π interactions, creating one-dimensionally extended packing motif as a charge carrier transport.

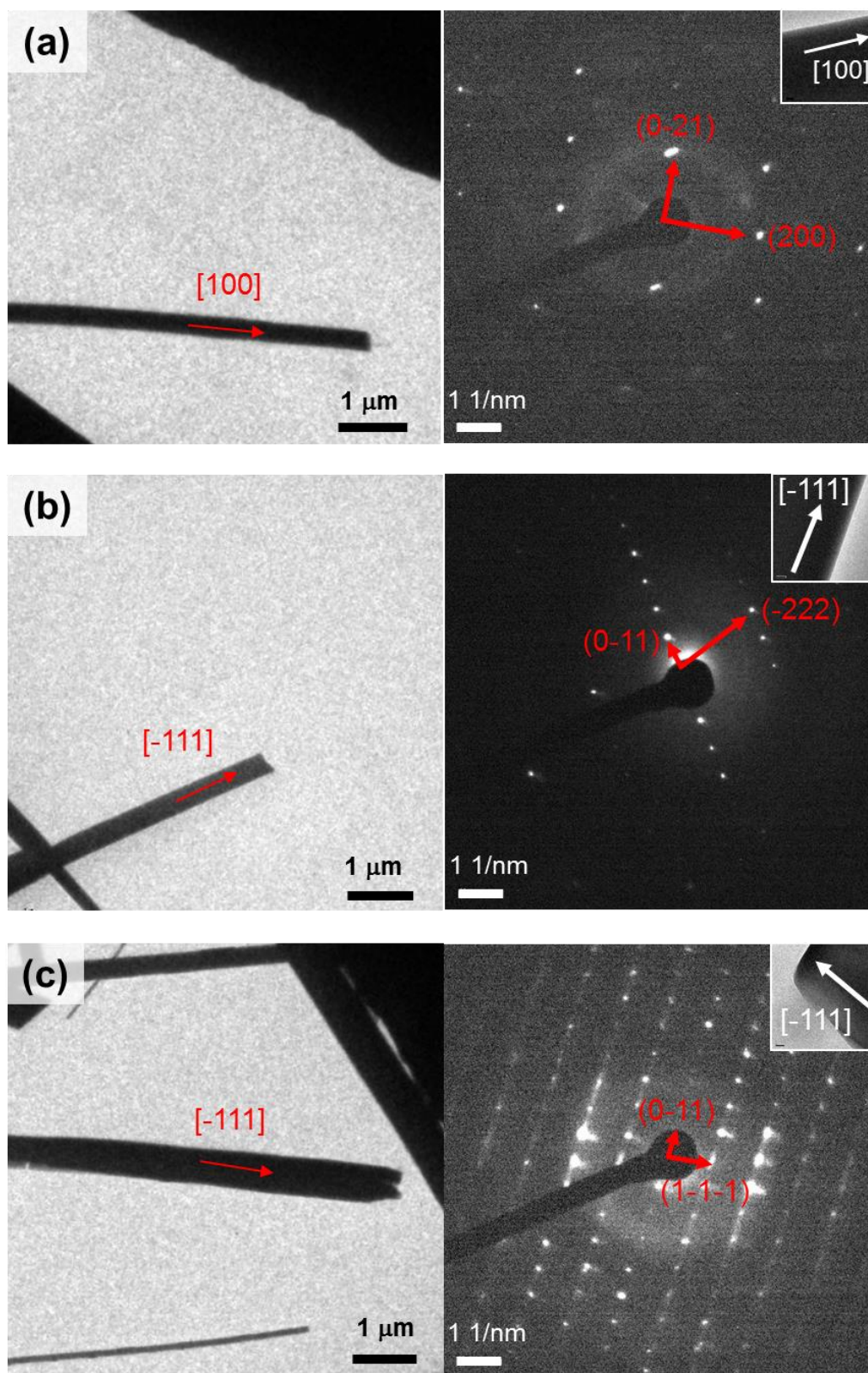


Figure 2-9. Representative TEM image and corresponding SAED pattern of (a) TIPS-H₂BP, (b) TIPS-ZnBP, and (c) TIPS-CuBP single crystal.

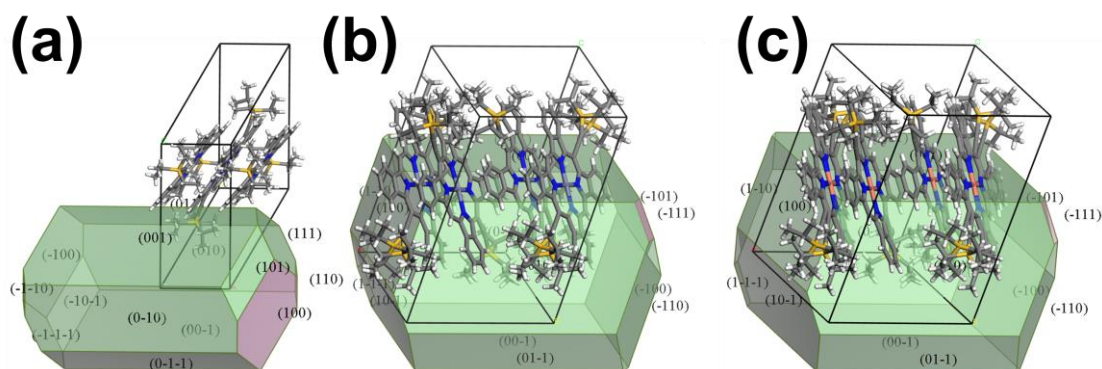


Figure 2-10. Theoretically predicted growth morphology of (a) **TIPS-H₂BP**, (b) **TIPS-ZnBP**, and (c) **TIPS-CuBP** by using the BFDH method. The assessment of the growth morphology was carried out using modelling routines available in Materials Studio.

2-6. Charge carrier mobility

Finally, the charge transport property of single crystals was evaluated by fabricating BGTC OFETs using “gold layer glue technique” which was introduced in the first chapter.³⁰ Briefly, gold source and drain electrodes were placed on a crystal which was grown by drop-casting of the toluene solution on Si/SiO₂/OTS substrate. The effective channel length and width were measured by microscope image of the substrate (Figure 2-11).

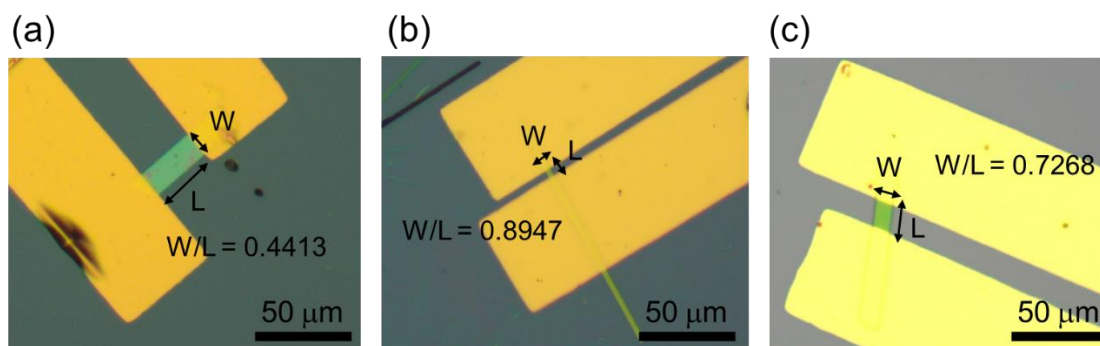


Figure 2-11. Representative microscope image of channel length and width of single-crystal-based OFET of (a) **TIPS-H₂BP**, (b) **TIPS-ZnBP**, and (c) **TIPS-CuBP**.

The ribbon-shaped crystals of **TIPS-H₂BP** exhibited the average values of $1.16 \text{ cm}^2 \text{ V}^{-1} \text{ s}^{-1}$ with 15 devices (Figure 2-12a,d), giving the maximum hole mobility of $2.16 \text{ cm}^2 \text{ V}^{-1} \text{ s}^{-1}$ with a threshold voltage V_{th} of 15.6 V and on/off ratio $I_{\text{on}}/I_{\text{off}}$ of 6.1×10^2 (Figure 2-13a). In the previous report, the one-dimensional columnar structure of **TIPS-H₂BP** prepared by drop-casting method exhibited the hole mobility of $0.027 \text{ cm}^2 \text{ V}^{-1} \text{ s}^{-1}$.⁶ Thus, the maximum hole mobility obtained in this study is approximately 87 times higher than the drop-casting one. This result supported that the molecular orientation of **TIPS-H₂BP** are preferable to SCFETs, with the charge transport through π - π stacking of **BP** units in the one-dimensional column. In addition, the efficient charge transport reflected the feature of single crystals with free of grain boundaries and minimized defects. It should be noted that nearly identical curves were observed after 10 cycles (Figure 2-14), suggesting the good bias-stress stability of SCFETs based on ribbon-shaped crystals of

TIPS-H₂BP. Here, SCFET devices based on TIPS-H₂BP often showed the hole carriers on operation mode specially for the device which exhibited the high hole mobility (Figure 2-14a, d), indicating that the transport channel was already formed even without gate bias ($V_G = 0$ V). This is probably due to the high hole density of TIPS-H₂BP. The holes not only filled the trap states, but also the excess holes became free carriers, forming a conducting channel even though at $V_G = 0$ V. Moreover, the decreased trap states would facilitate carrier transport, thus improved the mobility of TIPS-H₂BP.³¹

On the other hand, the ribbon-shaped crystals of the metal complexes, **TIPS-ZnBP** and **TIPS-CuBP**, showed clearly lower hole mobilities compared with **TIPS-H₂BP** (Figure 2-12b,c,e,f, Figure 2-13), although those values were much higher than the ones prepared by spin-coating method ($1.1 \times 10^{-5} \text{ cm}^2 \text{ V}^{-1} \text{ s}^{-1}$ for **TIPS-ZnBP** and $5.6 \times 10^{-3} \text{ cm}^2 \text{ V}^{-1} \text{ s}^{-1}$ for **TIPS-CuBP**).²¹ The maximum hole mobility of $0.12 \text{ cm}^2 \text{ V}^{-1} \text{ s}^{-1}$ (average values of $0.05 \text{ cm}^2 \text{ V}^{-1} \text{ s}^{-1}$ with 12 devices) with a threshold voltage V_{th} of 6.6 V and on/off ratio I_{on}/I_{off} of 7.6×10^5 for **TIPS-ZnBP**, while **TIPS-CuBP** showed the maximum hole mobility of $0.16 \text{ cm}^2 \text{ V}^{-1} \text{ s}^{-1}$ (average values of $0.14 \text{ cm}^2 \text{ V}^{-1} \text{ s}^{-1}$ with 4 devices) with a threshold voltage V_{th} of 3.0 V and on/off ratio I_{on}/I_{off} of 1.1×10^3 . This result is rationalized by the fact that charge transport is suppressed in the cases of **TIPS-ZnBP** and **TIPS-CuBP** because of their triad-like structures (Figure 2-7), clearly indicating the metalation

gave negative effects on the charge transport property.

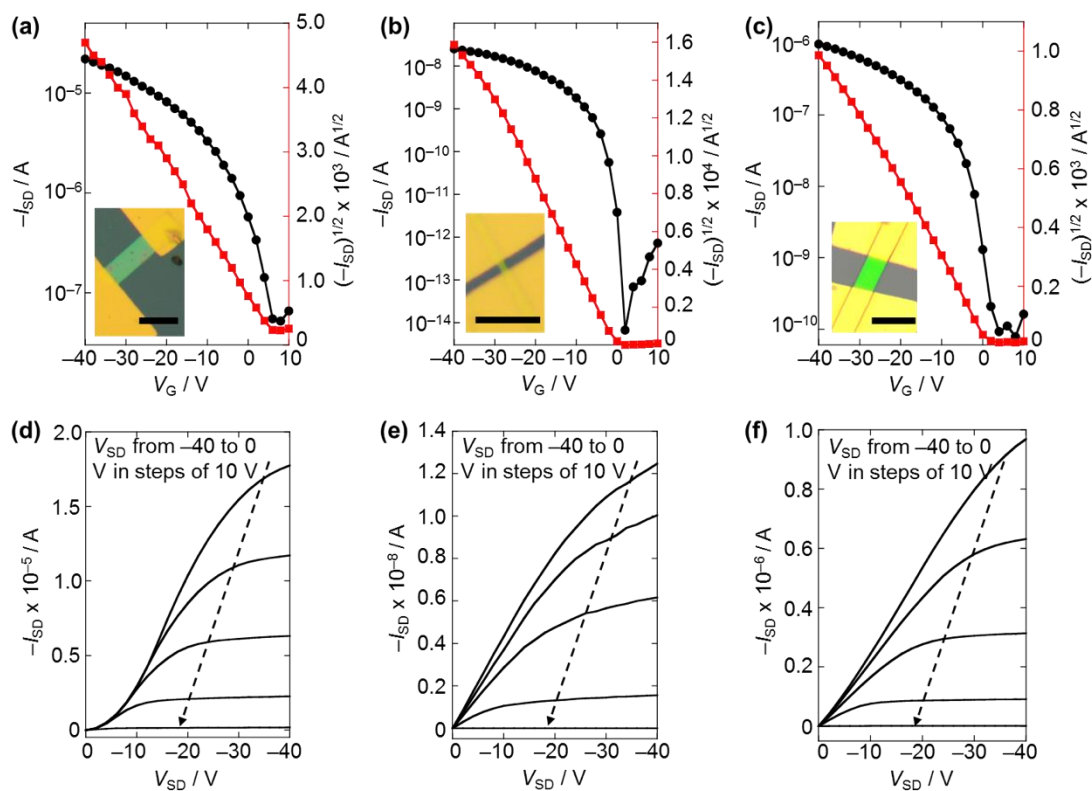


Figure 2-12. Typical transfer (a–c) and output (d–f) characteristics of the device of (a, d) TIPS-H₂BP, (b, e) TIPS-ZnBP, and (c, f) TIPS-CuBP crystals at a fixed source/drain voltage, $V_{SD} = -40$ V. Insets show image of device. Scale bar: 25 μm.

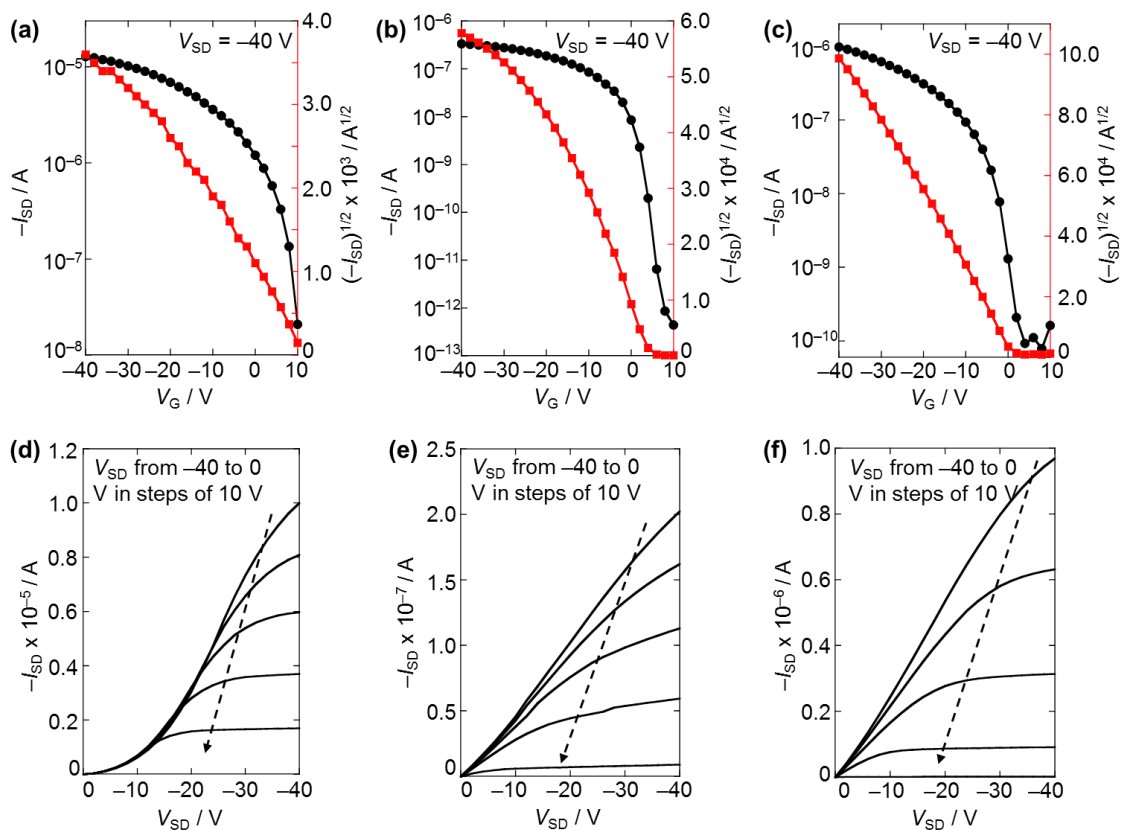


Figure 2-13. Transfer (a–c) and output (d–f) characteristics of the device of (a, d) **TIPS-H₂BP**, (b, e) **TIPS-ZnBP**, and (c, f) **TIPS-CuBP** crystals which showed the best hole mobility.

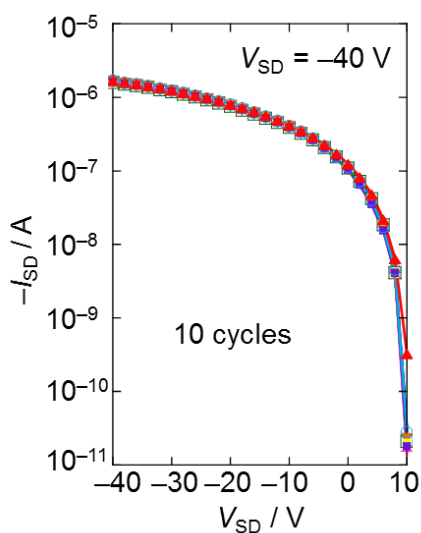


Figure 2-14. Bias stress stability curves of OFETs based on ribbon-shaped crystals of **TIPS-H₂BP**.

2-7. Summary and outlook

In summary, SCFETs of **TIPS-H₂BP** and its metal complexes were fabricated and their charge transport properties were evaluated. **TIPS-H₂BP** exhibited the best mobility (2.16 cm² V⁻¹ s⁻¹) among the **BP** derivatives employed in this study. XRD and TEM analyses unveiled that the long-range one-dimensional columnar structure of **TIPS-H₂BP** contributed the high charge transport property. It should be noted that the deviation between the maximum and average hole mobilities of **TIPS-H₂BP** would stem from the quality of single crystals, meaning that finding of optimized conditions for single crystal formation could improve the charge transport property. More importantly, recent synthetic efforts are providing the variety of chemical modification for **BP** cores.^{6,32-34} Considering that **TIPS-H₂BP** shows excellent stability, elaborately-designed **BP** derivatives have a great potential to be a promising semiconducting material. We believe that fine-tuning of **BP** structure enables the significant improvement in the charge transport property.

2-8. Experimental Section

2-8-1. General: Materials and Methods

Reagents for synthesis were purchased from Wako, Nacalai Tesque, and Sigma Aldrich, and were reagent-grade quality, obtained commercially, and used without further purification. X-ray crystallographic data were recorded at 103 K on a Rigaku R-AXIS RAPID/S using Mo-K α radiation ($\lambda = 0.71073 \text{ \AA}$). Polarized optical images of the thin films were obtained using ZEISS Axio Scope.A1 microscope. Out-of-plane thin-film XRD measurements were carried out on a Rigaku SmartLAB X-ray reflectometer equipped with a rotating anode (Cu-K α , $\lambda = 1.5418 \text{ \AA}$) operated at 15 kW. Measurements were performed in the θ - 2θ mode with a scan range of $2\theta = 2$ - 30° . TEM observation was carried out with a JEOL JEM-3100FEF operated at 300 kV. Indexing of SAED patterns was carried out by using DigitalMicrograph 3.43.

2-8-2. Morphology predictions

A theoretical study of morphology predictions of these micro/nanometersized single-crystals was implemented and conducted to relate the morphology to the crystalline structures. Crystal morphology predictions were performed allowing a minimum dhkl of 1.300 \AA and a maximum values for the three Miller indexes were set to 3, 3, 3,

respectively. The overall number of growing faces was limited to 200.

2-8-3. Fabrication and evaluation of the SC-OFFTs

The highly *n*-doped silicon wafers with a 300 nm-thick thermally grown SiO₂ layer (capacitance of 10 nF/cm²) were cleaned with deionized (DI) water, piranha solution (H₂SO₄:H₂O₂ = 2:1), deionized (DI) water, pure isopropanol for 10 min under an ultrasonic bath. Then substrates were dried with a flow of nitrogen gas. Treatment of the Si/SiO₂ wafers with OTS was carried out by the vapor-deposition method. The clean wafers were dried under vacuum at 90 °C for 1 h in order to eliminate the influence of moisture. After cooling to RT, one drop of OTS was placed on the center of system. Subsequently, this system was heated to 120 °C and maintained for 2 h under vacuum followed with an ultra-sonication in hexane, chloroform and isopropanol for 10 min. Then, a toluene solution of **TIPS-BP** (1.0 mg/ml **TIPS-H₂BP** and **TIPS-CuBP**, 0.5 mg/ml **TIPS-ZnBP**) was drop-casted on the OTS-modified substrate, giving single crystals on surface. Source and drain electrodes were deposited on the crystal by using gold layer glue technique.

All electrical characteristics of the devices were measured at room temperature using a semiconductor parameter analyser (Keithley 4200 SCS) and Micromanipulator 6150

probe station. The field-effect hole mobilities were determined in the saturation regime by using the equation of $I_{DS} = (\mu WC_i/2L)(V_G - V_{th})^2$, where I_{DS} is the drain-source current, μ is the field-effect mobility, W is the channel width, L is the channel length, C_i (10 nF cm⁻² for OTS-modified Si/SiO₂ substrate) is the capacitance per unit area of the gate dielectric layer, V_G is the gate voltage, and V_{th} is the threshold voltage, respectively. The effective channel length and width were measured by microscope image of the substrate.

2-9. Reference

- (1) V. Coropceanu, J. Cornil, D. A. S. Filho, Y. Olivier, R. Silbey, and J Brédas, *Chem. Rev.*, **2007**, *107*, 926–952.
- (2) B. Kuei, and E. D. Gomez, *Soft Matter*, 2017, **13**, 49–67. C. Zhan, and J. Yao, *Chem. Mater.*, **2016**, *28*, 1948–1964.
- (3) C. Zhan, and J. Yao, *Chem. Mater.*, **2016**, *28*, 1948–1964.
- (4) J. Mei, Y. Diao, A. L. Appleton, L. Fang, and Z. Bao, *J. Am. Chem. Soc.*, **2013**, *135*, 6724–6746.
- (5) C. M. B. Carvalho, T. J. Brocksom, and K. T. Oliveira, *Chem. Soc. Rev.*, **2013**, *42*, 3302–3317.
- (6) H. Yamada, D. Kuzuhara, M. Suzuki, H. Hayashi, and N. Aratani, *Bull. Chem. Soc.*

- Jpn.*, **2020**, *93*, 1234–1267.
- (7) J. E. Anthony, J. S. Brooks, D. L. Eaton, and S. R. Parkin, *J. Am. Chem. Soc.*, **2001**, *123*, 9482–9483.
- (8) Y. Diao, B. C.-K. Tee, G. Giri, J. Xu, D. H. Kim, H. A. Becerril, R. M. Stoltenberg, T. H. Lee, G. Xue, S. C. B. Mannsfeld, and Z. Bao, *Nat. Mater.*, **2013**, *12*, 665–671.
- (9) S. Ito, T. Murashima, H. Uno, and N. Ono, *Chem. Commun.*, **1998**, *16*, 1661–1662.
- (10) S. Aramaki, Y. Sakai, and N. Ono, *Appl. Phys. Lett.*, **2004**, *84*, 2085–6563.
- (11) N. Noguchi, S. Junwei, H. Asatani, and M. Matsuoka, *Cryst. Growth Des.*, **2010**, *10*, 1848–1853.
- (12) K. Takahashi, B. Shan, X. Xu, S. Yang, T. Koganezawa, D. Kuzuhara, N. Aratani, M. Suzuki, Q. Miao, and H. Yamada, *ACS Appl. Mater. Interfaces*, **2017**, *9*, 8211–8218.
- (13) K. S. Chichak, S. J. Cantrill, A. R. Pease, S.-H. Chiu, G. W. V. Cave, J. L. Atwood, and J. F. Stoddart, *Science*, **2004**, *304*, 1308–1311.
- (14) K. Suzuki, S. Sato, and M. Fujita, *Nat. Chem.*, **2010**, *2*, 25–29.
- (15) J. Guo, P. C. Mayers, G. A. Breault, and C. A. Hunter, *Nat. Chem.*, **2010**, *2*, 218–222.
- (16) J. B. Beves, B. A. Blight, C. J. Campbell, D. A. Leigh, and R. T. McBurney, *Angew. Chem., Int. Ed.*, **2011**, *50*, 9260–9327.

- (17) Z. Bao, A. J. Lovinger, A. Dodabalapur, *Adv. Mater.* **1991**, *9*, 42–44.
- (18) O. A. Melville, B. H. Lessard, T. P. Bender, *Appl. Mater. Interfaces*, **2015**, *7*, 13105–13118.
- (19) C. M. Che, H. F. Xiang, S. Y. Chui, Z. X. Xu, V. A. L. Roy, J. J. Yan, W. F. Fu, P. T. Lai, I. D. Williams. *Chem. Asian J.* **2008**, *3*, 1092–1103.
- (20) M. H. Hoang, Y. Kim, S. J. Kim, D. H. Choi, S. J. Lee, *Chem. Eur. J.* **2011**, *17*, 7772–7776.
- (21) K. Takahashi, N. Yamada, D. Kumagai, D. Kuzuhara, M. Suzuki, Y. Yamaguchi, N. Aratani, K. Nakayama, and H. Yamada, *J. Porphyr. Phthalocyanines*, **2015**, *19*, 465–478.
- (22) Crystallographic data for **TIPS-H₂BP**: C₅₈H₆₂N₄Si₂, $M_w = 871.29$, Triclinic, space group *P*-1, $a = 8.9318(8)$, $b = 15.8384(14)$, $c = 18.7438(17)$ Å, $\alpha = 63.316(5)^\circ$, $\beta = 78.745(6)^\circ$, $\gamma = 81.031(6)^\circ$, $V = 2354.7$ Å³, $T = 103$ K, $Z = 2$, reflections measured 32403, 8610 unique. The final R_1 was 0.0986 ($I > 2\sigma(I)$), and the final wR on F^2 was 0.2446 (all data), GOF = 0.998. CCDC:2099221.
- (23) Crystallographic data for **TIPS-ZnBP**: C₅₈H₆₀N₄Si₂Zn, $M_w = 934.65$, Triclinic, space group *P*-1, $a = 12.9207(2)$, $b = 15.7074(3)$, $c = 19.0205(4)$ Å, $\alpha = 101.5873(7)^\circ$, $\beta = 108.2265(7)^\circ$, $\gamma = 97.6339(7)^\circ$, $V = 3511.50$ Å³, $T = 103$ K, $Z = 3$, reflections

measured 61191, 16079 unique. The final R_1 was 0.0403 ($I > 2\sigma(I)$), and the final wR on F^2 was 0.1127 (all data), GOF = 1.072. CCDC:2099222.

(24) Crystallographic data for **TIPS-CuBP**: $C_{58}H_{60}N_4Si_2Cu$, $M_W = 932.82$, Triclinic, space group $P-1$, $a = 12.9584(3)$, $b = 15.6807(3)$, $c = 19.0596(4)$ Å, $\alpha = 101.5277(7)^\circ$, $\beta = 108.3473(7)^\circ$, $\gamma = 97.3928(7)^\circ$, $V = 3524.59$ Å³, $T = 103$ K, $Z = 3$, reflections measured 60254, 16310 unique. The final R_1 was 0.0621 ($I > 2\sigma(I)$), and the final wR on F^2 was 0.1956 (all data), GOF = 1.156. CCDC:2099223.

(25) S. Tanaka, M. Shirakawa, K. Kaneko, M. Takeuchi, and S. Seiji, *Langmuir*, **2005**, *21*, 2163–2172.

(26) H. Hayashi, N. Aratani, and H. Yamada, *Chem. Eur. J.*, **2017**, *23*, 7000–7008.

(27) J. D. H. Donnay, and D. Harker, *Am. Mineral.*, **1937**, *22*, 446–467.

(28) A. L. Briseno, S. C. B. Mannsfeld, X. Lu, Y. Xiong, S. A. Jenekhe, Z. Bao, and Y. Xia, *Nano Lett.*, **2007**, *7*, 668–675.

(29) C. Wang, Z. Liang, Y. Liu, X. Wang, N. Zhao, Q. Miao, W. Hu, and J. Xu, *J. Mater. Chem.*, **2011**, *21*, 15201–15204.

(30) L. Jiang, H. Dong, W. Hu, *J. Mater. Chem.*, **2010**, *20*, 4994–5007.

(31) H. Wang, X. Wang, H. Huang, and D. Yan, *Appl. Phys. Lett.*, **2008**, *93*, 103307.

(32) S. Kumar, X. Jiang, W. Shan, R. G. W. Jinadasa, K. M. Kadish, H. Wang, *Chem.*

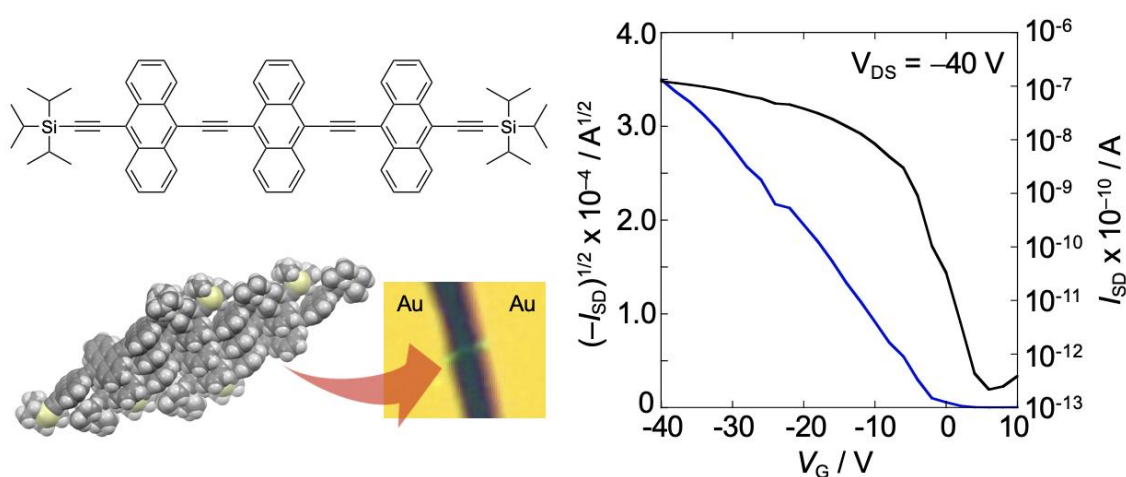
Commun., **2018**, *54*, 5303–5306.

(33) M. Ruppel, L.-P. Gazetas, D. Lungerich, F. Hampel, N. Jux, *J. Org. Chem.*, **2020**, *85*, 7781–7792.

(34) K. Muramatsu, T. Okujima, S. Mori, M. Takase, and H. Uno, *Chem. Lett.*, **2021**, *50*, 841–843.

Chapter 3.

Synthesis and Evaluation of Charge Transport Property of Ethynylene-bridged Anthracene Oligomers



In this chapter, a set of ethynylene-bridged anthracene oligomers from monomer to tetramer was synthesized and characterized. The organic field-effect transistors were fabricated and it was revealed that trimer showed better charge transport property ($8.0 \times 10^{-3} \text{ cm}^2 \text{ V}^{-1} \text{ s}^{-1}$) than dimer ($8.9 \times 10^{-4} \text{ cm}^2 \text{ V}^{-1} \text{ s}^{-1}$). Furthermore, the single-crystal field-effect transistor of trimer showed mobility up to $0.14 \text{ cm}^2 \text{ V}^{-1} \text{ s}^{-1}$, which was higher than that of tetramer ($3.3 \times 10^{-2} \text{ cm}^2 \text{ V}^{-1} \text{ s}^{-1}$).

3-1. Introduction

As introduced in the chapter 1, π -conjugated system owing to its delocalized π -electron have been regarded as a promising OFET material. Especially, [*n*]acenes, that is a class of organic compounds and polycyclic aromatic hydrocarbons made up of linearly fused benzene rings, are known to exhibit some of the highest OFET mobilities.¹ Considering the importance of molecular core π -system elongation for the packing motif of molecules, large acenes more than pentacene are expected to be promising materials. Indeed, pentacene, which is regarded as a benchmark compound, is useful as a building block in organic semiconducting materials. Hexacene itself also exhibits the very high OFET mobility up to $4.28 \text{ cm}^2 \text{ V}^{-1} \text{ s}^{-1}$.² However, [*n*]acenes higher than pentacene are easily oxidized in air because of the high highest occupied molecular orbital (HOMO). In addition, their planar structures without any functional groups lead to poor solubility. These factors result in the difficulty in molecular π -system elongation by the chemical functionalization.

Anthracene has a rigid and planar structure with high air stability because of its appropriate HOMO level. Compared with higher [*n*]acenes, anthracene derivatives showed better solubility together with relatively easy chemical modification to tune the packing structure.³ The π -system elongation at the 2,6-positions of anthracene by the

oligomerization or functionalization presents the most potential candidates for p-type FET mobility with the highest mobility of $34 \text{ cm}^2 \text{ V}^{-1} \text{ s}^{-1}$ (Figure 3-1a).⁴ At the same time, the functionalization at 9,10-positions of anthracene has also been widely examined by solution synthesis and recently on-surface synthesis.⁵ In terms of molecular design, the substituents and/or linkers at 9,10-positions of anthracene need to be carefully considered because the steric hindrance causes a large torsion between substituents and anthracene cores. To avoid steric hindrance between the adjacent anthracene units, ethynylene-bridges are suitable spacers, conjugating anthracene units in a potentially planar or twisted structure. The availability of efficient synthetic protocols for ethynylene-bridging allows the easy modification of the effective π -conjugation length by controlling the number of anthracene-ethynylene repeating units, providing shape-persistent rod-like structures. For example, Hu and co-workers fabricated single-crystal OFETs of di-anthrylene-ethynylene (Figure 3-1b) by using an organic mask ribbon technique.⁶ This “H”-type molecule exhibited high OFET mobility of $0.82 \text{ cm}^2 \text{ V}^{-1} \text{ s}^{-1}$. In addition, Suranna and co-workers have reported the synthesis of a set of ter-anthrylene-ethynylene derivatives (Figure 3-1c), and the charge transport property was evaluated by solution-processing FETs, with the FET mobility measured to be $10^{-2} \text{ cm}^2 \text{ V}^{-1} \text{ s}^{-1}$ order.⁷

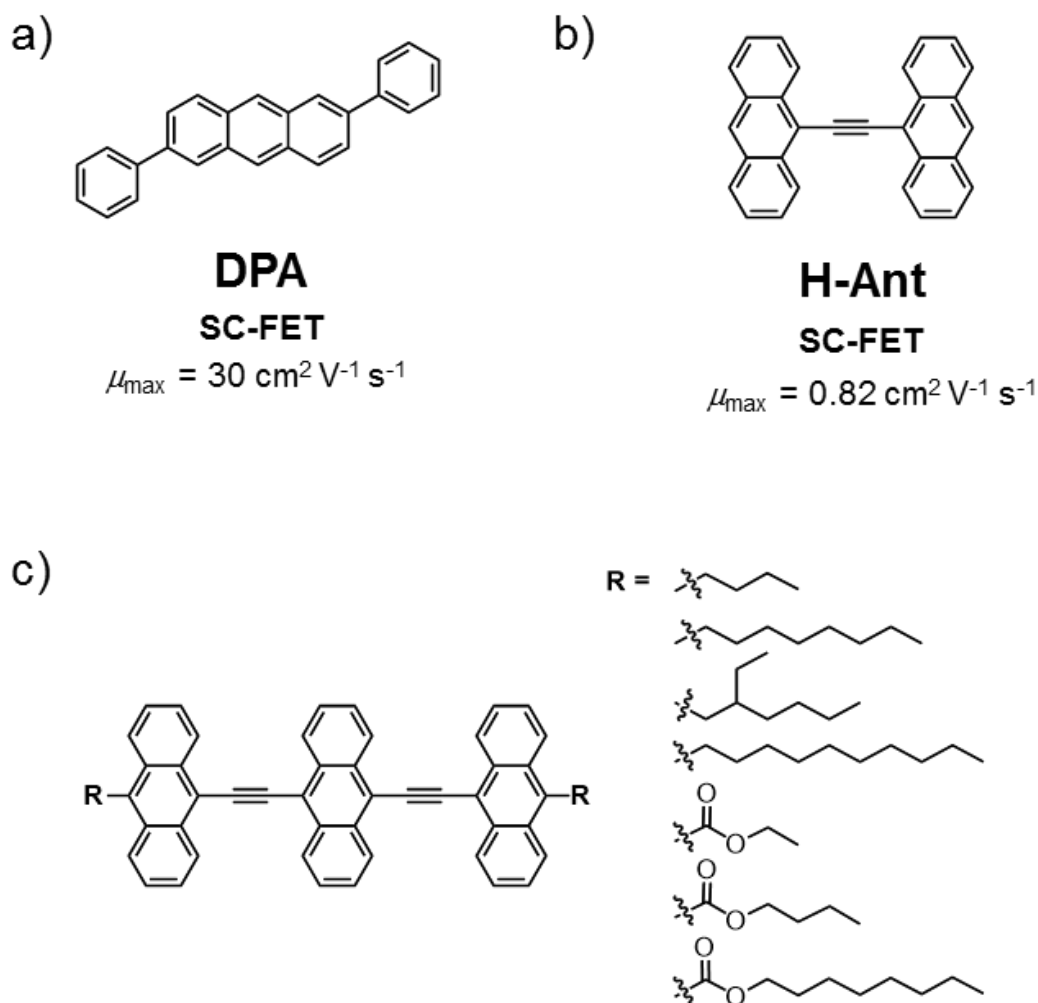


Figure 3-1. Previous reported ethylene-bridged anthracene derivatives.

These results prompt us to investigate the property of a further oligomer, namely tetra-anthrylene-ethynylene derivatives, to understand the oligomerization effect on the packing structure and charge transport property.

In this study, a set of ethynylene-bridged anthracene oligomers up to **4mer** were synthesized and characterized (Figure 3-2). TIPSethynyl group was chosen as the terminal groups of the anthracene oligomers to ensure the solubility. The optical,

electrochemical, packing structure, and charge transport properties were investigated.

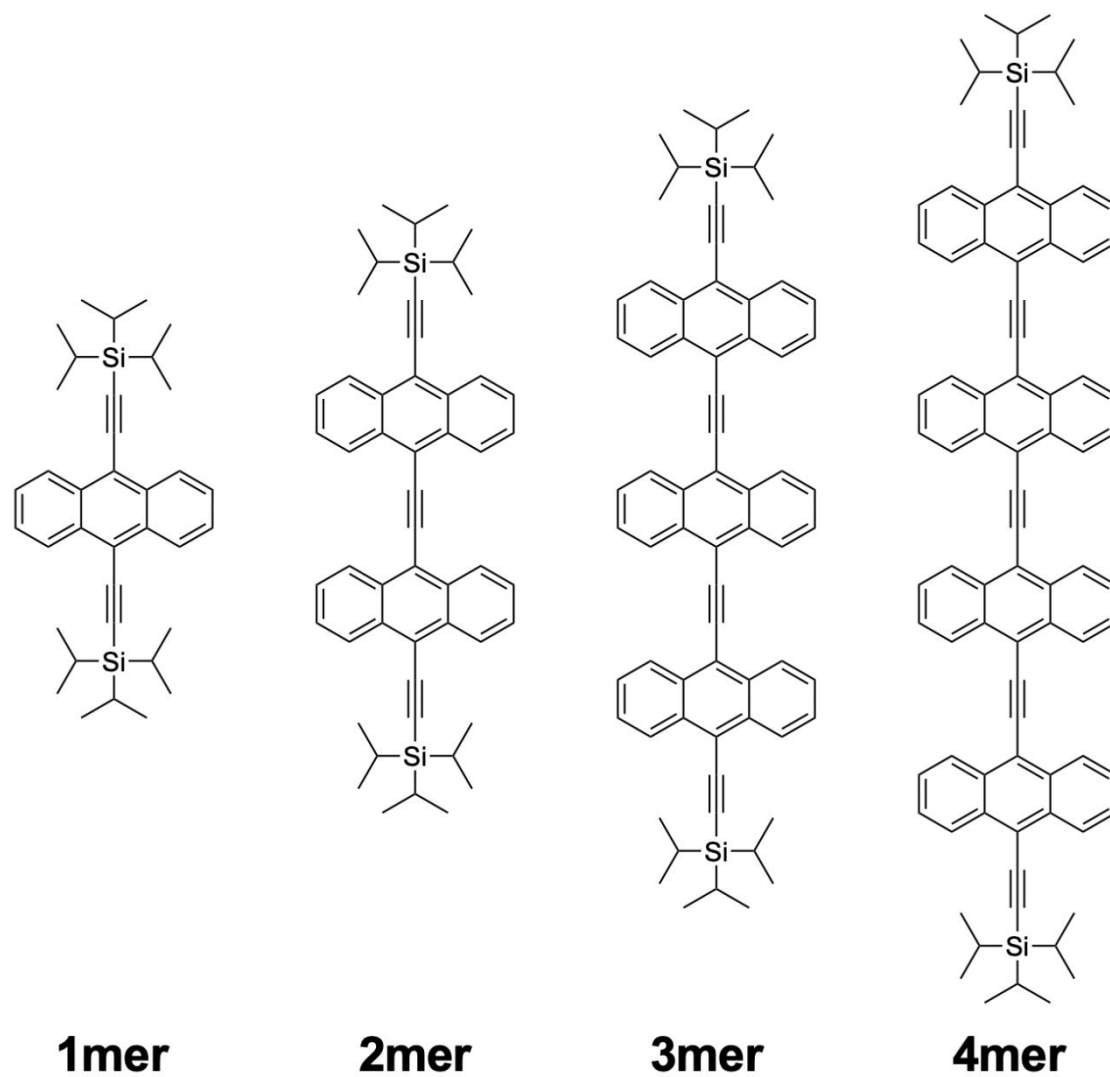
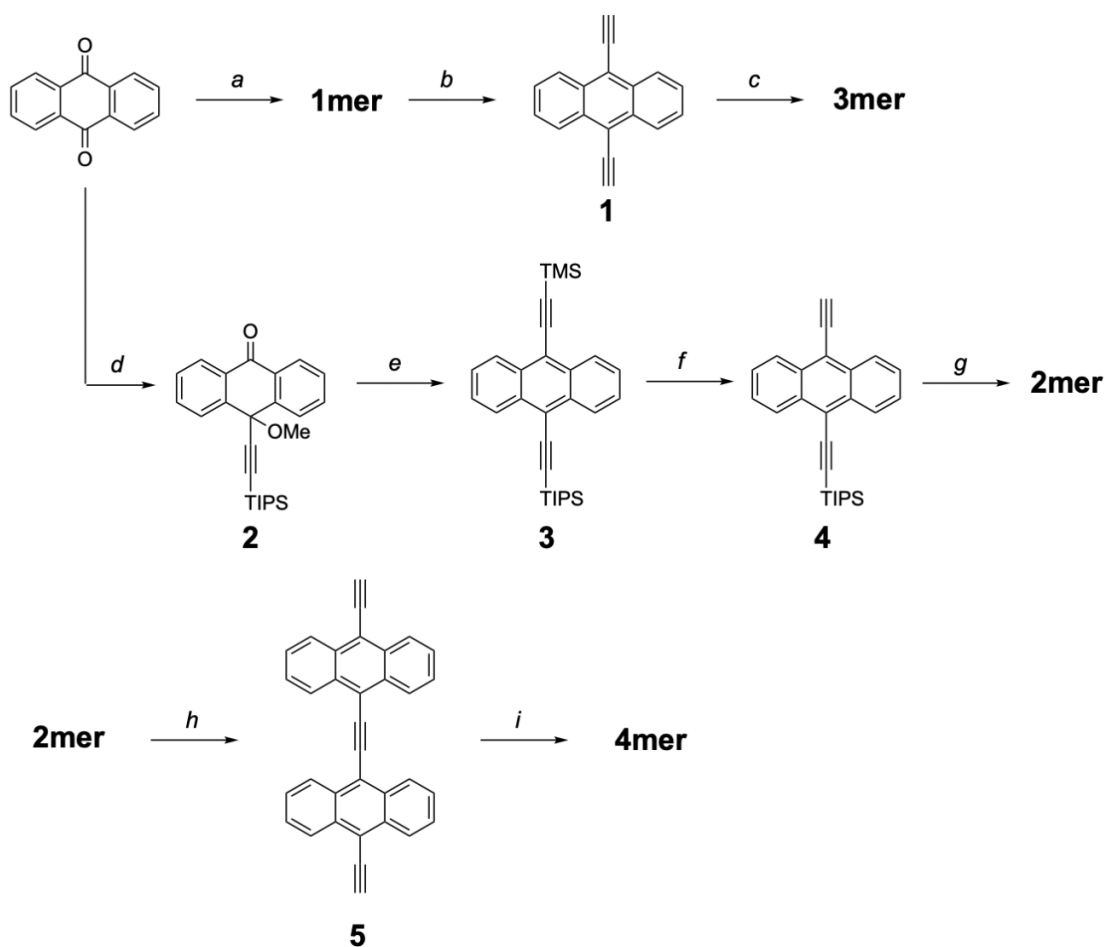


Figure 3-2. Molecular structures employed in this chapter.

3-2. Molecular design and synthesis

The synthetic pathway of the ethynylene-bridged anthracene oligomers is shown in

Scheme 3-1.



Scheme 3-1. Synthetic route for ethynylene-bridged anthracene oligomers. a) 1) TIPSethynylene, *n*-BuLi (2.6 M in hexanes), dry THF, $-5\text{ }^{\circ}\text{C}$, RT, 12 h, 2) $\text{SnCl}_2 \cdot 2\text{H}_2\text{O}$, 3 M HCl, RT, 12 h, 78%; b) TBAF, THF, water, RT, 2 h, 97%; c) 1) 2, *n*-BuLi (2.6 M in hexanes), dry THF, $-5\text{ }^{\circ}\text{C}$, RT, 12 h, 2) $\text{SnCl}_2 \cdot 2\text{H}_2\text{O}$, 10% H_2SO_4 , RT, 12 h, 73%; d) 1) TIPSethynylene, *n*-BuLi (2.6 M in hexanes), 2) MeI, dry THF, $-78\text{ }^{\circ}\text{C}$, RT, 12 h, 80%; e) 1) TMSethynylene, *n*-BuLi (2.6 M in hexanes), dry THF, $-5\text{ }^{\circ}\text{C}$, RT, 8 h, 2) $\text{SnCl}_2 \cdot 2\text{H}_2\text{O}$, 10% H_2SO_4 , RT, 12 h, 87%; f) K_2CO_3 , THF, MeOH, water, RT, 1 h, 97%; g) 1) 2, *n*-BuLi (2.6 M in hexanes), dry THF, $-5\text{ }^{\circ}\text{C}$, RT, 12 h, 2) $\text{SnCl}_2 \cdot 2\text{H}_2\text{O}$, 10% H_2SO_4 , RT, 12 h, 36%; h) TBAF, THF, water, RT, 2 h, 95%; i) 1) 2, *n*-BuLi (2.6 M in hexanes),

dry THF, $-5\text{ }^{\circ}\text{C}$, RT, 12 h, 2) $\text{SnCl}_2 \cdot 2\text{H}_2\text{O}$, 10% H_2SO_4 , RT, 12 h, 5%. RT = room temperature. TBAF = Tetrabutylammonium fluoride.

Briefly, TIPSEthynyl groups were introduced at the 9,10-positions of anthracene by using standard conditions with TIPSEthynylene and anthraquinone, giving **1mer** as a pale yellow solid. The addition of 1.5 equivalent of acetylide of TIPSEthynylene to anthraquinone followed by trapping of the resulting alkoxide with iodomethane afforded methyl-ether protected compound **2**.⁸ Then, further functionalization with acetylide of trimethylsilyl(TMS)ethynylene followed by the reductive aromatization gave compound **3**. Desilylation of the TMS groups of compound **3** with K_2CO_3 provided compound **4** in good yield. The addition of terminal acetylenes-lithiated compound **4** to tetrahydrofuran (THF) solution of compound **2** followed by the reductive aromatization gave **2mer** as an orange solid. Additionally, the **3mer** was obtained with lithiation of proto-desilylated 1mer (**1**) and compound **2** by using similar conditions. Finally, the addition of lithiated compound **5** to a THF solution of compound **2** followed by the reductive aromatization gave **4mer**. Note that, undesirable polymerization and/or decomposition of lithiated compound **5** led to low yield of 4mer. These oligomers are soluble in common organic solvents for spectroscopic measurements, even though they do not have any solubilizing groups on the anthracene backbones. The structures were characterized by ^1H NMR, ^{13}C

NMR, HRMS, melting point, and IR measurements.

3-3. Optical properties

UV-vis absorption spectra of oligomers in dichloromethane (DCM) are shown in

Figure 3-3a.

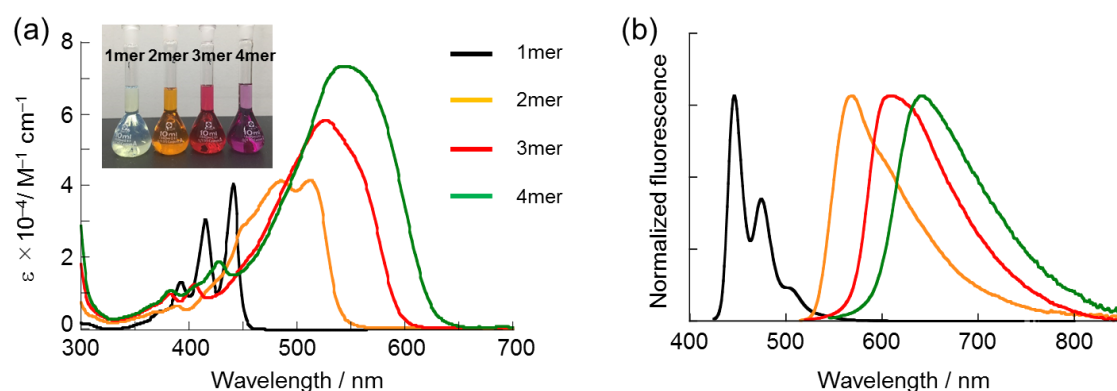


Figure 3-3. a) UV-vis absorption and b) fluorescence spectra of oligomers in DCM. Excited at 416 nm for **1mer**, 500 nm for **2mer**, 510 nm for **3mer**, and 535 nm for **4mer**.

The absorption band at the longest wavelength red-shifted with an increasing molar extinction coefficient (ϵ) as the number of anthracene units increased. The absorption maximum of **2mer** ($\lambda_{\max} = 512$ nm, $\epsilon = 41500$ m⁻¹ cm⁻¹) shifted to a longer wavelength (71 nm) compared with **1mer** ($\lambda_{\max} = 441$ nm, $\epsilon = 40400$ m⁻¹ cm⁻¹) (Figure 3-3 and Table 3-1). Then, **3mer** and **4mer** exhibited absorption bands with the maxima at 526 nm ($\epsilon = 58400$ m⁻¹ cm⁻¹) and 544 nm ($\epsilon = 72600$ m⁻¹ cm⁻¹), respectively, while the degree of red-

shifting becomes gradually smaller. **3mer** and **4mer** showed the featureless absorption spectra, although **1mer** exhibits a well-resolved absorption band. The featureless absorption phenomenon of **3mer**, as a representative example, implies that the rotation of the central anthracene unit contributes to the broadening of the absorption spectra. For example, it was experimentally demonstrated in a previous study that planar and twisted structures of acetylene-linked anthracene dimer exhibited different absorption spectra.⁹ Additionally, the previously reported calculations that were carried out on an anthracene trimer without terminal TIPSEthynylene units revealed that the relative energy differences between the molecular conformations with different torsional angles were relatively small ($\sim 3 \text{ kcal mol}^{-1}$).^{7b,10} This indicates that oligomers could have several conformations in solution, giving the featureless absorption spectra as increasing of the degree of oligomerization. The fluorescence spectra followed the similar trend (Figure 3-3b). The fluorescence maximum was red-shifted from 446 nm (**2mer**) to 641 nm (**4mer**) with Stokes shifts of 0.24 eV (**2mer**) to 0.34 eV (**4mer**) (Table 3-1). The longer oligomers showed weak fluorescence quantum yield Φ_f ($\approx 1\text{--}2\%$) (Table 3-1). As seen in diethynylene-linked anthracene oligomers, the presence of ethynylene units facilitates quenching *via* nonradiative pathways.¹¹

Table 3-1. Summary of optical and electrochemical properties (measured in DCM).

	$\lambda_{\text{max}}^{\text{a)}$ [nm]	$\lambda_{\text{em}}^{\text{b)}$ [nm]	$\Phi_{\text{f}}^{\text{c)}$ [%]	Stokes shift [eV]	$E_{\text{g}}^{\text{opt d)}$ [eV]	HOMO ^{e)} [eV]	LUMO ^{e)} [eV]
1mer	441	446	76	0.032	2.76	-5.62	-2.91
2mer	512	569	2	0.24	2.30	-5.44	-3.13
3mer	526	611	2	0.33	2.11	-5.27	-3.22
4mer	544	641	1	0.34	2.01	-5.06	-3.24

^{a)}The longest absorption peaks; ^{b)}Excited at 416 nm for **1mer**, 500 nm for **2mer**, 510 nm for **3mer**, and 535 nm for **4mer**; ^{c)}Absolute fluorescence quantum yields. Excited wavelength is the same with the fluorescence measurement; ^{d)}Energy gaps calculated from absorption onset. ^{e)} E_{ox}^{n} and $E_{\text{red}}^{\text{l}}$ are determined from respective DPV measurements with Ag/AgNO₃ as a reference. HOMO and LUMO energy levels were calculated from the potentials of the first oxidation (E_{ox}^{l}) and the first reduction wave ($E_{\text{red}}^{\text{l}}$) according to the following equations: HOMO = $-(4.8 + E_{\text{ox}}^{\text{l}})$ and LUMO = $-(4.8 + E_{\text{red}}^{\text{l}})$, where the potentials are referred to $E_{\text{Fc}/\text{Fc}^{\text{+}}}$.

3-4. Electrochemical properties

To investigate the electrochemical properties, cyclic voltammetry (CV) using 0.10 M $n\text{Bu}_4\text{NPF}_6$ as a supporting electrolyte was performed in DCM (Figure 3-4a).

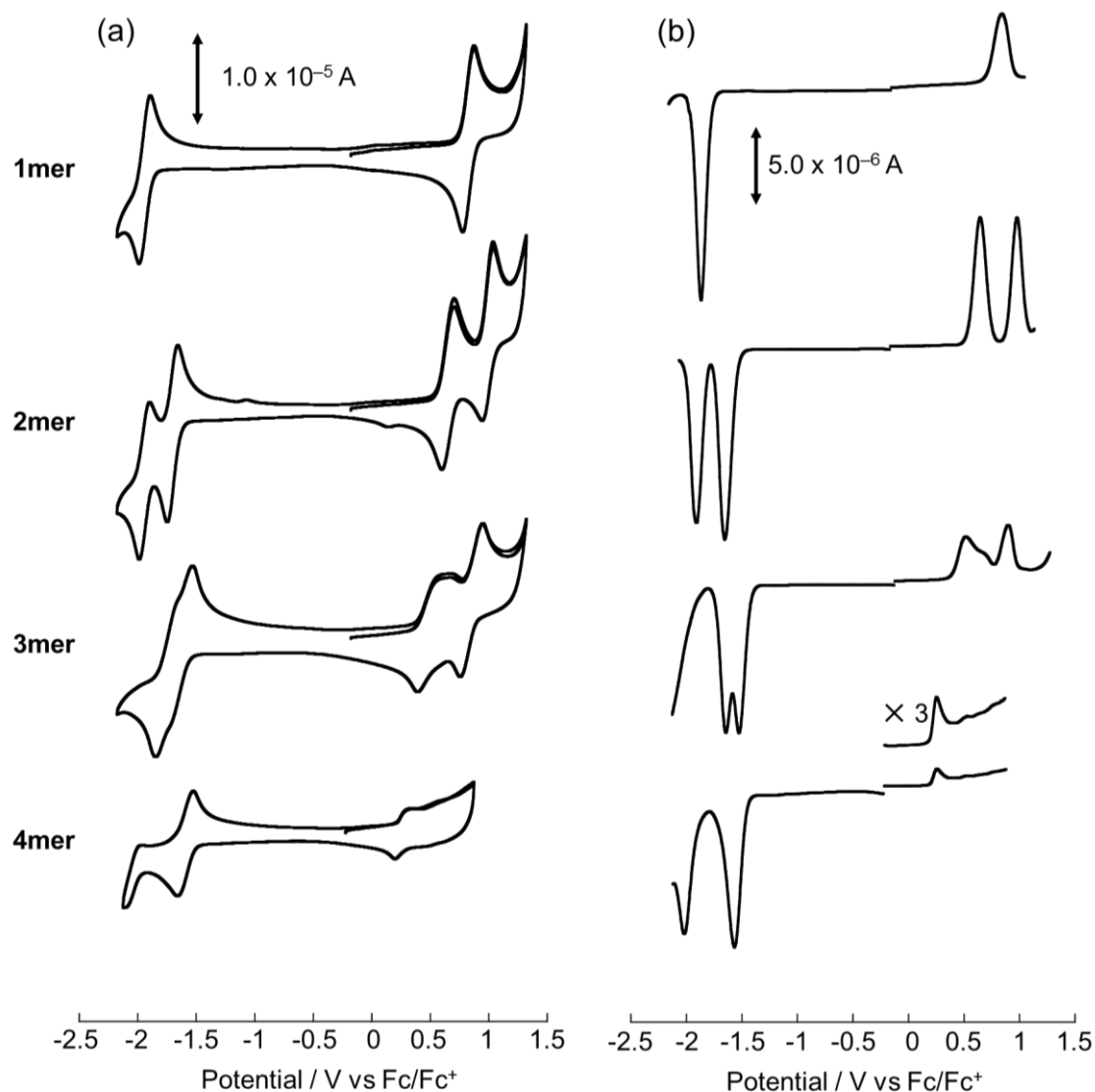


Figure 3-4. a) CVs (left) and b) DPVs (right) of oligomers measured in 0.1M $n\text{Bu}_4\text{NPF}_6$ in DCM. Scan rate: 100 mV s^{-1} , working electrode: glassy carbon, reference electrode: Ag/AgNO₃, electrolyte: $n\text{Bu}_4\text{NPF}_6$.

All potentials are given versus the ferrocene/ferrocenium (Fc/Fc^+) couple. The CVs of the compounds showed that the redox potentials were significantly varied with an increase in the anthracene units. The first oxidation potentials (E_{ox}^1) decrease from 0.82 V of 1mer to 0.26 V of 4mer (Table 3-2). In addition, the oligomers exhibited reversible

oxidation waves corresponding to the number of anthracene units (Figure 3-4, Table 3-2).

While oxidation waves of **3mer** and **4mer** are relatively broad, differential pulse voltammetry (DPV) clearly showed the oxidation peaks (Figure 3-4b). Although the result indicates that more anthracene units in the oligomers lead to more susceptible oxidation,¹¹ even **4mer** showed the suitable HOMO level as a stable compound.

Meanwhile, the reduction potentials showed the same trend. These results indicate the electronic communication between anthracene units as seen in the similar systems.^{8,11} The estimated HOMO and the lowest unoccupied molecular orbital (LUMO) are summarized in Table 3-2. The electrochemically determined HOMO–LUMO gaps are in agreement with the optically estimated values (Table 3-1).

Table 3-2. Electrochemical property^[a] of oligomers.

	E_{ox}^1	E_{ox}^2	E_{ox}^3	E_{ox}^4	E_{red}^1	HOMO	LUMO	Gap ^[b]	Gap ^[c]
	(V)	(V)	(V)	(V)	(V)	(eV)	(eV)	(eV)	(eV)
1mer	0.82				-1.89	-5.62	-2.91	2.71	2.76
2mer	0.64	0.97			-1.67	-5.44	-3.13	2.31	2.30
3mer	0.47	0.64	0.85		-1.58	-5.27	-3.22	2.05	2.11
4mer	0.26	0.54	0.65	0.78	-1.56	-5.06	-3.24	1.82	2.01

[a] E_{ox}^n and E_{red}^1 are half-wave potentials for respective redox waves with Ag/AgNO₃ as a reference. HOMO and LUMO energy levels were calculated from the potentials of the first oxidation (E_{ox}^1) and the first reduction wave (E_{red}^1) according to the following equations: HOMO

= $-(4.8 + E_{\text{ox}}^1)$ and LUMO = $-(4.8 + E_{\text{red}}^1)$, where the potentials are referred to $E_{\text{Fc}/\text{Fc}^+}$. [b] Electrochemically determined gaps. [c] Optically determined gaps.

3-5. Thermal stability of anthracene-based oligomers

As described above, one of the advantages of anthracene-based materials is to show reasonable stabilities. Indeed, these oligomers, even 4mer, were stable under room light because of the appropriate HOMO level. At the same time, the thermogravimetric analysis (TGA) indicated that **2mer**, **3mer**, and **4mer** showed no significant weight loss (<5%) below 400 °C, suggesting good thermal stability (Figure 3-5). Note that the significant weight loss for **1mer** is the sublimation during the measurement because of the small molecular weight.

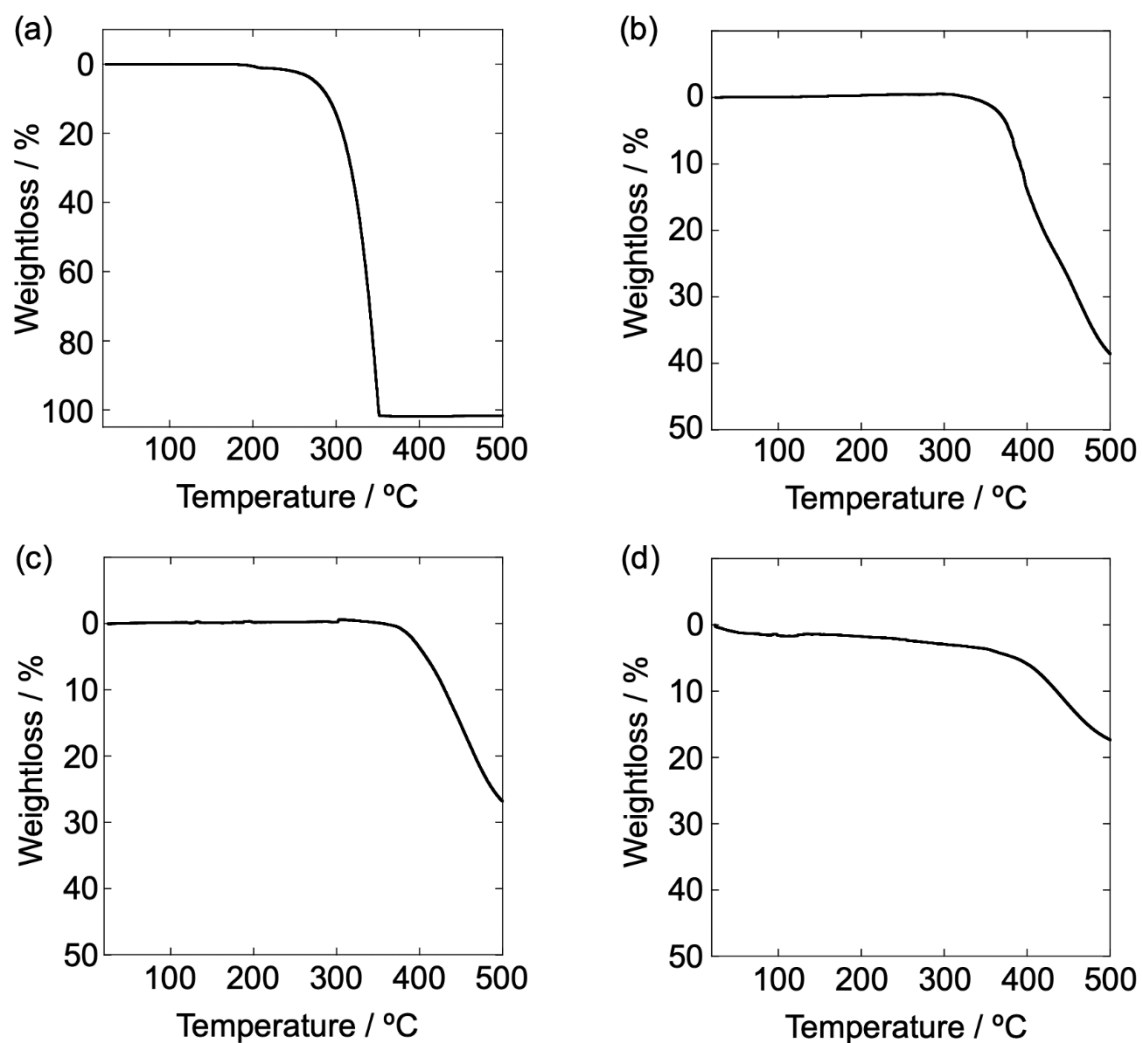


Figure 3-5. Thermogravimetric analysis data of (a) **1mer**, (b) **2mer**, (c) **3mer**, and (d) **4mer** under N₂ atmosphere. Scan rate: 5 °C/min.

3-6. Solid state structure

The oligomer structures were further confirmed by single crystal X-ray analysis. First, crystals of **2mer** were obtained by the diffusion of hexane vapor into a DCM solution of **2mer**, giving two structural conformations in the crystal (Figure 3-6). Relevant measurement and structural parameters are summarized in Table 3-3.

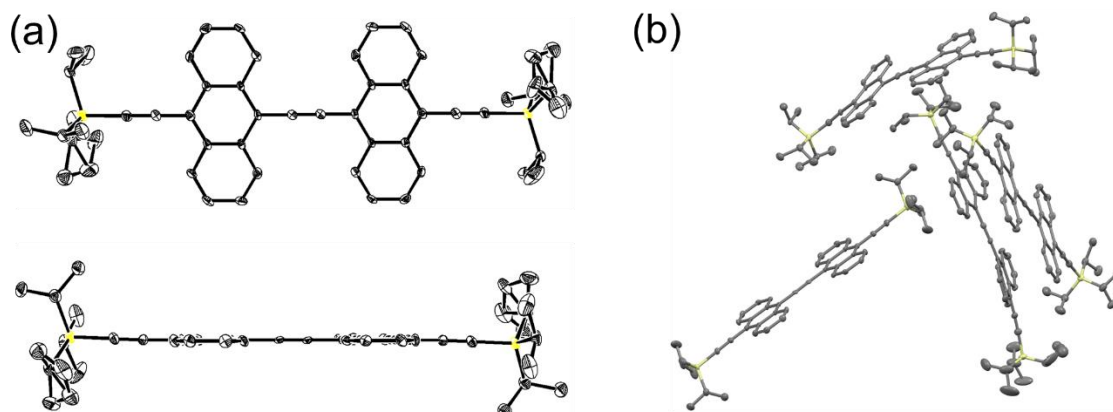


Figure 3-6. a) Top and side views of crystal structure of **2mer**. The planar structure was shown as a representative example. b) Packing structure of **2mer**.

Table 3-3. Single-crystal X-ray diffraction parameters and crystal data of 2mer.

Empirical formula	$C_{52}H_{58}Si_2$	
Formula weight	739.16	
Temperature	103 K	
Wavelength	0.71075 Å	
Crystal system	Triclinic	
Space group	$P-1$	
Unit cell dimensions	$a = 15.1341(3)$ Å	$\alpha = 88.692(6)^\circ$
	$b = 20.2246(4)$ Å	$\beta = 83.199(6)^\circ$
	$c = 21.5399(4)$ Å	$\gamma = 88.280(6)^\circ$
Volume	$6542.4(2)$ Å ³	
Z	6	
Density (calculated)	1.126 Mg/m ³	
Absorption coefficient	0.115 mm ⁻¹	
$F(000)$	2388	
Crystal size	$0.110 \times 0.040 \times 0.030$ mm ³	
Theta range for data collection	2.015 to 25.351°	
Index ranges	$-18 \leq h \leq 18, -24 \leq k \leq 24, -25 \leq l \leq 25$	
Reflections collected	91222	
Independent reflections	23912 [$R(\text{int}) = 0.1211$]	
Completeness to theta = 23.500°	99.9%	

Absorption correction	Semi-empirical from equivalents
Max. and min. transmission	1.0000 and 0.5629
Refinement method	Full-matrix least-squares on F^2
Data / restraints / parameters	23912 / 0 / 1521
Goodness-of-fit on F^2	1.020
Final R indices [$I > 2\sigma(I)$]	$R_1 = 0.0674$, $wR_2 = 0.1527$
R indices (all data)	$R_1 = 0.1093$, $wR_2 = 0.1718$
Extinction coefficient	n/a
Largest diff. peak and hole	0.795 and $-0.398 \text{ e.}\text{\AA}^{-3}$

In a planar structure, two anthracene moieties in **2mer** exhibit a completely coplanar arrangement, which is similar with the case of ethynylene-bridged pentacene dimer.¹² The presence of the ethynylene spacer weakens the repulsion of the hydrogen atoms in adjacent anthracene units. On the other hand, **2mer** with slightly twisted anthracene against the neighboring anthracene was also observed in the same crystal. On the whole, **2mer** showed an unfavorable packing to the charge transport in the obtained crystal.

Block and needle crystals of **3mer** were easily obtained from the combination with halogenated solvent and alkane or alcohol (Figure 3-7). Relevant measurement and structural parameters of block single crystal (Table 3-4) and needle crystal (Table 3-5) of **3mer** are summarized.

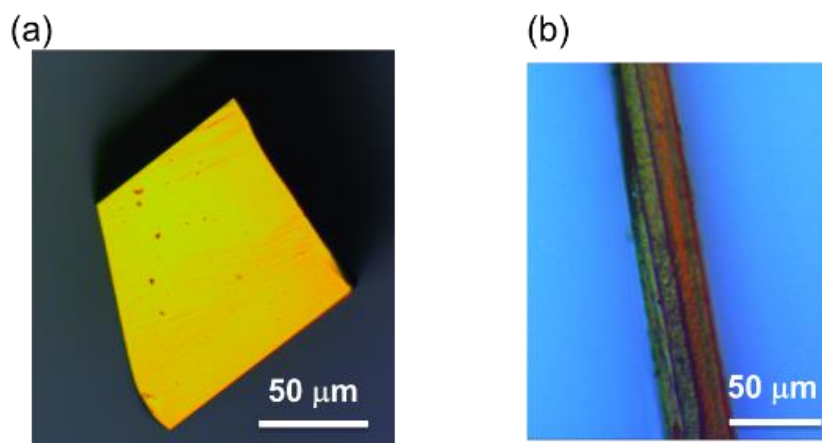


Figure 3-7. Optical microscope image of a) block crystal of **3mer**, b) needle crystal of **3mer**.

Table 3-4. Single-crystal X-ray diffraction parameters and crystal data of block crystal of **3mer**.

Empirical formula	$C_{68}H_{66}Si_2$	
Formula weight	939.38	
Temperature	113 K	
Wavelength	0.71073 Å	
Crystal system	Monoclinic	
Space group	$P2_1/n$	
Unit cell dimensions	$a = 9.0808(9)$ Å	
	$b = 15.4784(15)$ Å	$\beta = 93.9491(19)^\circ$
	$c = 18.8657(19)$ Å	
Volume	$2645.4(5)$ Å ³	
Z	2	
Density (calculated)	1.179 Mg/m ³	
Absorption coefficient	0.109 mm ⁻¹	
$F(000)$	1004	
Crystal size	$0.300 \times 0.200 \times 0.200$ mm ³	
Theta range for data collection	1.703 to 27.012°	
Index ranges	$-8 \leq h \leq 11, -19 \leq k \leq 17, -24 \leq l \leq 12$	
Reflections collected	16520	
Independent reflections	5759 [$R(\text{int}) = 0.0370$]	
Completeness to theta = 23.500°	99.9%	
Absorption correction	Semi-empirical from equivalents	

Max. and min. transmission	0.979 and 0.874
Refinement method	Full-matrix least-squares on F^2
Data / restraints / parameters	5759 / 0 / 322
Goodness-of-fit on F^2	1.019
Final R indices [$I > 2\sigma(I)$]	$R_1 = 0.0427$, $wR_2 = 0.1005$
R indices (all data)	$R_1 = 0.0642$, $wR_2 = 0.1142$
Extinction coefficient	n/a
Largest diff. peak and hole	0.270 and $-0.279 \text{ e.}\text{\AA}^{-3}$

Table 3-5. Single-crystal X-ray diffraction parameters and crystal data of needle crystal of **3mer**.

Empirical formula	$\text{C}_{68}\text{H}_{66}\text{Si}_2$
Formula weight	939.38
Temperature	90 K
Wavelength	0.71073 \AA
Crystal system	Triclinic
Space group	$P-1$
Unit cell dimensions	$a = 10.325(8) \text{ \AA}$ $\alpha = 90.713(13)^\circ$ $b = 14.096(11) \text{ \AA}$ $\beta = 91.337(12)^\circ$ $c = 18.967(15) \text{ \AA}$ $\gamma = 100.598(14)^\circ$
Volume	2712(4) \AA^3
Z	2
Density (calculated)	1.150 Mg/m^3
Absorption coefficient	0.106 mm^{-1}
$F(000)$	1004
Crystal size	$0.300 \times 0.050 \times 0.020 \text{ mm}^3$
Theta range for data collection	1.470 to 23.500°
Index ranges	$-10 \leq h \leq 11$, $-14 \leq k \leq 15$, $-21 \leq l \leq 21$
Reflections collected	12286
Independent reflections	7937 [$R(\text{int}) = 0.1151$]
Completeness to $\theta = 23.500^\circ$	98.8%
Absorption correction	Semi-empirical from equivalents
Max. and min. transmission	0.998 and 0.686

Refinement method	Full-matrix least-squares on F^2
Data / restraints / parameters	7937 / 73 / 715
Goodness-of-fit on F^2	1.000
Final R indices [$I > 2\sigma(I)$]	$R_1 = 0.1189$, $wR_2 = 0.2865$
R indices (all data)	$R_1 = 0.2664$, $wR_2 = 0.3755$
Extinction coefficient	n/a
Largest diff. peak and hole	0.643 and $-0.476 \text{ e.}\text{\AA}^{-3}$

In both cases (block and needle crystals), **3mer** molecules are densely packed through π - π interactions and CH- π interactions. In the block crystal, the three anthracene planes are approximately coplanar along the linear molecular axis, while the molecule is slightly S-shaped as seen in diethynylene-bridged anthracene trimer (Figure 3-8).¹¹

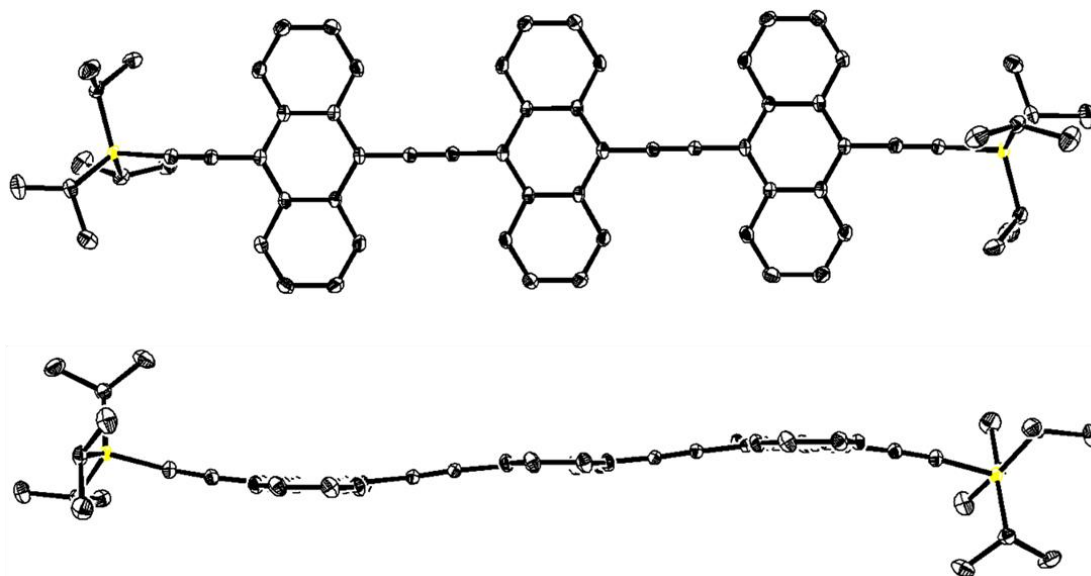


Figure 3-8. Top and side views of crystal structure of **3mer** in block crystal. Thermal ellipsoids represent 50% probability. Hydrogen atoms are omitted for clarity.

Interestingly, the position of TIPS groups was confirmed at one position without the disorder, implying the packing rigidity. The anthracene moiety adopts a face-to-face π -stack structure with a slip-stacked packing. This result indicates that the rotation of ethynylene unit can occur freely in solution (*vide supra*). Indeed, the theoretical calculations suggest that the planar structure seems to be thermodynamically the most stable conformation.^{7b,10}

The interplanar distance between stacked anthracenes is 3.4 Å, and the corresponding transfer integral between HOMOs¹³ is calculated to be 37.7 meV, associating with relatively short interplane distance (Figure 3-9). The transfer integral value between intercolumn anthracene units is low (0.3 meV), indicating the weak 2D electronic interaction between the columns.

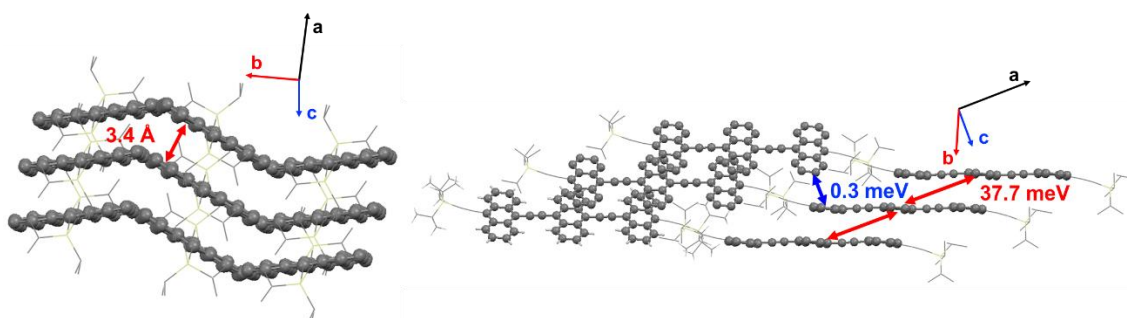


Figure 3-9. Packing structure and transfer integrals of block crystal of **3mer**. Thermal ellipsoids represent 50% probability. Hydrogen atoms are omitted for clarity.

In the needle crystal, anthracene units display a twisted arrangement with a torsion

angle of about 36° , while the anthracene moiety also adopts a face-to-face packing structure with the interplanar distance of 3.4 \AA (Figure 3-10).

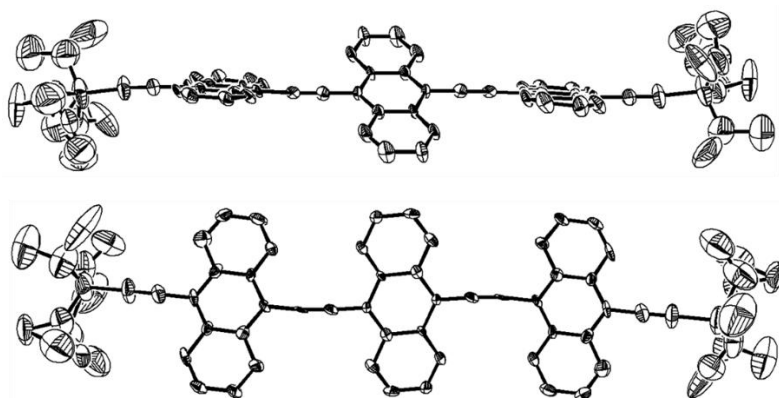


Figure 3-10. Top and side views of crystal structure of **3mer** in needle crystal. Thermal ellipsoids represent 50% probability. Hydrogen atoms are omitted for clarity.

Additionally, the corresponding transfer integral of needle crystal is calculated to be 18.8 meV , while the ones between anthracene units of intercolumn are 5.2 and 7.8 meV (Figure 3-11).

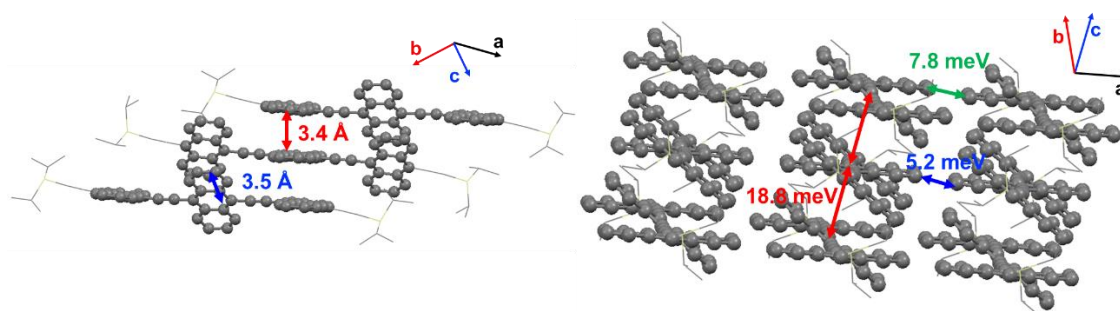


Figure 3-11. Packing structure and transfer integrals of needle crystal of **3mer**. Thermal ellipsoids represent 50% probability. Hydrogen atoms are omitted for clarity.

On the other hand, the 4mer always gave very thin needle crystals with any good/poor solvent combinations. Although the quality of the crystal is unacceptable for obtaining the detailed information, the **4mer** twisted structure in the crystal could be seen (Figure 3-12). The interplanar distance between anthracenes seems to be close in value with the **3mer** needle crystal, resulting in the close transfer integral values. Considering that the transfer integral value reflects the strength of intermolecular interactions, **3mer** and **4mer** possess the similar degree of π -orbital overlap in the crystal.

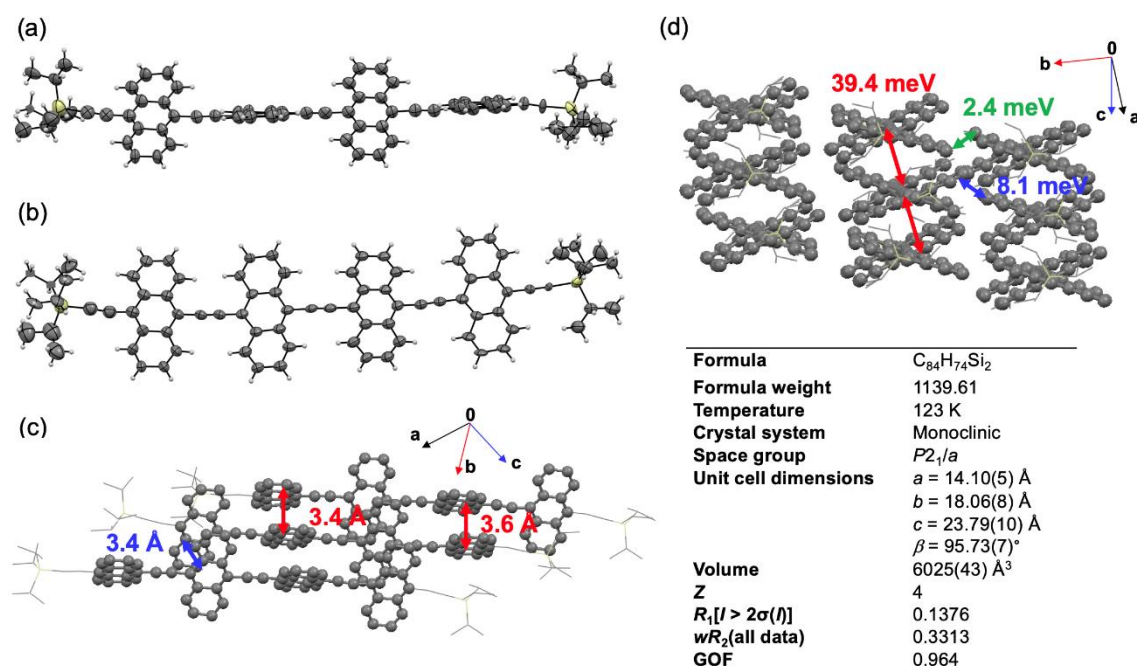


Figure 3-12. Crystal structure of **4mer** obtained by the diffusion of hexane vapor into a CS_2 solution of **4mer**. (a) Side view, (b) top view, (c) packing structure, and (d) Calculated charge transfer integrals with GGA:BP/DZP level of theory using ADF program for **4mer** crystal. Hydrogen atoms are omitted for clarity for (c) and (d). Note that the data is shown for reference purpose because of the low quality of crystal.

3-7. Film Morphology of 2mer and 3mer

Carrier-transport characteristics in oligomer films were evaluated in bottom-gate-top-contact organic field-effect transistors (OFETs) prepared on Si/SiO₂/AlO_x dielectric layers. The substrate surface was pretreated with a self-assembled monolayer of 12-cylohexyldodecylphosphonic acid (CDPA).¹⁴ First, the dip-coated method from a mixture of DCM and acetone (1:1, v/v) of **2mer** (2.0 mg mL⁻¹) at a pull rate of 900 μm min⁻¹ successfully provided crystalline films on Si/SiO₂/AlO_x/CDPA surface (Figure 3-13a,). Similarly, crystalline **3mer** films on Si/SiO₂/AlO_x/CDPA surface were also obtained by the dip-coated method from a DCM/hexane (1:1, v/v) of **3mer** (1.0 mg mL⁻¹) at a pull rate of 50 μm min⁻¹ (Figure 3-13b).

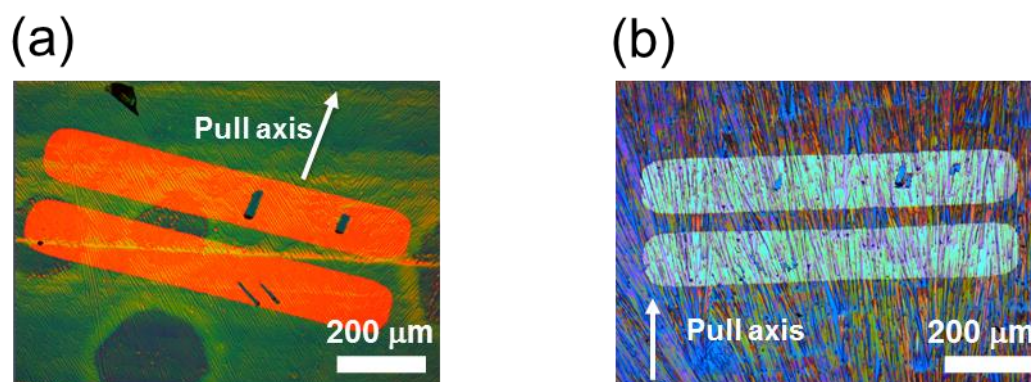


Figure 3-13. POM images of dip-coated film of (a) **2mer** (CH₂Cl₂/acetone = 1:1 (v/v), 2.0 mg/ml, pull rate: 900 μm/min) and (b) **3mer** (CH₂Cl₂/hexane = 1:1 (v/v), 1.0 mg/ml, pull rate: 50 μm/min) on a Si/SiO₂/AlO_x substrate.

Specially, the polarized optical microscopy (POM) image of **3mer** dip-coated films reminds the needle crystal of **3mer**. Further optimization for the dip-coating method was performed. It was found that very slow pull rate (natural evaporation method, Figure 3-14) provided higher-quality film (Figure 3-15a, b), resulting in the improved charge transport properties (*vide infra*). Unfortunately, because of the low solubility, **4mer** tended to be aggregated/crystallized on a surface, resulting in separated domains on a surface. As the results, the suitable crystalline films were not obtained with any conditions.

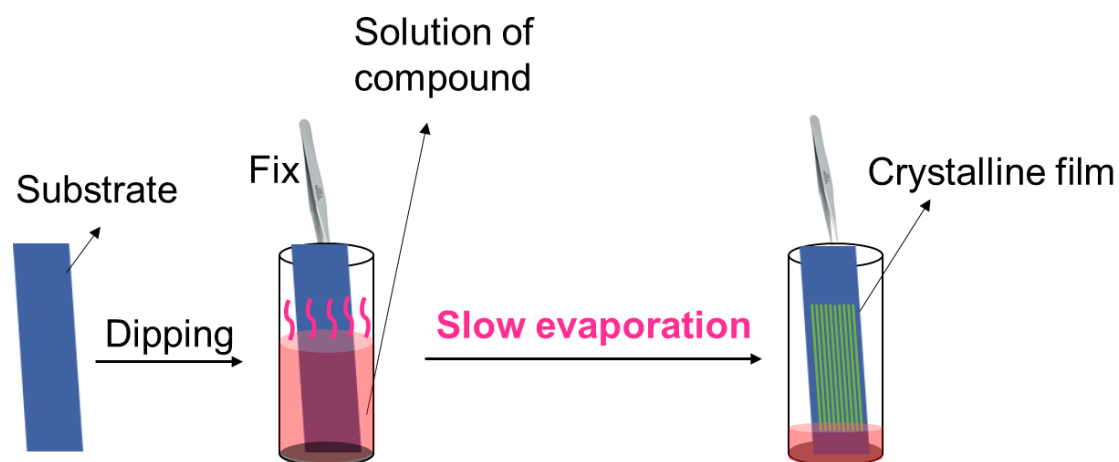


Figure 3-14. Schematic of natural evaporation method.

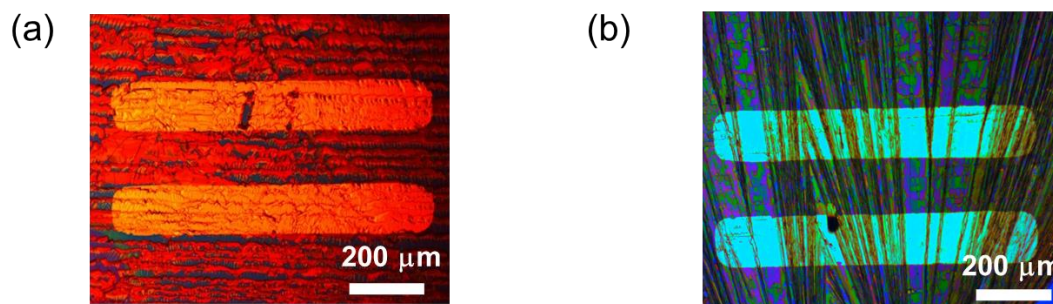


Figure 3-15. POM images of naturally evaporated a) **2mer** and b) **3mer** films on a Si/SiO₂/AlO_x/CDPA substrate.

3-8. Molecular Orientation of anthracene-based oligomers

The structure of the crystalline films was evaluated using out-of-plane X-ray diffraction (XRD) analysis (Figure 3-16).

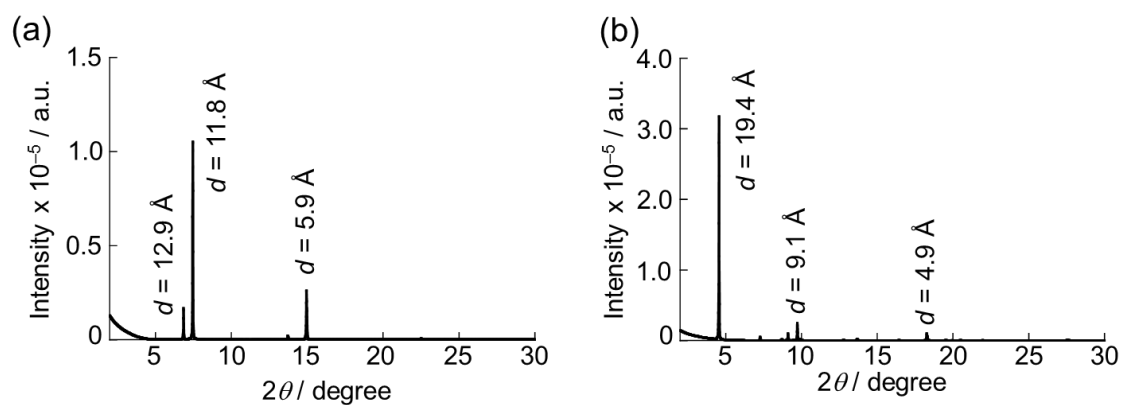


Figure 3-16. Out-of-plane XRD pattern of dip-coated film of (a) **2mer** and (b) **3mer** on a Si/SiO₂/AlO_x/CDPA substrate.

Sharp peaks were clearly observed, indicating the polycrystalline feature of the films.

In the case of **2mer**, the intense peaks at $2\theta = 7.5^\circ$ with a d -spacing of 11.8 Å together

with peaks at $2\theta = 6.9^\circ$ (d -spacing = 12.9 Å) and at $2\theta = 15.0^\circ$ (d -spacing = 5.9 Å) were observed (Figure 16a), suggesting the presence of the ordered arrangement in the films. Note that, even if naturally evaporated films have the similar arrangement with the packing structure in the single-crystal (Figure 3-6b), it seems to be nonpreferable to charge transport in FET devices. On the other hand, the primary peak of **3mer** observed at $2\theta = 4.6^\circ$, which corresponds to 19.4 Å (Figure 16b), can be assigned to [001] direction of **3mer** (*vide infra*). This implies that **3mer** molecules stand in an end-on mode with the *ab* plane parallel to the substrate (Figure 17a). Although in-plane XRD measurements are required for detailed analysis, the molecular orientation of **3mer**, combined with the POM image, seems to be suitable for the charge transport in FET devices.

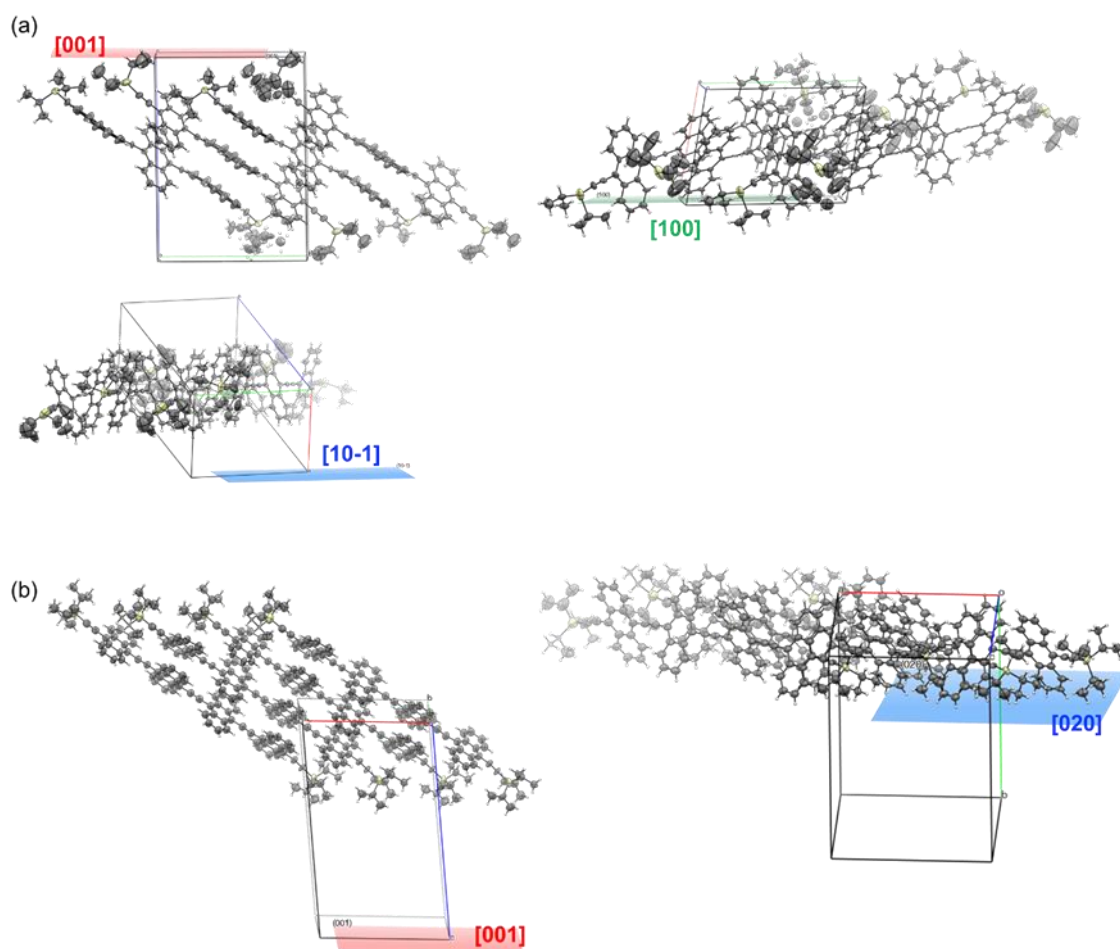


Figure 3-17. Proposed molecular orientation of (a) **3mer** and (b) **4mer** on a Si/SiO₂/CDPA substrate.

Since the quality of the dip-coated **4mer** films was inadequate for the charge transport property measurements due to the aggregation, single-crystal FET (SCFET)s were fabricated to evaluate the effect of oligomerization on the charge transport property. Crystals of **3mer** and **4mer** were grown by drop-casting the toluene solution (0.5 mg mL⁻¹) on octadecyltrichlorosilane (OTS) modified Si/SiO₂ surface. Note that OTS was chosen as a dielectric layer for SCFETs,¹⁵ because Si/SiO₂/OTS substrates gave slightly better

charge mobilities than Si/SiO₂/AlO_x/CDPA substrates in our preliminary screening. XRD of **3mer** crystals exhibited the similar sharp Bragg reflections with the one of naturally evaporated films. The primary peak at $2\theta = 4.6^\circ$ with a d -spacing of 19.2 Å is well-consistent with the simulated [001] diffraction according to the crystallographic data for the bulk crystal (Figure 3-17a; Figure 3-18a), while the secondary peak at $2\theta = 9.8^\circ$ with a d -spacing of 9.0 Å could be assigned to the simulated [10-1] diffraction. Similarly, the primary peak in **4mer** case was observed at $2\theta = 3.8^\circ$ with a d -spacing of 23.4 Å that also can be assigned to the simulated [001] diffraction (Figure 3-17b; Figure 3-18b). In addition, minor peaks at $2\theta = 7.4^\circ$ (d -spacing = 11.9 Å) and 9.8° (d -spacing = 9.0 Å) also could be assigned to the simulated [002] and [020] diffractions, respectively. Considering π - π stacking direction in the needle crystal, the orientations of **3mer** and **4mer** molecules in the crystals on Si/SiO₂/OTS substrates are supposed to be preferable to SCFETs, with the charge transports through π - π stacking of anthracene units (Figure 3-17).

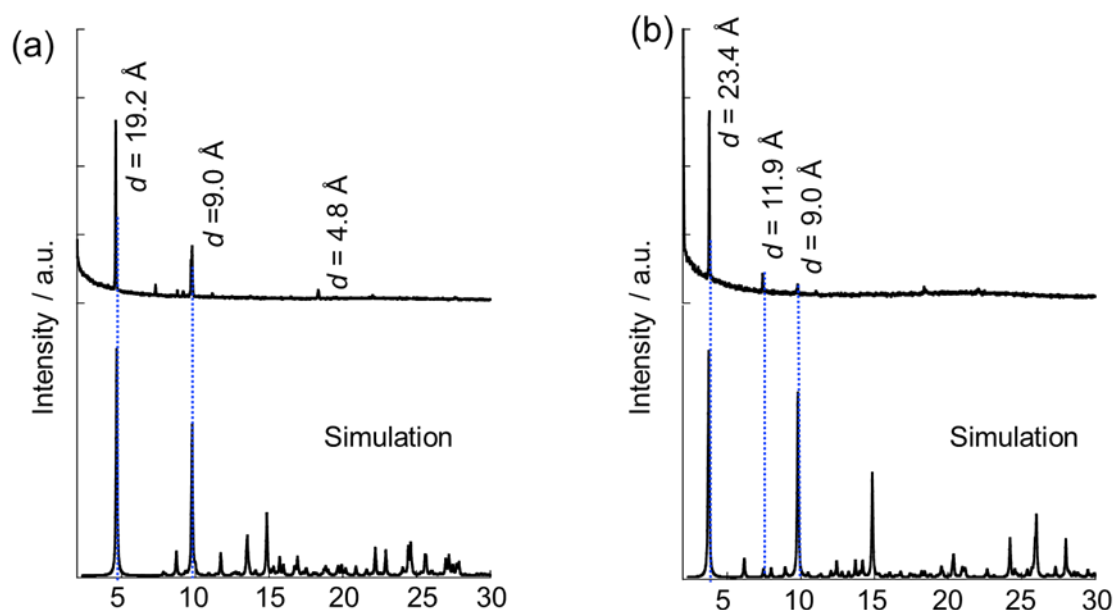


Figure 3-18. Experimental out-of-plane XRD and simulated powder XRD patterns of a) **3mer** and b) **4mer** single crystals on a Si/SiO₂/OTS substrate. Simulated powder XRD patterns are also shown for comparison.

3-9. Charge-carrier mobilities

The charge transport property of **2mer** and **3mer** were evaluated with naturally evaporated films. In the case of **2mer**, the maximum field-effect hole mobilities of $8.9 \times 10^{-4} \text{ cm}^2 \text{ V}^{-1} \text{ s}^{-1}$ (average values of $5.6 \times 10^{-4} \text{ cm}^2 \text{ V}^{-1} \text{ s}^{-1}$ with five devices) with a threshold voltage V_{th} of -19.9 V and on/off current ratio $I_{\text{on}}/I_{\text{off}}$ of 1.2×10^3 was observed. On the other hand, **3mer** showed the maximum field-effect hole mobilities of $8.0 \times 10^{-3} \text{ cm}^2 \text{ V}^{-1} \text{ s}^{-1}$ (average values of $2.4 \times 10^{-3} \text{ cm}^2 \text{ V}^{-1} \text{ s}^{-1}$ with 17 devices) with a threshold voltage V_{th} of -6.6 V and on/off current ratio $I_{\text{on}}/I_{\text{off}}$ of 5.2×10^2 (Figure 3-19a–d). Thus, **3mer** showed one order of magnitude higher hole mobility than **2mer**. This result implies

that the higher degree of π -conjugation of anthracene oligomers contributes to the strong intramolecular interaction in the solid state, providing the better charge-transport property, together with the better orientation on a substrate.

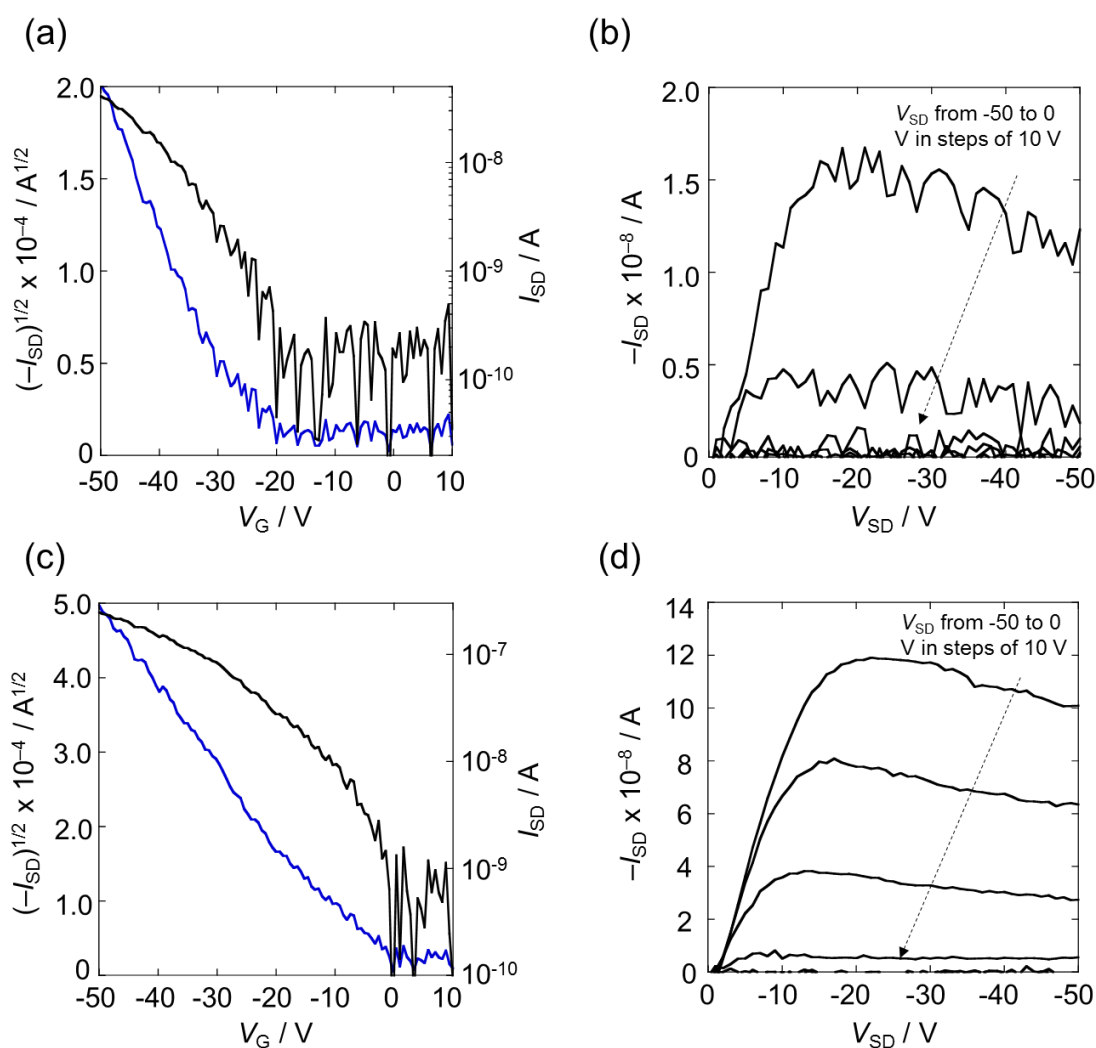


Figure 3-19. Transfer characteristics of the device for a) **2mer** and c) **3mer** at a fixed source/drain voltage, $V_{SD} = -50$ V. Output characteristics of the device for b) **2mer** and d) **3mer**.

Finally, bottom-gate-top-contact OFETs of micro/nanometre-sized **3mer** and **4mer**

were fabricated by using “gold layer glue technique”.¹⁶ The effective channel length and width were measured by microscope image of the substrate was shown in the Figure 3-20. Briefly, gold source/drain electrodes were placed on a needle-type crystal that was grown by drop-casting the toluene solution on Si/SiO₂/OTS. The maximum field-effect hole mobilities of 0.14 cm² V⁻¹ s⁻¹ (average values of 8.2×10^{-2} cm² V⁻¹ s⁻¹ with eight devices) with a threshold voltage V_{th} of -0.34 V and on/off current ratio I_{on}/I_{off} of 5.6×10^5 for **3mer** and 3.3×10^{-2} cm² V⁻¹ s⁻¹ (average values of 2.9×10^{-2} cm² V⁻¹ s⁻¹ with 11 devices) with a threshold voltage V_{th} of -6.3 V and on/off current ratio I_{on}/I_{off} of 4.4×10^5 for **4mer** were obtained (Figure 3-21a–c). Thus, **3mer** crystals showed one order of magnitude higher hole mobility than the one of naturally evaporated films. Note that the average value is in good agreement with the one in the case of alkoxychain-terminated ethynylene-bridged anthracene trimer.⁷

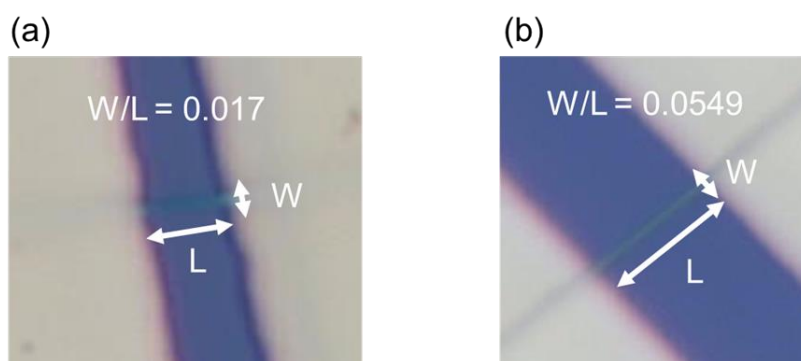


Figure 3-20. Representative microscope image of channel length and width of single-crystal FET of (a) **3mer** and (b) **4mer**.

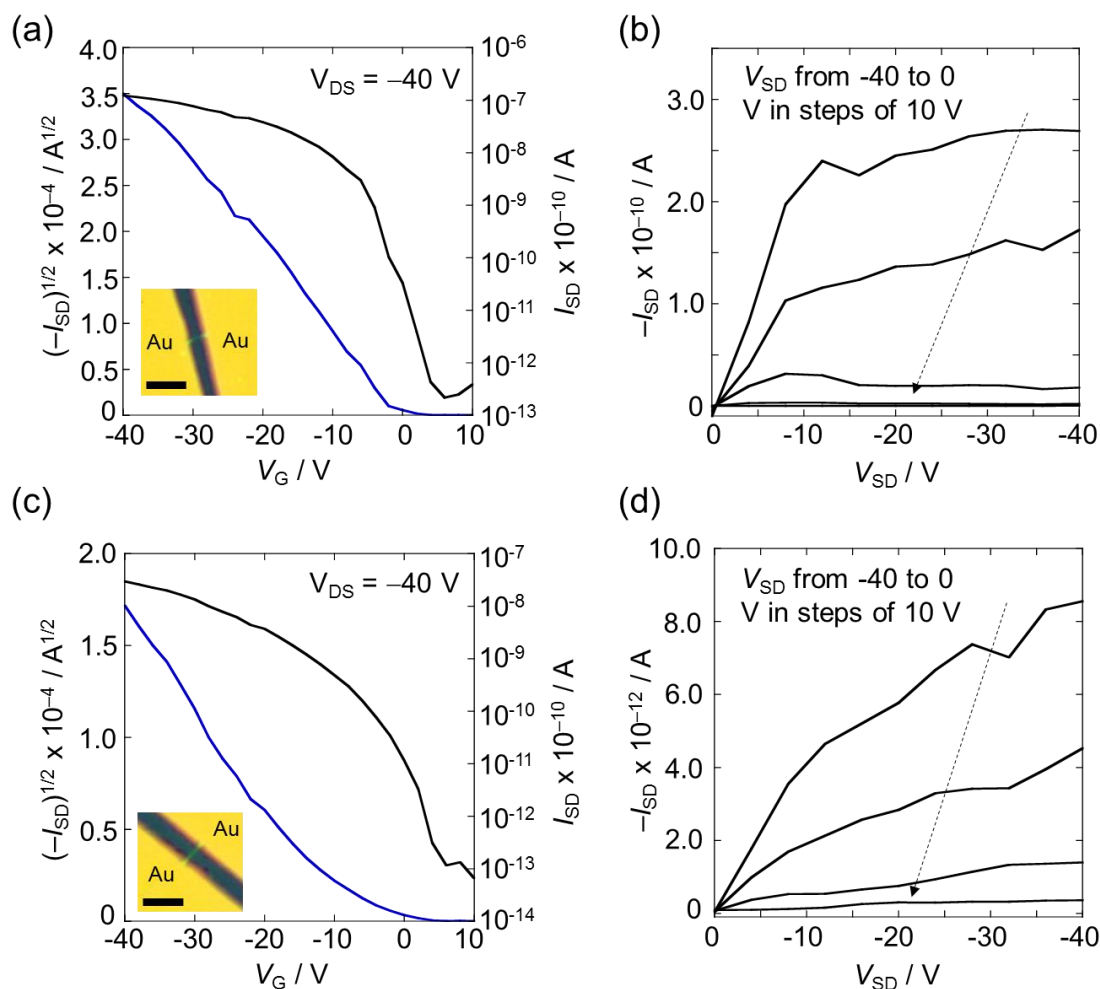


Figure 3-21. Transfer characteristics of the device of a) **3mer** and c) **4mer** at a fixed source/drain voltage, $V_{SD} = -40$ V. Insets show image of device. Scale bar: 10 μm . Output characteristics of the device of c) **3mer** and d) **4mer**.

Contrary to our expectations, the hole mobility of **4mer** crystals was slightly lower than **3mer** crystals, although the packing structure seems to be similar. This discrepancy could arise, for instance, as a result of a larger amount of defects in **4mer** due to the crystal and interface structural quality.¹⁷ In fact, the threshold voltage in **4mer** (-6.3 V) is slightly larger than in **3mer** (-0.34 V). This is rationalized by the fact that, considering the free

rotation of ethynylene units, the “complexity” of the structure, namely planar and twisted conformations, increases as the increased degree of π -conjugation through ethynylene bridges. This factor might affect the quality of 4mer crystal, implying that **3mer** strikes a good balance between the effective π -conjugation and defect-less crystal formation. Further optimization for preparing defect-free **4mer** crystal also has a chance to improve the charge transport property.

Besides, considering that ethynylene-bridged anthracene trimers with different terminal substituents at 10,10''-positions exhibited the similar charge transport property (ca. $10^{-2} \text{ cm}^2 \text{ V}^{-1} \text{ s}^{-1}$) in the previously reports,⁷ critical changes in the molecular design need to be considered. For this purpose, the enhancement of two-dimensional (2D) electronic interaction in the system by π -expansion of core acene, for example, anthracene to pentacene, would be effective for improving the charge transport property. For example, 6,6'-linked pentacene dimer, which has twisted structure, forms the desired 2D π -stacking network due to the orthogonal orientation of the two pentacenes, exhibiting isotropic charge transport with FET hole mobilities of up to $0.11 \text{ cm}^2 \text{ V}^{-1} \text{ s}^{-1}$.¹⁸ The combination with π -expansion of core acene and ethynylene-linked oligomerization at 9,10-positions could be one promising way to improve charge transport property. One problem is the instability of π -extended acenes. In this context, synthesis of acetylene-linked π -extended

acene oligomers with “precursor method”¹⁹ to avoid undesirable oxidation is ongoing in the next chapter.

3-10. Summary and outlook

I have successfully synthesized and characterized a set of ethynylene-bridged anthracene oligomers up to tetramer. The planar and twisted conformations of trimer were found by the single-crystal X-ray analysis, suggesting the free rotation of ethynylene units in the solution state. Theoretical calculations unveiled the intermolecular interaction by means of the charge transfer integrals between HOMOs. Finally, the charge transport property of the oligomers was measured by bottom-gate-top-contact OFETs and SCFETs. Specifically, the trimer showed the best mobility ($0.14 \text{ cm}^2 \text{ V}^{-1} \text{ s}^{-1}$) among the oligomers employed in this study, implying that the balance of π -conjugation and packing quality played an important role in the case of anthracene oligomers with ethynylene-bridges at 9,10-positions. This effect on charge transport property can be overcome by changing the packing structure *via* the further introduction of substituent groups at 2,6-positions of anthracene or utilization of π -extended acenes for the backbone. Thus, I believe that the combination of ethynylene bridging at 9,10-positions together with further modification to extra molecular interactions has a great chance to achieve better charge transport

property.

3-11. Experimental section

3-11-1. General

Reagents for synthesis were purchased from Wako, Nacalai Tesque, and Sigma Aldrich, and were reagent-grade quality, obtained commercially, and used without further purification. For spectral measurements, spectral-grade solvents were purchased from Nacalai Tesque. Unless stated otherwise, column chromatography was carried out on silica gel 60N (Kanto Chemical, 40–50 μm). Analytical thin-layer chromatography (TLC) was performed on Art. 5554 (Merck, KGaA). Melting points (m.p.) were measured with a YAMAKO MP-J3. IR spectra were recorded on a JASCO FP-6600 and are reported as wavenumbers, ν , in cm^{-1} with band intensities indicated as strong (s), medium (m), weak (w). ^1H NMR (500 MHz and 600 MHz) and ^{13}C NMR (100 Hz, 126 Hz, and 150 MHz) spectra were recorded (as indicated) with JEOL JNM-ECX 400 P, JEOL JNM-ECX 500, and JEOL JNM-ECX 600 spectrometer at ambient temperature by using tetramethylsilane as an internal standard. High resolution MS was performed on a matrix-assisted laser desorption ionization–time of flight mass spectrometry (MALDI-TOF-MS) (Bruker Autoflex II). X-ray crystallographic data for **2mer** and **4mer** were recorded at 103 K on

a Rigaku R-AXIS RAPID/S using Mo-K α radiation. X-ray crystallographic data for **3mer** were recorded at 113 K (for block crystal) or 90 K (for needle crystal) on a Bruker APEX II X-Ray diffractometer equipped with a large area CCD detector by using graphite monochromated Mo-K α radiation ($\lambda = 0.71073 \text{ \AA}$). The structures were solved by direct method (SHELXS-97) and refined with the SHELXS-97 program. CCDC 2057099 (**2mer**), 2047423 (block crystal of **3mer**), and 2047402 (needle crystal of **3mer**) contain the supplementary crystallographic data for this paper. Polarized optical images of the thin films were obtained using Nikon 50iPOL microscope. Out-of-plane thin-film XRD measurements were carried out on a Rigaku SmartLab X-ray reflectometer with θ - 2θ scan mode. UV/vis absorption spectra in solution were measured with a JASCO UV/Vis/NIR spectrometer V-650.

3-11-2. Synthetic procedures

Synthesis-1mer: To a solution of TIPSEthynylene (6.4 ml, 5.3 g, 28.8 mmol) in dry THF (30 mL) at $-5 \text{ }^\circ\text{C}$ was added *n*-butyllithium (2.5 M in hexanes, 10.8 mL, 26.9 mmol). This solution was stirred for 40 min before being transferred into a solution of 9,10-anthracenequinone (2.0 g, 9.6 mmol) in dry THF (30 mL) cooled to $-5 \text{ }^\circ\text{C}$. The reaction mixture was allowed to warm to room temperature (RT), and stirred for 12 h before

adding SnCl₂ saturated with 3 m HCl (27 ml). The reaction mixture was stirred for 12 h. The mixture was extracted with DCM (500 mL). The combined organic phase was washed with water, brine, dried over Na₂SO₄, and the solvent was removed *in vacuo*. Purification with silica gel column chromatography (DCM/hexanes = 1:1) afforded 1mer as a pale yellow solid (4.0 g, 7.5 mmol, 78%). *R*_f = 0.5 (hexane); m.p. 210 °C; ¹H NMR (500 MHz, CDCl₃): δ 8.65–8.58 (m, 4*H*; Ar-H), 7.62–7.55 (m, 4*H*; Ar-H), 1.26 (s, 42*H*; [(CH₃)₂CH]₃Si); UV–vis (DCM, 1.2 × 10⁻⁵ mol L⁻¹) λ_{max} (ε) = 441 (40353), 415 (30515), 393 nm (12910); fluorescence (DCM): λ_{ex} = 416 nm; λ_{em} = 446, 475 nm; HRMS (MALDI–spiral-TOF, *trans*-2-[3-(4-*tert*-butylphenyl)-2-methyl-2-propenylidene]malononitrile (DCTB)) *m/z*: calcd for C₃₆H₅₀Si₂⁺: 538.3446 [M⁺]; found: 548.3449. (Note that the ¹H NMR and HR-MS matched with previously reported data.²⁰)

Synthesis–Compound 1: 1mer (94 mg, 0.17 mmol) was dissolved in 6 mL of THF, to which a small amount of water (0.06 mL) and a THF solution of tetrabutylammonium fluoride (TBAF, 1.0 m, 0.06 mL, 0.06 mmol) were sequentially added. After stirring at RT for 2 h, the completion deprotection was confirmed by TLC (hexane, *R*_f = 0.2). Then, the mixture was diluted with DCM (20 ml). The combined organic phase was washed with water, brine, dried over Na₂SO₄, and then the solvent was removed *in vacuo* to afford compound **1** (39 mg, 0.17 mmol, 97%). ¹H NMR (500 MHz, CDCl₃) δ 8.6 (q, *J* = 3.2 Hz,

4H; Ar-H), 7.62 (q, $J = 3.5$ Hz, 4H; Ar-H), 4.07 (s, 2H; C \equiv CH). (Note that the ^1H NMR matched with previously reported data.²⁰)

Synthesis–Compound 2: To a solution of TIPSEthynylene (3.4 mL, 2.8 g, 15 mmol) in THF (20 mL) at -78 °C was added *n*-butyllithium (2.5 M in hexanes, 4.8 mL, 12 mmol). This solution was stirred for 10 min before being transferred into a solution of 9,10-anthraquinone (2.08 g, 10 mmol) in dry THF (30 mL) cooled to -78 °C. The reaction mixture was allowed to warm to RT and stir for 3 h before adding dropwise MeI (1.9 mL, 4.3 g, 30 mmol). The reaction mixture was stirred for 12 h. Then the mixture was poured into saturated aqueous NH_4Cl (33 mL) and H_2O (10 mL). The mixture was extracted with DCM (300 mL). The combined organic phase was washed with 5% aqueous NH_4Cl (30 mL), water, brine (100 mL), dried over Na_2SO_4 , and the solvent was removed in vacuo. Purification with silica gel column chromatography (DCM/hexane = 2:1, $R_f = 0.4$) afforded crude product as an oil. This oil was dissolved in DCM (≈ 0.5 mL) and MeOH (2 mL) was added followed by cooling to -15 °C. The resulting precipitate was filtered and washed with cold MeOH to afford **2** (3.25 g, 8.04 mmol, 80%) as a white solid. $R_f = 0.4$ (DCM/hexane 2:1); m.p. 88 °C (decomp); ^1H NMR (500 MHz, CDCl_3): δ 8.26 (dd, $J = 8, 1.5$ Hz, 2H; Ar-H), 8.09 (dd, $J = 8, 1.5$ Hz, 2H; Ar-H), 7.70 (td, $J = 7.5, 1.5$ Hz, 2H;

Ar-H), 7.54 (td, $J = 7.5, 1.5$ Hz, 2H; Ar-H), 2.93 (s, 3H; OCH₃), 1.07–1.03 (m, 21H; [(CH₃)₂CH]₃Si); ¹³C NMR (126 MHz, CDCl₃): 183.48 (C=O), 141.05 (C), 133.61 (CH), 131.28 (C), 129.27 (CH), 128.85 (CH), 127.29 (CH), 106.58 (C), 90.02 (C), 72.41 (C), 51.68 (OCH₃), 18.69 (CH₃), 11.28 (CH); IR (KBr) ν (cm⁻¹): 3067 (m), 2942 (s), 2863 (s), 2821 (m), 2172 (w), 1952 (w), 1846 (w), 1733 (w), 1671 (s), 1601 (s), 1454 (s), 1382 (w), 1314 (s), 1264 (s), 1213 (m), 1173 (w), 1127 (w), 1123 (m), 1080 (s), 1041 (m), 996 (m), 943 (w), 927 (s), 883 (s), 814 (m), 780 (s), 767 (s), 704 (s), 679 (s), 626 (s), 572 (m); HRMS (MALDI–spiral-TOF, (DCTB)) m/z : calcd for C₂₆H₃₂O₂SiNa⁺: 427.2060 [M+Na]⁺; found: 427.2064.

Synthesis–Compound 3: To a solution of TMSethynylene (0.31 mL, 219 mg, 2.2 mmol) in dry THF (6 mL) at –5 °C was added *n*-butyllithium (2.6 M in hexanes, 0.71 mL, 1.85 mmol). This solution was stirred for 30 min before being transferred into a solution of **2** (300 mg, 0.74 mmol) in dry THF (5 mL) cooled to –5 °C. The reaction mixture was warmed to RT and then stirred for 8 h. Then, the mixture was diluted with DCM (300 mL). The combined organic phase was washed with water, brine, dried over Na₂SO₄, and then the solvent was removed in vacuo. Purification with silica gel column chromatography afforded **3** as a light yellow oil (293 mg, 0.65 mmol, 87%). $R_f = 0.43$

(hexane); $^1\text{H NMR}$ (500 MHz, CDCl_3) δ 8.64–8.60 (m, 2H; Ar-H), 8.59–8.55 (m, 2H; Ar-H), 7.60 (q, $J = 3.2$ Hz, 4H; Ar-H), 1.34–1.25 (m, 21H; $[(\text{CH}_3)_2\text{CH}]_3\text{Si}$), 0.42 (s, 9H; $(\text{CH}_3)_3\text{Si}$). (Note that the $^1\text{H NMR}$ matched with previously reported data.²¹)

Synthesis–Compound 4: Compound **3** (132 mg, 0.29 mmol) was dissolved in 4 mL of THF, to which a small amount of water (one drop) and a MeOH (2 ml) solution of K_2CO_3 (6.5 mg, 0.05 mmol) were sequentially added. After stirring at RT for 1 h, the completion deprotection was confirmed by TLC (hexane, $R_f = 0.43$) and APCI mass. Then, the mixture was diluted with DCM (40 ml). The combined organic phase was washed with water, brine (10 mL), dried over Na_2SO_4 , and the solvent was removed in vacuo to afford **4** (107 mg, 0.28 mmol, 97%). $R_f = 0.43$ (hexane); $^1\text{H NMR}$ (500 MHz, CDCl_3) δ 8.66–8.62 (m, 2H; Ar-H), 8.62–8.57 (m, 2H; Ar-H), 7.60 (q, $J = 3.3$ Hz, 4H; Ar-H), 4.06 (s, 1H; $\text{C}\equiv\text{CH}$), 1.26 (s, 21H; $[(\text{CH}_3)_2\text{CH}]_3\text{Si}$). (Note that the $^1\text{H NMR}$ matched with previously reported data.²¹)

Synthesis–Compound 5: 2mer (50 mg, 0.068 mmol) was dissolved in 3 mL of THF, to which a small amount of water (20 μL) and a THF solution of TBAF (1.0 m, 30 μL , 30 μmol) were sequentially added. After stirring at RT for 2 h, the completion deprotection

was confirmed by TLC. Then, 3 ml MeOH was poured in the container, and the resulting precipitate was filtered and washed with MeOH and diethyl ether to afford **5** (28 mg, 0.065 mmol, 95%) as an orange solid. $R_f = 0.7$ (DCM/hexane 1:1); m.p. 105 °C (decomp); IR (KBr) $\nu(\text{cm}^{-1})$: 3300 (s), 3054 (w), 2094 (w), 1927 (w), 1846 (w), 1700 (w), 1619 (w), 1559 (w), 1520 (w), 1425 (m), 1395 (m), 1174 (w), 1150 (w), 1026 (w), 948 (w), 881 (w), 757 (s), 635 (s), 588 (m); ^1H NMR (500 MHz, CDCl_3) δ 8.92 (dd, $J = 6.5, 2.5$ Hz, 4H; Ar-H), 8.69 (dd, $J = 6.9, 2.3$ Hz, 4H; Ar-H), 7.73–7.66 (m, 8H; Ar-H), 4.13 (s, 2H; $\text{C}\equiv\text{CH}$); ^{13}C NMR (126 MHz, CDCl_3): 132.86 (C), 132.26 (C), 127.38 (CH), 127.27 (CH), 119.15 (C), 117.88 (C), 99.16 (C), 90.21 (CH), 80.47 (CH); HRMS (MALDI–spiral-TOF, (DCTB)) m/z : calcd for $\text{C}_{34}\text{H}_{18}^+$: 426.1402 [M^+]; found: 426.1403.

Synthesis–2mer: To a solution of **4** (107 mg, 0.28 mmol) in dry THF (8 mL) at -5 °C was added *n*-butyllithium (2.6 M in hexanes, 0.17 mL, 0.44 mmol). This solution was stirred for 40 min before being transferred into a solution of **2** (153 mg, 0.38 mmol) in dry THF (8 mL) cooled to -5 °C. The reaction mixture was warmed to RT and stirred for 7 h before adding $\text{SnCl}_2 \cdot 2\text{H}_2\text{O}$ (654 mg, 2.9 mmol) in 10% aqueous H_2SO_4 (0.5 mL). The reaction mixture was stirred for 12 h. The mixture was extracted with DCM (200 mL). The combined organic phase was washed with water, brine, dried over Na_2SO_4 , and then the

solvent was removed in vacuo. Purification with silica gel column chromatography followed with recrystallization (DCM/hexane) afforded 2mer as a deep red crystal (76.8 mg, 0.104 mmol, 36%). $R_f = 0.75$ (DCM/hexane 1:1); m.p. 246 °C; IR (KBr) ν (cm⁻¹): 3060 (m), 2938 (s), 2860 (s), 2135 (m), 1935 (w), 1791 (w), 1699 (w), 1619 (w), 1558 (w), 1521 (m), 1459 (s), 1435 (s), 1397 (s), 1364 (w), 1290 (m), 1240 (m), 1131 (m), 1057 (s), 998 (m), 994 (m), 889 (m), 881 (s), 804 (m), 760 (s), 691 (s), 638 (s), 583 (m); ¹H NMR (500 MHz, CDCl₃): δ 8.92 (dd, $J = 7.5, 1.5$ Hz, 4H; Ar-H), 8.72 (dd, $J = 7.5, 2$ Hz, 4H; Ar-H), 7.72–7.65 (m, 8H; Ar-H), 1.38–1.29 (m, 42H; [(CH₃)₂CH]₃Si); ¹³C NMR (126 MHz, CDCl₃): 132.73 (C), 132.34 (C), 127.60 (CH), 127.39 (CH), 127.28 (CH), 127.10 (CH), 119.37 (C), 118.60 (C), 105.49 (C), 103.42 (C), 99.30 (C), 19.03 (CH₃), 11.62 (CH); UV–vis (DCM, 2.1×10^{-5} mol L⁻¹) λ_{\max} (ϵ) = 512 (41466), 485 (41288); fluorescence (DCM): λ_{ex} = 500 nm; λ_{em} = 569 nm; HRMS (MALDI–spiral-TOF, (DCTB)) m/z : calcd for C₅₂H₅₈Si₂⁺: 738.4089 [M⁺]; found: 738.4072.

Synthesis–3mer: To a solution of **1** (1.2 g, 5.33 mmol) in dry THF (50 mL) at –5 °C was added *n*-butyllithium (2.5 M in hexanes, 4.7 mL, 11.7 mmol). This solution was stirred for 1 h before being transferred into a solution of **1** (5.6 g, 13.8 mmol) in dry THF (30 mL) cooled to –5 °C. The reaction mixture was warmed to RT and stirred for 16 h before

adding $\text{SnCl}_2 \cdot 2\text{H}_2\text{O}$ (12 g, 53 mmol) in 10% aqueous H_2SO_4 (2 mL). The reaction mixture was stirred for 14 h. The mixture was diluted with DCM (400 mL). The combined organic phase was washed with water, brine, dried over Na_2SO_4 , and then the solvent was removed in vacuo. The crude material was purified by recrystallization with DCM/MeOH to give pure product **3mer** as a deep red needle crystal (3.7 g, 3.9 mmol, 73%). m.p. >300 °C; IR (KBr) $\nu(\text{cm}^{-1})$: 3417 (m), 3057 (m), 2939 (s), 2871 (s), 2862 (s), 2140 (m), 1921 (w), 1802 (w), 1700 (w), 1618 (m), 1554 (w), 1520 (m), 1460 (s), 1429 (s), 1402 (s), 1381 (s), 1352 (m), 1276 (m), 1242 (m), 1148 (m), 1115 (m), 1060 (s), 997 (s), 994 (s), 920 (w), 889 (m), 881 (s), 760 (s), 733 (s), 678 (s), 636 (s), 592 (s); ^1H NMR (600 MHz, CDCl_3): δ 8.98–8.94 (m, 8H; Ar-H), 8.72 (d, $J = 9.6$ Hz, 4H; Ar-H), 7.75–7.67 (m, 12H; Ar-H), 1.36–1.27 (m, 42H; $[(\text{CH}_3)_2\text{CH}]_3\text{Si}$); ^{13}C NMR (151 MHz, CDCl_3): 132.72 (C), 132.48 (C), 132.35 (C), 127.63 (2C, CH), 127.37 (2C, CH), 127.27 (CH), 127.08 (CH), 119.44 (C), 119.13 (C), 118.56 (C), 105.53 (C), 103.46 (C), 99.81 (C), 99.45 (C), 19.02 (CH_3), 11.63 (CH); UV–vis (DCM, 9.2×10^{-6} mol L^{-1}) λ_{max} (ϵ) = 526 (58358); fluorescence (DCM): λ_{ex} = 510 nm; λ_{em} = 611 nm; HRMS (MALDI–spiral-TOF, (DCTB)) m/z : calcd for $\text{C}_{68}\text{H}_{66}\text{Si}_2^+$: 938.4700 [M^+]; found: 938.4698.

Synthesis–4mer: To a solution of **5** (107 mg, 0.25 mmol) in dry THF (10 mL) at -5 °C

was added *n*-butyllithium (2.5 M in hexanes, 0.22 mL, 0.55 mmol). This solution was stirred for 1 h before being transferred into a solution of **1** (264 mg, 0.65 mmol) in dry THF (10 mL) cooled to $-5\text{ }^{\circ}\text{C}$. The reaction mixture was warmed to RT and stirred for 7 h before adding $\text{SnCl}_2 \cdot 2\text{H}_2\text{O}$ (567 mg, 2.5 mmol) in 10% aqueous H_2SO_4 (0.2 mL). The reaction mixture was stirred for 12 h. The mixture was extracted with DCM (800 mL). The combined organic phase was washed with water, brine, dried over Na_2SO_4 , and the solvent was removed in vacuo. Purification with silica gel column chromatography afforded 4mer as a deep red solid (7.6 mg, 0.0068 mmol, 5.4%). $R_f = 0.88$ (DCM/hexane = 2:1); m.p. $>300\text{ }^{\circ}\text{C}$; IR (KBr) ν (cm^{-1}): 3447 (m), 3056 (m), 2939 (s), 2861 (s), 2138 (m), 1917 (w), 1801 (w), 1700 (w), 1618 (w), 1559 (w), 1521 (m), 1439 (m), 1434 (s), 1404 (m), 1374 (m), 1060 (s), 946 (w), 918 (s), 881 (m), 804 (m), 757 (s), 687 (s), 634 (s); ^1H NMR (600 MHz, CDCl_3): δ 9.02–8.94 (m, 12H; Ar-H), 8.72 (d, $J = 9.0$ Hz, 4H; Ar-H), 7.77–7.75 (m, 8H; Ar-H), 7.71–7.67 (m, 8H; Ar-H), 1.33–1.28 (m, 42H; $[(\text{CH}_3)_2\text{CH}]_3\text{Si}$); ^{13}C NMR (151 MHz, CDCl_3): 132.71 (C), 132.51 (C), 132.48 (C), 132.35 (C), 127.70 (CH), 127.64 (2C, CH), 127.41 (CH), 127.38 (CH), 127.35 (CH), 127.27 (CH), 127.07 (CH), 119.46 (C), 119.23 (C), 119.07 (C), 118.54 (C), 105.55 (C), 103.47 (C), 99.92 (C), 99.89 (C), 99.45 (C), 19.01 (CH_3), 11.63 (CH); UV–vis (DCM, 9.7×10^{-6} mol L^{-1}) λ_{max} (ϵ) = 544 (72617); fluorescence (DCM): λ_{ex} = 535 nm; λ_{em} =

641 nm; HRMS (MALDI–spiral-TOF, (DCTB)) m/z : calcd for $C_{84}H_{74}Si_2^+$: 1138.5326

$[M^+]$; found: 1138.5324.

Thermogravimetric Analysis: Thermogravimetric analysis was carried out on a DSC7000X/STA7200 instrument (Hitachi) under nitrogen gas flow at a heating rate of 5 °C min⁻¹.

Electrochemical measurements: CV measurements were conducted in a solution of 0.1 m nBu_4NPF_6 in dry DCM with a scan rate of 100 mV s⁻¹ at RT in an Ar-filled cell. A glassy carbon electrode and a Pt wire were used as a working and a counter electrode, respectively. An Ag/AgNO₃ electrode was used as a reference electrode, which was externally calibrated with the half-wave potential of ferrocene/ferrocenium (Fc/Fc⁺) redox couple.

Charge transfer integral calculation: Charge transfer integrals were calculated by fragment orbital method with the GGA:BP/DZP level of theory using Amsterdam Density Functional (ADF) program.¹³

OFET measurements–Dip-Coating Film Based OFETs: Si/SiO₂ substrates were

cleaned with deionized (DI) water, acetone, pure isopropanol for 10 min in an ultrasonic bath. Then, substrates were dried with a stream of nitrogen gas and treated with oxygen plasma for 3 min. $\text{Al}(\text{NO}_3)_3 \cdot 9\text{H}_2\text{O}$ (75 mg) was dissolved in ethanol (2 mL) and stirred for 1 h, resulting a solution of $\text{Al}(\text{NO}_3)_3$ in ethanol (0.1 mol L^{-1}), which was spin-coated onto the cleaned Si substrate at 5000 rpm for 40 s. The resulting film was annealed at 300 °C for 30 min to achieve complete decomposition of nitrate and a high degree of dehydration. To form the CDPA-modified Si/SiO₂/AlO_x substrate, the substrate was treated with oxygen plasma for 3 min and soaked in a solution of CDPA in isopropanol ($1.5 \times 10^{-3} \text{ m}$) at RT for 12 h, rinsed with isopropanol subsequently and dried with a flow of nitrogen. The substrate was immersed vertically in an oligomer solution and then pulled up at a constant speed as controlled by a Longer Pump TJ-3A syringe pump controller, or films were fabricated by natural evaporation method (**Figure 3-15**). Then, the substrates were transferred to a N₂-filled glovebox for vapor-deposition of Au (30 nm) at high vacuum ($\approx 10^{-5} \text{ Pa}$). The field-effect hole mobilities were determined in the saturation regime by using the equation of $I_{\text{DS}} = (\mu W C_i / 2L)(V_{\text{G}} - V_{\text{th}})^2$, where I_{DS} is the drain-source current, μ is the field-effect mobility, W is the channel width, L is the channel length, C_i (10 nF cm^{-2} for CDPA-modified Si/SiO₂/AlO_x substrate,²² and OTS-modified Si/SiO₂ substrate) is the capacitance per unit area of the gate dielectric layer, V_{G} is the

gate voltage, and V_{th} is the threshold voltage. The effective channel length ($\approx 1000 \mu\text{m}$) and width ($\approx 50, 100, \text{ or } 150 \mu\text{m}$) were measured by microscope image of the substrate.

OFET measurements–Single-Crystal-Based OFETs: Si/SiO₂ substrates were cleaned with deionized (DI) water, piranha solution (H₂SO₄:H₂O₂ = 2:1), deionized (DI) water, pure isopropanol for 10 min under an ultrasonic bath. Then substrates were dried with a flow of nitrogen gas. Treatment of the Si/SiO₂ wafers with OTS was carried out by the vapor-deposition method. The clean wafers were dried under vacuum at 90 °C for 1 h in order to eliminate the influence of moisture. After cooling to RT, one drop of OTS was placed on the center of system. Subsequently, this system was heated to 120 °C and maintained for 2 h under vacuum followed with an ultra-sonication in hexane, chloroform and isopropanol for 10 min. Then, a toluene solution of oligomer was drop-casted on the OTS-modified substrate, giving single crystals on surface. Source and drain electrodes were deposited on the crystal by using gold layer glue technique.¹⁹

3-12. Reference

- (1) a) J. E. Anthony, *Chem. Rev.* **2006**, *106*, 5028–5048; b) J. E. Anthony, *Angew. Chem. Int. Ed.* **2008**, *47*, 452–483; b) C. Wang, H. Dong, W. Hu, Y. Liu, D. Zhu, *Chem. Rev.* **2012**, *112*, 2208–2267; c) Z. Sun, Q. Ye, C. Chi, J. Wu, *Chem. Soc. Rev.* **2012**, *41*, 7857–7889; d) M. Watanabe, K.-Y. Chen, Y. J. Chang, T. J. Chow, *Acc. Chem. Res.* **2013**, *46*, 1606–1615; e) Q. Ye, C. Chi, *Chem. Mater.* **2014**, *26*, 4046–4056; f) U. H. F. Bunz, *Acc. Chem. Res.* **2015**, *48*, 1676–1686.
- (2) M. Watanabe, Y. J. Chang, S.-W. Liu, T.-H. Chao, K. Goto, Md. M. Islam, C.-H. Yuan, Y.-T. Tao, T. Shinmyozu, T. J. Chow, *Nat. Chem.* **2012**, *4*, 574–578.
- (3) M. Chen, L. Yan, Y. Zhao, I. Murtaza, H. Meng, W. Huang, *J. Mater. Chem. C* **2018**, *6*, 7416–7444.
- (4) J. Liu, H. Zhang, H. Dong, L. Meng, L. Jiang, L. Jiang, Y. Wang, J. Yu, Y. Sun, W. Hu, A. J. Heeger, *Nat. Commun.* **2015**, *6*, 10032/1–8.
- (5) a) S. Kawai, O. Krejčí, A. S. Foster, R. Pawlak, F. Xu, L. Peng, A. Orita, E. Meyer, *ACS Nano* **2018**, *12*, 8791–8797; b) A. Sánchez-Grande, B. de la Torre, J. Santos, B. Cirera, K. Lauwaet, T. Chutora, S. Edalatmanesh, P. Mutombo, J. Rosen, R. Zboril, R. Miranda, J. Björk, P. Jelínek, N. Martín, D. Ecija, *Angew. Chem. Int. Ed.* **2019**, *58*, 6559–6563; c) B. Cirera, A. Sánchez-Grande, B. de la Torre, J. Santos, S.

- Edalatmanesh, E. Rodríguez-Sánchez, K. Lauwaet, B. Mallada, R. Zboril, R. Miranda, O. Gröning, P. Jelínek, N. Martín, D. Ecija, *Nat. Nanotechnol.* **2020**, *15*, 437–443.
- (6) L. Jiang, J. Gao, E. Wang, H. Li, Z. Wang, W. Hu, L. Jiang, *Adv. Mater.* **2008**, *20*, 2735–2740.
- (7) a) A. D. Aquila, F. Marinelli, J. Tey, P. Keg, Y. Lam, O. L. Kapitanchuk, P. Mastrorilli, C. F. Nobile, P. Cosma, A. Marchenko, D. Fichou, S. G. Mhaisalker, G. P. Suranna, L. Torsi, *J. Mater. Chem. C* **2008**, *18*, 786–791; b) P. Keg, A. D. Aquila, F. Marinelli, O. L. Kapitanchuk, D. Fichou, P. Mastrorilli, G. Romanazzi, G. P. Suranna, L. Torsi, Y. M. Lam, S. G. Mhaisalker, *J. Mater. Chem.* **2010**, *20*, 2448–2456; c) G. Romanazzi, A. D. Aquila, G. P. Suranna, F. Marinelli, S. Cotrone, D. Altamura, C. Giannini, L. Torsi, P. Mastrorilli, *J. Mater. Chem.* **2011**, *21*, 15186–15189.
- (8) a) D. Lehnerr, A. H. Murray, R. McDonald, M. J. Ferguson, R. R. Tykwinski, *Chem. Eur. J.*, **2009**, *15*, 12580–12584; b) D. Lehnerr, A. H. Murray, R. McDonald, R. R. Tykwinski, *Angew. Chem. Int. Ed.*, **2010**, *49*, 6190–6194.
- (9) B. Eichler, J. Erickson, J. Keppen, A. Sykes, G. Sereda, *Tetrahedron Lett.*, **2015**, *56*, 4574–4577.
- (10) a) S. J. Greaves, E. J. Flynn, E. L. Fatcher, E. Wrede, D. P. Lydon, P. J. Low, S. R.

- Rutter, A. Beeby, *J. Phys. Chem. A* **2006**, *110*, 2114–2121; b) S. Toyota, *Chem. Rev.* **2010**, *110*, 5398–5424; c) O. L. Kapitanchuku, *Mol. Cryst. Liq. Cryst.* **2016**, *639*, 55–63.
- (11) M. Nagaoka, E. Tsurumaki, M. Nishiuchi, T. Iwanaga, S. Toyota, *J. Org. Chem.* **2018**, *83*, 5784–5790.
- (12) K. Kawano, H. Hayashi, S. Yoshimoto, N. Aratani, M. Suzuki, J. Yoshinobu, H. Yamada, *Chem. Eur. J.* **2018**, *24*, 14916–14920.
- (13) G. te Velde, F. M. Bickelhaupt, E. J. Baerends, C. Fonseca Guerra, S. J. A. van Gisbergen, J. G. Snijders, T. Ziegler, *J. Comput. Chem.*, **2001**, *22*, 931–967.
- (14) D. Liu, Z. He, Y. Su, Y. Diao, S. C. B. Mannsfeld, Z. Bao, J. Xu, Q. Miao, *Adv. Mater.* **2014**, *26*, 7190–7196.
- (15) G. Zhang, N. Xue, W. Gu, X. Yang, A. Lv, Y. Zheng, L. Zhang, *Chem. Sci.* **2020**, *11*, 11235–11243.
- (16) a) Q. Tang, Y. Tong, H. Li, Z. Ji, L. Li, W. Hu, Y. Liu, D. Zhu, *Adv. Mater.* **2008**, *20*, 1511–1515; b) Q. Tang, Y. Tong, H. Li, W. Hu, *Appl. Phys. Lett.* **2008**, *92*, 083309/1–3; c) Q. Tang, L. Jiang, Y. Tong, H. Li, Y. Liu, Z. Wang, W. Hu, Y. Liu, D. Zhu, *Adv. Mater.* **2008**, *20*, 2947–2951; d) Y. Zhang, Q. Tang, H. Li, W. Hu, *Appl. Phys. Lett.* **2009**, *94*, 203304/1–3; e) L. Jiang, H. Dong, W. Hu, *J. Mater. Chem.* **2010**,

- 20, 4994–5007; f) X. Wu, R. Jia, J. Pan, X. Zhang, J. Jie, *Nanoscale Horiz.* **2020**, *5*, 454–472.
- (17) L. Zhang, A. Fonari, Y. Zhang, G. Zhao, V. Coropceanu, W. Hu, S. Parkin, J. Brédas, A. L. Briseno, *Chem. Eur. J.* **2013**, *19*, 17907–17916.
- (18) X. Zhang, X. Jiang, J. Luo, C. Chi, H. Chen, J. Wu, *Chem. Eur. J.* **2010**, *16*, 464–468.
- (19) a) H. Yamada, Y. Yamashita, M. Kikuchi, H. Watanabe, T. Okujima, H. Uno, T. Ogawa, K. Ohara, N. Ono, *Chem. Eur. J.* **2005**, *11*, 6212–6220; b) H. Yamada, T. Okujima, N. Ono, *Chem. Commun.* **2008**, *26*, 2957–2974; c) H. Yamada, D. Kuzuhara, M. Suzuki, H. Hayashi, N. Aratani, *Bull. Chem. Soc. Jpn.* **2020**, *93*, 1234–1267.
- (20) Y. Zhang, J. Björk, P. Weber, R. Hellwig, K. Diller, A. C. Papageorgiou, S. C. Oh, S. Fischer, F. Allegretti, S. Klyatskaya, M. Ruben, J. V. Barth, F. Klappenberger, *J. Phys. Chem. C* **2015**, *119*, 9669–9679.
- (21) F. Montigny, G. Argouarch, C. Lapinte, *Synthesis*, **2006**, *2*, 293–298.
- (22) S. Hayakawa, K. Matsuo, H. Yamada, N. Fukui, H. Shinokubo, *J. Am. Chem. Mater.* **2020**, *142*, 11663–11668.

3-13. Supporting information

3-13-1. NMR spectrum

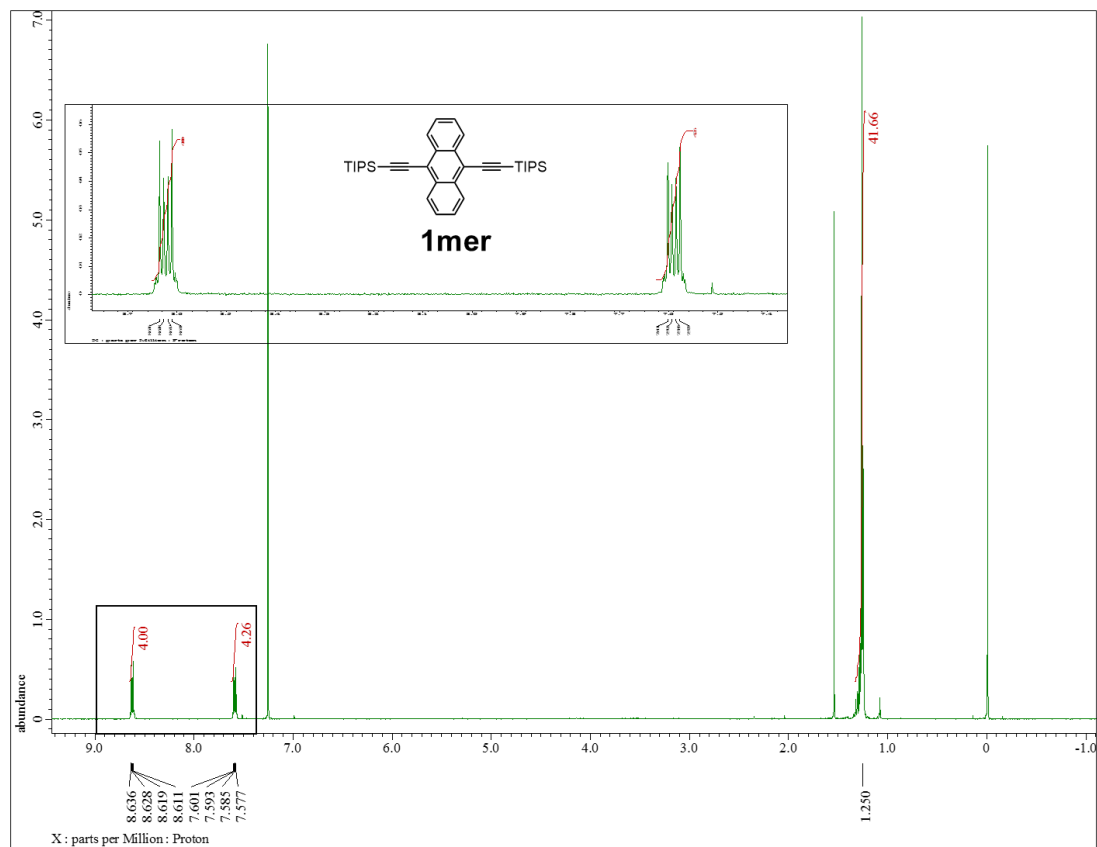


Figure S1. ^1H NMR spectrum of **1mer** in CDCl_3 .

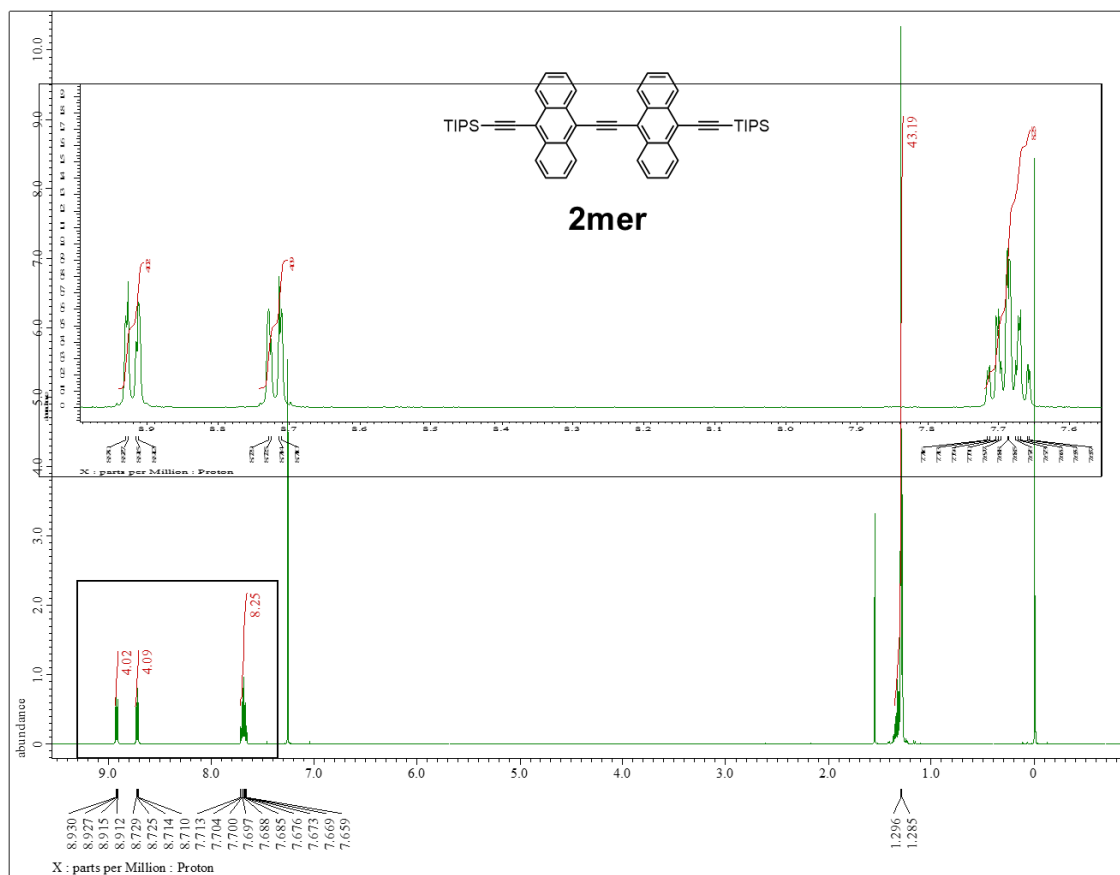


Figure S2. ^1H NMR spectrum of **2mer** in CDCl_3 .

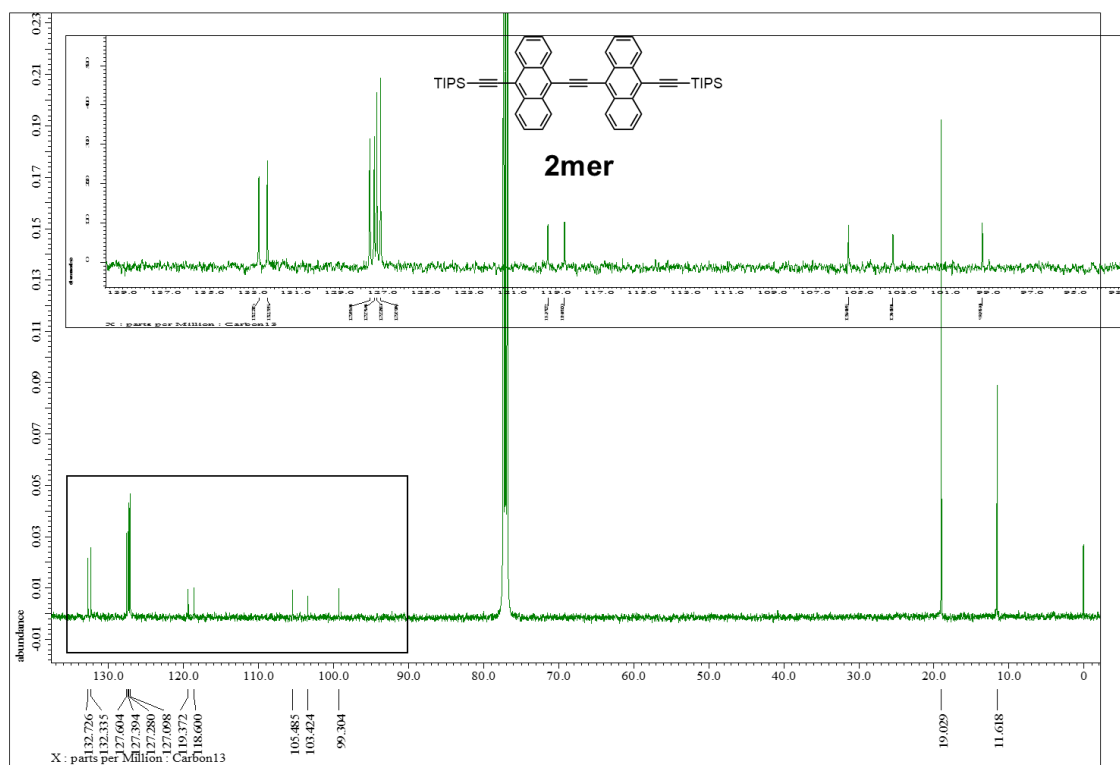


Figure S3. ^{13}C NMR spectrum of **2mer** in CDCl_3 .

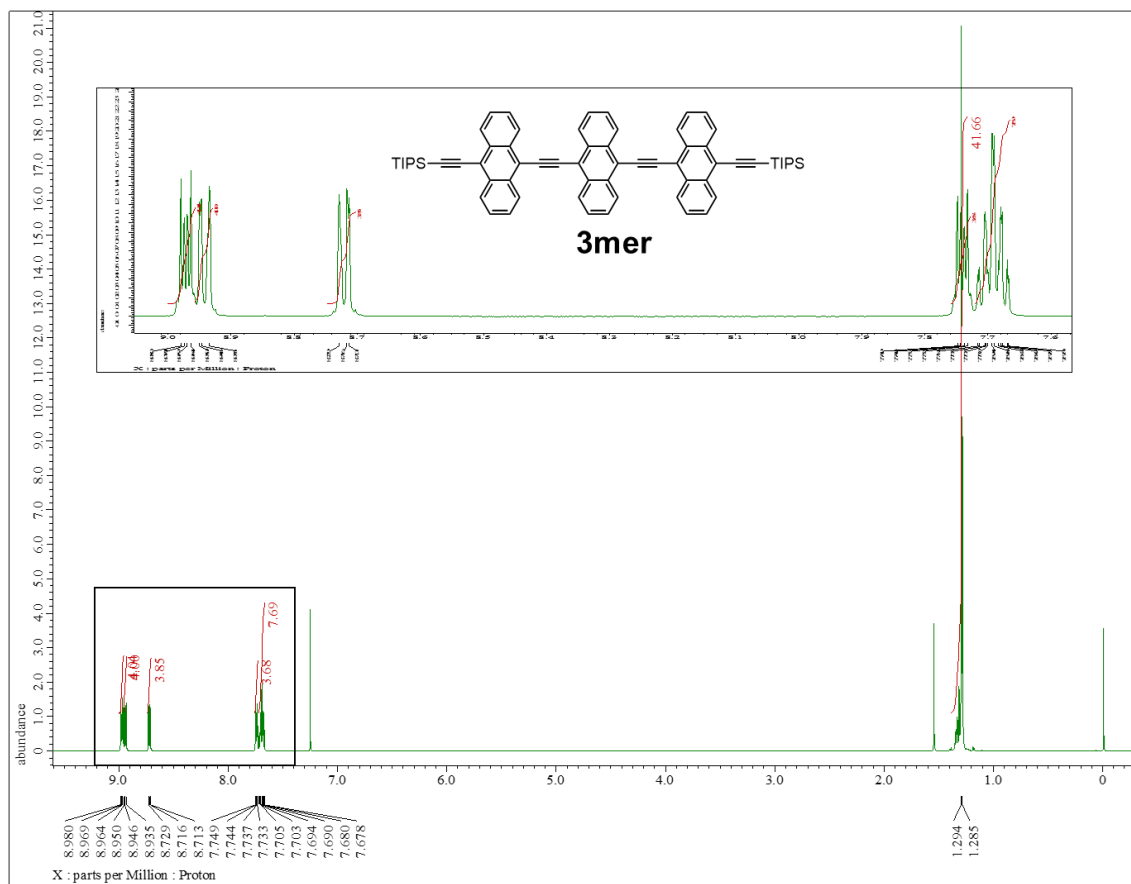


Figure S4. ^1H NMR spectrum of **3mer** in CDCl_3 .

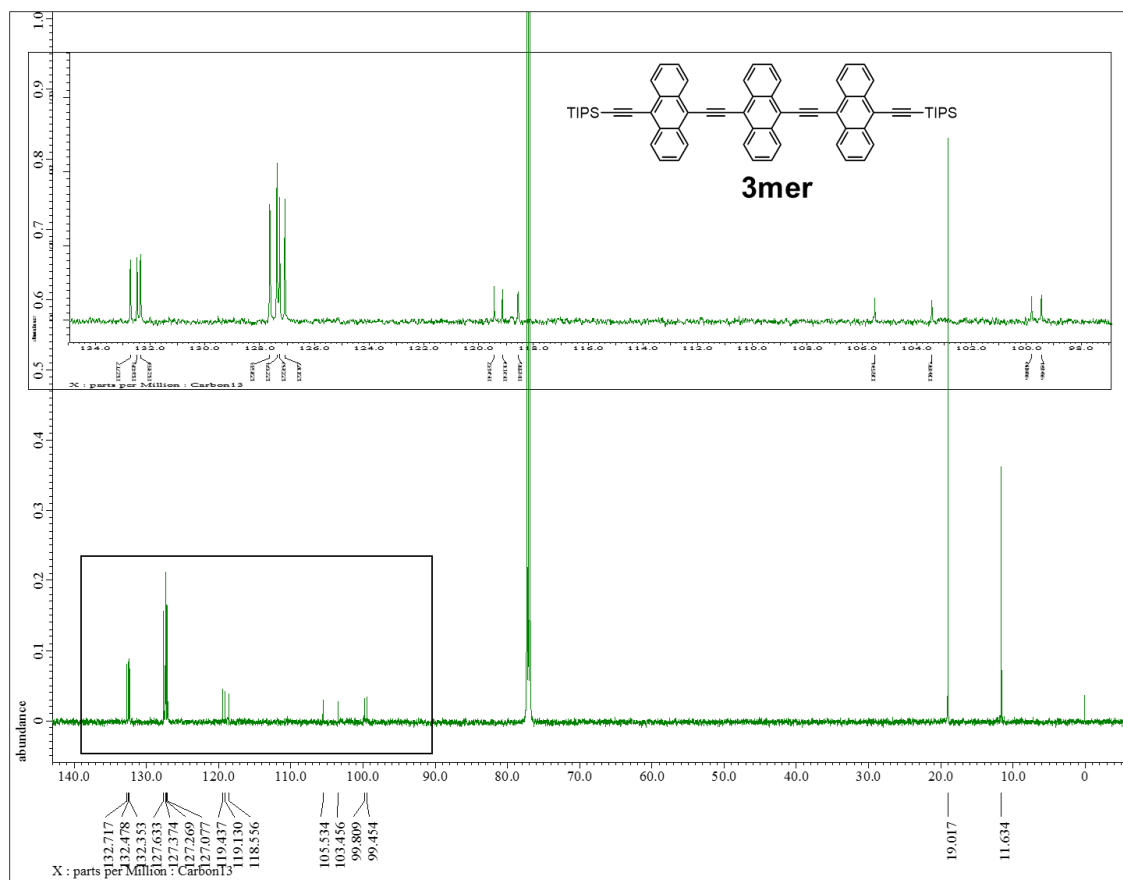


Figure S5. ^{13}C NMR spectrum of **3mer** in CDCl_3 .

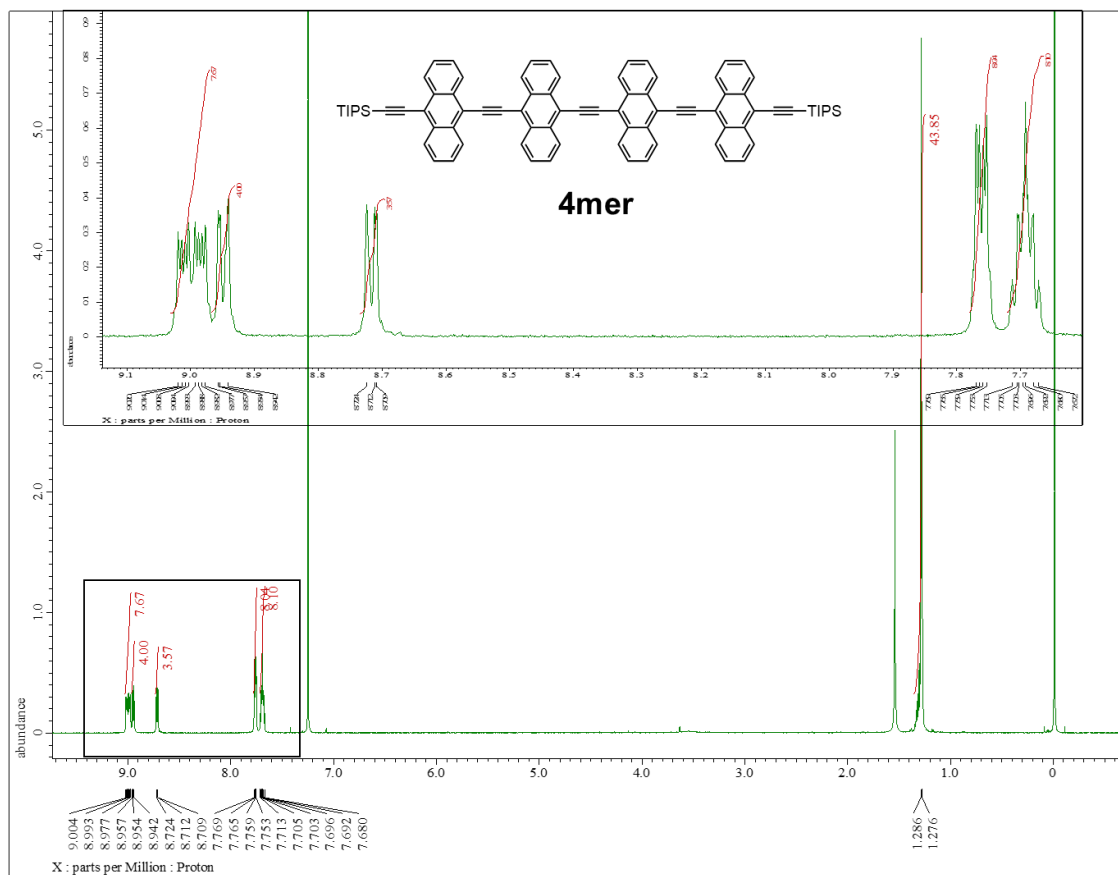


Figure S6. ^1H NMR spectrum of 4mer in CDCl_3 .

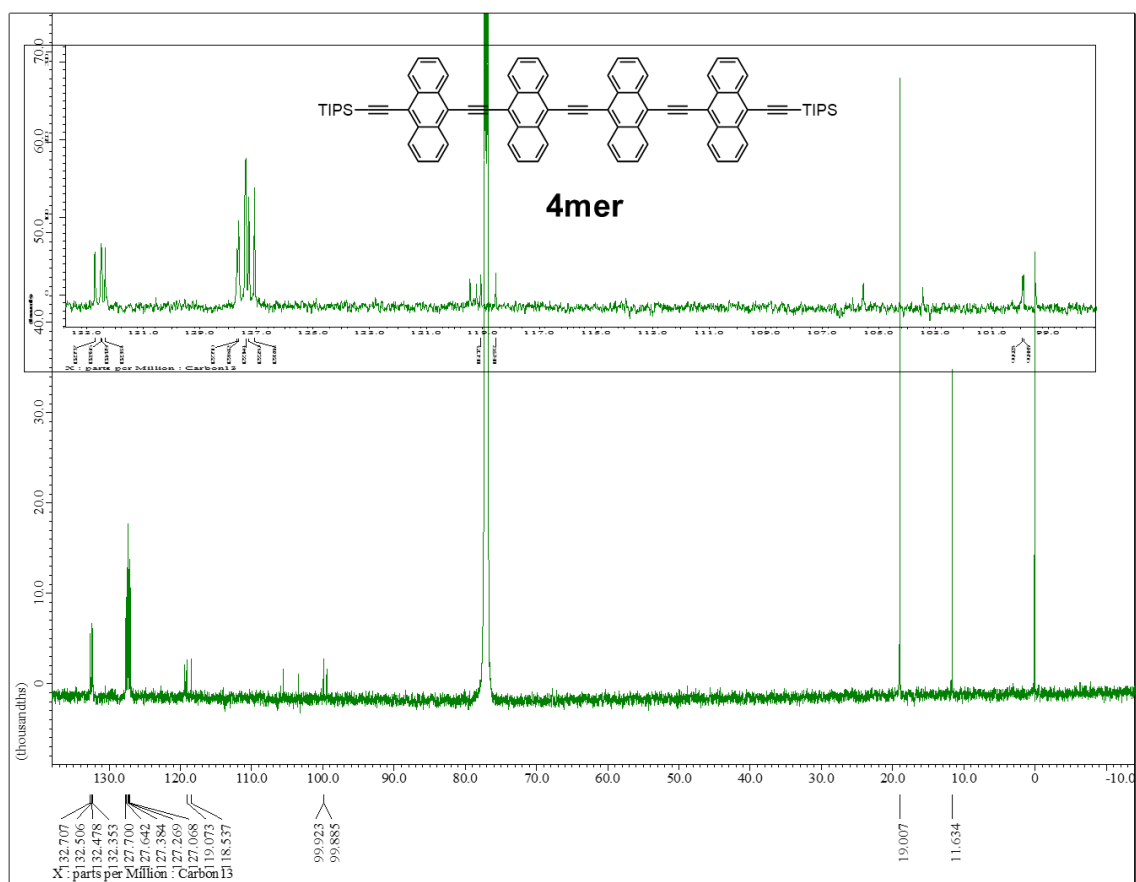


Figure S7. ^{13}C NMR spectrum of **4mer** in CDCl₃.

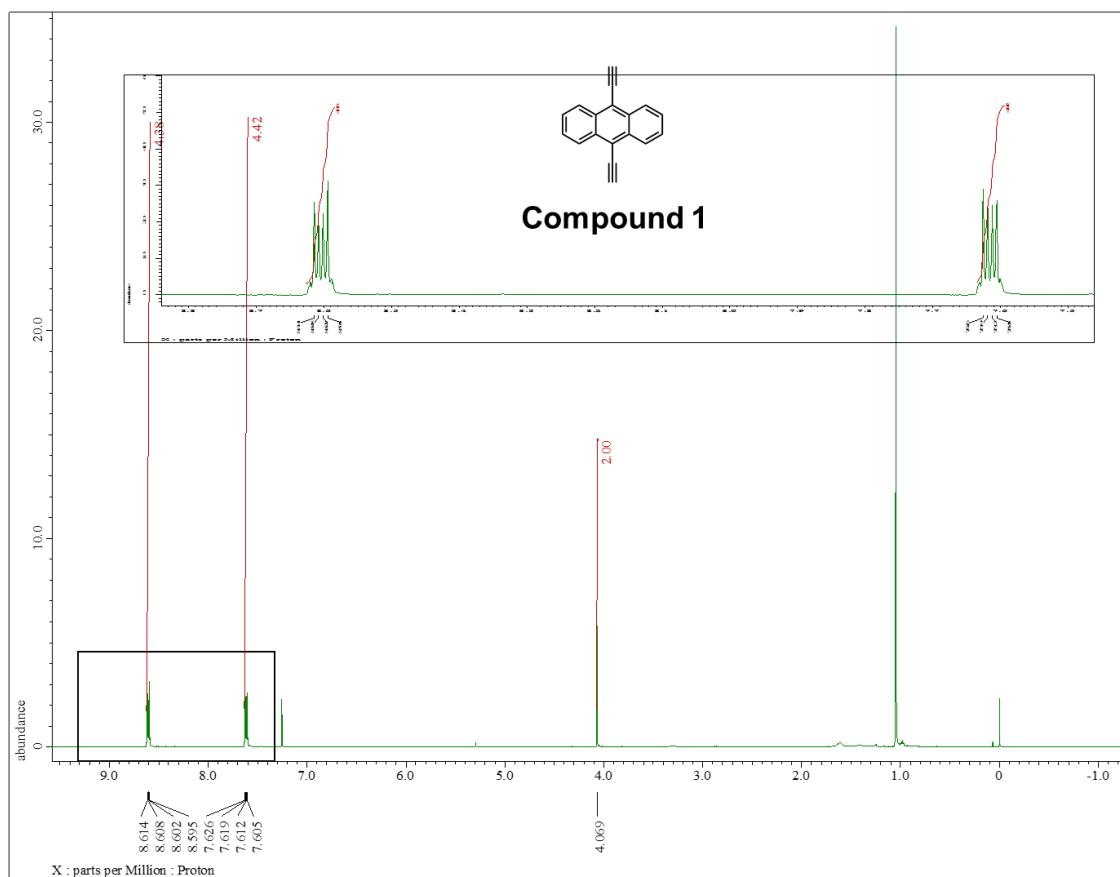


Figure S8. ^1H NMR spectrum of compound 1 in CDCl_3 .

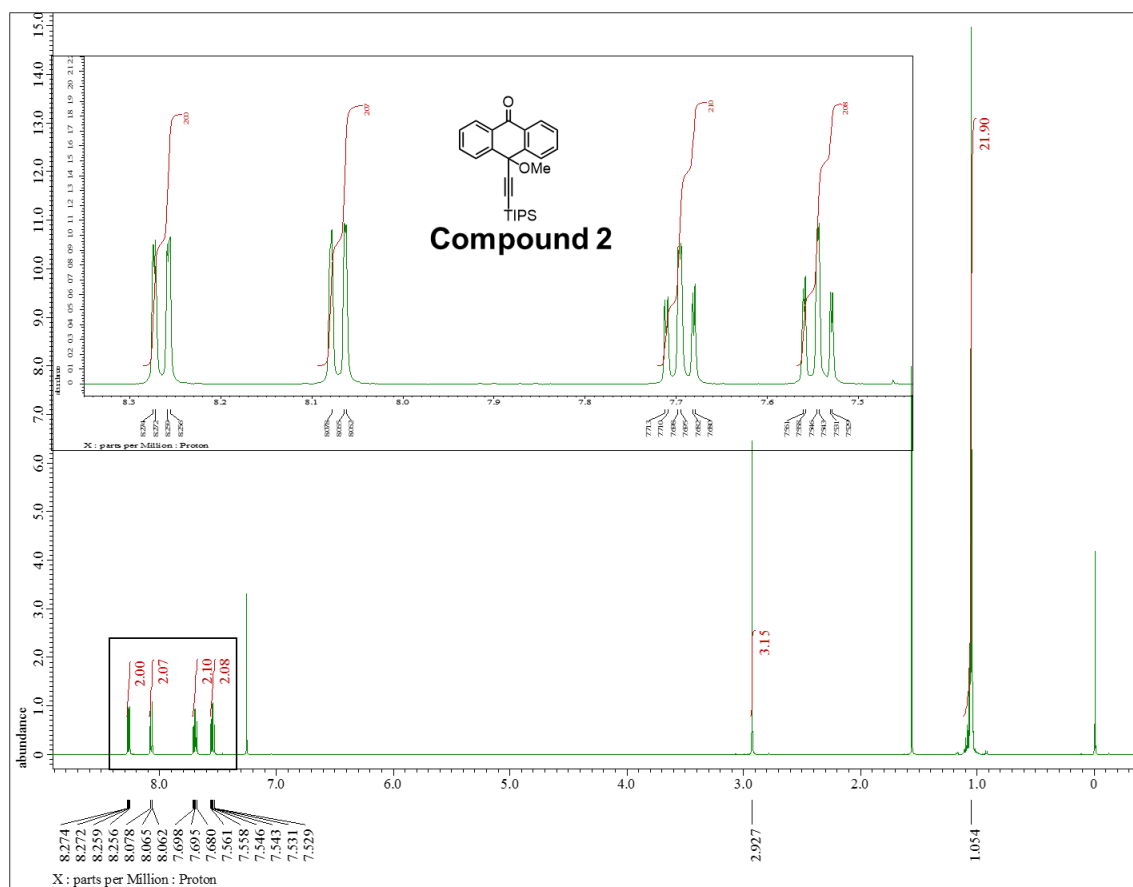


Figure S9. ^1H NMR spectrum of compound 2 in CDCl_3 .

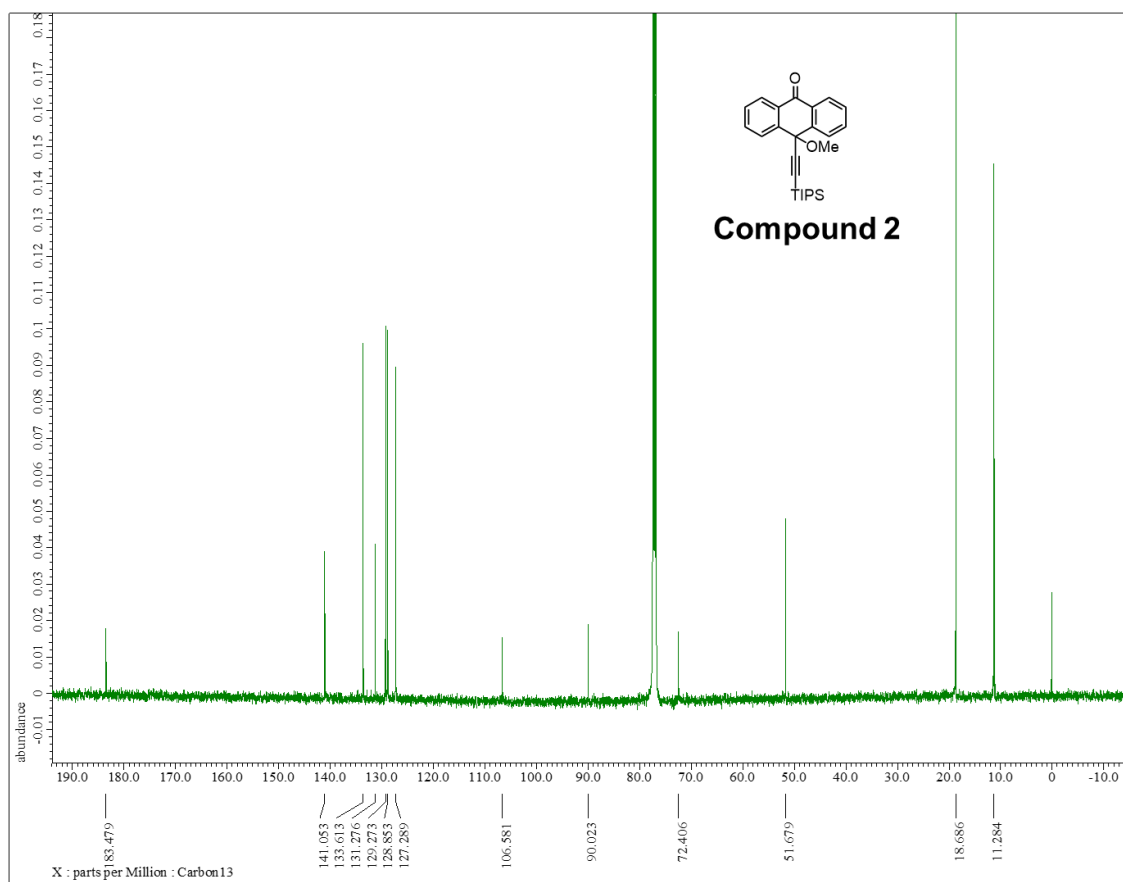


Figure S10. ^{13}C NMR spectrum of **compound 2** in CDCl_3 .

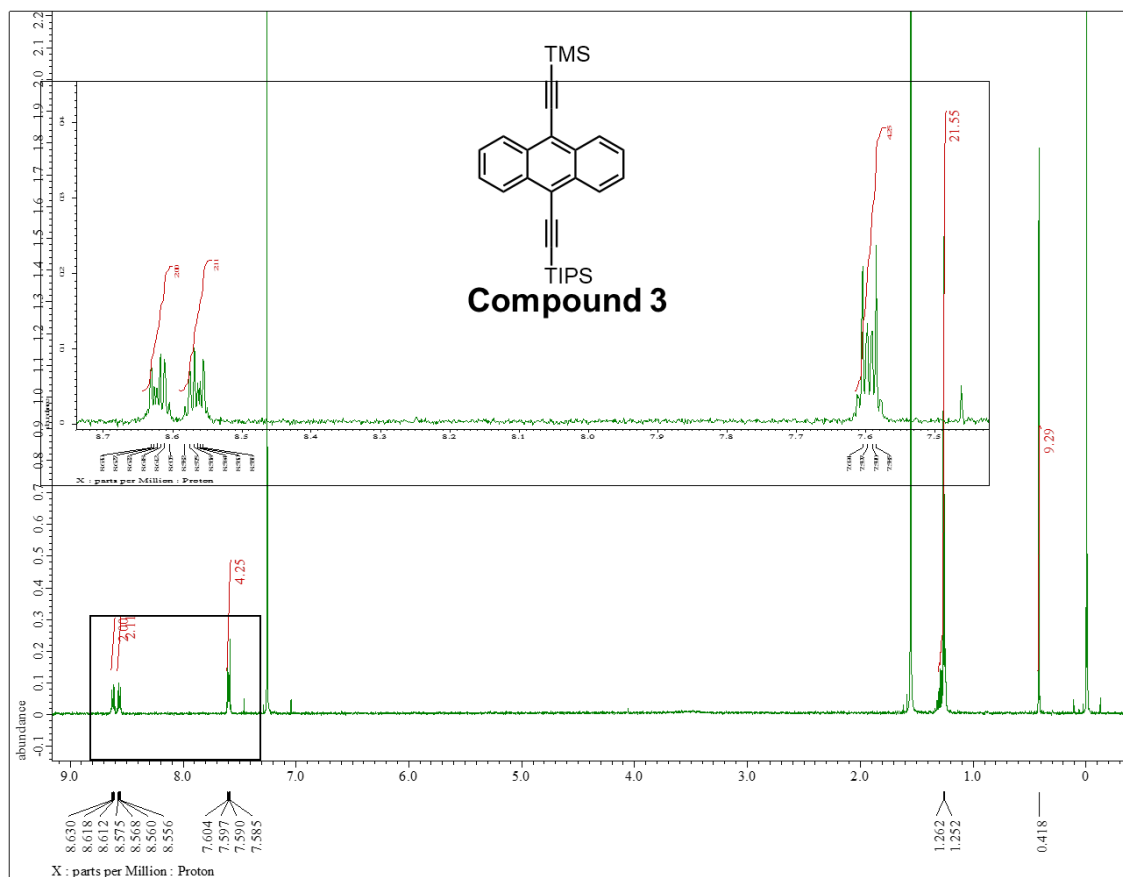


Figure S11. ^1H NMR spectrum of compound 3 in CDCl_3 .

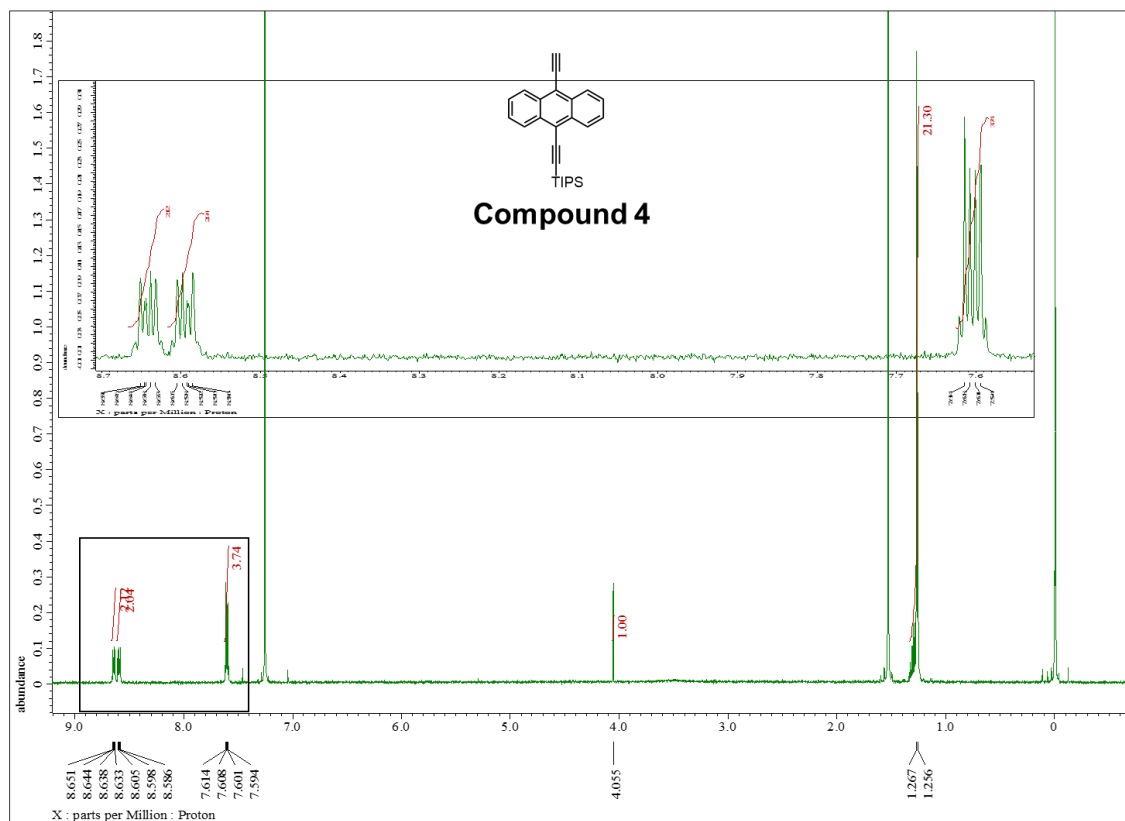


Figure S12. ^1H NMR spectrum of compound 4 in CDCl_3 .

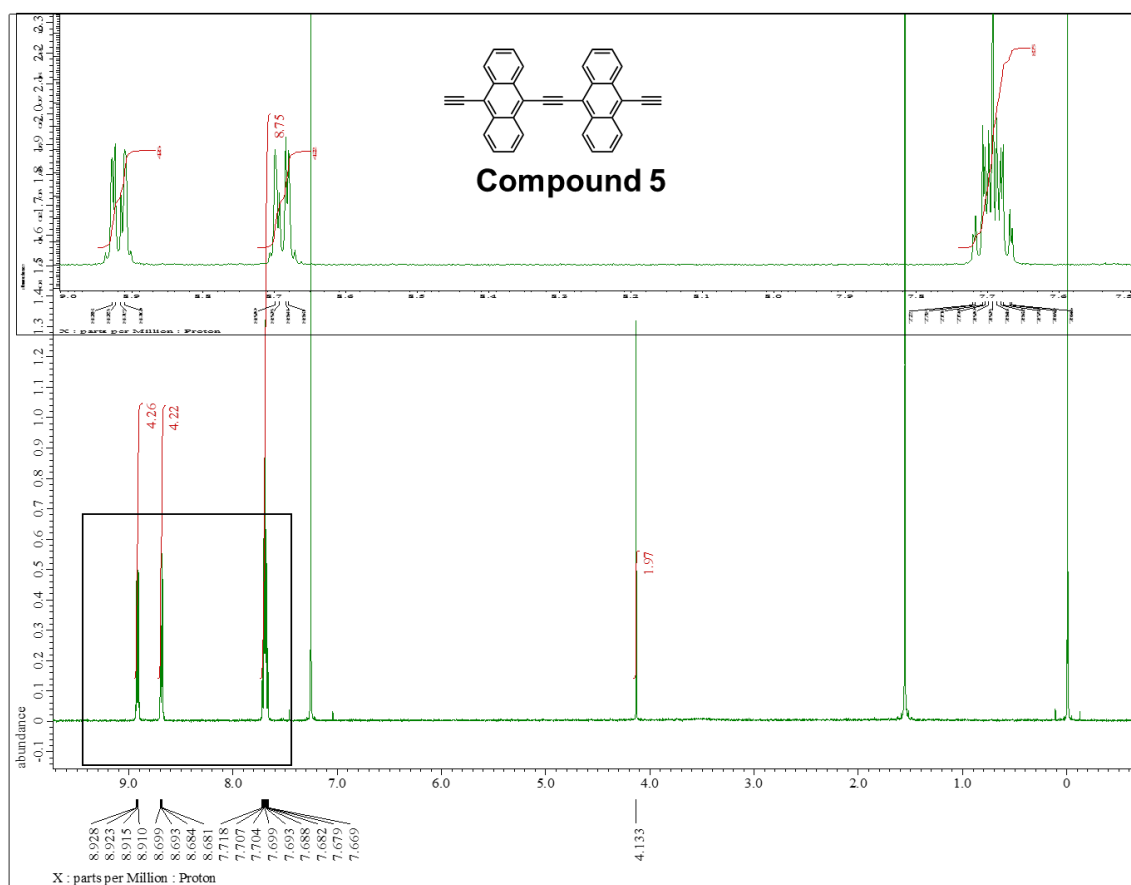


Figure S13. ^1H NMR spectrum of compound 5 in CDCl_3 .

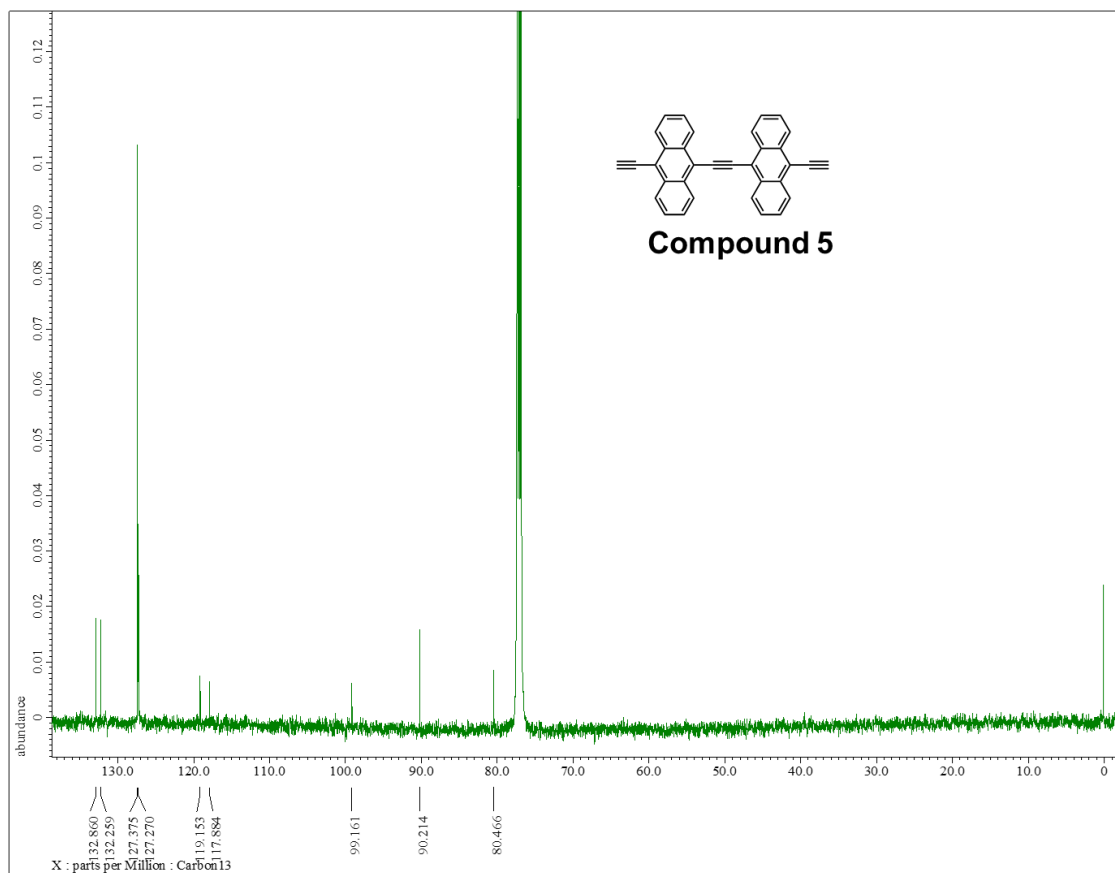
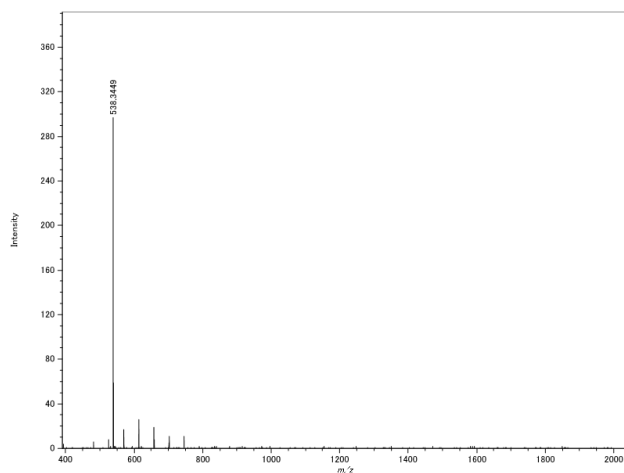


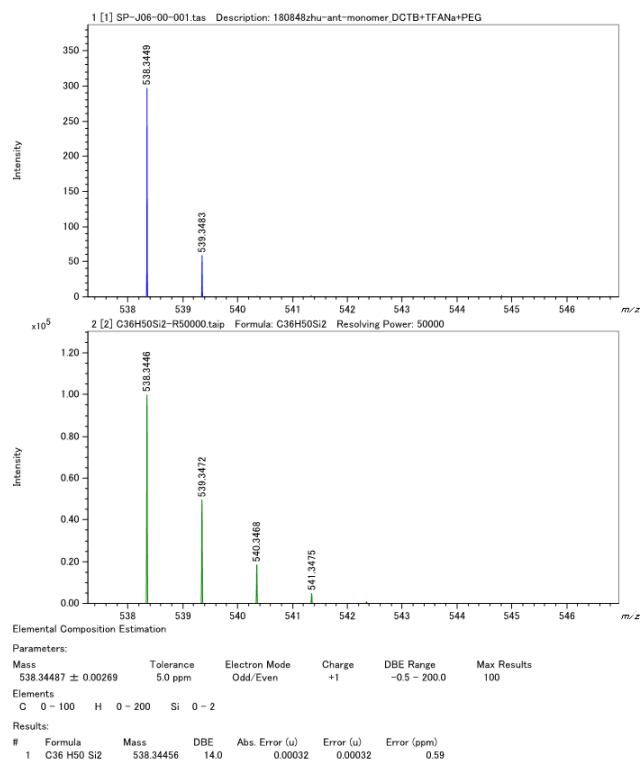
Figure S14. ^{13}C NMR spectrum of **compound 5** in CDCl_3 .

3-13-2. MS spectrum

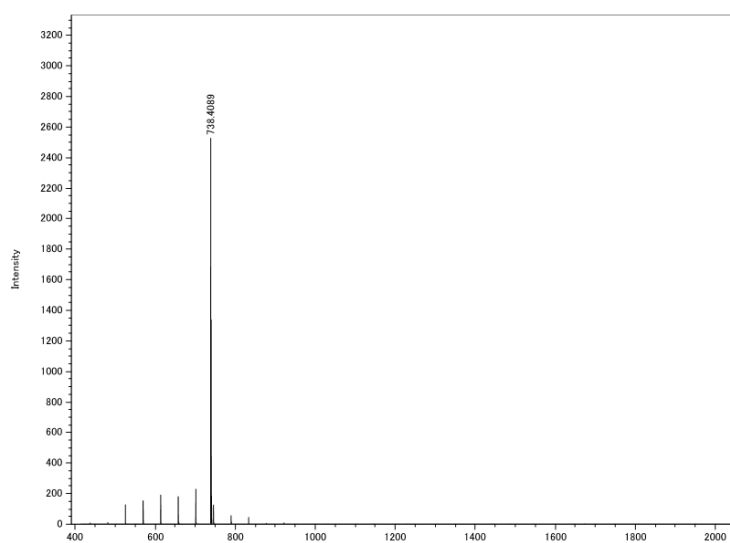
a)



b)

Figure S15. (a) MS spectrum and (b) HRMS spectra of **1mer**.

a)



b)

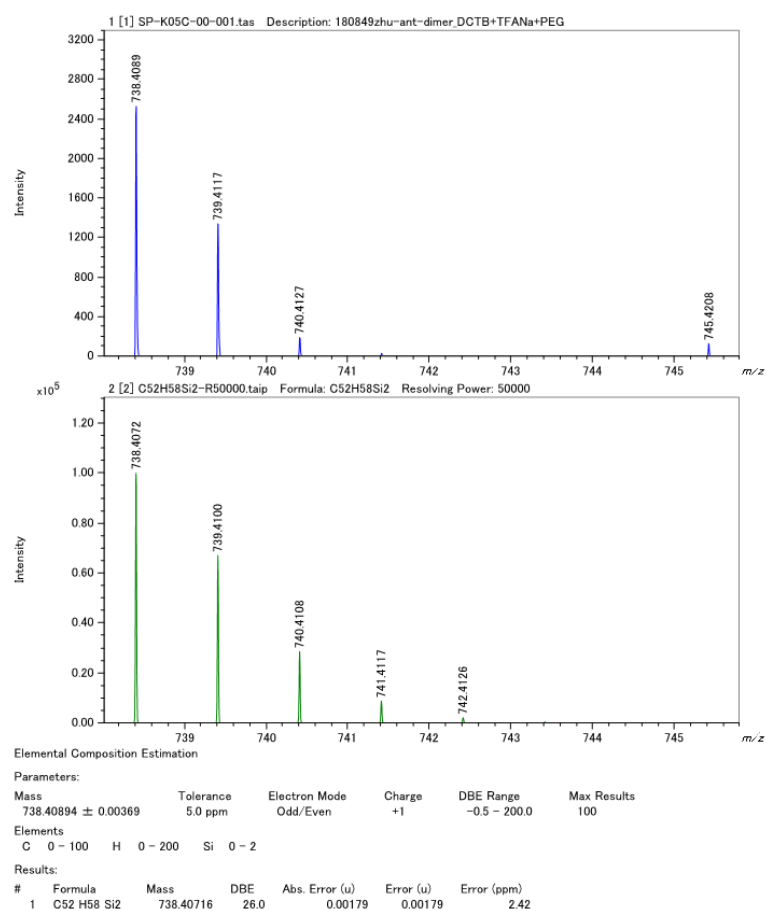
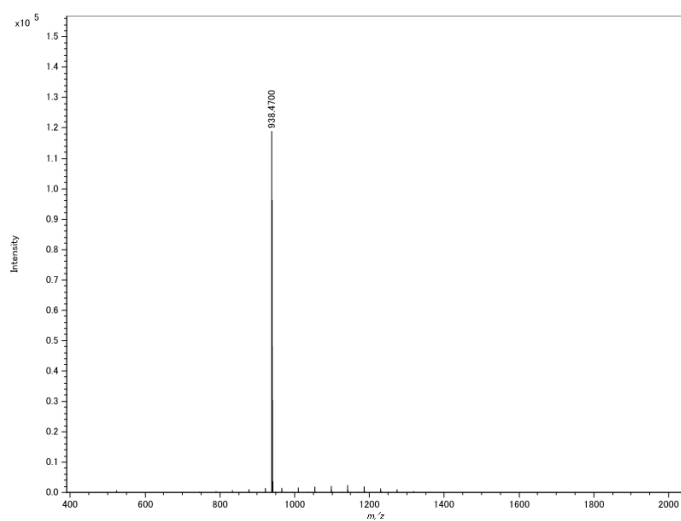
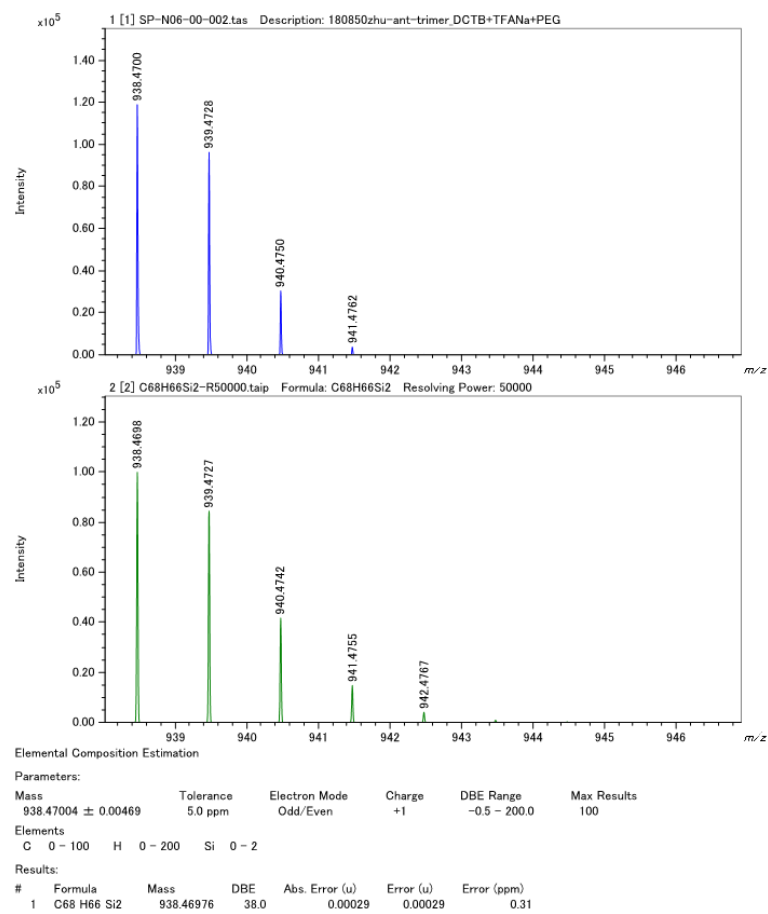


Figure S16. (a) MS spectrum and (b) HRMS spectra of 2mer.

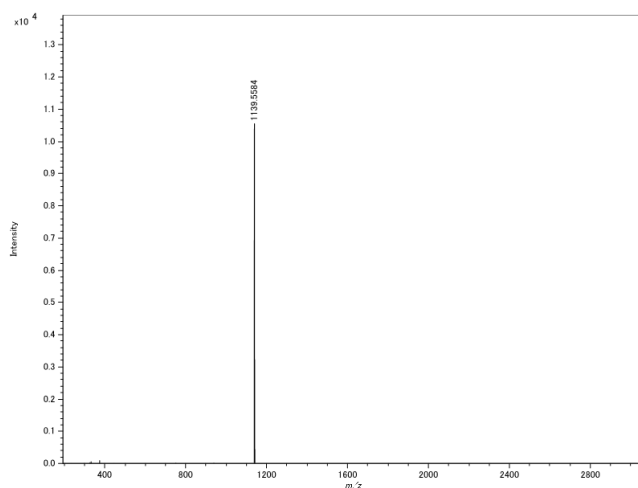
a)



b)

Figure S17. (a) MS spectrum and (b) HRMS spectra of **3mer**.

a)



b)

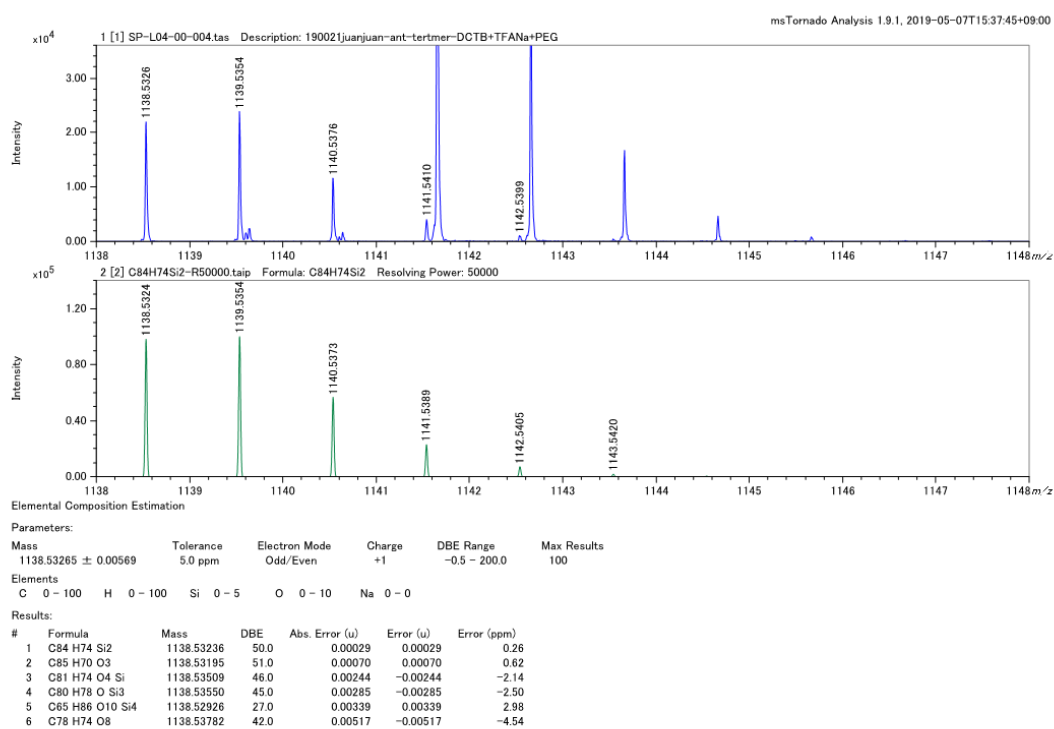
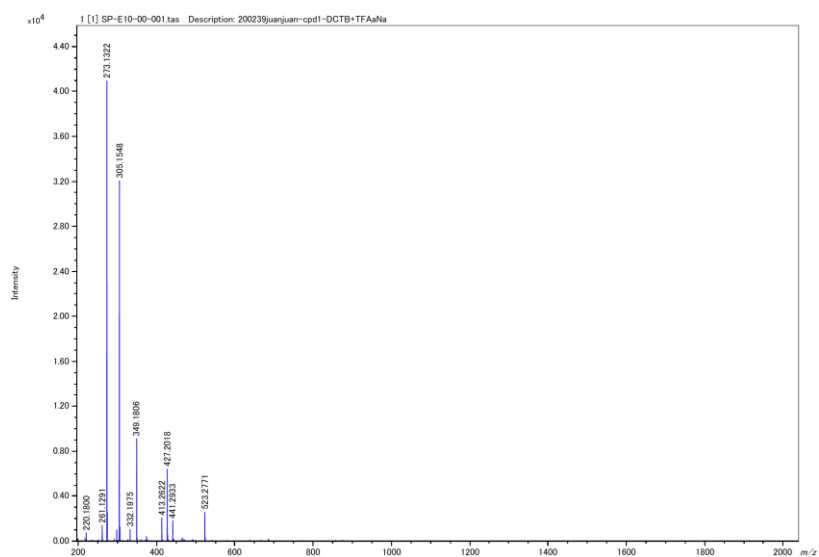
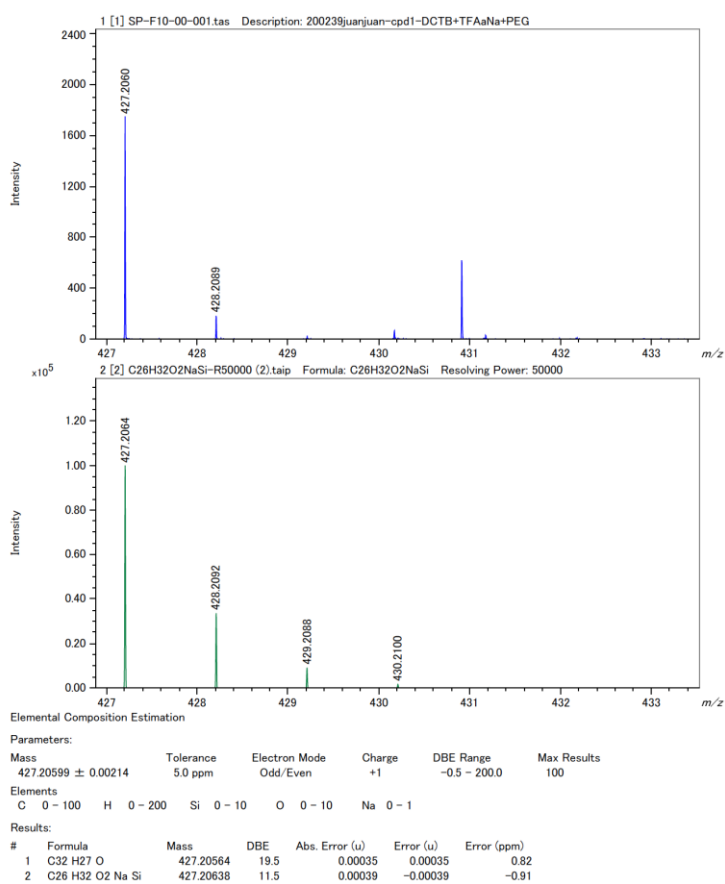


Figure S18. (a) MS spectrum and (b) HRMS spectra of 4mer.

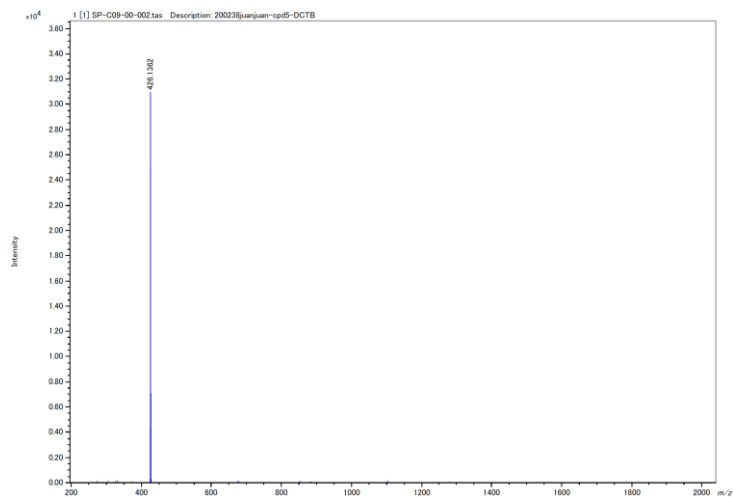
a)



b)

Figure S19. (a) MS spectrum and (b) HRMS spectra of **compound 2**.

a)



b)

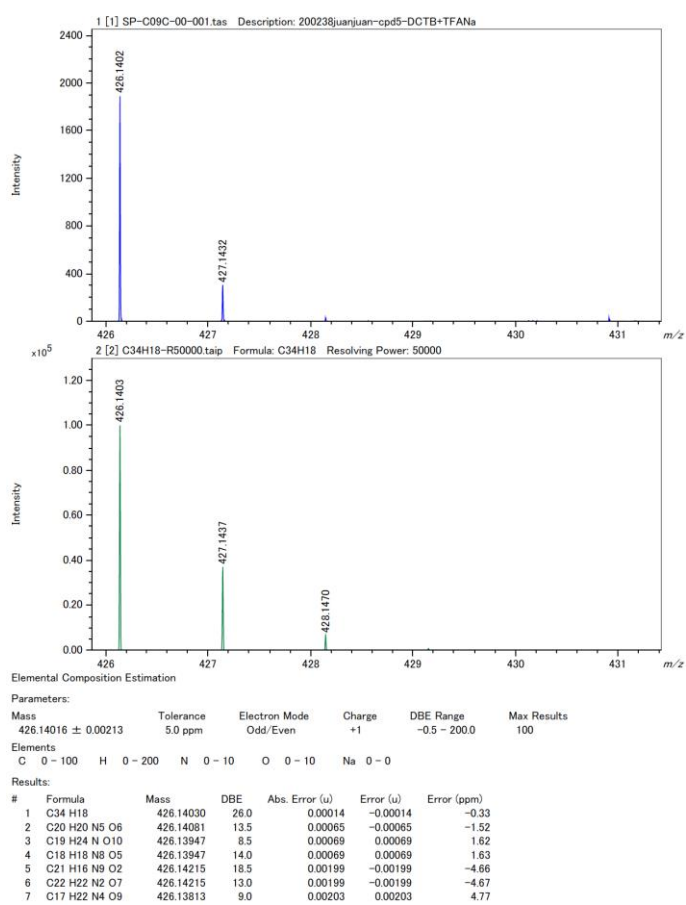
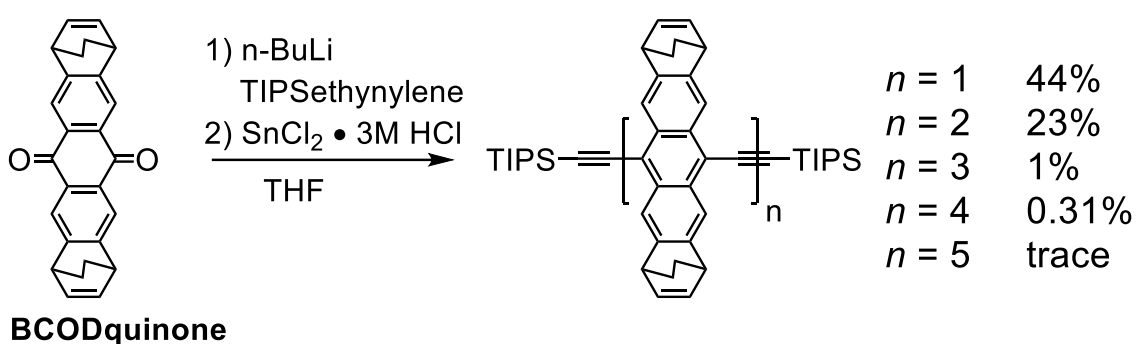


Figure S20. (a) MS spectrum and (b) HRMS spectra of compound 5.

Chapter 4.

Conventional Reaction with Quinone and Lithiated Silylethyne to Generate Long Ethynylene-bridged Oligomers in One-pot



In this chapter, ethynylene-bridged oligomers of pentacene precursor up to pentamer has been synthesized in one-pot by using a conventional reaction with lithiated silylethyne and quinone of pentacene precursor. The reaction conditions were optimized by changing reaction temperature, reaction time, and ratio of lithiated silylethyne.

4-1. Introduction

As introduced in Chapter 3, ethynylene-bridged anthracene trimer exhibited the best hole mobility ($0.14 \text{ cm}^2 \text{ V}^{-1} \text{ s}^{-1}$) among a set of ethynylene-bridged anthracene oligomers. However, the calculation of charge transfer integrals showed the strong interaction only along the column direction, while the intercolumn interaction was very small due to the bulky terminal group. To improve the charge transport property, the aromatic core extension from anthracene to pentacene seems to be promising, because of the improved two-dimensional (2D) electronic interaction in the system. Actually, several researchers reported that pentacene dimer with solubilizing silylethynylene groups could provide suitable packing motifs for OFETs. For instance, 6,6'-linked pentacene dimer (**Dip-TIPS**) with hole mobilities of $0.11 \text{ cm}^2 \text{ V}^{-1} \text{ s}^{-1}$ forms the desired two-dimensional (2D) π -stacking network due to the orthogonal orientation of the two pentacenes.¹ As the similar system, Kawano and coworkers reported a 6,6'-linked (triisopropylsilylethynyl) ethynylene-bridged pentacene dimer (**TIPS-PenD**) exhibited field-effect hole mobilities of up to $0.24 \text{ cm}^2 \text{ V}^{-1} \text{ s}^{-1}$, showing the stronger π - π interaction in solid-state, owing to the similar molecular weight and thermal stability with **Dip-TIPS**.²

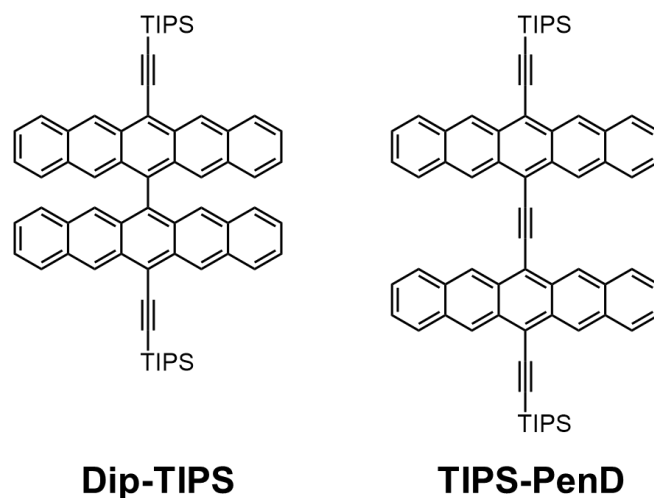


Figure 4-1. Molecular structures of pentacene dimer.

It is interesting that **TIPS-PenD** was synthesized from pentacenequinone in two-steps, skipping the conventional stepwise approach. A plausible reaction mechanism for the dimer formation started from the deprotection of the silyl group, competing with the hydrolysis/reduction step in a kinetic process (Figure 4-2). Firstly, an oxyanion of the intermediate A attacks the triple bond of TIPSacetylene moiety, resulting in an intramolecular cyclization. Although this cyclization should be quickly reversible, the resulting carbanion of the intermediate B reacts with pentacenequinone, forming an intermediate C. Then, due to the relatively large Si–O bond energy, the oxyanion of the intermediate C would attack the Si of TIPSethynylene moiety to regenerate the triple bond.^{2,3} The discovery of this side reaction in a conventional synthesis provides a great clue to the effective synthetic approach of ethynylene-bridged acene compounds.

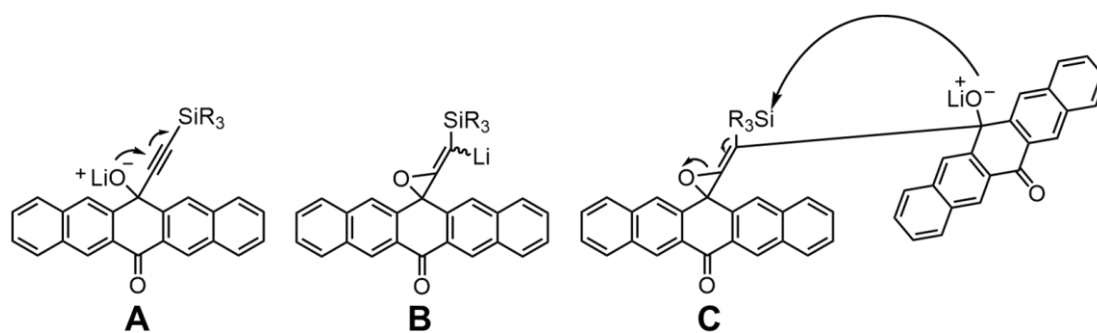
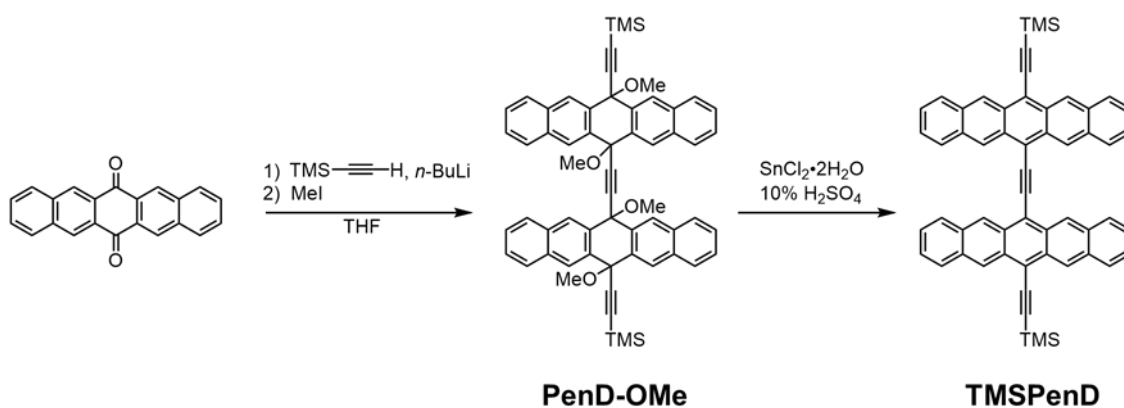


Figure 4-2. Intermediate A, B, and C in the plausible reaction mechanism.

With these in mind, the reaction condition for efficient synthesis of pentacene dimer was firstly investigated. In addition, this method was used for preparing further π -extended acene dimer, namely heptacene dimer.

4-2. Synthesis of ethynylene-bridged pentacene dimer with TMSethynylene

At first, the substitution effect of ethynylene-bridged pentacene dimer synthesis was investigated with TMSethynylene. As shown in the Scheme 4-1, the synthetic scheme is similar with the one for **TIPS-PenD**.²



Scheme 4-1. Synthetic scheme of **TMSPenD**.

Here, in this study, methyl ether substituted group was firstly introduced to obtain a soluble key intermediate of pentacene dimer (**PenD-OMe**).⁴ The introduction of methyl ether substituted group provided not only soluble **PenD-OMe** but also decreased the polarity of the compound compared with **PenD-OH**, so that the purification of **PenD-OMe** by silica gel column chromatography was easier than the case with **PenD-OH** in the previous report. The yield of **PenD-OMe** was improved to 13%, and the chemical structure of **PenD-OMe** was confirmed by ¹H NMR spectrum and HRMS. Then, the subsequent reductive aromatization of **PenD-OMe** with SnCl₂ in 10% concentrated H₂SO₄ gave **TMSPenD** as a deep-green crystal with almost quant yield.⁵ Similar with **TIPS-PenD**, the solubility of resulting **TMSPenD** is not good enough to purify with silica gel column chromatography. However, the recrystallization of **TMSPenD** with carbon disulfide and acetonitrile successfully gave pure **TMSPenD**.⁶ Crystals of **TMSPenD**

suitable for X-ray diffraction analysis were grown via slow diffusion of acetonitrile vapor into a carbon disulfide solution of **TMSPenD**. Interestingly, **TMSPenD** adopted two near coplanar pentacene moieties in the arrangement with typical columnar π - π stacking. At the same time, the substituent diameter is less than half of the length of acene, resulting the stronger C–H interactions in adjacent pentacene units.

Next, the survey of reaction condition of **PenD-OMe** was performed to improve the yield of dimeric product. The effect of reaction temperature, lithiated silylethynylene ratio, and reaction time in the first step were investigated, and the isolated products were summarized in the Figure 4-3.

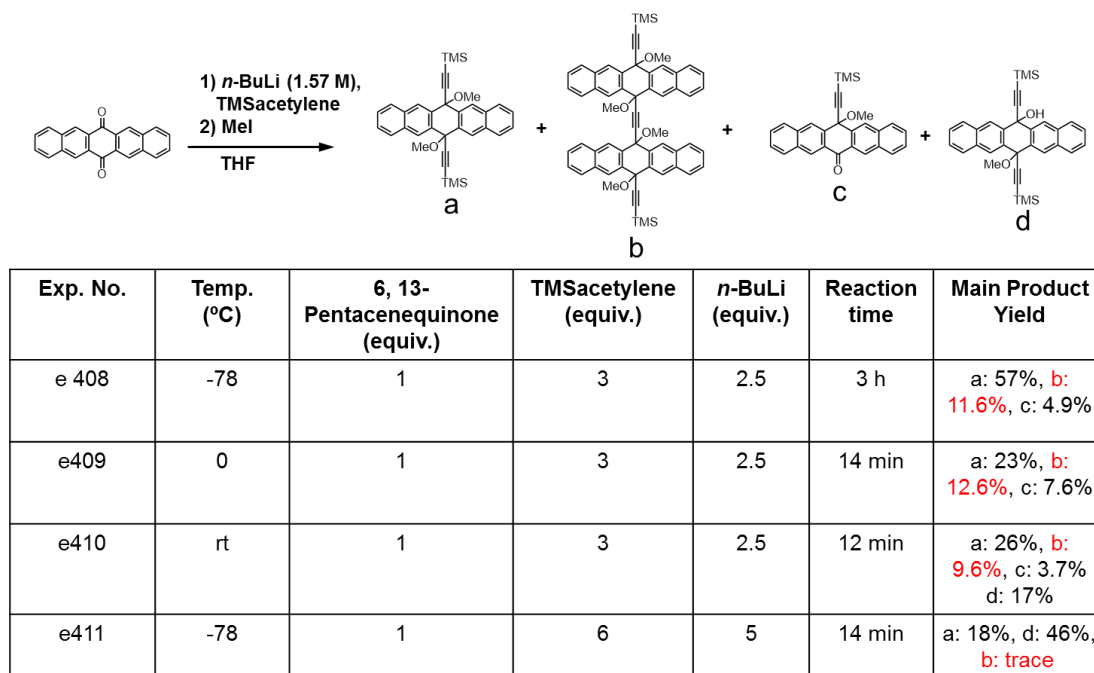


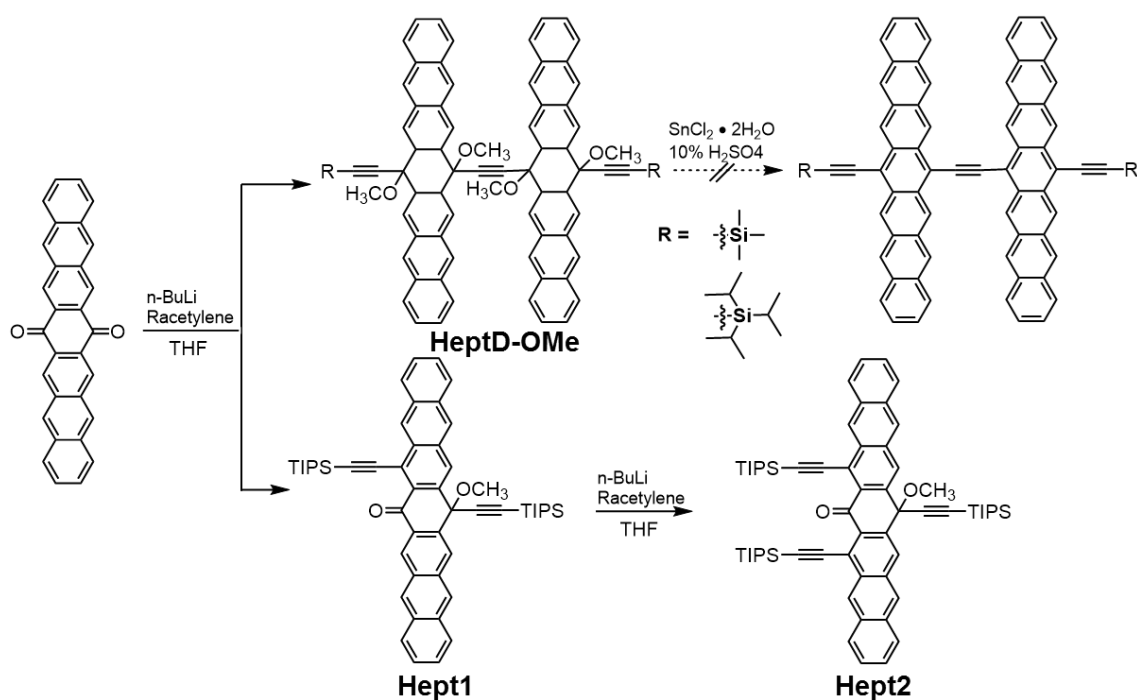
Figure 4-3. Optimization condition of dimerization.

The results showed that the appropriate equivalent of lithiated silylethynylene gave a great effect on the dimer formation. For example, excessive amount of lithiated silylethynylene lead to the low yield of dimeric product. Additionally, the formation of dimeric product was not significantly influenced by the reaction temperature. Meanwhile, although the yield of dimer was not dramatically affected by changing the reaction temperature, the ratio of monomer/dimer gradually increased along with the rise of temperature. According to the plausible reaction mechanism for **TIPSPenD**, it seems that the ratio of lithiated silylethynylene close to 0.8 would promote the first intramolecular cyclization in a plausible reaction mechanism. In general, as TMS group is easily cleaved compared with TIPS group, the reaction time of lithiated silylethynylene could be shorten in ten minutes in the case of **TMSPenD**.⁷⁻⁹ Larger substituents decrease the rate of hydrolysis¹⁰ of the silyl group. The yield of **TMSPenD-OMe** in this study achieved 13%, whereas only 6% yield was reported for **TIPSPenD-OH** in the previous report.²

4-3. Synthesis of ethynylene-bridged heptacene dimer

To extend the π -conjugation as well as heptacene dimer, the similar reaction was performed for 7,16-heptacenequinone. Fortunately, as shown in the Scheme 4-2, the key intermediate **HeptD-OMe** was successfully obtained in one pot. Two terminal

silylethynylene groups of TMSethynylene and TIPSethynylene were introduced at the *meso*-position of heptacene to control the molecular arrangement of final ethynylene-bridged heptacene dimer (**HeptD**). The synthesis of **HeptD** started from 7,16-heptacenequinone. The addition of an appropriate equivalent of lithiated silylethynylene to a suspension of 7,16-heptacenequinone in THF followed by the trapping of the resulting intermediate with iodomethane directly afforded **HeptD-OMe** with TMSethynylene and TIPSethynylene as 12% and 7%, respectively.



Scheme 4-2. Synthetic scheme of heptacene dimer.

Even though the yield of **HeptD-OMe** is not high, the direct synthetic route instead

of classic protection/deprotection method proves an easy way to obtain heptacene dimer derivatives. As mentioned in the case of **PenD-OMe**, **HeptD-OMe** with large substituted group, namely TIPS vs. TMS, gave lower yield due to the decreasing the rate of hydrolysis. In addition, the unexpected Michal addition product (**Hept1**) was formed together with 1,2-addition product (**HeptD-OMe**). The latter product was further reacted with excessive amount of lithiated silylethynylene (more than 20 times compared with pristine acene dione) for generating **Hept1**. The results showed that Michal addition product **Hept2** (42%) was obtained, providing unreacted starting materials **Hept1** (58%). These results clearly indicated the reason that the triisopropylsilyl substituted heptacene monomer could not be prepared in the previous report by Anthony.¹¹ In fact, they changed the substituent from TIPSethynylene to tri-*tert*-butylsilyl (TTBS) ethynylene to stabilize heptacene, because the reason for the failure of synthesis of TIPSethynylene substituted heptacene monomer was expected to be due to the undesirable Diels-Alder addition. However, based on my results, the reason was probably because of the formation of **Hept1**. In addition, only TTBS substituted heptacene monomer was successfully isolated in the previous research possibly due to the steric hindrance between adjacent silyl groups as large substituents, preventing Michael addition on the aromatic ring.¹²

The structures of **HeptD-OMe**, **Hept1**, and **Hept2** were unambiguously characterized

by ^1H NMR, HRMS and X-ray single crystal structure. Crystals of **HeptD-OMe** were grown through the diffusion of acetonitrile vapor into a carbon disulfide solution of **HeptD-OMe**. The X-ray structure demonstrates that the ethynylene-bridge is approximately coplanar along to the heptacene units (Table 4-1, Figure 4-4). C10 bears one "up" of methyl ether and one "down" of TMSethynylene, each of them are nearly perpendicular (109°) to the C10 symmetry axis, giving the stair-like conformation. This structure contributes to the increase in the solubility of **HeptD-OMe**.

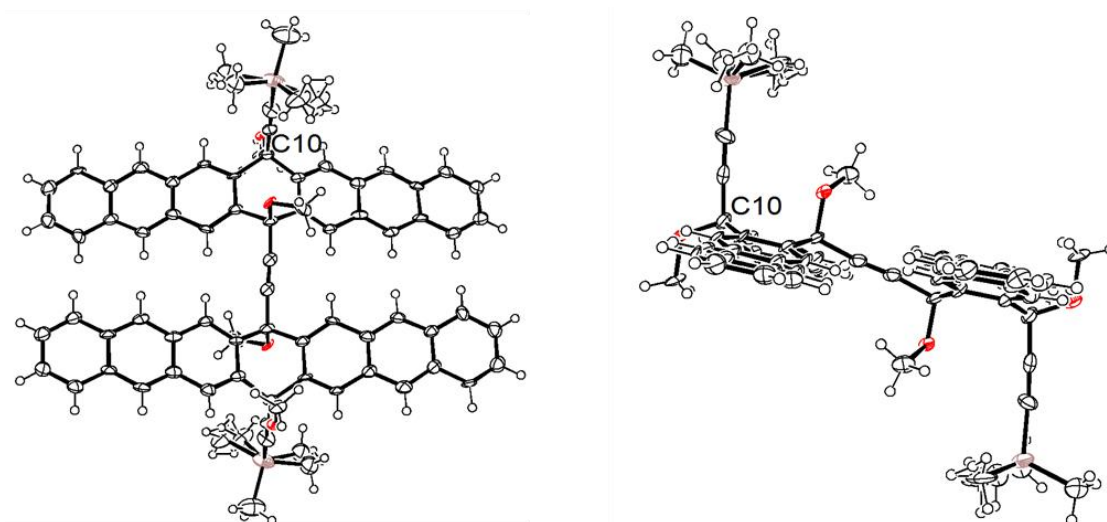


Figure 4-4. Top and side views of crystal structure of **HeptD-OMe**. Thermal ellipsoids represent 50% probability.

Table 4-1. Single-crystal X-ray diffraction parameters and crystal data of **HeptD-OMe**.

Empirical formula	$\text{C}_{76.81}\text{H}_{62}\text{O}_4\text{S}_{1.62}\text{Si}_2$
Formula weight	1157.22
Temperature	93 K

Wavelength	0.71073 Å	
Crystal system	Triclinic	
Space group	<i>P</i> -1	
Unit cell dimensions	$a = 9.293(14)$ Å	$\alpha = 88.81(2)^\circ$
	$b = 12.817(19)$ Å	$\beta = 75.83(2)^\circ$
	$c = 13.38(2)$ Å	$\gamma = 79.43(2)^\circ$
Volume	1519(4) Å ³	
Z	1	
Density (calculated)	1.265 Mg/m ³	
Absorption coefficient	0.167 mm ⁻¹	
<i>F</i> (000)	609	
Crystal size	0.150 x 0.050 x 0.010 mm ³	
Theta range for data collection	1.570 to 23.398°	
Index ranges	$-10 \leq h \leq 10, -11 \leq k \leq 14, -14 \leq l \leq 14$	
Reflections collected	6852	
Independent reflections	4404 [R(int) = 0.2367]	
Completeness to theta = 23.500°	99.1%	
Absorption correction	Semi-empirical from equivalents	
Max. and min. transmission	0.998 and 0.533	
Refinement method	Full-matrix least-squares on <i>F</i> ²	
Data / restraints / parameters	4404 / 242 / 401	
Goodness-of-fit on <i>F</i> ²	1.084	
Final <i>R</i> indices [<i>I</i> > 2σ(<i>I</i>)]	$R_1 = 0.1576, wR_2 = 0.2444$	
<i>R</i> indices (all data)	$R_1 = 0.3909, wR_2 = 0.3742$	
Extinction coefficient	n/a	
Largest diff. peak and hole	0.346 and -0.335 e.Å ⁻³	

Parallelogram yellow single crystals of **Hept2** suitable for X-ray diffraction analysis were grown *via* slow diffusion of methanol into chlorobenzene solution of **Hept2** at room temperature. The X-ray single crystal of **Hept2** is shown in Table 4-2, Figure 4-5. Given

in the large torsion of central ring, whole molecule exhibits a butterfly-like structure with a bent angle of 110.3° and the dihedral angle between the planes of the anthracene units is ca. 33° . The molecular structure of **Hept2** shows the steric congestion of adjacent TIPSEthynylene groups at C3 and C29. Therefore, the additional reaction could not take place at C1 even under the excess amount of lithiated silylethynylene.

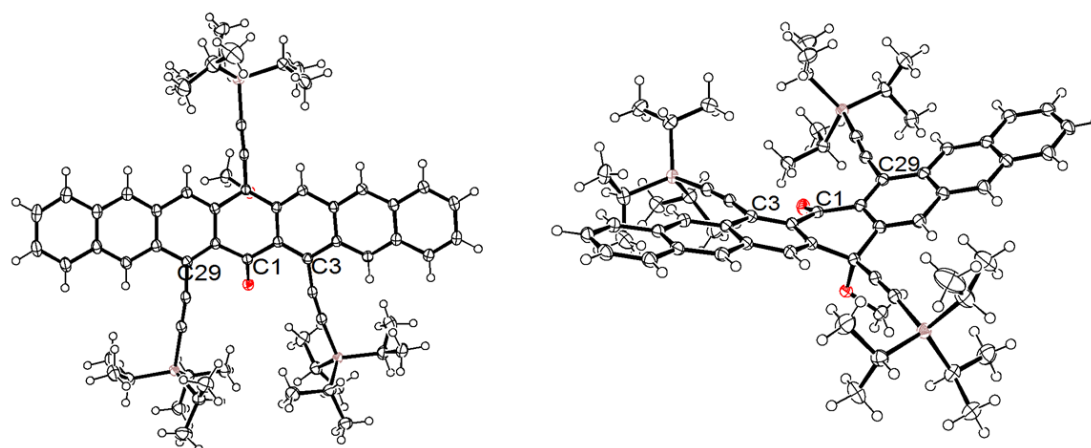


Figure 4-5. Top and side views of crystal structure of **Hept2**. Thermal ellipsoids represent 50% probability.

Table 4-2. Single-crystal X-ray diffraction parameters and crystal data of **Hept2**.

Empirical formula	$C_{64}H_{80}O_2Si_3$	
Formula weight	965.59	
Temperature	103 K	
Wavelength	0.71075 Å	
Crystal system	Monoclinic	
Space group	$P2_1/c$	
Unit cell dimensions	$a = 16.7042(3)$ Å	$\beta = 113.301(8)^\circ$
	$b = 24.4685(5)$ Å	

	$c = 15.1306(3) \text{ \AA}$
Volume	$5679.9(4) \text{ \AA}^3$
Z	4
Density (calculated)	1.129 g/m^3
Absorption coefficient	1.253 cm^{-1}
$F(000)$	2088
Crystal size	$0.260 \times 0.200 \times 0.110 \text{ mm}^3$
Reflections collected	93771
Independent reflections	13019 [$R(\text{int}) = 0.0545$]
Absorption correction	Semi-empirical from equivalents
Max. and min. transmission	0.986 and 0.576
Refinement method	Full-matrix least-squares on F^2
Goodness-of-fit on F^2	1.021
Final R indices [$I > 2\sigma(I)$]	$R_1 = 0.0488$
R indices (all data)	$R_1 = 0.0577, wR_2 = 0.1314$
Extinction coefficient	n/a
Largest diff. peak and hole	1.28 and -0.54 e \AA^{-3}

Then, according to the synthetic scheme for **TIPS-Pen**, Sn^{II} -mediated reductive aromatization was treated to give the desired **HeptD**. Unfortunately, target **HeptD** could not be obtained probably because of the low stability and solubility.¹³⁻¹⁵ Although MALDI-TOF-MS detected the mass which matched with the expected mass of **HeptD** (Figure 4-6, 4-7), it is not a strong evidence to prove the formation of **HeptD**. As Anthony and coworkers reported, silylethynylene-substituted hexacene derivatives performed dimerization not only in solution state but also in solid state even without light.¹⁶ The mass spectra of well characterized dimeric products showed the same peaks with pristine

silylethynylene-substituted hexacene monomer. It seemed the undesirable products such as dimeric product of **HeptD** were simultaneously formed during the reductive aromatization reaction, although the reaction was performed in the dark condition.

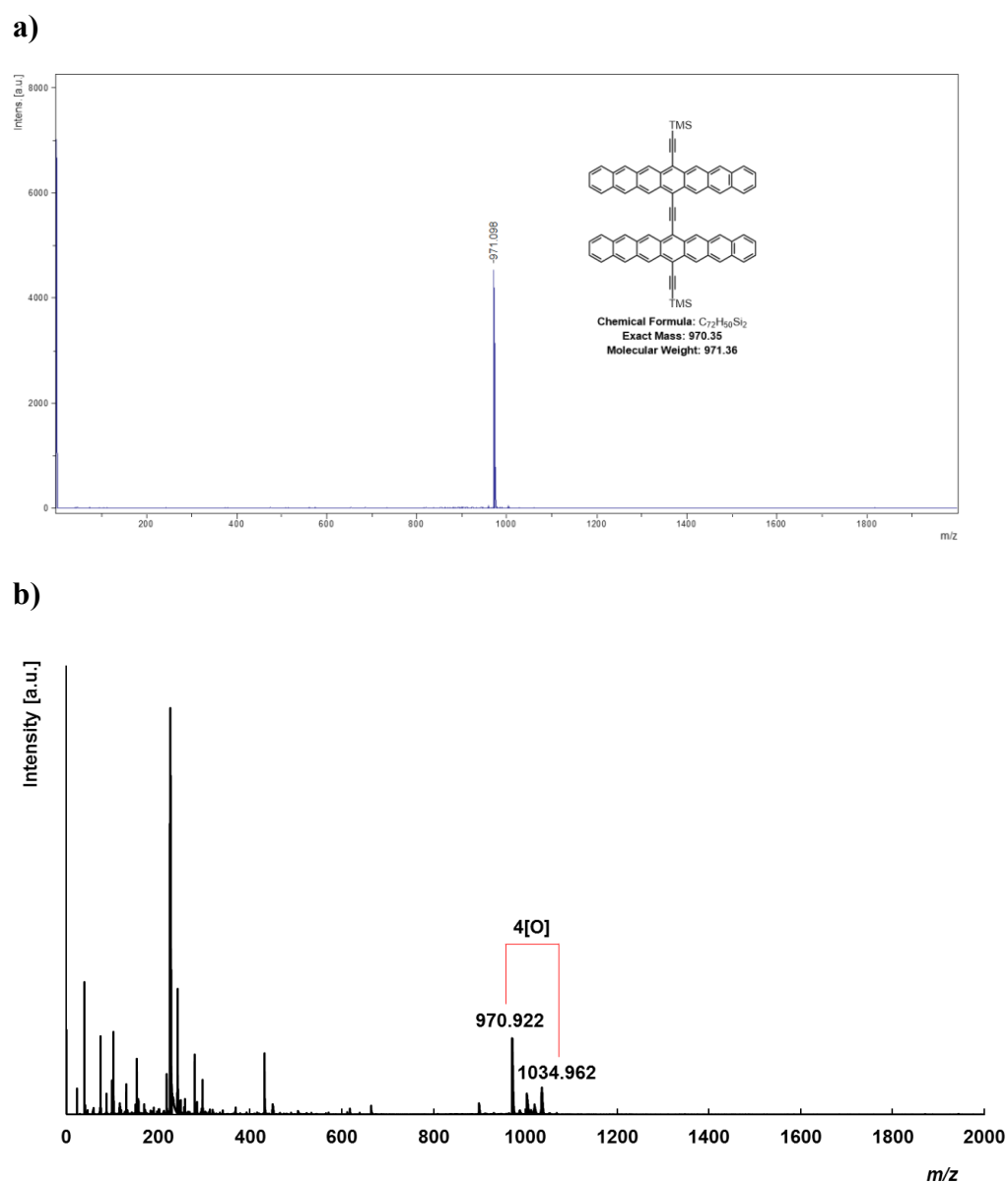


Figure 4-6. MS spectrum of TMSHeptD (a) immediately after reaction and (b) after 2 h.

a)

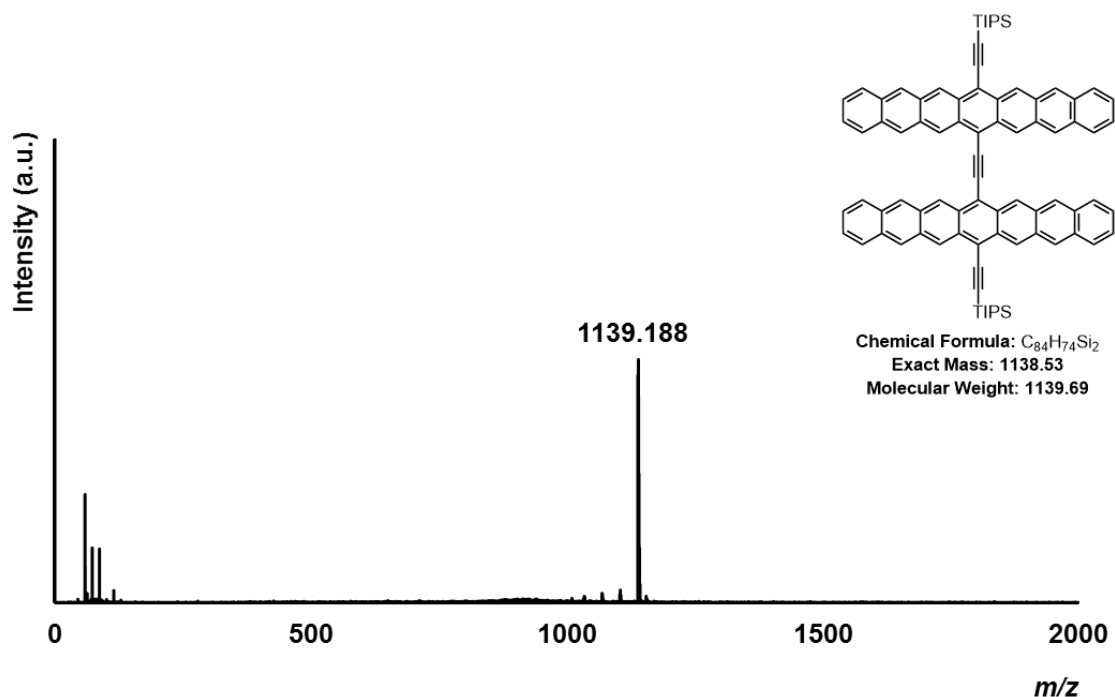


Figure 4-7. MS spectrum of TIPSHeptD immediately after reaction.

Subsequently, UV-vis absorption spectra and ¹H NMR were measured to prove the generation of **HeptD**. However, from ¹H NMR measurement, it was impossible to be identified because there was no signal at first, and then complexed peaks began to appear after a while. The UV-vis absorption spectra were measured for checking the stability of obtained product under the dark condition (Figure 4-8). It was found that the color of solution changed from pale pink to purple, and a small peak located around 940 nm disappeared in 30 minutes. This result implied the low stability of resulting species and the immediate decomposition after the reductive aromatization reaction.

The generation of ethynylene-bridged heptacene dimer seems to be difficult due to its low stability. However, this scheme is still a convenient approach towards heptacene dimer precursor compared with conventional several synthetic steps.

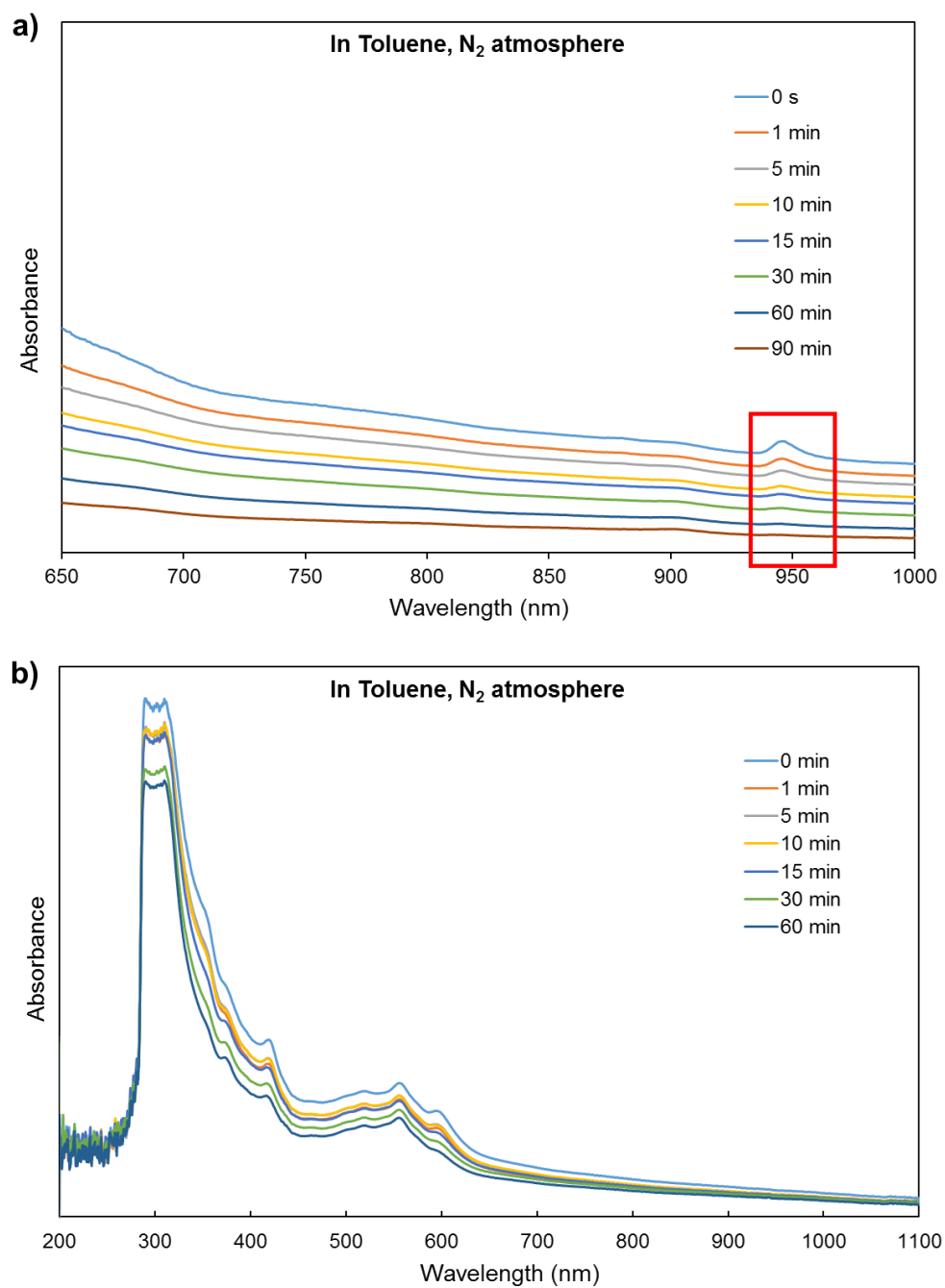


Figure 4-8. UV-vis absorption spectra in the regions of a) 650–1000 nm and b) 250–1000 nm.

4-4. Oligomerization of ethynylene-bridged BCODquinone

Although the introduction of methyl ether substituted group could stabilize **HeptD-OMe**, the stability of desired π -extended acene dimer is not good enough to be isolated. Therefore, “precursor approach” attracted my attention to prevent the limitations of solubility and stability in π -conjugated moiety. The precursor approach is an effective synthetic strategy to prepare π -extended aromatic compounds by using quantitatively conversion reaction from pure precursors to the target molecules *via* a retro-Diels Alder reaction or Strating Zwanenburg photodecarbonylation reaction.¹⁷ For example, the synthesis of directly 6,6'-linked bispentacenes from bicyclo[2.2.2]octadiene (BCOD) bispentacene precursors *via* the retro-Diels-Alder reaction demonstrated that introduction of BCOD substituted group would be a suitable approach to prepare ethynylene-bridged pentacene trimer (Figure 4-9).¹⁸

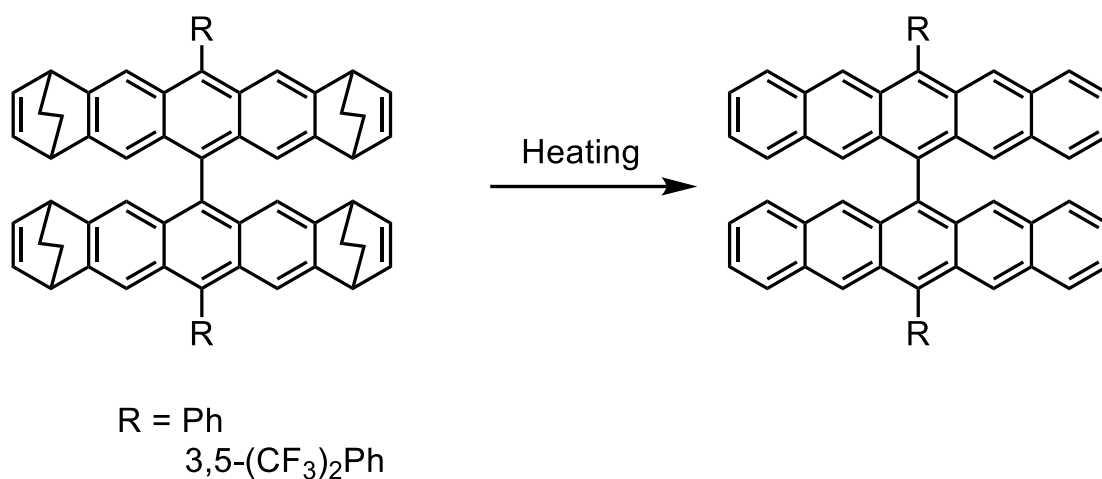
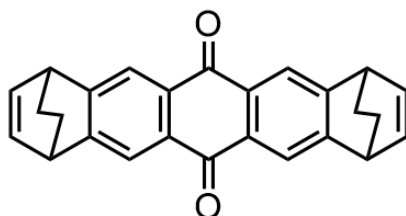


Figure 4-9. Thermal conversion of 6,6'-linked bispentacenes from BCOD bispentacene precursors.

Here, BCOD-pentacene quinone was used as a starting material to proceed the synthetic scheme (Figure 4-10).

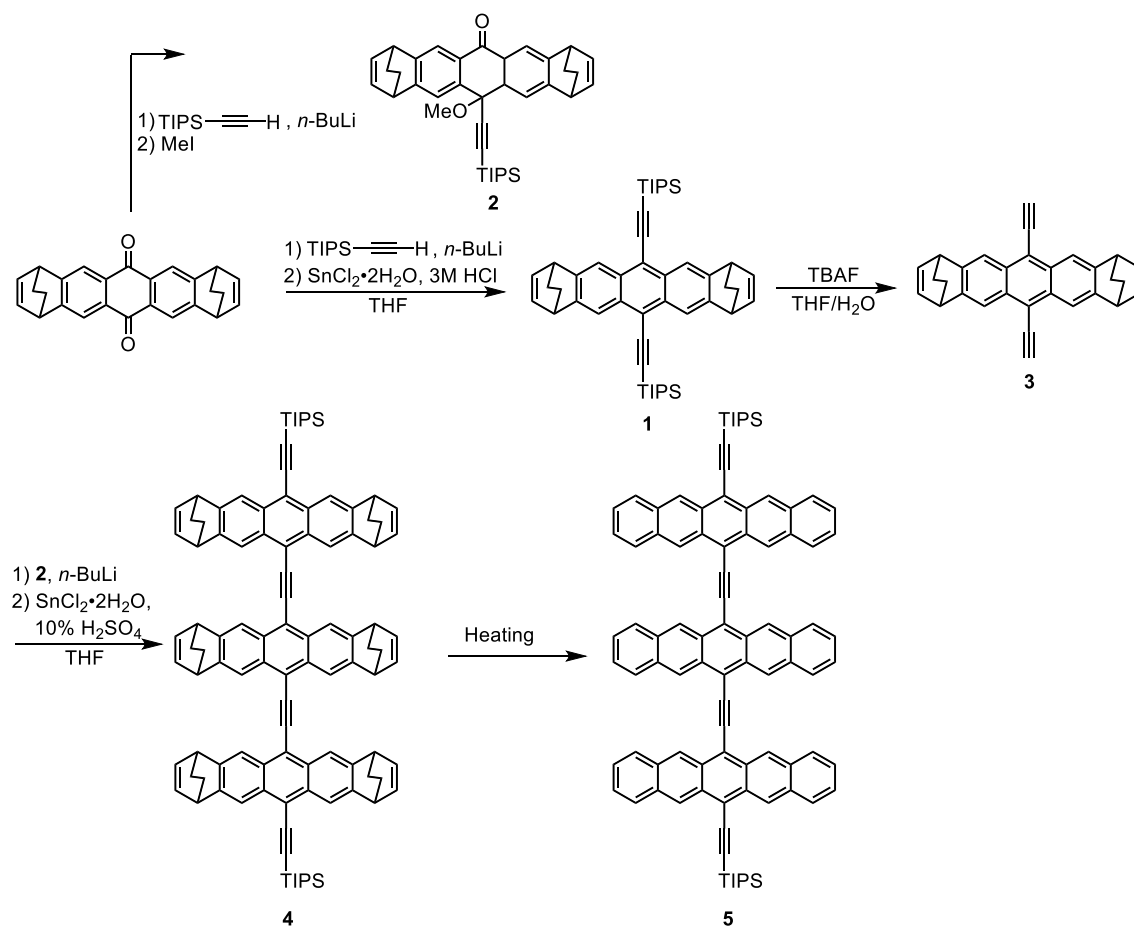


BCOD-pentacene quinone

Figure 4-10. The chemical structure of BCOD-pentacene quinone.

The proposed synthetic scheme is shown in the Scheme 4-3. Firstly, TIPSethynyl groups are introduced at the 6,13-positions of pentacene precursor by using standard conditions. The addition of lithiated TIPSethynylene to BCOD-pentacene quinone

followed by the trapping of the resulting intermediate with iodomethane would afford methyl ether substituted compound **2**. Then, the desilylation of monomer would generate compound **3**. Finally, the addition of terminal lithiated compound **3** to THF solution of compound **2** followed by the reductive aromatization was expected to afford BCOD ethynylene-bridged pentacene trimer.



Scheme 4-3. The proposed synthetic scheme of ethynylene-bridged pentacene trimer.

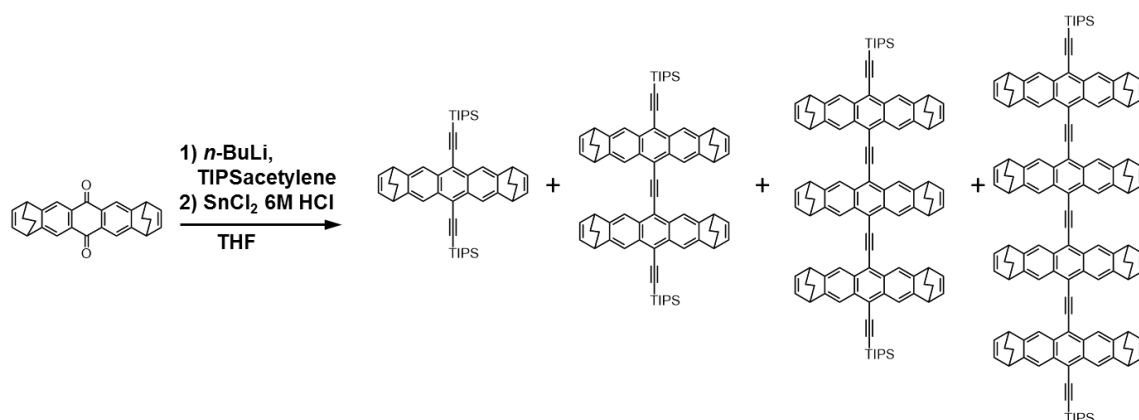
Surprisingly, the oligomerization of BCOD-pentacene was observed in the first step.

The reaction reagents are similar with previous research. However, in this case, not only dimer but also oligomers up to pentamer were detected by MS spectra.

Considering the mechanism of dimerization reaction, the plausible oligomerization of BCOD-pentacene quinone possibly went through the similar intermediates of dimerization reaction. In addition, probably due to the improved solubility and stability stemming from BCOD group, further intramolecular cyclization could occur during the reaction, resulting in the formation of longer chains as trimer, tetramer and pentamer.

Subsequently, the reaction condition was optimized by changing the reaction temperature, lithiated silylethynylene ratio and reaction time to investigate the effect on the yield of oligomers (Figure 4-11). The isolated products implied that the appropriate ratio of lithiated silylethynylene and reaction time were important for the oligomerization. Reaction time longer than 4 h resulted in the low yield of oligomers, which implied that intramolecular cyclization intermediate might generate in a quick reversible way. Then, the less amount of lithiated silylethynylene would result in the lower yield of BCOD oligomers. Among these conditions, the best yield of oligomers was obtained with a considerably excess amount of lithiated silylethynylene, keeping the reaction for 40 minutes. This condition gave 1mer (36%), 2mer (27%), 3mer (1%), 4mer (0.31%) and 5mer (trace) after purifying them by silica gel column followed with recrystallization with

DCM/MeOH.



Exp. No.	Temp. (°C)	TIPSacetylene (equiv.)	<i>n</i> -BuLi (equiv.)	Active time	Main Product Yield
e 425	0	4	3.3	120 min	Monomer, Dimer: trace
e436	0	6.3	5	40 min	Dimer: 8.8% Trimer: trace
e441	0	6.3	5.5	40 min	Monomer: 38.4%, dimer: 9.2%, trimer: 0.09%, tetramer: trace
YM190	-78	10	10	40 min	Monomer: 44%, dimer: 23%, trimer: 1%, tetramer: 0.31% pentamer: trace
NM	-78	10	10	4h	Monomer: 70%, dimer: x%, trimer: x%, tetramer: x%
NM	-78	10	10	8h	Monomer: 91%, dimer: x%, trimer: x%, tetramer: x%
NM	-78	10	6	4h	Monomer: 20%, dimer: x%, trimer: x%, tetramer: x% pentamer: trace

Figure 4-11. Optimization of BCODquinone. X means the isolation haven't been done.

4-5. Thermal conversion reaction of BCOD oligomers

The thermal conversion of BCOD pentacene precursor oligomers to pentacene

oligomers were primarily screening with thermogravimetric analysis (TGA) (Figure 4-12).

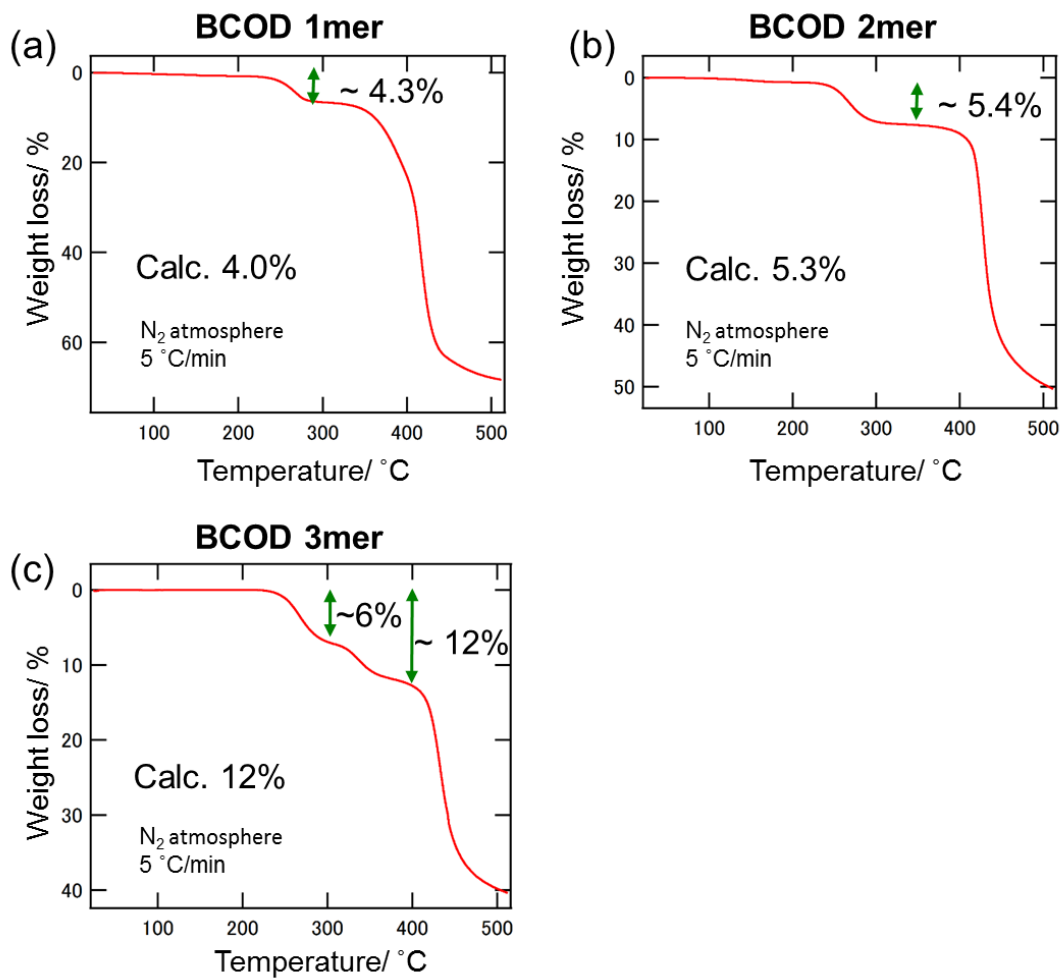
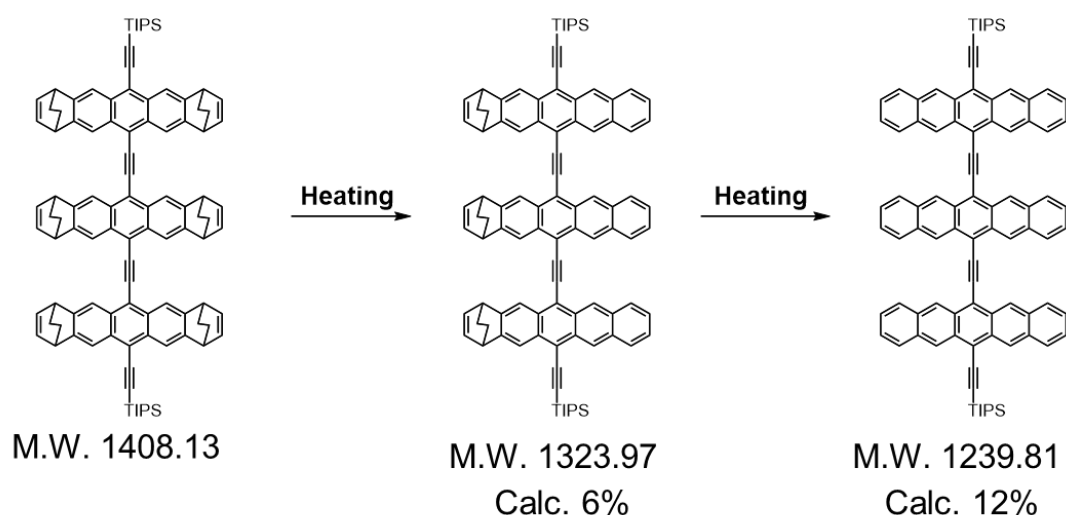


Figure 4-12. TGA analysis of BCOD pentacene oligomers (monomer to trimer) under the N_2 atmosphere, $5\text{ }^\circ\text{C}/\text{min}$.

TG analysis indicated weight loss of **BCOD 1mer** and **BCOD 2mer** below $400\text{ }^\circ\text{C}$. In the case of **BCOD 1mer**, the retro-Diels-Alder reaction started at around $247\text{ }^\circ\text{C}$ and ended at around $282\text{ }^\circ\text{C}$. For **BCOD 2mer**, the thermal conversion reaction started at

around 260 °C and ended at around 302 °C. These weight losses can be attributed to be cleaving of only one ethylene molecule from the precursor. On the other hand, the TGA showed that **BCOD 3mer** showed stepwise elimination of ethylene molecules. As shown in the Figure 4-13, the first step of weight loss is about 6% which can be attributed to the calculated value for the intermediate possessing three BCOD groups (the figure 4-13 just shows the representative structure). Subsequently, the further elimination of ethylene molecules leads to the weight loss of about 12%. This experimental weight loss is good agreement with the calculated values of ethynylene-bridged pentacene trimer, which indicated the **BCOD 3mer** would be converted to the desired pentacene trimer *via* thermal conversion reaction.



Additionally, the characterization of thermally converted ethynylene-bridged pentacene monomer and dimer were performed by checking the changing of UV-vis absorption spectrum of the films and ^1H NMR. The thermal conversion reaction of **BCOD 1mer** (Figure 4-14) and **2mer** (Figure 4-15) were performed in the vacuum condition and hot plate in glovebox. However, after heating, broad peaks were observed. In addition, the thermally converted products were hardly soluble in the organic reagent such as chloroform and toluene, preventing ^1H NMR measurements. Considering the MALDI TOF mass spectrum of thermally converted products (Figure 4-16), BCOD oligomers could not be completely thermally converted to the corresponding acene oligomers. It seemed that the compounds were converted to unknown byproducts *via* partially thermally-converted products under high temperature.¹⁶

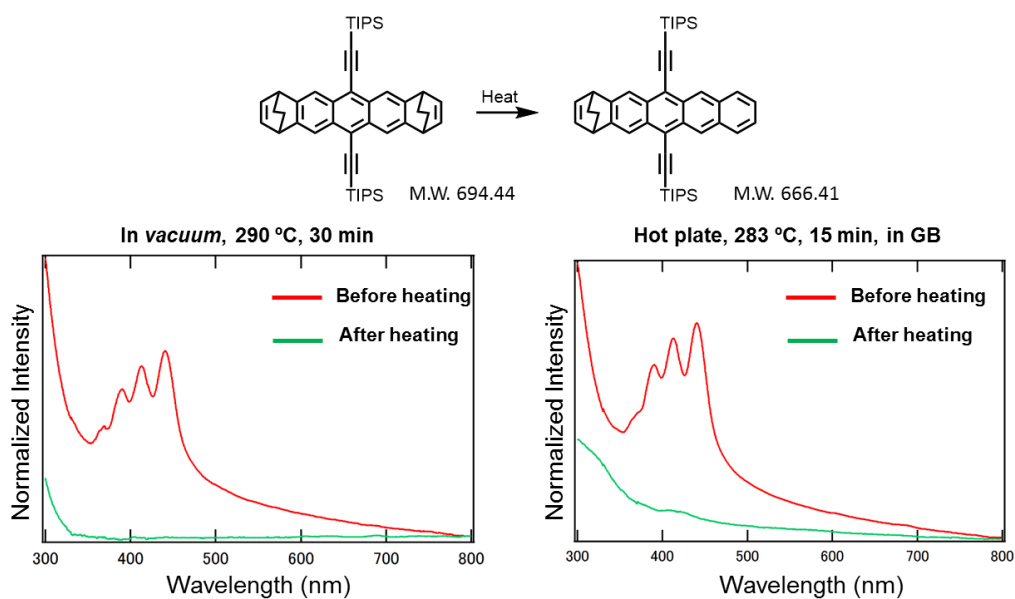


Figure 4-14. UV-vis absorption spectra in the solid state (drop casting of **BCOD 1mer** 1 mg in 1 ml toluene solution)

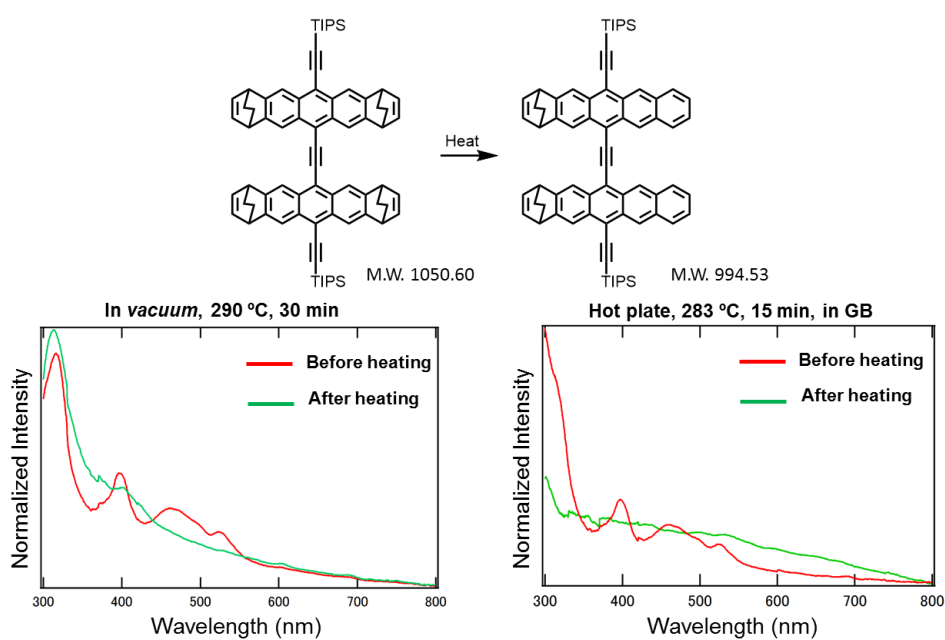


Figure 4-15. UV-vis absorption spectra in the solid state (drop casting of **BCOD 2mer** 1 mg in 1 ml toluene solution).

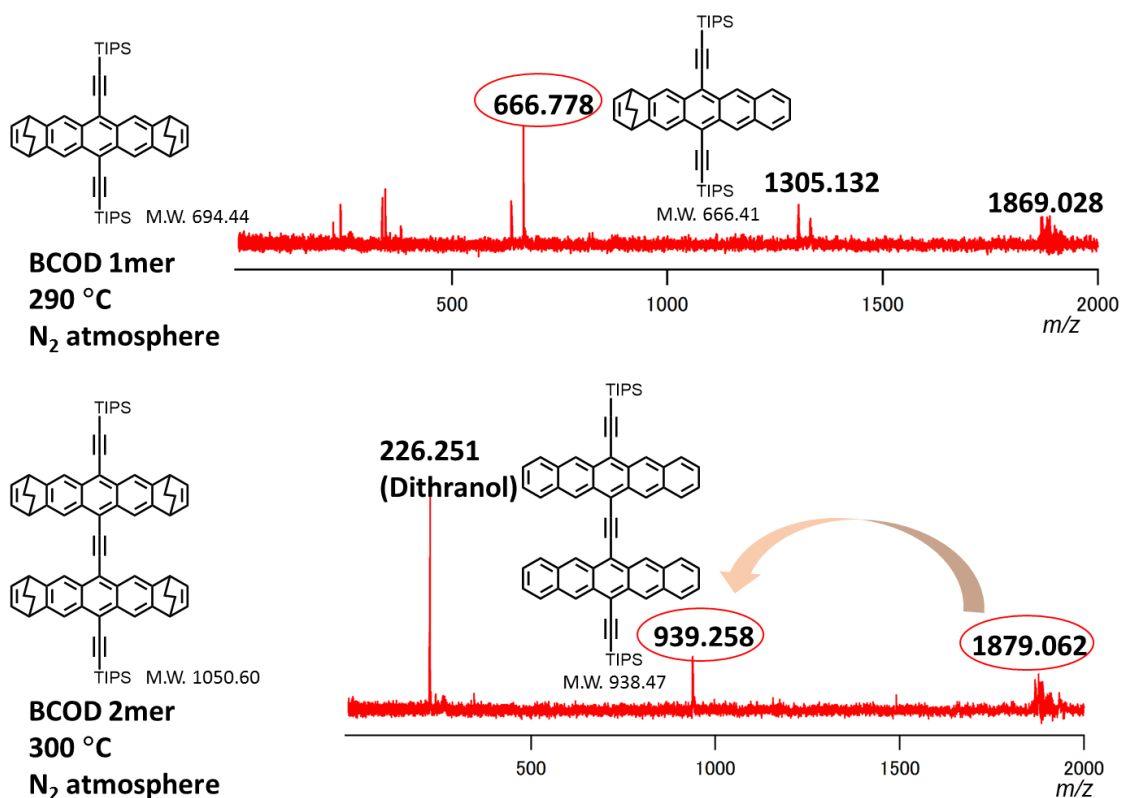


Figure 4-16. MALDI TOF mass spectrum of thermal converted products.

4-7. Summary and outlook

In this chapter, the synthesis of ethynylene-bridged π -extended acene oligomers was studied. A precursor of ethynylene-bridged heptacene dimer was successfully synthesized from heptacene quinone in one pot, skipping the conventional stepwise protection/deprotection approach. Interestingly, the reaction with lithiated triisopropylsilylethynylene and BCODquinone followed by the reductive aromatization afforded oligomers of ethynylene-bridged pentacene precursor. This discovery provides a great clue to the effective synthetic approach of ethynylene-bridged π -conjugated

systems. The study of oligomerization of BCO Dquinone showed the convenient approach towards π -extended aromatic conjugation system by using conventional alkynyl lithium reagents.

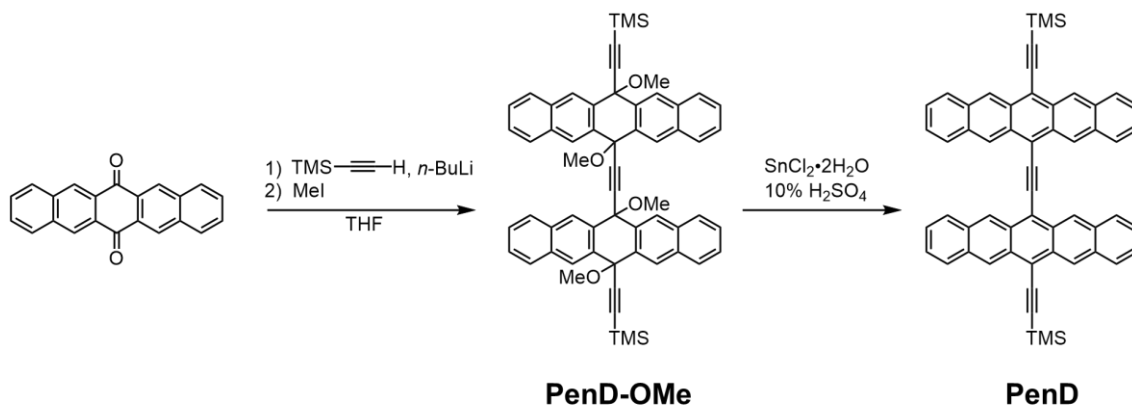
4-8. Experimental section

4-8-1. General: Materials and methods

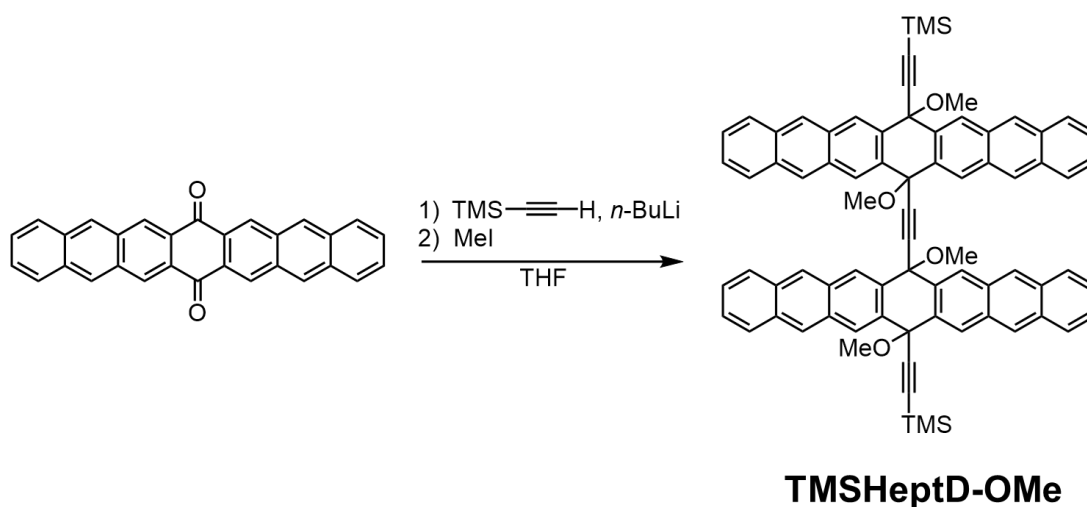
Reagents for synthesis were purchased from Wako, Nacalai Tesque, and Sigma Aldrich, and were reagent-grade quality, obtained commercially, and used without further purification. For spectral measurements, spectral-grade solvents were purchased from Nacalai Tesque. Unless stated otherwise, column chromatography was carried out on silica gel 60N (Kanto Chemical, 40–50 μm). Analytical thin-layer chromatography (TLC) was performed on Art. 5554 (Merck, KGaA). ^1H NMR (500 MHz and 600 MHz) and ^{13}C NMR (100 Hz, 126 Hz, and 150 MHz) spectra were recorded (as indicated) with JEOL JNM-ECX 400 P, JEOL JNM-ECX 500, and JEOL JNM-ECX 600 spectrometer at ambient temperature by using tetramethylsilane as an internal standard. High resolution MS was performed on a matrix-assisted laser desorption ionization–time of flight mass spectrometry (MALDI-TOF-MS) (Bruker Autoflex II). X-ray crystallographic data for **HeptD-OMe**, **Hept1** and **Hept2** were recorded at 103 K on a Rigaku R-AXIS RAPID/S

using Mo-K α radiation. The structures were solved by direct method (SHELXS-97) and refined with the SHELXS-97 program. Thermogravimetric analysis was carried out on a DSC7000X/STA7200 instrument (Hitachi) under nitrogen gas flow at a heating rate of 5 °C min⁻¹.

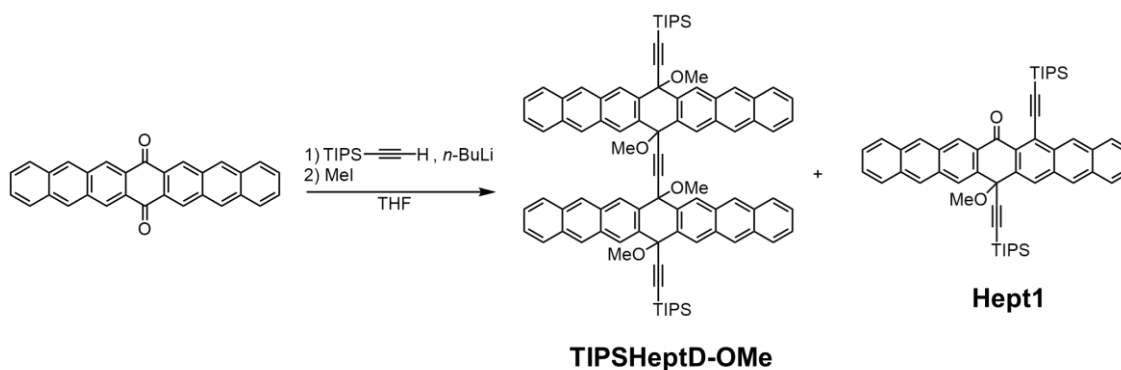
4-8-2. Synthetic procedures

Synthesis–PenD-OMe:

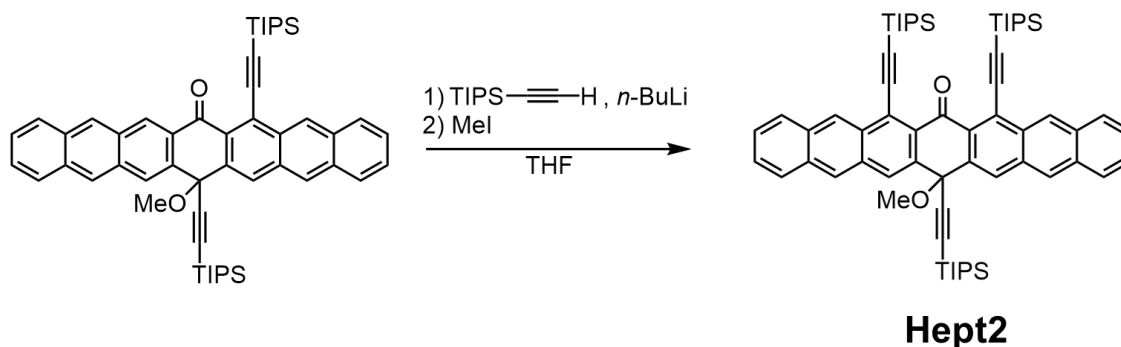
n-Butyllithium (1.6 M in hexanes, 1.5 mL, 2.4 mmol) was added to a solution of TMSethynylene (0.4 mL, 287 mg, 2.9 mmol) in dry THF (8 mL) at 0 °C. This solution was stirred for 14 min before being transferred into a solution of 6,13-pentacenequinone (300 mg, 0.98 mmol) in dry THF (8 mL) cooled to 0 °C. The reaction mixture was allowed to warm to RT and stir for 3 h before adding dropwise MeI (0.6 mL, 1.4 g, 9.7 mmol) over a period of 7 min. The reaction was stirred for 19 h at RT before cooling to –15 °C and pouring the mixture into satd. aq. NH₄Cl (5 mL). Then, the mixture was diluted with DCM (300 mL). The combined organic phase was washed with water, brine, dried over Na₂SO₄, and then the solvent was removed in vacuo. Purification with silica gel column chromatography (CH₂Cl₂/hexanes) afforded dimer and then followed with reprecipitation (DCM/MeOH) to obtain PenD-OMe (55 mg, 0.06 mmol, 13%) as a green solid.

Synthesis–TMSHept-OMe:

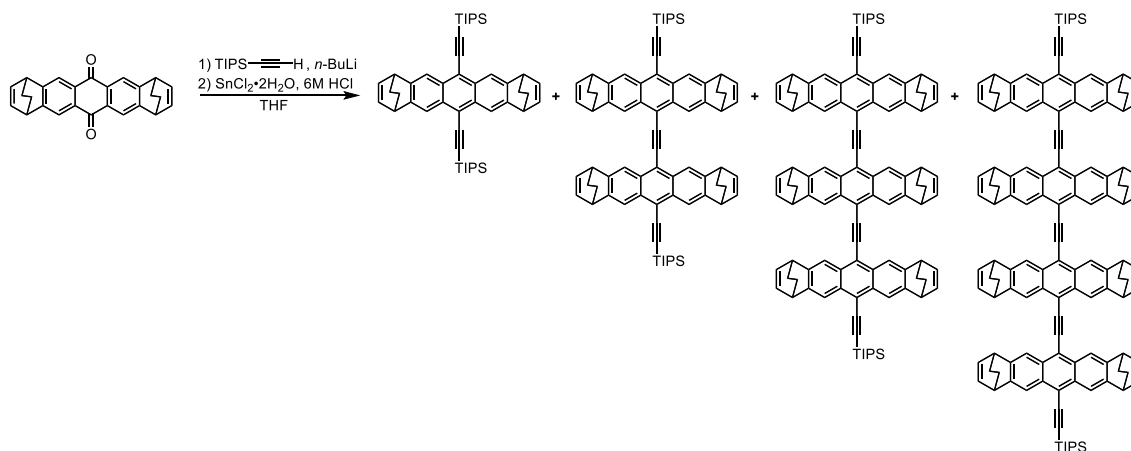
n-Butyllithium (1.6 M in hexanes, 1.6 mL, 2.5 mmol) was added to a solution of TMSethynylene (0.42 mL, 290 mg, 3 mmol) in dry THF (10 mL) at 0 °C. This solution was stirred for 15 min before being transferred into a solution of 7, 16-heptacenequinone (408 mg, 1 mmol) in dry THF (10 mL) cooled to 0 °C. The reaction mixture was allowed to warm to RT and stir for 3 h before adding dropwise MeI (0.65 mL, 1.5 g, 10.4 mmol) over a period of 4 min. The reaction was stirred for 24 h at RT before cooling to –15 °C and pouring the mixture into satd. aq. NH₄Cl (4 mL). Then, the mixture was diluted with DCM (1.2 L). The combined organic phase was washed with water, brine, dried over Na₂SO₄, and then the solvent was removed in vacuo. Purification with silica gel column chromatography (CH₂Cl₂/hexanes = 2/1) afforded TMSHeptD-OMe (66.3 mg, 0.06 mmol, 12%) as a pale yellow solid.

Synthesis–TIPSHeptD-OMe, Hept1:

n-BuLi (1.6 M in hexane, 3.4 ml, 5.4 mmol) was added to a solution of TIPSEthynylene (1.5 ml, 6.5 mmol) in dry THF (20 mL) at 0 °C. This solution was stirred for 40 min at 0 °C and then warmed to RT keeping stir for 70 min before being transferred into a solution of 7,16-heptacenequinone (660 mg, 1.6 mmol) in dry THF (40 mL) cooled to 0 °C. The reaction mixture was allowed to warm to RT and stir for 3 h before adding dropwise MeI (2 mL, 32.4 mmol) over a period of 5 min. The reaction was stirred for 17 h at RT before cooling to –15 °C and adding satd. aq. NH₄Cl (4 mL) to quench. The mixture was extracted with CH₂Cl₂ (1.5 L). The combined organic phase was washed with water, brine, dried over Na₂SO₄, and then the solvent was removed in vacuo. Purification with column chromatography (2:1 CH₂Cl₂/hexanes) afforded the mixture of TIPSHeptD-OMe and Hept1, then GPC separation successfully gave TIPSHeptD-OMe as a yellow solid (71 mg, 0.056 mmol, 7%), Hept1 as a yellow solid (130 mg, 0.16 mmol, 10%).

Synthesis–Hept2:

n-BuLi (1.6 M in hexane, 0.06 ml, 0.1 mmol) was added to a solution of TIPSethynylene (0.025 ml, 21 mg, 0.114 mmol) in dry THF (6 ml) at $-5\text{ }^{\circ}\text{C}$. The solution was stirred for 30 min at $-5\text{ }^{\circ}\text{C}$, and then warmed to r.t., and the solution was kept stirred for 60 min. To a suspension of Hept1 (30 mg, 0.04 mmol) in THF (10 ml) was added the prepared lithium reagent at RT. The mixture was stirred for 22 h. The reaction was monitored with TLC, however, the reactant was still remained a lot. Then the excessive lithium reagent was prepared again (*n*-BuLi, 1.6 M in hexane, 0.5 ml, 0.75 mmol; TIPSacetylene, 0.18 ml, 0.82 mmol) followed by adding in the reaction mixture and stirred for another 20 h. The mixture was extracted with DCM (300 mL). The combined organic phase was washed with water, brine, dried over Na_2SO_4 , and then the solvent was removed in vacuo. Purification with column chromatography (1:1 CH_2Cl_2 /hexanes) afforded the Hept2 (15 mg, 0.016 mmol, 42%) as an orange solid, starting material (18 mg, 60%) as a yellow solid.

Synthesis–BCOD oligomer:

n-BuLi (1.64 M in hexane, 5 ml, 8 mmol) was added to a solution of TIPSethynylene (2 ml, 8.9 mmol) in dry THF (ml) at 0 °C. The solution was stirred for 40 min at 0 °C. To a suspension of BCOD-pentacenequinone (516 mg, 1.4 mmol) in THF (170 ml) was added the prepared lithium reagent at r.t. The reaction was stirred for 9 h at rt. Then the mixture was added saturated SnCl₂ aqueous solution of 3 M HCl (4.8 ml) and stirred for 10 h. The mixture was extracted with CH₂Cl₂ (800 ml). The combined organic phase was washed with water, satd. aq. NaCl (100 mL), dried (Na₂SO₄), and the solvent was removed *in vacuo*. Purification with flash column chromatography (silica gel, CH₂Cl₂: hexane = 1 : 1, -> CH₂Cl₂: hexane = 1 : 9, -> CH₂Cl₂: hexane = 1 : 10) to obtain monomer as a yellow solid (373.3 mg, 38.4%), dimer as a deep red solid (68 mg, 9.2%), trimer as a purple solid (0.6 mg, 0.00043 mmol, 0.09%), tetramer as a purple solid (0.6 mg, 0.00043 mmol, 0.09%), pentamer can be detected from MALDI mass spectrum.

4-8-3. NMR spectrum

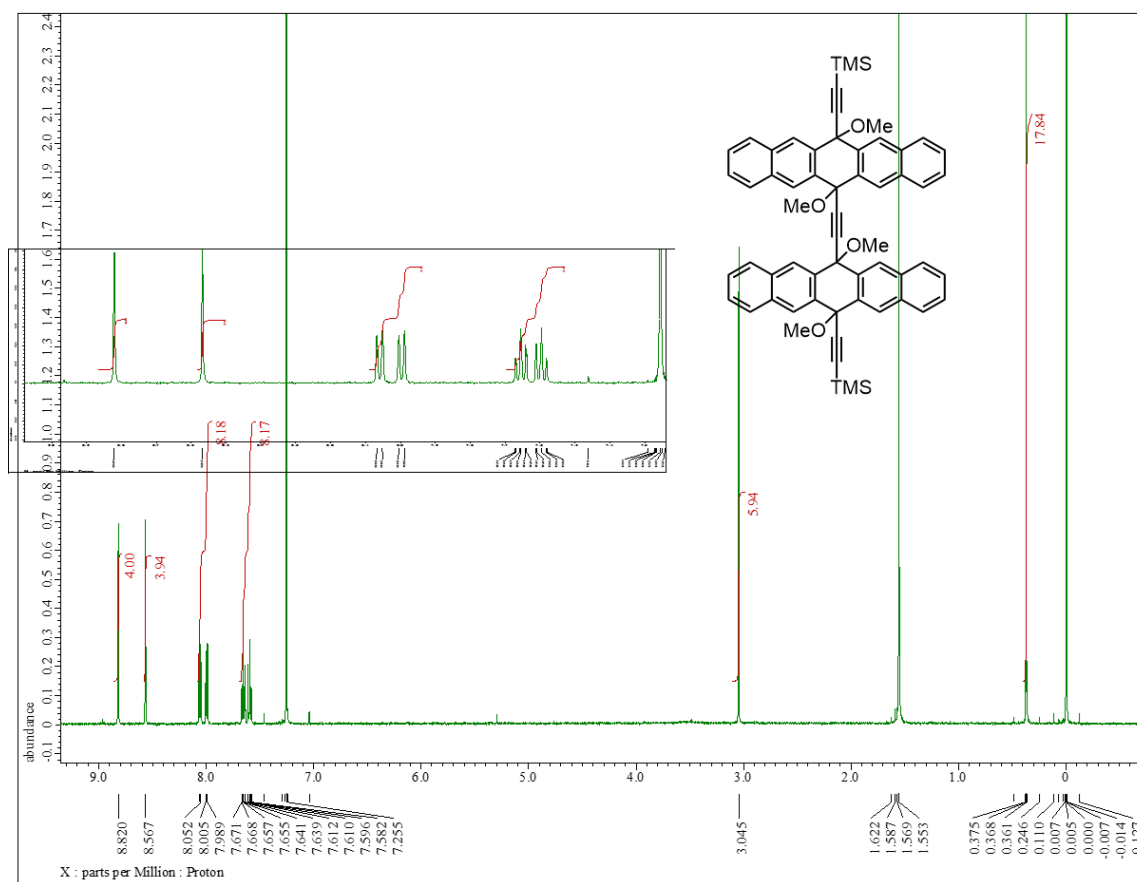


Figure S1. ^1H spectrum of PenD-OMe. (CDCl_3 , 500MHz)

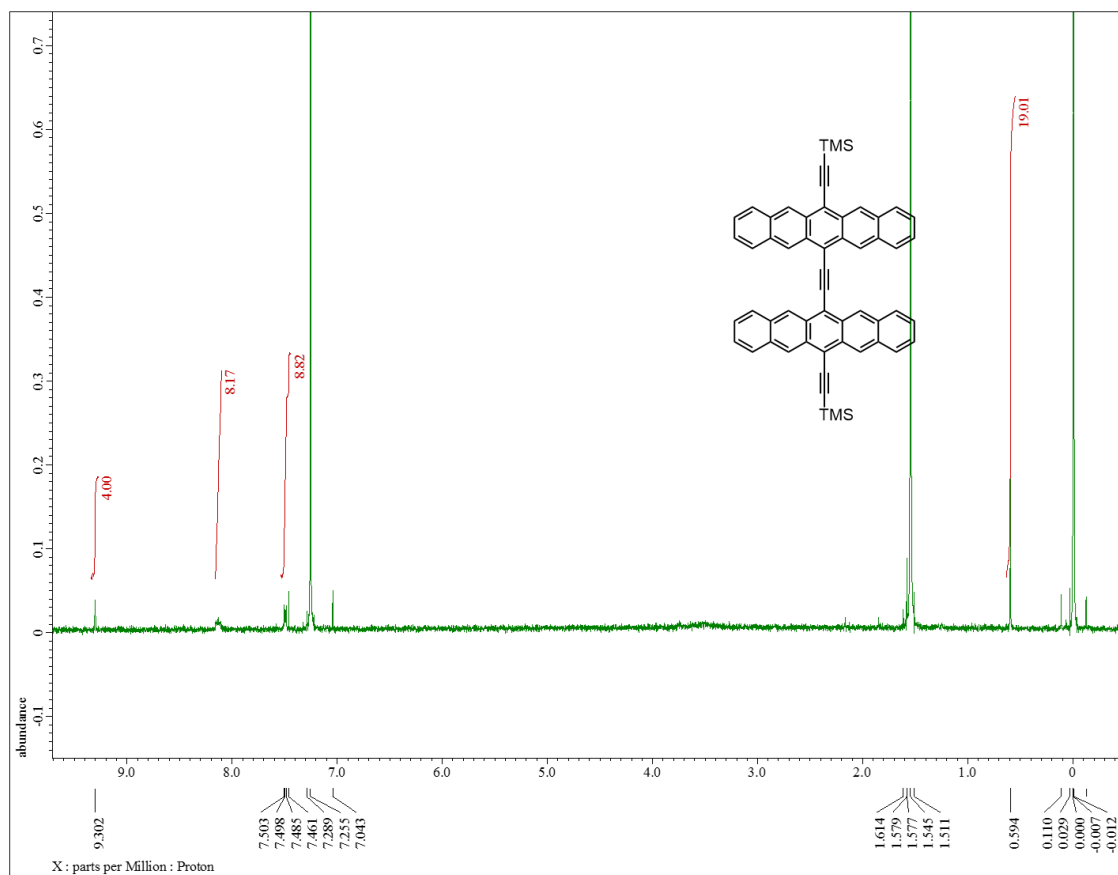


Figure S2. ^1H spectrum of TMSPenD. (CDCl_3 , 500MHz)

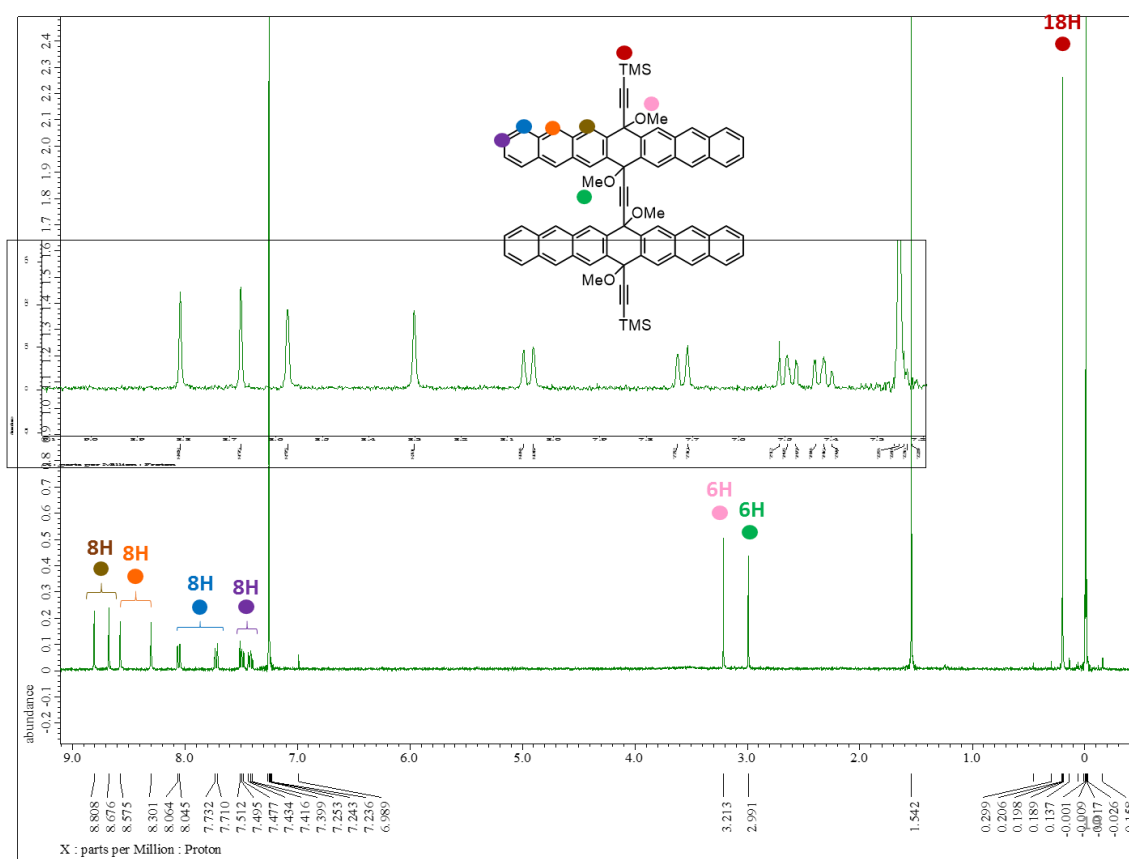


Figure S3. ^1H spectrum of TMSHeptD-OMe. (CDCl_3 , 500MHz)

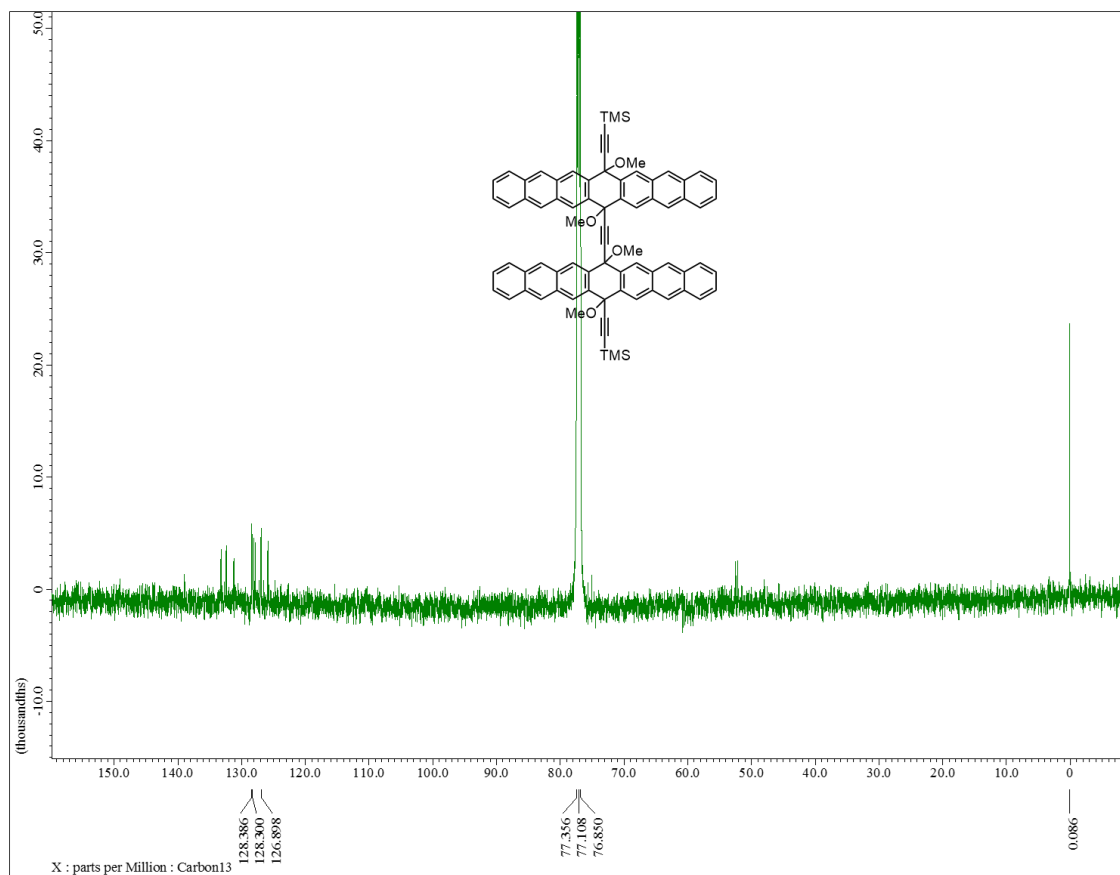


Figure S4. ^{13}C spectrum of TMSHeptD-OMe. (CDCl_3 , 500MHz)

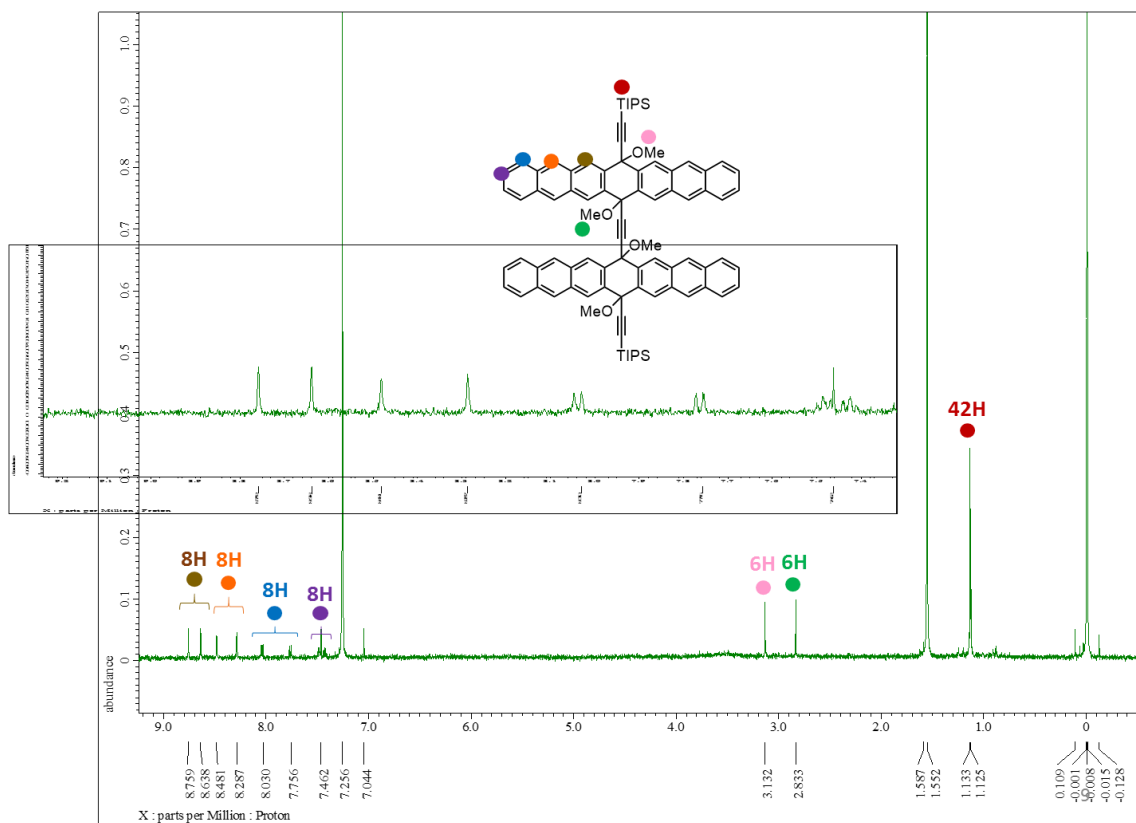


Figure S5. ^1H spectrum of TIPSheptD-OMe. (CDCl_3 , 500MHz)

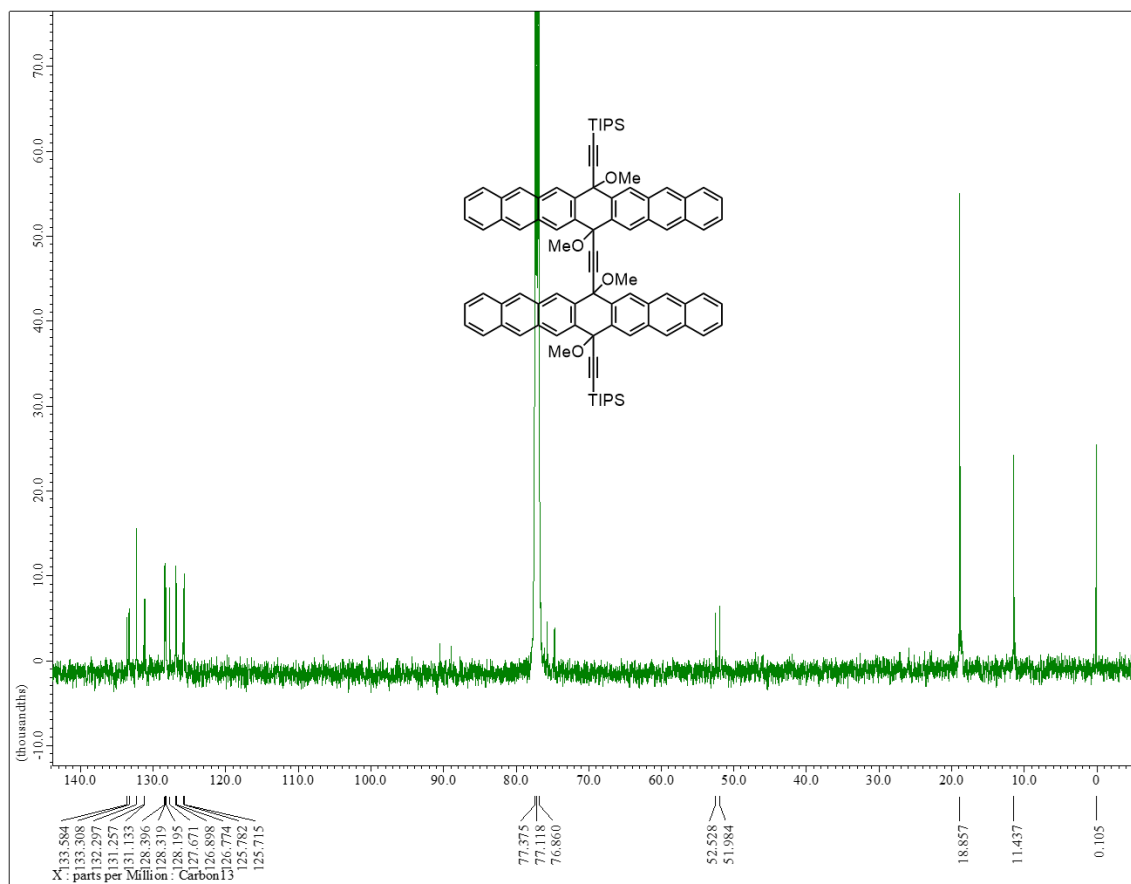


Figure S6. ^{13}C spectrum of TIPSHeptD-OMe. (CDCl_3 , 500MHz)

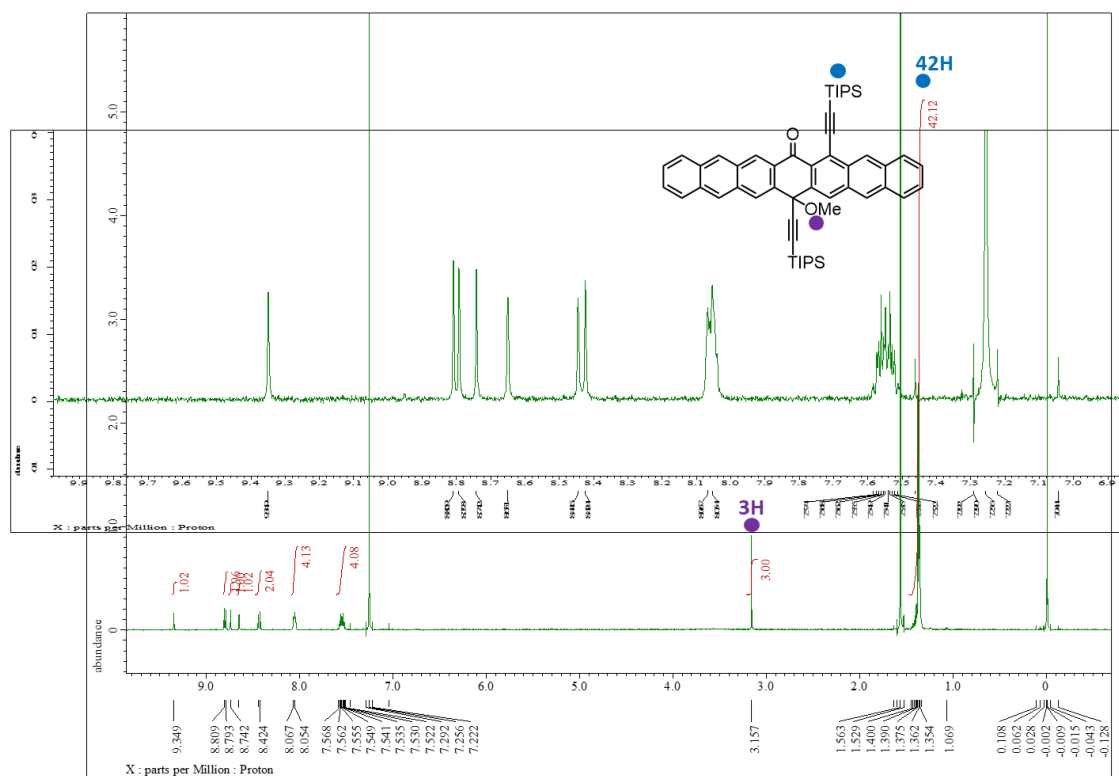
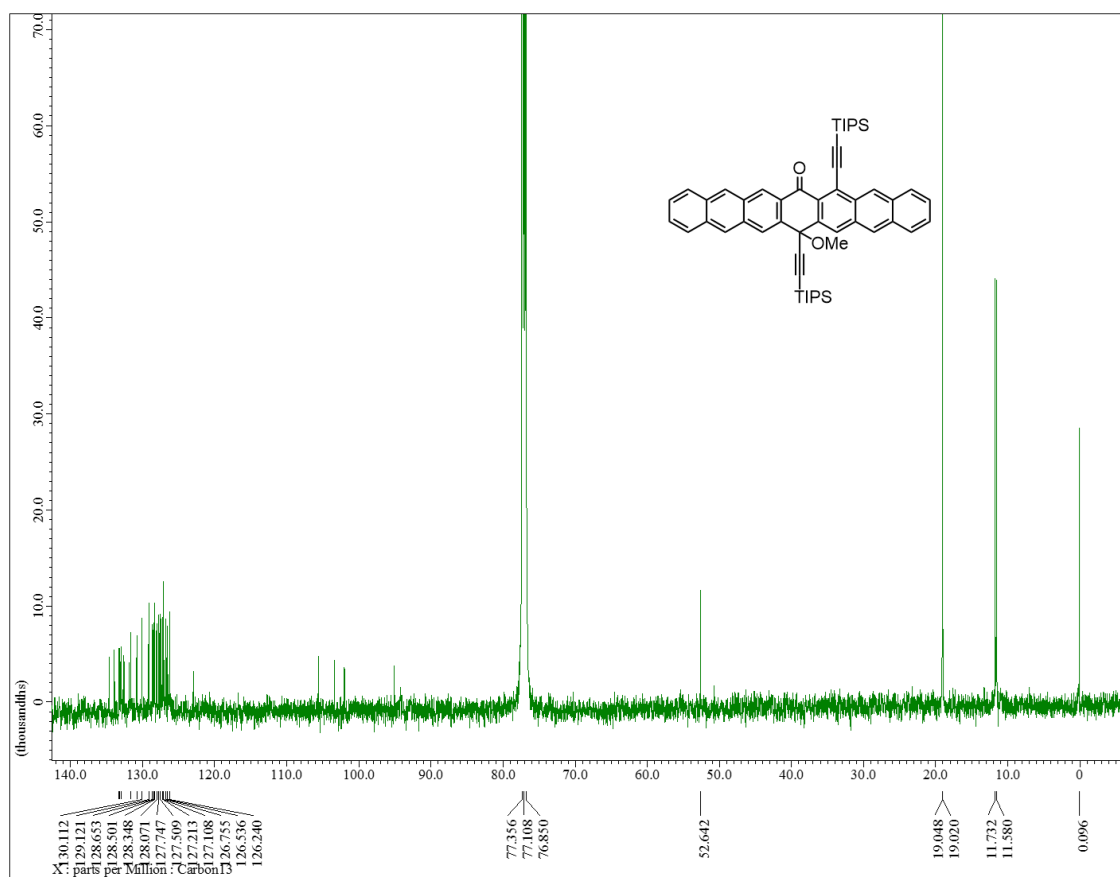


Figure S7. ^1H spectrum of Hept1. (CDCl_3 , 500MHz)



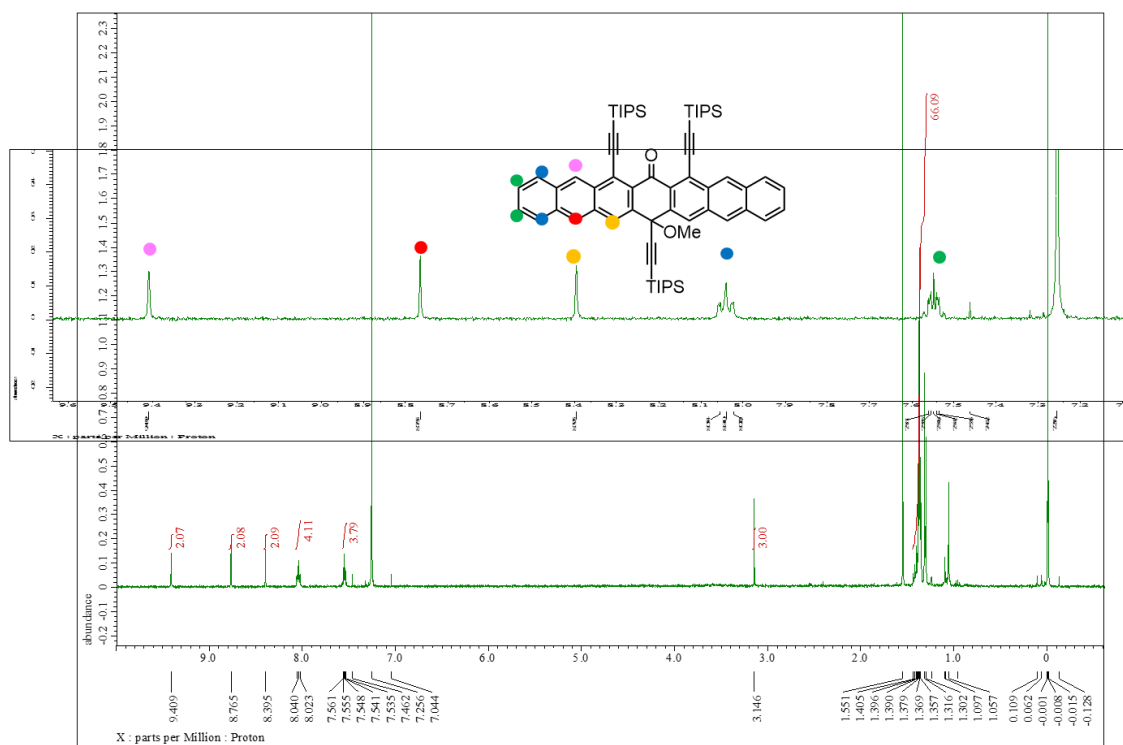


Figure S9. ^1H spectrum of Hept2. (CDCl_3 , 500MHz)

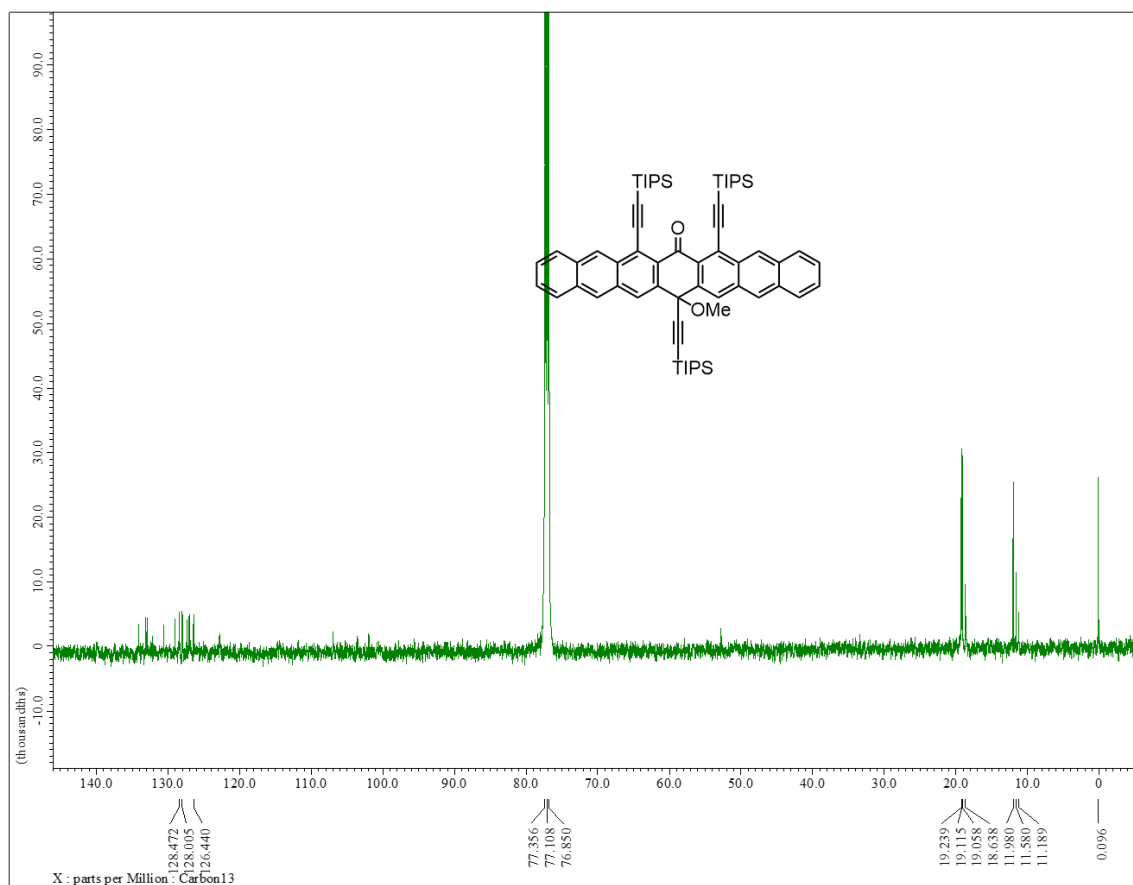


Figure S10. ^{13}C spectrum of **Hept2**. (CDCl₃, 500MHz)

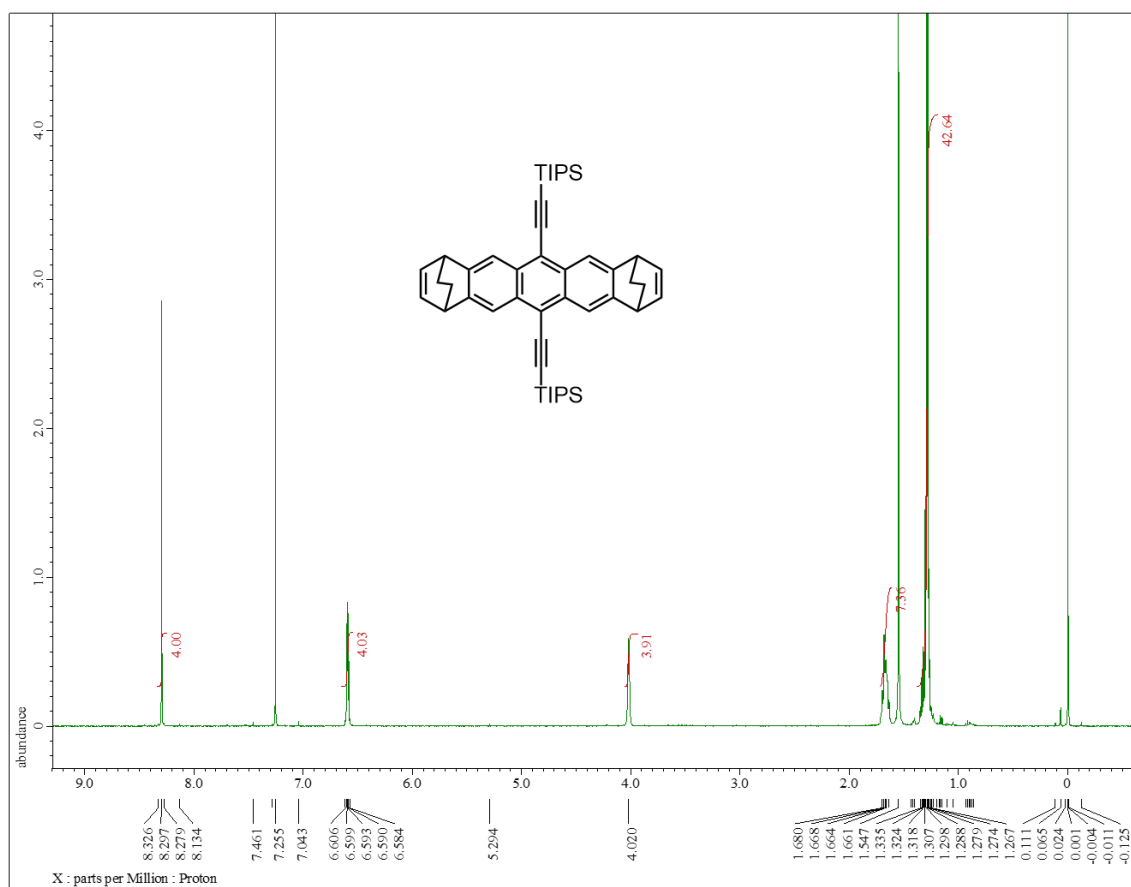


Figure S11. ^1H spectrum of BCOD 1mer. (CDCl_3 , 500MHz)

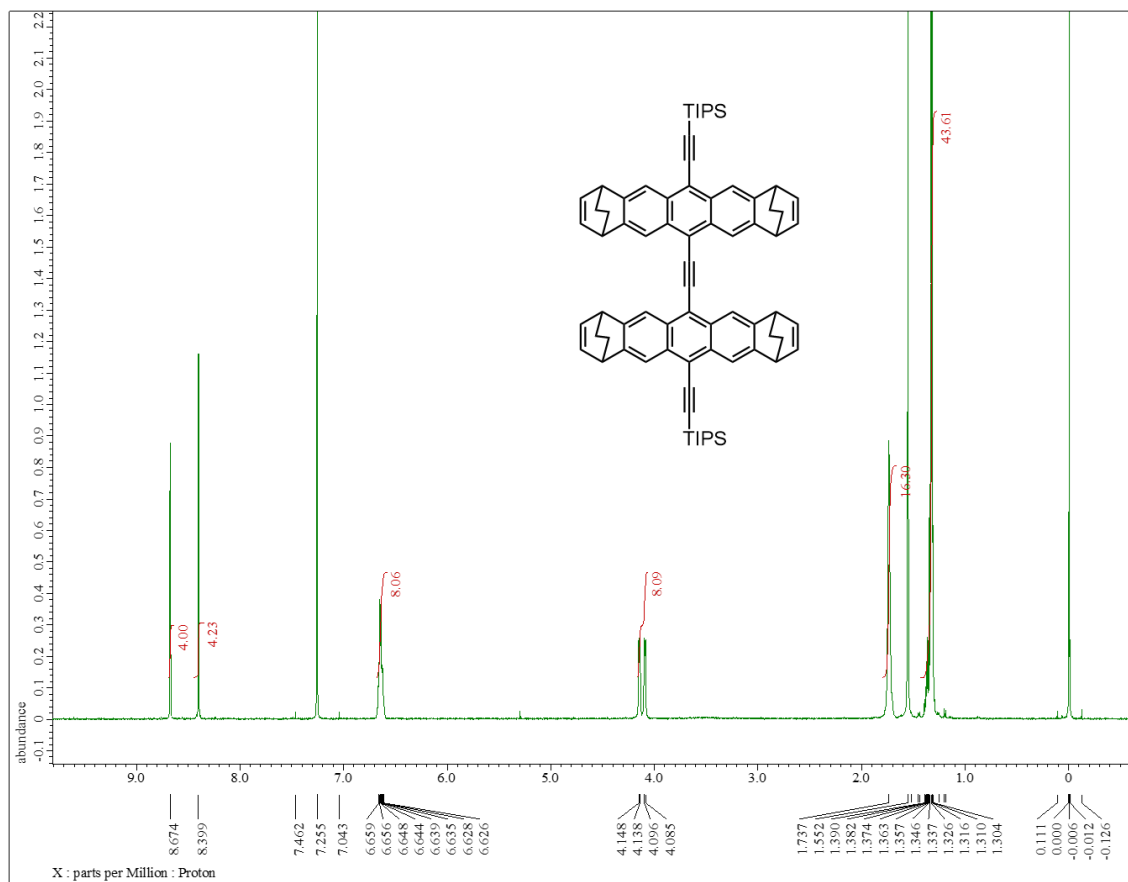


Figure S12. ^1H spectrum of BCOD 2mer. (CDCl₃, 500MHz)

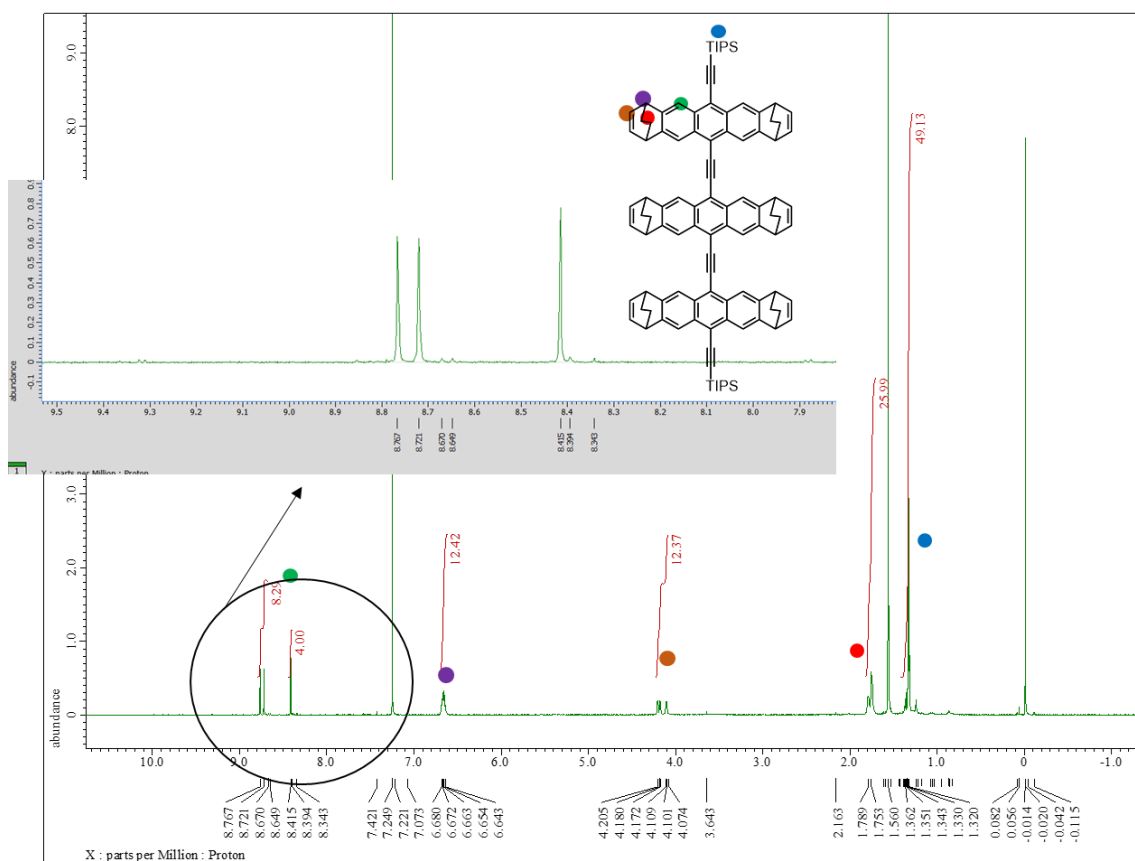
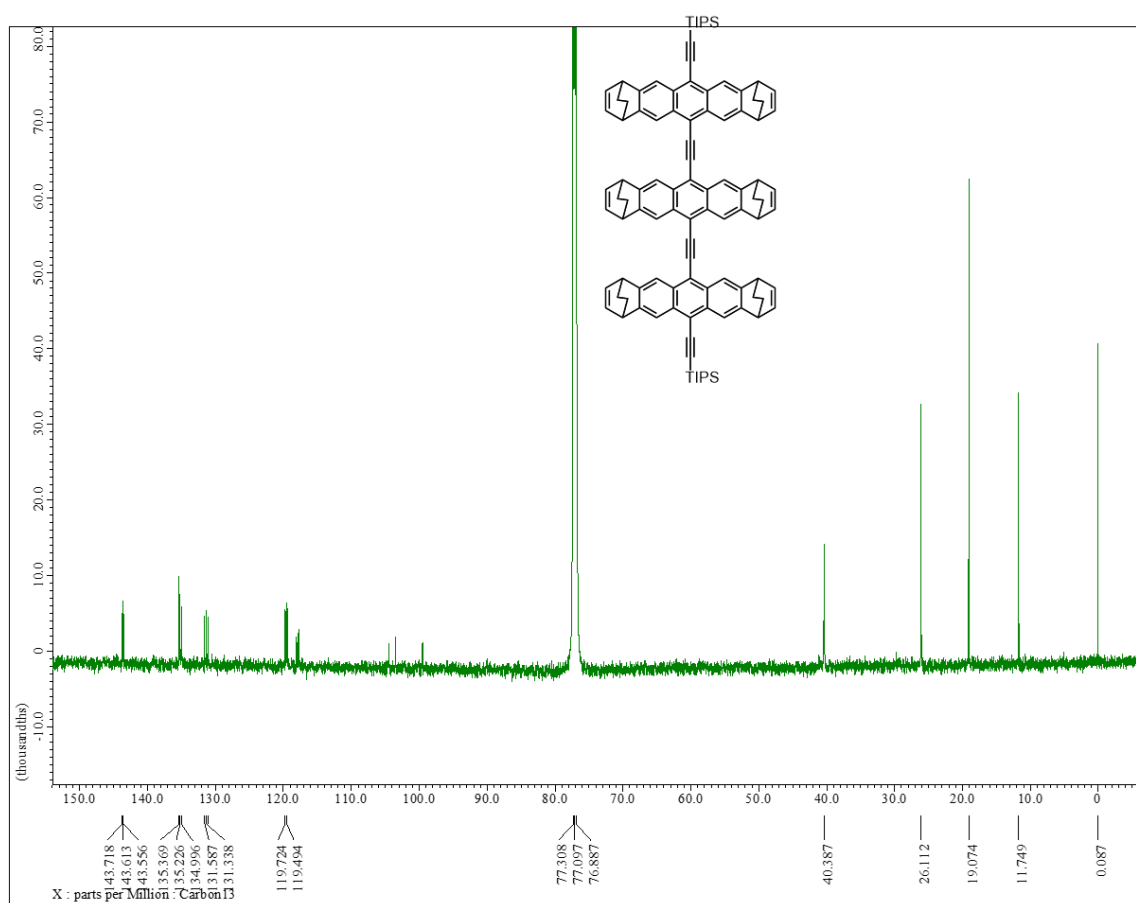


Figure S14. ^1H spectrum of BCOD 3mer. (CDCl_3 , 600MHz)



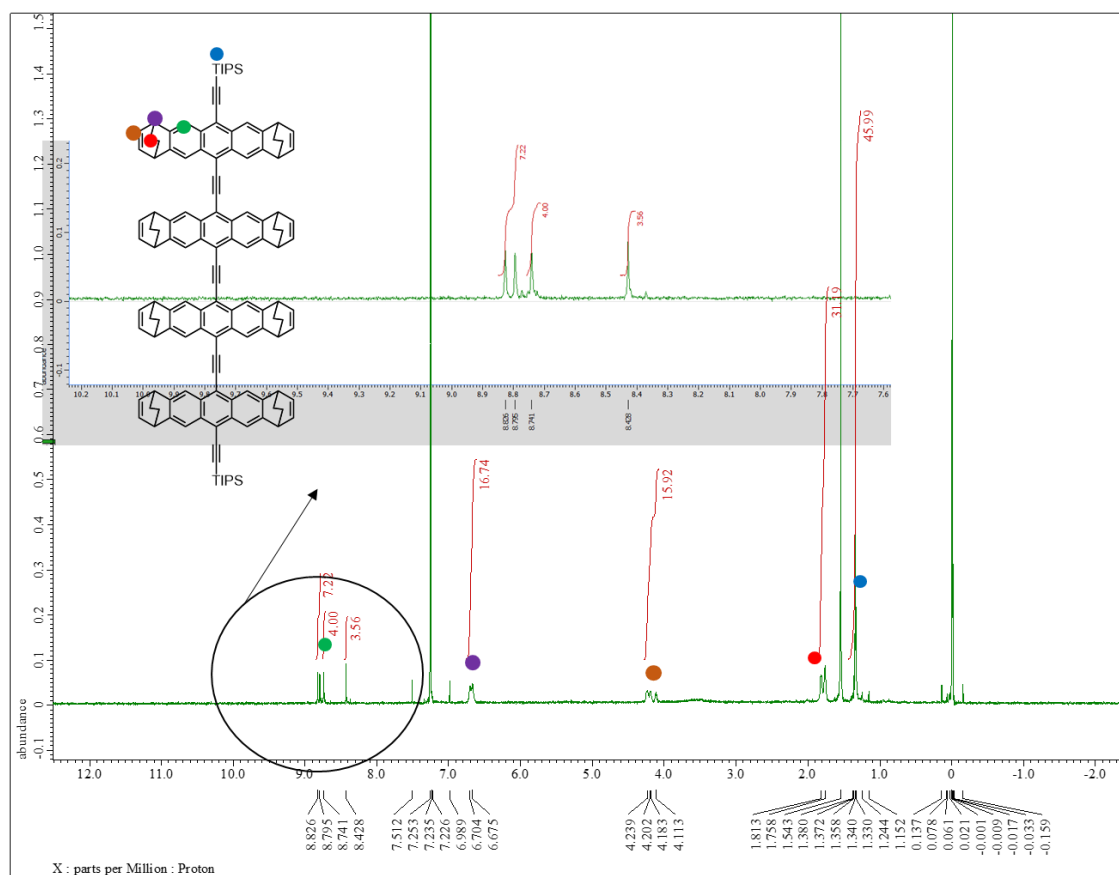


Figure S16. ^1H spectrum of BCOD 4mer. (CDCl_3 , 600MHz)

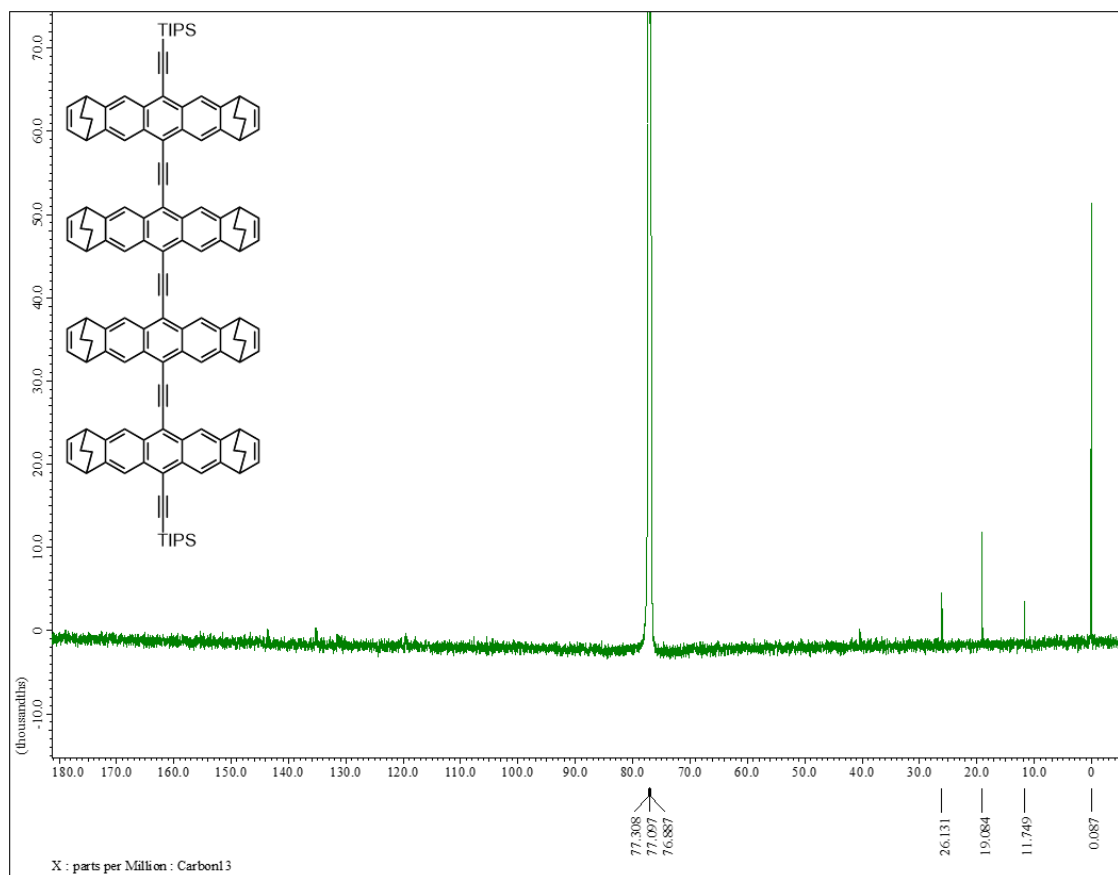
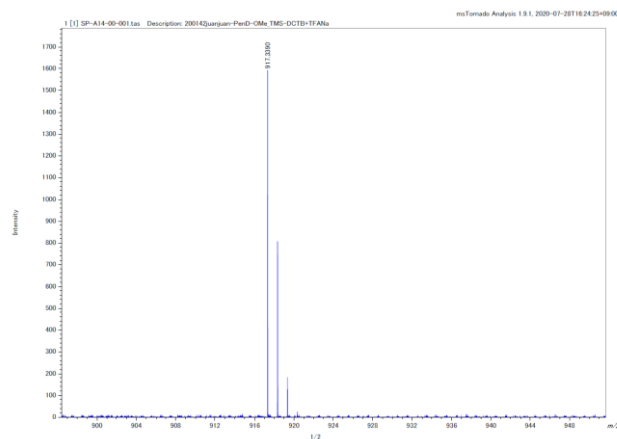


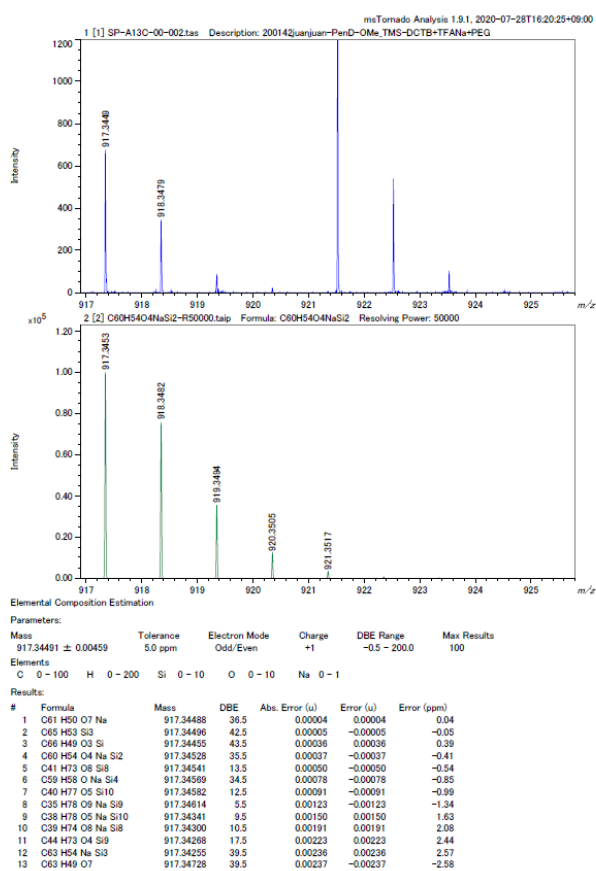
Figure S17. ^{13}C spectrum of BCOD 4mer. (CDCl_3 , 600MHz)

4-8-4. MS spectrum

a)

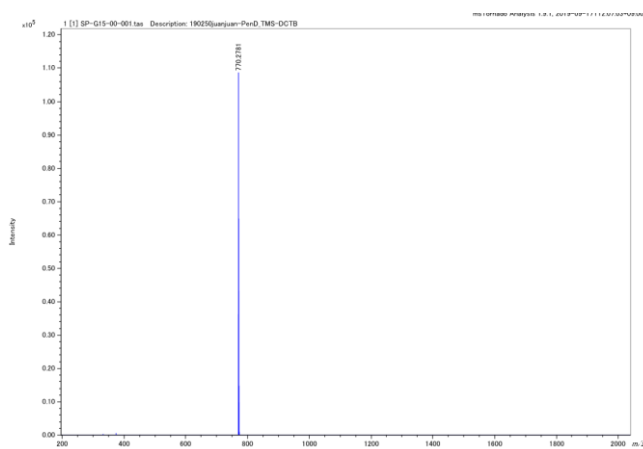


b)

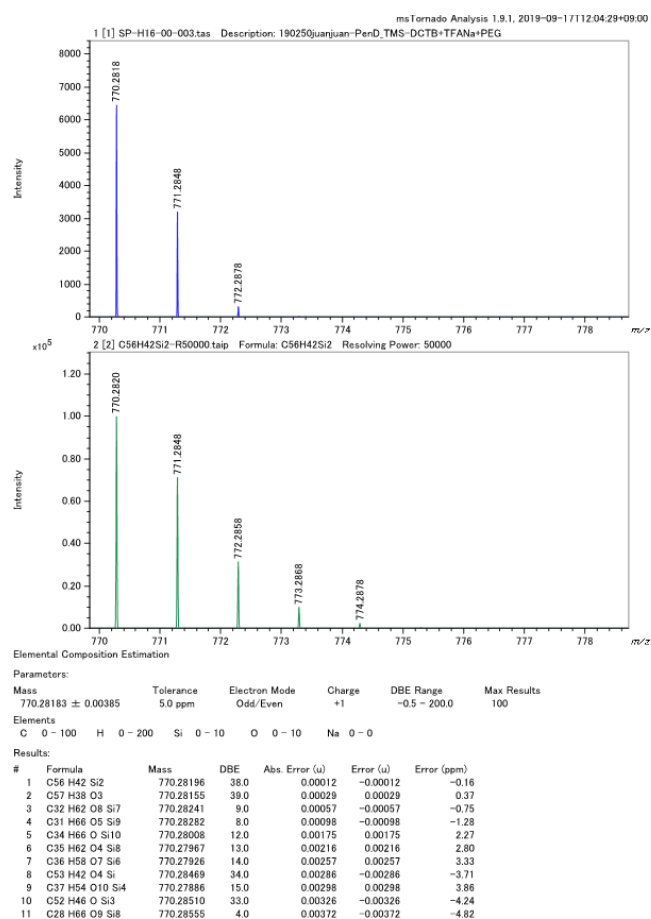


FigureS18. (a) MS spectrum and (b) HRMS spectra of PenD-OMe.

a)

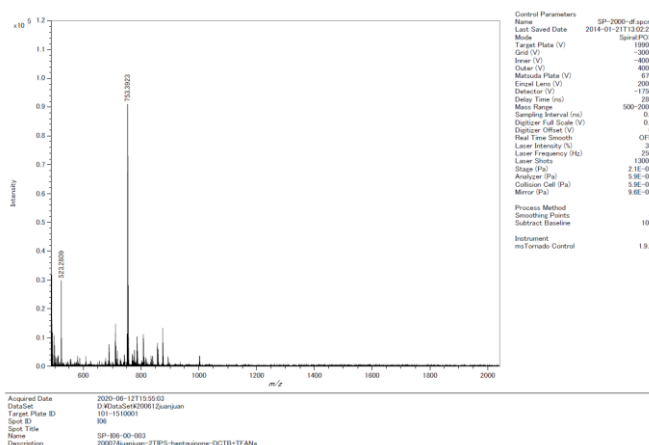


b)

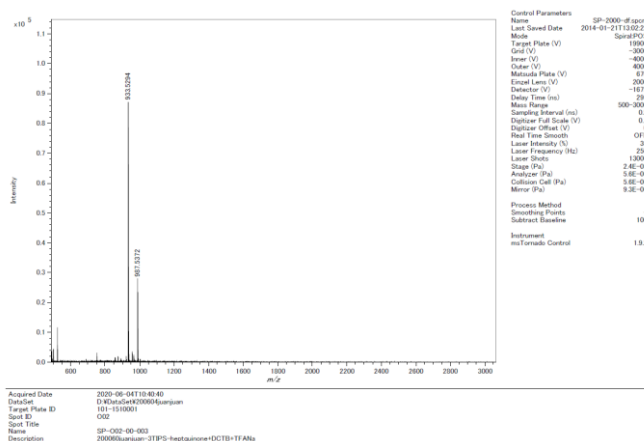


FigureS19. (a) MS spectrum and (b) HRMS spectra of TMS-PenD.

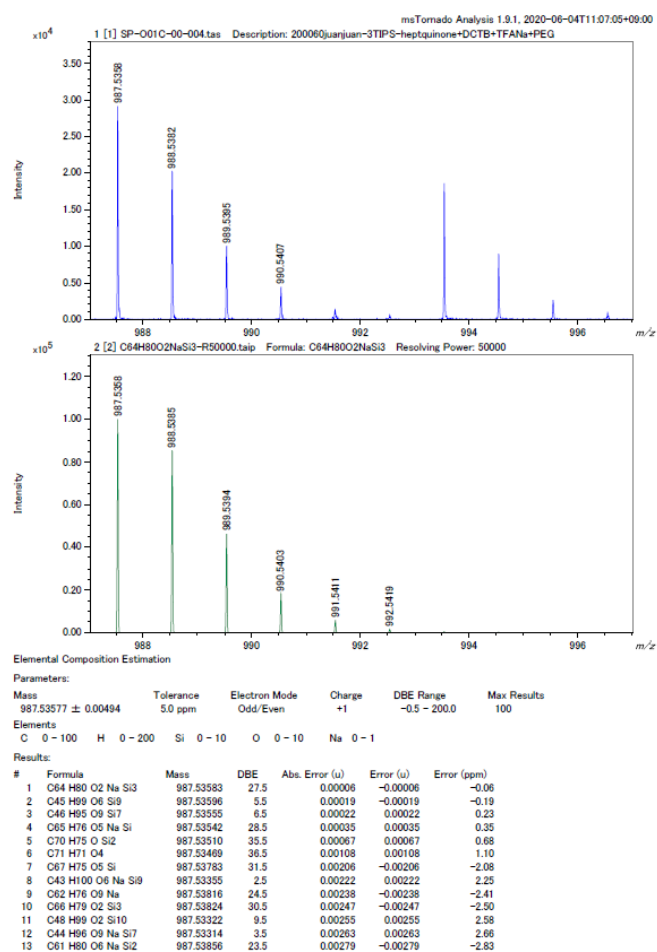
a)



a)

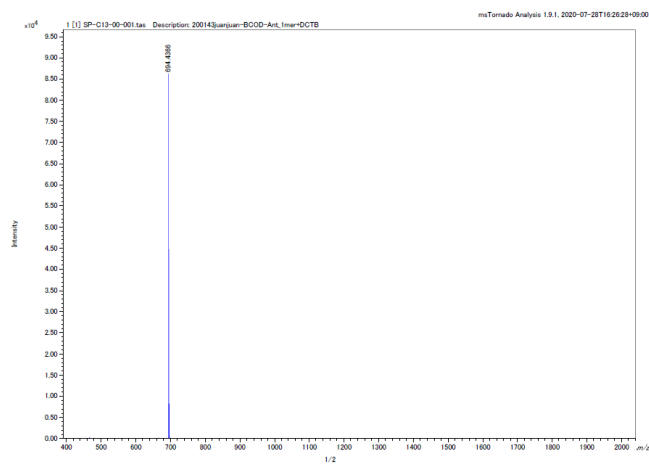


b)

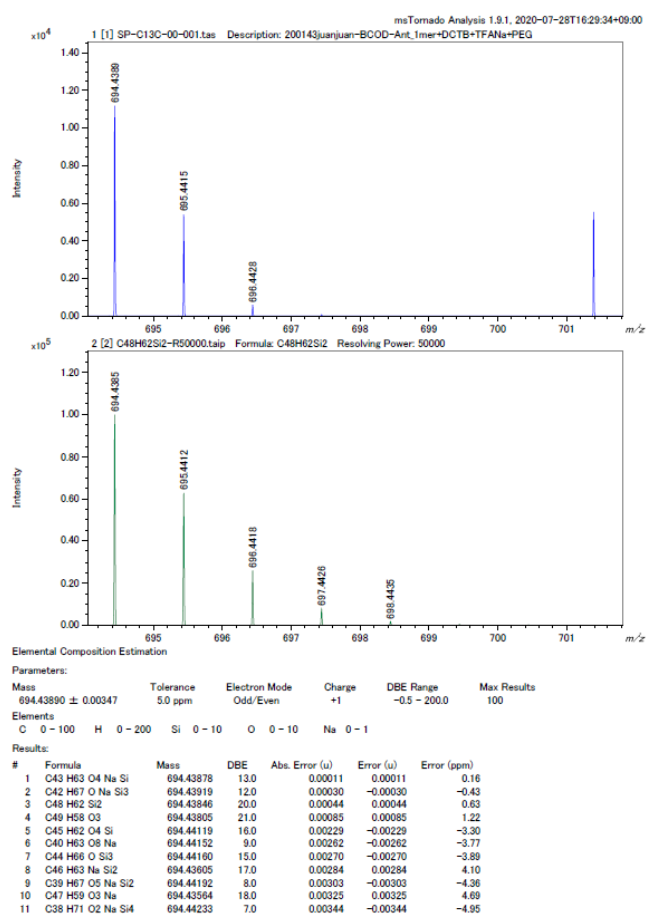


FigureS21. (a) MS spectrum and (b) HRMS spectra of Hept2.

a)

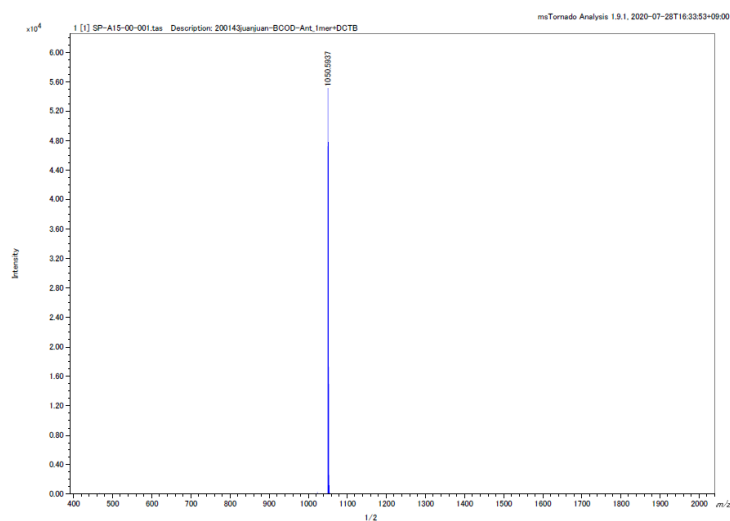


b)

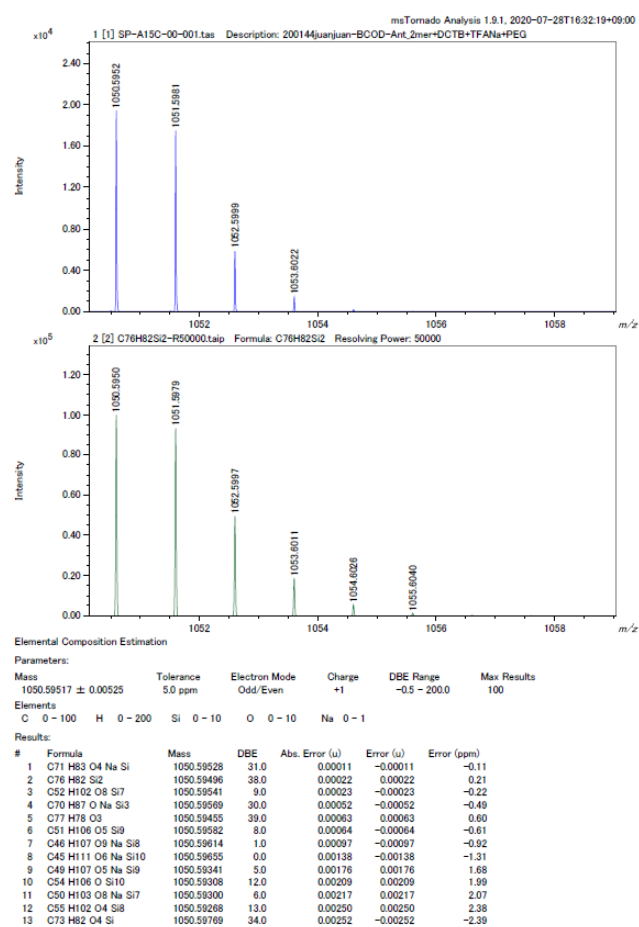


FigureS22. (a) MS spectrum and (b) HRMS spectra of BCOD 1mer.

a)

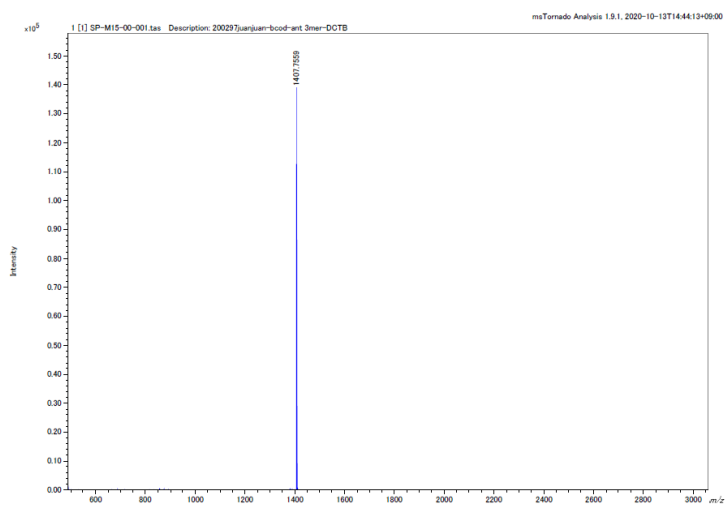


b)

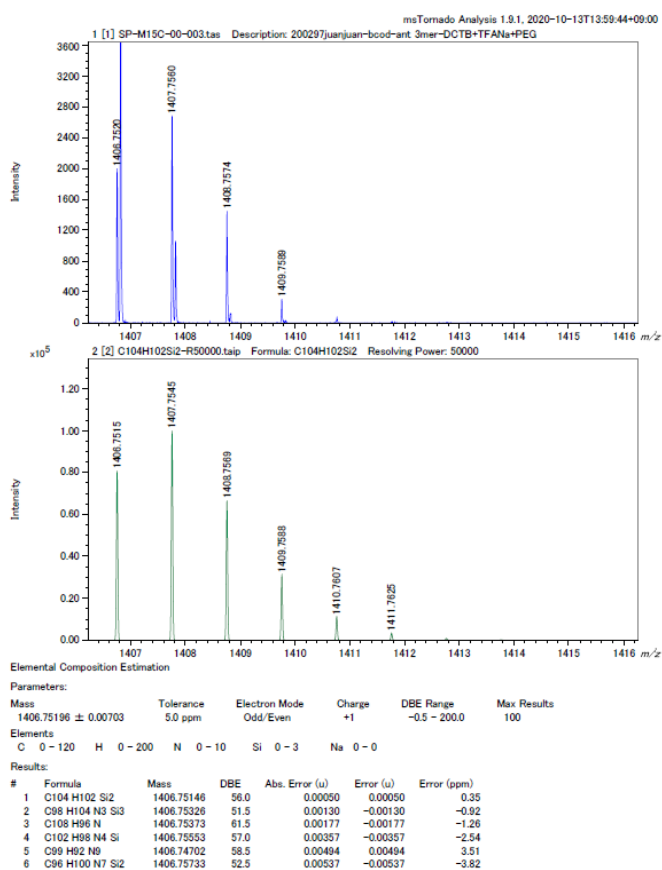


FigureS23. (a) MS spectrum and (b) HRMS spectra of BCOD 2mer.

a)

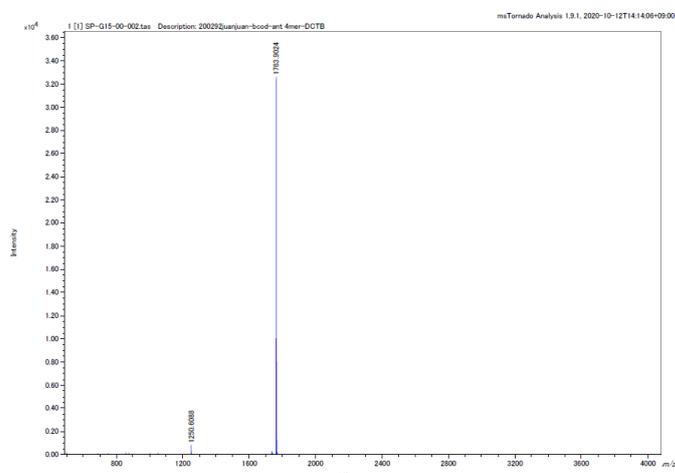


b)

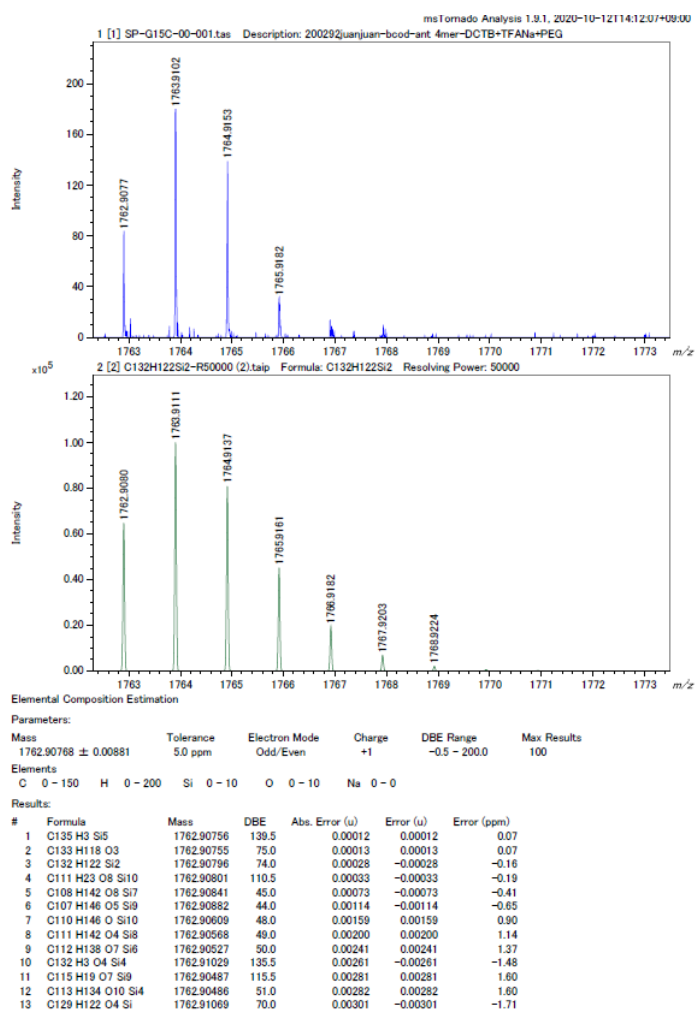


FigureS24. (a) MS spectrum and (b) HRMS spectra of BCOD 3mer.

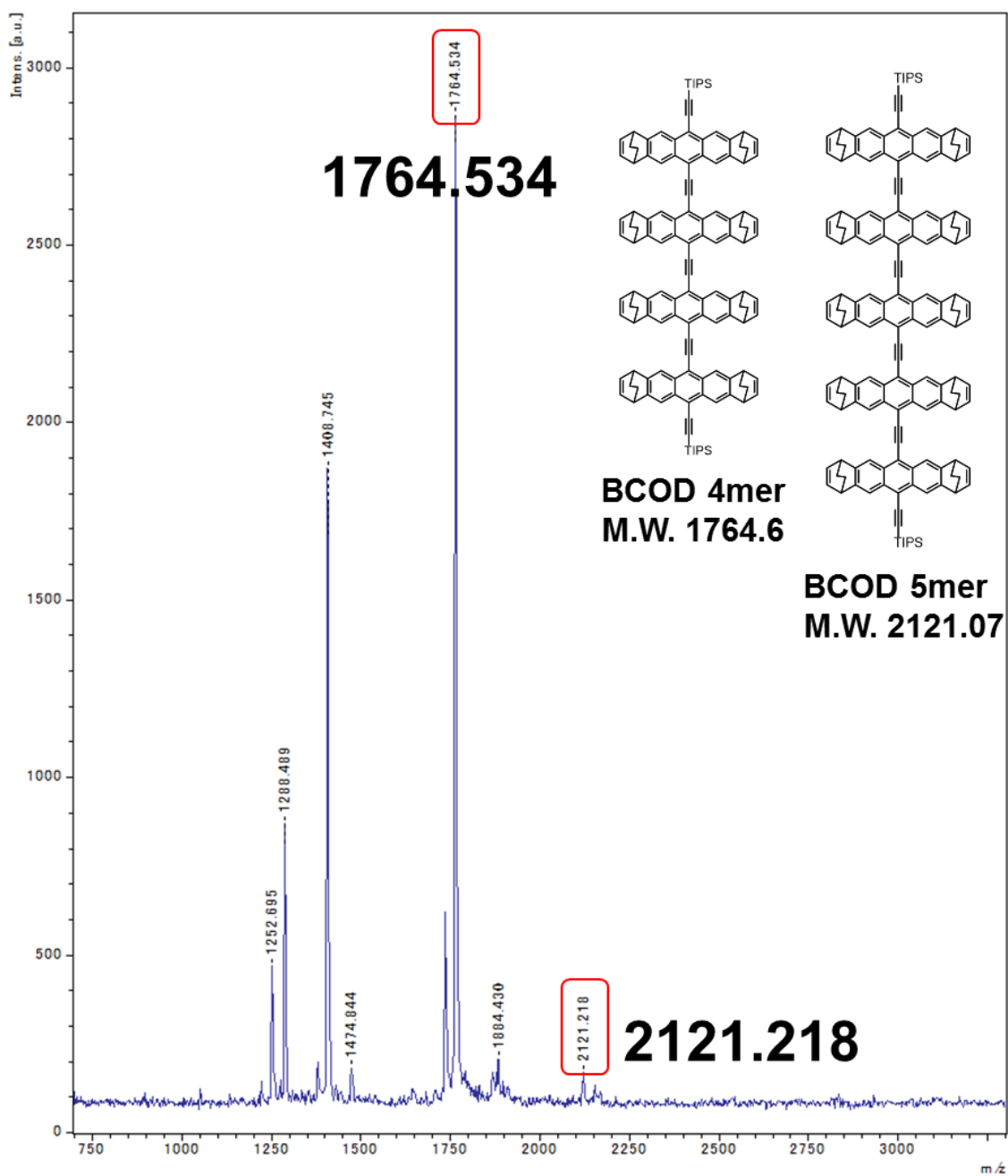
a)



b)



FigureS25. (a) MS spectrum and (b) HRMS spectra of BCOD 4mer.



FigureS26. MS spectrum of BCOD 5mer after purification with column chromatography.

4-9. Reference

- (1) X. Zhang, X. Jiang, J. Luo, C. Chi, H. Chen, J. Wu, *Chem. Eur. J.* **2010**, *16*, 464–468.
- (2) K. Kawano, H. Hayashi, S. Yoshimoto, N. Aratani, M. Suzuki, J. Yoshinobu, J. and H. Yamada, *Chem. Eur. J.* **2018**, *24*, 14916–14920.
- (3) K. Gilmore, I. V. Alabugin, *Chem. Rev.* **2011**, *111*, 6513–6556.
- (4) D. Lehnerr, A. H. Murray, R. McDonald, R. R. Tykwinski, *Angew. Chem. Int. Ed.* **2010**, *122*, 6326–6330.
- (5) V. S. Barlier, C. W. Schlenker, S. W. Chi, M. E. Thompson, *Chem. Commun.* **2011**, *47*, 3754–3756.
- (6) J. Anthony, A. M. Boldi, C. Boudon, J. P. Gisselbrecht, M. Gross, P. Seiler, C. B. Knobler, F. Diederich, *Helv. Chim. Acta*, **1995**, *78*, 797–817.
- (7) S. Kim, S. Kim, T. Lee, H. Ko, D. Kim, *Org. Lett.* **2004**, *6*, 3601–3604.
- (8) S. Kim, Y. M. Lee, H. R. Kang, J. Cho, T. Lee, D. Kim, *Org. Lett.* **2007**, *9*, 2127–2130.
- (9) J. P. Marino, H. N. Nguyen, *J. Org. Chem.* **2002**, *67*, 6841–6844.
- (10) R. David Crouch, *Tetrahedron*, **2004**, *60*, 5833–5871.
- (11) J. E. Anthony, J. S. Brooks, D. L. Eaton, S. R. Parkin, *J. Am. Chem. Soc.* **2001**, *123*,

9482–9483.

(12) C. Reus, M.P. Lechner, M. Schulze, D. Lungerich, C. Diner, M. Gruber, J. M.Stryker, F. Hampel, N. Jux, N. and R. R. Tykwinski, *Chem. Eur. J.* **2016**, *22*, 9097–9101.

(13) D. Chun, Y. Cheng, F. Wudl, *Angew. Chem. Int. Ed.* **2008**, *47*, 8380–8385

(14) M. M. Payne, S. R. Parkin, J. E. Anthony, *J. Am. Chem. Soc.* **2005**, *127*, 8028–8029.

(15) I. Kaur, N. N. Stein, R. P. Kopreski, G. P. Miller, *J. Am. Chem. Soc.* **2009**, *131*, 3424–3425.

(16) B. Purushothaman, S. R. Parkin, J. E. Anthony, *Org. Lett.* **2010**, *12*, 2060–2063.

(17) H. Yamada, D. Kuzuhara, M. Suzuki, H. Hayashi, N. Aratani, *Bull. Chem. Soc. Jpn.* **2020**, *93*, 1234–1267.

(18) Tanaka, N. Aratani, D. Kuzuhara, S. Sakamoto, T. Okujima, N. Ono, H. Uno, H. Yamada, *RSC Adv.* **2013**, *3*, 15310–15315.

Chapter 5

General Conclusion

This dissertation focuses on the oligoarylethylenes which are π -conjugated triple bond-containing systems. Tetrabenzoporphyrin (**BP**) and acene derivatives were chosen as the molecular cores of oligoarylethylenes.

Firstly, as the simple ethynylene substituted π -conjugated system, the charge transport property of triisopropylsilylethynylene substituted **BP** derivatives was investigated. The results showed **TIPS-BP** gave one-dimensionally extended columnar packing motif. Single crystal field-effect transistor of free-base **TIPS-BP** exhibited clearly better hole mobility ($2.16 \text{ cm}^2 \text{ V}^{-1} \text{ s}^{-1}$) than its metal complexes (ca. $0.1 \text{ cm}^2 \text{ V}^{-1} \text{ s}^{-1}$), with the efficient charge transports through π - π stacking of tetrabenzoporphyrin units.

Secondly, the efficient synthetic strategy and characterization of a series of ethynylene-bridged acene oligomers was developed. The single-crystal X-ray analysis of oligomers, suggested the free rotation of ethynylene units in the solution state. Theoretical calculations unveiled the intermolecular interaction by means of the charge transfer integrals between HOMOs. Finally, by fabricating the BGTC OFETs, the trimer was found to show the best mobility ($0.14 \text{ cm}^2 \text{ V}^{-1} \text{ s}^{-1}$) among the oligomers employed, implying that the balance of π -conjugation and packing quality played an important role in the case

of anthracene oligomers with ethynylene-bridges at 9,10-positions.

Then, the extension of π -conjugation for ethynylene-bridged acenes was further studied. Precursors of ethynylene-bridged heptacene dimer were obtained from heptacene quinone in one pot. In addition, the conventional reaction with lithiated TIPSEthynylene and BCODquinone followed by the reductive aromatization afforded oligomers of ethynylene-bridged pentacene precursor. This discovery provides a great clue to the effective synthetic approach of ethynylene-bridged π -conjugated systems.

Overall, this study developed the synthesis of π -conjugated ethynylene-bridged systems. In addition, the knowledge of relationship between electronic properties and repeating π -conjugated units will contribute to the development of efficient organic semiconductors including oligoarylethynylene systems toward achieving highly efficient organic electronic devices.

List of Achievements

Publication

1. Synthesis and evaluation of charge transport property of ethynylene-bridged anthracene oligomers

Juanjuan Zhu, Hironobu Hayashi, Meng Chen, Chengyi Xiao, Kyohei Matsuo, Naoki Aratani, Lei Zhang, and Hiroko Yamada

Macromol. Chem. Phys., **2021**, 222, 2100024/1–10.

2. Single crystal field-effect transistor of tetrabenzoporphyrin with one-dimensionally extended columnar packing motif exhibiting efficient charge transport property

Juanjuan Zhu, Hironobu Hayashi, Meng Chen, Chengyi Xiao, Kyohei Matsuo, Naoki Aratani, Lei Zhang, and Hiroko Yamada

J. Mater. Chem. C, **2021**, in press.

3. Effect of edge functionalization on the bottom-up synthesis of nano-graphenes

Manabu Ohtomo, Hironobu Hayashi, Kenjiro Hayashi, Hideyuki Jippo, **Juanjuan Zhu**, Ryunosuke Hayashi, Junichi Yamaguchi, Mari Ohfuchi, Hiroko Yamada, and Shintaro Sato

ChemPhysChem., **2019**, 20, 3366–3372.

International Conferences

1. Synthesis and evaluation of charge transport property of ethynylene-bridged anthracene oligomers

Juanjuan Zhu, Hironobu Hayashi, Hiroko Yamada

10th International Conference on Molecular Electronics & BioElectronics, Nara, Japan, June, 2018

2. Evaluation of charge transport property of ethynylene-bridged anthracene oligomers

Juanjuan Zhu, Hironobu Hayashi, Hiroko Yamada

Materials Research Meeting 2019, Yokohama, Japan, December, 2019

Foundation

1. 2018 NAIST Grant-in-Aid (150,000 JPY)

Juanjuan Zhu, Hironobu Hayashi, Hiroko Yamada

Synthesis of nonplanar PAHs including benz[a]anthracene or pentaphene by using precursor method for organic field effect transistors

2. 2019 NAIST Grant-in-Aid (400,000 JPY)

Juanjuan Zhu, Hironobu Hayashi, Hiroko Yamada

Synthesis and evaluation of charge transport property of ethynylene-bridged anthracene oligomers

Acknowledgements

I would like to express my special thanks of gratitude to Prof. Hiroko Yamada and Asst. Prof. Hironobu Hayashi who gave me precious guidance, tremendous encouragement, and advice throughout my study at NAIST.

I would like to thank Prof. Hiroharu Ajiro and Prof. Shun Hirota for letting me defense be an enjoyment moment, and for their brilliant comments and suggestions.

I would like to express my deep and sincere gratitude to Ass. Prof. Naoki Aratani for giving me golden advice in X-ray single crystal analysis.

I would like to thank Asst. Prof. Kyohei Matsuo for the kind guidance in ADF calculation.

I would like to express my gratitude to Prof. Lei Zhang, and his lab members in the Beijing University Chemical Technology, Beijing for giving me an opportunity to study with them.

I would like to thank Dr. Chengyi Xiao for the valuable advice in TEM and SAED analysis.

I acknowledge the contribution of NAIST technical staff including Mr. Shohei Katao, Mr. Fumio Asanoma, Ms. Yoshiko Nishikawa, Ms. Sakiko Fujita, and Ms. Tomoko Ohno for the XRD and X-ray single crystal analyses, ¹³C NMR (DEPT) analyses, the mass

spectroscopy measurements and the TEM measurement, respectively.

I would like to thank Japan Student Services Organization for financially supporting me during my master's and doctoral course.

Last but not least, I would like to express the deepest appreciation to my family.

Juanjuan Zhu